New approaches to modulate VPS34 PI 3-kinase activity

Elena Rebollo Gómez

Supervisor:

Prof. Bart Vanhaesebroeck

UCL Cancer Institute

Doctor Of Philosophy

2020

Declaration

I, Elena Rebollo Gómez, confirm that the work presented in this thesis is my own. Where information has been derived from other sources, I confirm that this has been indicated in the thesis.

Abstract

Phosphoinositide 3-kinases (PI3Ks) regulate signalling and vesicular trafficking [1-3]. Mammals have eight PI3K isoforms divided in three classes. Class I PI3Ks, frequently mutated in different pathologies [4-6], are the most studied PI3Ks and regulate signalling downstream of membrane receptors and monomeric small GTPases. In contrast, class II and III are involved in vesicular trafficking and their signalling roles have recently started to be uncovered.

VPS34, the sole class III PI3K member, is found in different protein complexes that regulate autophagy, endosomal sorting, phagocytosis and signalling [7]. VPS34 functions have been studied using approaches that deplete VPS34.Those do not distinguish its scaffolding *versus* kinase-dependent functions, and result in VPS34-associated protein depletion, which has confounded the interpretation of the phenotypes.

The aim of this study was to develop different ways of modulating VPS34 activity using two models. First, using a genetic approach, the host laboratory developed a knock-in strategy to inactivate VPS34 lipid kinase activity in mice while preserving its scaffolding function. This was a theoretical targeting approach based on VPS34 protein structure, but the resulting knock-in allele remained functionally uncharacterised. Using mammalian cells, I characterise this truncated version of VPS34 whereby exon21 is deleted and showed that is expressed and lacks lipid kinase activity.

The second approach was using the nanobodies' properties to stabilise VPS34 complexes in different conformational states to obtain VPS34 complex-specific binders, stabilizing them in active or inactive state. This is particularly relevant since pharmacological inhibition of VPS34 kinase activity disables the functions of all VPS34 complexes. Here, by overexpression in mammalian cells, I characterise nanobodies that can bind different VPS34 complexes. I focus on CI60, a VPS34 complex I-specific binder nanobody and uncover its potential as research tool to reveal unknown complex I functions and as autophagy inducer, although further experiments are required to fully address this function.

Impact statement

VPS34 is the sole member of class III PI3K. VPS34 is found and functions as part of multiprotein complexes. Numerous knock-out (KO) mouse models highlighted the importance of VPS34 in maintaining tissue homeostasis. However, loss of VPS34 often results in the destabilisation of the core components of the VPS34 complexes raising the question of whether the phenotype observed is due to VPS34 ablation itself or to the loss of expression of the binding partners.

The aim of this work was to find new ways of modulating VPS34 activity without affecting its scaffolding role. The first approach -developed by the host laboratory- was targeting exon21 located in the kinase domain, expressing, in theory, a truncated protein but kinase inactive. This strategy has been previously reported in different conditional mouse models without being fully characterised [8-11]. Here, I characterised VPS34 cDNAs harbouring this deletion and confirmed *in vitro* that this truncated version is expressed in cells and lacks its kinase activity. This work is currently included in a manuscript in preparation as part of collaboration with K.Okkenhaug lab.

The VPS34-dependent functions are mediated via association with its exclusive partners (defining the two main functional complexes) [12, 13]. Currently, no specific tools are available to assess the function of each specific complex. In this study, I described a way to achieve this by using nanobodies that bind specific VPS34 complex. I show through cell based studies that some nanobodies are specific binders of either complex I, VPS34 core complex (VPS34, VPS15 and Beclin 1), or complex I and II. I focus on a particular nanobody that specifically binds complex I, revealing its potential to specifically induce autophagy and track VPS34 complex I activity in mammalian cells. This study opens new avenues on how to modulate and track distinct VPS34 complexes in cells, and undoubtedly will increase the current knowledge of its biology. Importantly, the contact site of such nanobodies with the specific VPS34 complex could eventually reveal some critical information that can be exploited to develop allosteric small molecule inhibitor or activator of each complex. This is relevant since modulating autophagy in certain disease context (cancer, neurodegenerative and immune diseases or aging) [14-17] appears critical yet remains challenging.

In addition, this study has encouraged collaboration between Professor B. Vanhaesebroeck's laboratory with Professor R.Williams' laboratory (MRC-LMB), a world expert in PI3K structural biology, and the Vlaams Instituut voor Biotechnologie (VIB). A short stay in V. Haucke's laboratory (FMP) also strengthened my knowledge in cellular imaging techniques important for the functional assays of this study.

Furthermore, thanks to the European grant that has funded me during this study, the inputs from excellent scientists in the PI3K field have been extremely useful, which have helped to develop a wide interactive network for future colloboration.

Acknowledgement

I would like to start by sincerely thanking my supervisor Bart Vanhaesebroeck, for the opportunity of doing my PhD at the Cell Sig lab, and his supervision. I can honestly say that your vision and perspective of the world of science has changed mine.

A very big thank you to Benoit, who, even though has probably forgotten more meetings than the ones we had, was always trying to make up for those, and was always supportive. You are a great crazy scientist and an amazing person, and I would have not reached the acknowledgment page on my thesis without you.

I would also like to thank the rest of the Cell Sig members: Elena, my mental health would have not been the same without you. Thank you for your friendship and for being my support these years both empathically and scientifically (if this and this are like that, then don't you think it would make sense to..?). Also, for being the best at doing calendars. Evelyn, and Haris, thank you for these years of PhD, dealing with my musical taste in the lab, and simply being there. Especially Evelyn, thanks for arriving to the lab just one month after me. I don't know what the thesis writing would have been if we wouldn't have been able to complain together. Veronica, you are the biggest problem-solver and you don't get enough recognition for it! I am very thankful for your help all through the project and for, together with Elena, making me feel at home. Priyanka, thank you for always offering a hand, whether explaining science-related concepts, life-related concepts, or cooking wonderful recipes. York, thank you for introducing me to the world of accuracy and the Friday pub. I have learnt a lot from you. Georgia and Victoria, thanks for coping with me and Dolly, sharing laughs, and for teaching me a thing or two about English. Thanks to Daniele, who is the most patient person I have ever known, for his tips and help in the lab. Grace, Sarah, Wayne and Lizzy, thanks for coping with all my jokes so gracefully. Also, thank you to Alex for proofreading the most boring part of a thesis. Thank you to the past members of the lab, Sandra, who helped me find my way in and gave me one of the best advices I have ever received, and Emily, for knowing what I wanted to say before I even articulated it ,and teaching me about immunity in the day-to-day life.

I am also very grateful for our floor neighbours. Manolito, Manolo, and María, thanks for the help and laughs during these years. It would have not been the same without you. Thanks so much to Sean as well for your friendship and good mood no matter what. You managed to make me smile every time.

Big thanks as well to the rest of the Cancer Institute members who helped me with advices, reagents and laughs, especially Celia and Itziar. Also, Jiten, Sam and Yanping for their help with the live imaging, confocal and flow cytometry.

Thank you to Roger Williams and Yohei Ohashi for their input and work in the structural part of the study, and for the fruitful discussions about my project.

I would like to thank INSTRUCT, part of the European Strategy Forum on Research Infrastructures (ESFRI), and the Research Foundation - Flanders (FWO) for their support to the Nanobody discovery, and Nele Buys for the technical assistance during Nanobody discovery.

My PhD thesis is part of a project that has received funding from the European Union's Horizon 2020 research and innovation programme under grant agreement Nº675392. I truly appreciate the opportunity of being part of this network. I have grown scientifically and personally from this experience, and I am very grateful. Thank you to all the group leaders for discussion, especially Volker Haucke, for everything that I learnt during my secondment at the FMP from him and his group. A big thank you to all my fellow PhD-PI3Ks: Abhi, Albie, Christina, Erhan, Fernanda, Iosif, Jasmina, Monica, Paula, Piotr, Piotr, Silvia and Vasugi. You made me enjoy every meeting we had together.

I would like to thank Christina for making her way (as always) first to my lab bench and then my life. Thanks for being such an amazing friend and unconditional support for me (and teaching me your kitchen skills). I don’t know what I would have done without our friendly rivalry, but I could have not got here without you.

Special thanks to Paula, the queen of the PtdIns3P staining, for the help you gave me with it and for being the calmest and down to Earth person I know, Giulia for sharing KitKats after 12 at night in the lab, and Albie for

just being so you. Thanks so much for making my stay in Berlin so wonderful.

I also want to thank those that helped me reach the PhD, especially Prof. Begoña Colás and Prof. Pedro Bonay.

Thanks to my friends at home, who have constantly supported me, and always found the time to meet when I travelled back to Spain; and to the friends I have made in London, it has been an amazing time. I would like to thank Izaskun and Paula in particular for their help with the thesis writing.

Gracias a mis padres, Sara, mi abuela y mi tío por apoyarme incondicionalmente y aguantarme (sé que no siempre es fácil) durante todo el proceso. No hubiera llegado nunca hasta aquí de no haber sido por vosotros.

Por último, pero para nada menos importante, gracias a Laura, por haber sido mi constante durante estos años. Has creído en mí, me has apoyado y me has dado todo lo que necesitaba. Me siento muy agradecida por compartir mi vida contigo. No podría haber conseguido todo esto sin ti.

This thesis is part of a project that has received funding from the European Union's Horizon 2020 research and innovation programme under grant agreement Nº675392.

Table of Contents

List of Figures

List of Tables

Abbreviations

ABD domain	Adaptor-binding domain
ALR	Autophagosome-lysosome reformation
Ambra1	ATG14L activating molecule in Beclin 1-regulated autophagy protein 1
AMPK	5’ AMP-activated protein kinase
APPL1	Adaptor protein, phosphotyrosine interacting with PH domain and leucine zipper 1
ATG13	Autophagy related 13
ATG14L	Autophagy related 14 like
ATG16L1	Autophagy related 16 like 1
BATS	Barkor/ATG14L autophagosome targeting sequence
BC	Both complex binders
Bcl2	B-cell lymphoma 2
Bcl-xL	B-cell lymphoma-extra large
BH3	Bcl-2 homology 3 domain
BIF-1	Bax-interacting factor 1/endophilin B1
C	Core binder
CC	Coiled-coil domain
CDK	Cyclin dependent kinase
CDR3	Complementarity determining region 3
CI	Complex I binder
CII	Complex II binder
CME	Clathrin- mediated endocytosis
DAPK	Death-associated protein kinase
DEL21	Deletion exon21
DFCP1	Double FYVE-containing protein 1
Drp1	Dynamin-related Protein
EEA1	Early endosome antigen 1

EGFR	Epidermal growth factor receptor
eNOS	Endothelial nitric oxide synthase
ER	Endoplasmic reticulum
ESCRT	Endosomal sorting complex required for transport
FIP200	FAK family kinase-interacting protein of 200 kDa
FYVE	Fab 1, YOTB, Vac 1, EEA1 (proteins where it was found)
FYVE-CENT	ZFYVE26, Zinc Finger FYVE-Type Containing 26
GAPs	GTPase-activating proteins
GPCRs	G protein-coupled receptors
GSK3β	Glycogen synthase kinase 3
GEF	Guanidine exchange factor
HDX-MS	Hydrogen-Deuterium eXchange-Mass Spectrometry
HEAT	Huntingtin, elongation factor 3, A subunit of protein phosphatase 2A TOR1 (four proteins originally found containing this repeat motif)
IF	Immunofluorescence
INTDEN	Integrated density
IP	Immunoprecipitation
IR	Insulin Receptor
KI	Knock-in
KO	Knock-out
LIR	LC3 interacting region
MEFs	Mouse embryonic fibroblast
MS	Mass spectrometry
MTDR	Mitotracker deep red
mTORC1	Mammalian target of rapamycin complex 1
mTORC2	Mammalian target of rapamycin complex 2
NAG	Neuroblastoma-amplified gene

Nb	nanobody
NRBF2	Nuclear receptor binding factor 2
OCRL	Oculocerebrorenal syndrome of Lowe
OH-group	Hydroxil-group
PACER	Protein associated with UVRAG as autophagy enhancer
PAQR3	Progestin and adipoQ receptor family member III
PDK1	Phosphoinositide-dependent protein kinase-1
PH domain	Pleckstrin homology domain
PI	Propidium Iodide
PI3Ks	Phosphoinositide 3-kinases
PI4Ks	Phosphoinositide 4-kinases
PI5K	Phosphoinositide 5-kinases
PIKFyve	Phosphoinositide Kinase, FYVE-Type Zinc Finger Containing
PIPKI	Type I phosphatidylinositol-4-phosphate 5-kinase
PIs	Phosphoinositides
PROPPIN	*β*-propellers that bind polyphosphoinositide
PtdIns	Phosphatidylinositol
PtdIns3P	Phosphatidylinositol 3-phosphate
PtdIns(3,4)P_2	Phosphatidylinositol 3,4-bisphosphate
PtdIns(3,5)P_2	Phosphatidylinositol 3,5-bisphosphate
PtdIns(4,5)P_2	Phosphatidylinositol 4,5-bisphosphate
PtdIns(3,4,5)P_3	Phosphatidylinositol (3,4,5)-trisphosphate
PTM	Post-translational modifications
PX domain	Phox homology domain
RBD domain	RAS-binding domain
RHEB	Ras homolog enriched in brain
RILP	Rab-interacting lysosomal protein

RINT1	RAD50 Interactor 1
RUBICON	RUN domain and cysteine-rich domain containing Beclin-1-interacting protein
SARs	Selective autophagy receptor
Snap29	Synaptosomal-associated protein 29
SNARE	Soluble NSF attachment protein receptor
S.O.C.	Super optimal broth
Stx17	Syntaxin17
TFEB	Transcription factor EB
TMRE	Tetramethylrhodamine
Treg	Regulatory T cell
TSC 1/2	Tuberoesclerosis complex
ULK1	Unc-51 like autophagy activating kinase 1
UVRAG	Ultraviolet radiation resistance associated gene
Vamp8	Vesicle-associated membrane protein 8
VPS15	Vacuolar protein sorting 15
VPS34	Vacuolar protein sorting 34
vps38	Yeast homolog of UVRAG
WB	Western blot
WIPI	WD-repeat protein interacting with phosphoinositide
WT	Wild type
ZW10	Zeste-white 10

1 Introduction

1.1 Phosphoinositides (PIs)

Phosphoinositides are lipids that belong to the phospholipid family, which comprises lipids with a glycerol molecule bound to two fatty acids, and an additional group (inositol in the case of PIs). Although they have been known for over forty years, it is only in the last ten to twenty years that we have started to understand their relevance. They have been shown to be crucial as second messengers in signal transduction, vesicular trafficking, lipid distribution and metabolism [3]. PIs (Table 1.1) derive from the precursor phosphatidylinositol (PtdIns), synthesised at the endoplasmic reticulum (ER) [18], by a number of phosphorylation and dephosphorylation events. These events take place by the action of kinases or phosphatases that modulate the activity of those protein effectors, which are localised intracellularly and regulate different functions on the cell [3, 19].

PIs have a high turnover, and their localisation to different subcellular compartments contributes to the identity of their membranes [20]. For instance, the phosphoinositide species phosphatidylinositol 3-phosphate (PtdIns3P) is more abundant in early endosomes or autophagosomes, while phosphatidylinositol (3,4,5)-trisphosphate (PtdIns(3,4,5)P_3) is more abundant at the plasma membrane. This high turnover rate is achieved by a tight regulation carried out by various phosphoinositide kinases and phosphatases that phosphorylate or dephosphorylate PIs hydroxil-group (OH-group) in their inositol ring at the 3, 4 or 5 position [21].

Phosphoinositide kinases family includes phosphoinositide 3-kinases (PI3Ks), for those that phosphorylate the inositol ring in the 3rd position; phosphoinositide 4-kinases (PI4Ks), which phosphorylate in the 4th position; and finally, the phosphoinositide 5-kinases PIKFyve and PIPKI α/β/γ, which phosphorylate in the 5th position. On the other hand, phosphatases are divided in groups in a similar manner to that of kinases, and therefore, can be separated in 3-phosphatases, 4-phosphatases, and 5-phosphatases. However, there is also a family of phosphatases that are able to dephosphorylate in more than one position, the Sac1 family. Because of the scope of our study, phosphatases and kinases

phosphorylating the 4th or 5th position of the inositol ring will not be further discussed here and the reader is referred to references [3, 21, 22] for further information on these enzymes. A summary of each group members is presented in Table 1.1.

Table 1.1 Summary table of the different groups that comprise PI kinases and PI phosphatases. The PI substrates of the most relevant kinases/phosphatase are shown in Fig. 1.1. For a complete review please refer to [3].

PI KINASES							
PI3K							
CLASS I				CLASS II			CLASS III
PIK3Cα	PIK3Cβ	PIK3Cγ	PIK3Cδ	C2α	C2β	C2γ	Vps34 (PI3KC3)
PI4K							
PI4KII		PI4KIII		PIPKII			
PI4KIIα	PI4KIIβ	PI4KIIIα	PI4KIIIβ	PIPKIIα	PIPKIIβ	PIPKIIγ	
PI5K							
PIKFyve	PIPKI						
	PIPKI α	PIPKI β	PIPKI γ				

PI PHOSPHATASES								
3-phosphatases								
Similar catalytic domain			Myotubularins					
PTEN	VSPs	TPIP	MTM1	MTMR3	MTMR6	MTMR14	Pseudophosphatases	
			MTM1 MTMR1 MTMR2	MTMR3 MTMR4	MTMR6 MTMR7 MTMR8		MTMR5, MTMR9, MTMR10, MTMR11, MTMR12, MTMR13	
4-phosphatases								
Substrate PI(3,4)P_2			Substrate PI(4,5)P_2					
INPP4A		INPP4B		TMEM55A			TMEM55B	
5-phosphatases								
Type I	Type II						Type III	Type IV
INPP5A	Synaptojanins	OCRL	INPP5B	INPPJ5	SKIP		SHIP-1	SHIP-2	INPP5E
SAC1 family								
Sac1	Fig4/Sac3						INPP5F	

There are seven species of PIs in mammals, which vary in their phosphorylation status. These molecules contribute very little to the total lipid content in eukaryotic cell membranes with percentages varying between 20% and even less than 10%, depending on the tissue and the

cells [3, 23]. Near to 5% of cellular PIs are phosphorylated at the 4-position, and another 5% is phosphorylated at both the 4- and 5-positions. However, regarding the 3-position, less than 0.25% of the total inositol-containing lipids are phosphorylated at this site. This is consistent with a more functional role of these lipids than scaffolding [3, 23]. The various classes of PIs and kinases/phosphatases that contribute to their turnover are summarized in Fig. 1.1

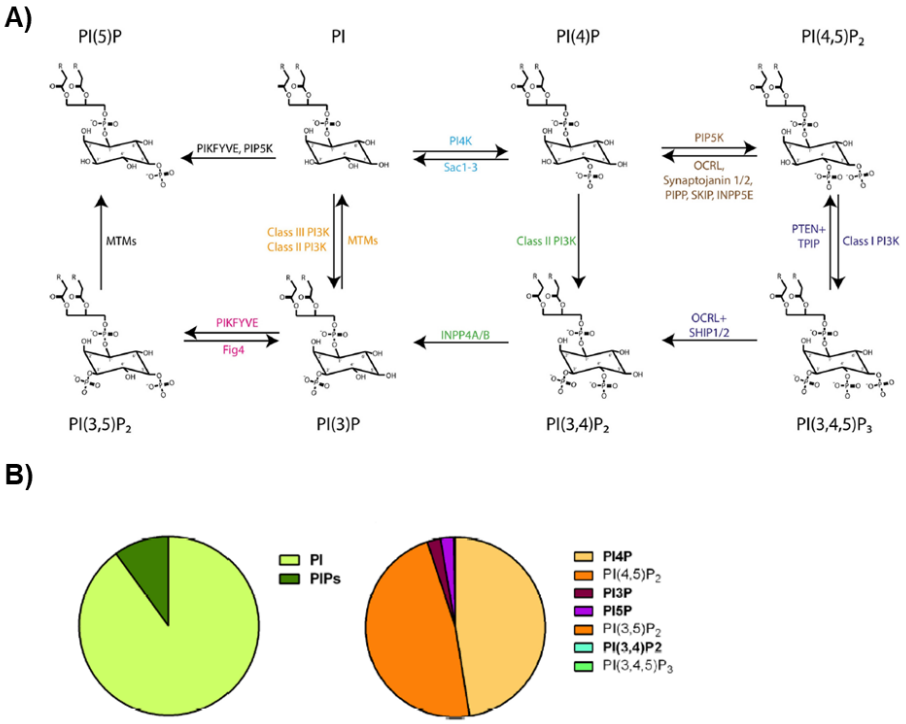

Fig. 1.1. Summary of PI species. A) Different PI species and their conversion. Taken from Wallroth et al. (2018) [21].B) Relative abundance of PIs in animal cells. Taken from Raghu et al. (2019) [24].

These different phosphoinositide species act as second messengers that regulate intracellular membrane trafficking by directing the localisation and activity of effector proteins. These proteins possess certain domains that have high affinity for a given phosphoinositide (for instance FYVE, PX or PROPPIN domains for PtdIns3P or PH domain for PtdIns(3,4,5)P_3) [25, 26]. The most common mechanism of interaction between these domains is electrostatically, whereby the basic residues within the different domains interact with the phosphate groups of the PIs. In addition to signalling events regulation, PIs also direct cytoskeleton regulation or gating of ion channels [22].

As previously mentioned, PIs have a high turnover, and their regulation and correct interchange is critical to maintain membrane identity and recruit the appropriate partners at any given time [18]. We can find an example of this exquisite regulation at the autophagosome-lysosome fusion, where five different PIs are required. Phosphatidylinositol 4-phosphate (PtdIns4P), are generated by PI4KIIα kinase (facilitated by GABARAP, a member of Atg8 family); phosphatidylinositol 3,5-bisphosphate (PtdIns(3,5)P_2) is obtained by PtdIns3P conversion via PIKfyve; and PtdIns3P, produced by PtdIns(3,5)P_2 turnover at the lysosome by INPP5E. Concomitantly, there is a transient increase of phosphatidylinositol 4,5-bisphosphate (PtdIns(4,5)P_2) at the lysosome, orchestrated by PI5K and required for clathrin/AP-2 assembly, followed by its turnover by the OCRL (oculocerebrorenal syndrome of Lowe) phosphatase to phosphatidylinositol 5-phosphate (PtdIns5P) [27].

The landscape of our knowledge about PIs has changed very recently and the actual scene is starting to be uncovered [21]. For instance, for a long time it was thought that the main PtdIns3P producer was class III PI3K, while recent work shows that PtdIns3P production in basal conditions is probably mainly produced by class II PI3K [28].

1.2 Phosphoinositide 3-kinases

1.2.1 PI3K, an overview

PI3Ks are a family of lipid kinases that phosphorylate the 3-OH group in the inositol ring of distinct species of PIs: PtdIns, PtdIns4P, and PtdIns(4,5)P_2. According to their different substrate specificities and structure, they are divided in three different classes; class I, II and III. In mammals, there are eight different isoforms: class I is divided in four different isoforms named p110α, p110β, p110γ and p110δ; class II in three denominated PI3K-C2α, PI3K-C2β and PI3K-C2γ; and the class III has an unique member, the vacuolar protein sorting 34 (VPS34) [2].

The class I PI3Ks are so far the best characterised and are the target of ongoing drug development efforts due to its implication in cancer, autoimmunity, inflammation and overgrowth syndromes [19]. They are acutely activated by tyrosine kinases, G protein-coupled receptors (GPCRs) and monomeric small GTPases, and are a major regulator of

signal transduction. In contrast, the cellular and organismal roles and signalling of the class II/III PI3Ks are poorly understood [2, 6].

1.2.2 Class I PI3K

From a structural point of view (Fig. 1.2A), class I PI3K are separated in two groups; class IA and IB. Class IA consist on p110α, p110β, and p110δ, and class IB has p110γ as its only representative. This differentiation comes from their regulatory subunit. The regulatory subunit of Class IA PI3Ks is encoded by a gene able to give rise to five different products (p85α, p55α, p50α, p85β and p55γ), whereas the regulatory subunit of class IB is either p84 or p101, which are activated by Gβγ subunits from activated GPCRs [1].

The domains of p110 subunits comprise an N-terminal adaptor-binding domain (ABD), present only in class IA PI3Ks. The ABD domain binds to the regulatory subunit, a RAS-binding domain (RBD) that binds membrane bound GTPases, principally RAS (in the case of p110 α, δ, and γ), or RAC1 or CDC42 (in the case of p110β), and the PI3K core, which consist on a C2, helical, and a catalytic domain. Interestingly, p110β is able to interact as well with Gβγ subunits and activated Rab5, a GTPase found in early endosome [1].

Class IA p110 isoforms are released from their regulatory subunit upon activation by cell surface receptors to phosphorylate $PI(4,5)P_2$ to $PI(3,4,5)P_3$ (also called PIP_3). This, in turn, recruits PH domain-containing effectors, such as the Ser/Thr kinase AKT (also known as PKB -Protein kinase B-), which will be later activated via phosphorylation by phosphoinositide-dependent protein kinase-1 (PDK1) and the mammalian target of rapamycin complex 2 (mTORC2). mTORC2 is insensitive to rapamycin, activates several pro- survival pathways and regulates cytoskeleton dynamics [29] (see Fig. 1.2B).

A)

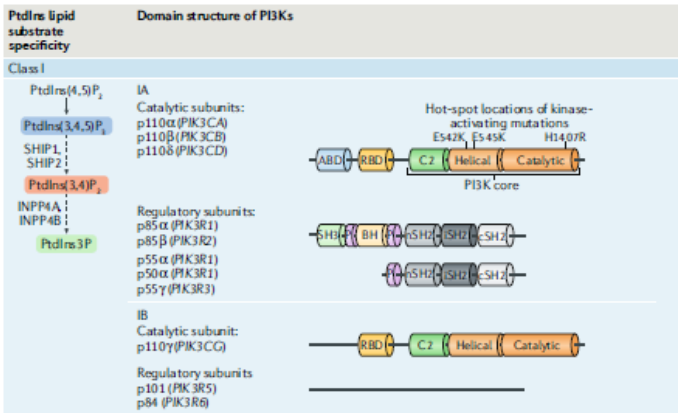

B)

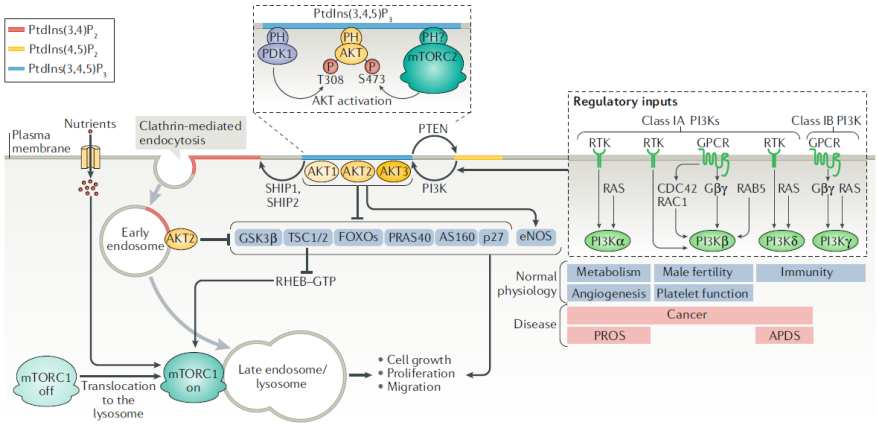

Fig. 1.2. Summary of class I PI3K. A) Schematic representation of Class IA and IB catalytic and regulatory subunits. B) Class I PI3K pathway. Regulatory input depend on the PI3K subclass and are represented on the right side of the scheme. Explanation of the metabolic pathway is detailed in the text above. At the right bottom, class I PI3K functions are displayed, both in normal physiology (in blue) and in disease (in red). Taken from Bilanges et al.(2019) [1].

Activation of AKT leads to inhibition of certain GTPase-activating proteins (GAPs) as the tubero sclerosis complex (TSC 1/2), transcription factors, protein kinases (e.g. GSK3β), proteins that abolish cell cycle, or inducers of apoptosis; and at the same time, activates the endothelial nitric oxide synthase (eNOS). Importantly, inhibition of TSC1/2 mediates the activation of the small GTPase RHEB and subsequently, the activation of the mammalian target of rapamycin complex 1 (mTORC1) at the lysosome [1] (Fig. 1.2). mTOR is a master regulator of metabolism and cellular growth. This protein kinase exist in two complexes, mTORC1 and mTORC2 (previously mentioned) which have distinct signalling roles in the cell. The rapamycin-sensitive complex mTORC1 integrates information about nutritional and environmental status to regulate

metabolism and cellular growth. mTORC1 is in complex with other two core proteins: Raptor (regulatory subunit that promotes recruitment of mTORC1 binding proteins and is required for mTORC1 localisation) and mLST8, which is thought to stabilise the kinase activation loop. Furthermore, the complex contains two inhibitory subunits, Deptor and PRAS40 [30].For further insight into mTORC1 and mTORC2, the reader is referred to Saxton et al. (2017) and Liu et al. (2020) [29, 30].

Amino acids input serves as a trigger for mTORC1 translocation to the lysosome, its activation place, by regulating (through different sensors) on one side the Ragulator-V-ATPase complex [31], and on the other side, the GATOR complex. The Ragulator complex acts as a guanidine exchange factor (GEF) for the RAGC/RAGA heterodimer -a small GTPase- and activates them by GDP to GTP exchange. Once active, this heterodimer recruits mTORC1 from the cytoplasm to the lysosome (where mTORC1 activator RHEB is). The GATOR complex acts as a GAP that upon nutrient deficiency removes GTP activity and thus inhibits RAGC/RAGA (Fig. 1.3).

Besides mTORC1 translocation to the lysosome, lysosomes also need to change their localisation, an event coordinated by nutrient sensing [32]. Amino acid depletion cause lysosomes to aggregate in the perinuclear region, while in the presence of nutrients they stay closed to the plasma membrane, where mTORC1 can be easily activated. PI3K-C2β and VPS34 take part in this process. Both of them have a dual role, participating in the transport of the lysosome to/from the plasma membrane and modulating mTORC1 activity [1], which will be later explained.

Once mTORC1 is at the lysosome and RAGC/RAGA heterodimer is activated, another branch of the regulation comes into place. Class I PI3K are downstream of growth factors signalling (Fig. 1.3). Activation of class I PI3K triggers AKT signalling pathway by binding PIP_3 protein to AKT PH domain. AKT is subsequently phosphorylated by mTORC2 and PDK1, and activated, which prompts phosphorylation of TSC2. TSC complex consist on TSC1 and TSC2, and is located at the lysosome, where maintains mTORC1 activator RHEB in an inactive state. Upon AKT phosphorylation, the TSC complex disengage and inactivates, thereby allowing RHEB to be in its GTP active form and thus, fully activate mTORC1 [1].

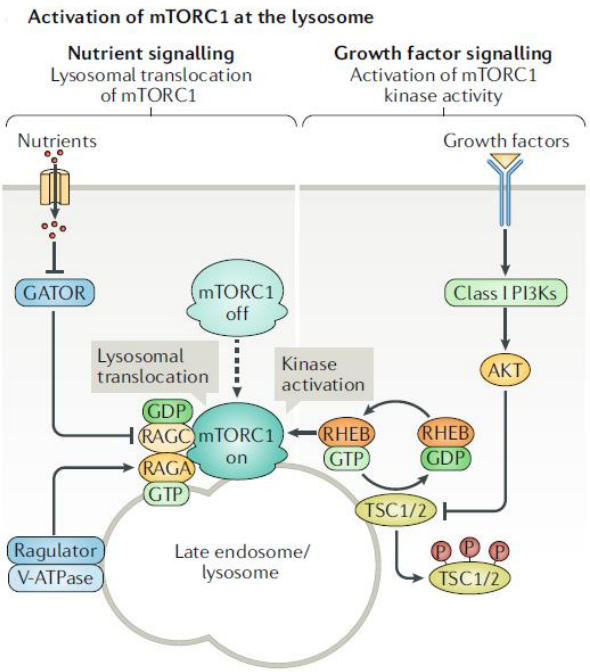

Fig. 1.3. Schematic view of mTORC1 translocation and activation. mTORC1 translocate to the lysosome upon amino acid release. Growth factors signals activate the class I PI3K-AKT pathway, which removes TSC1/2 inhibition of RHEB, triggering mTORC1 activation. Taken from Bilanges et al.(2019) [1].

1.2.3 Class II PI3K

In contrast to class I, class II isoforms do not have a regulatory subunit, but they do have regulatory mechanisms that are being uncover. For instance, their N-terminal domains are larger and used for additional interactions [33]. In PI3K-C2α and PI3K-C2β, N-terminal deletion increase their catalytic activity, and in PI3K-C2β, interaction of the N-terminal region with Grb2 increases its activity as well. This suggests that N-terminal regions may be have an inhibitory function [33]. Additionally, it is known that in solution, PI3K-C2α is self-inhibited by its C-terminal domain due to the C-terminal domain bending towards the catalytic domain [34]. This physical inhibition is released once the protein is recruited to the plasma membrane, where PI3K-C2α binds indirectly by attaching to clathrin using its N-terminal domain. In addition to this, the PX and C2 domains of PI3K-C2α bind to $PI(4,5)P_2$, and subsequently, liberating the catalytic domain [1]. Since these domains are highly similar in the three isoforms of class II PI3K, it would be possible that they share this mechanism [33]. For a summary of class II PI3K domains, see Fig. 1.4A.

Class II PI3Ks are involved in endosomal sorting, exocytosis, and production of both PtdIns3P and $PtdIns(3,4)P_2$, probably dependent on

the lipid availability at their different localisations. These lipids do not have redundant functions with the ones produced by other kinases or phosphatases.

Regarding distribution, while PI3K-C2α and PI3K-C2β are ubiquitously expressed, PI3K-C2γ expression is limited to the liver [1, 22]. Functions of class II PI3K are summarised in Fig. 1.4B.

A)

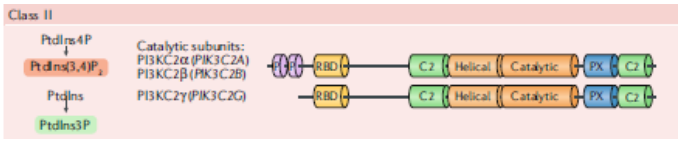

B)

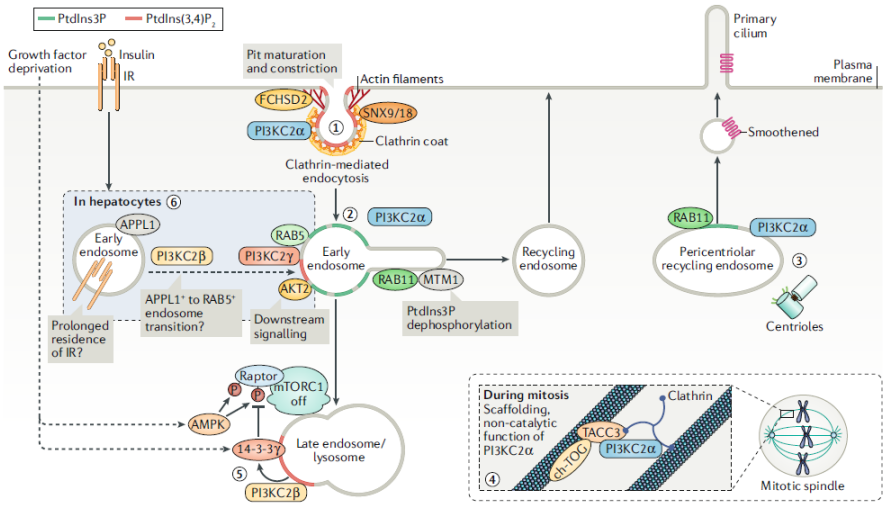

Fig. 1.4. PI3K class II isoform structure and function. A) Schematical representation of the class II PI3K structure and lipid substrate specificity. B) Class II PI3K isoforms function in different localisations. PI3K-C2α is represented in blue. It is present at 1) clathrin-coated pits, where it produces PI(3,4)P_2 to promote maturation and constriction of the pit; 2) early endosomes, where it contributes to the endosome recycling by producing PtdIns3P; 3) periocentriolar recycling endosomes, where it also synthesises PtdIns3P to allow Rab11 activation and cargo transport to primary cillium, and 4) kinetochore fibres during mitosis, where it has a scaffolding function as stabiliser of ch-TOG complex, TACC and clathrin. PI3K-C2β is localised at the lysosome. When growth factors are absence, PI3K-C2β inhibits mTORC1 activation. In hepatocytes, PI3K-C2β is involved in insulin receptor signalling in an opposite trend to that of PI3K-C2γ. This last isoform stimulates insulin signal transduction by its PI(3,4)P_2 synthesis. Taken from Bilanges et al.(2019) [1].

As it has been mentioned in 1.2.2, the relationship of PI3K and mTORC1 is intricate since mTORC1 modulation depends on the separate inputs from class I PI3K, PI3K-C2α, PI3K-C2β, and VPS34.

PI3K-C2β exerts mTORC1 inhibition under serum starvation conditions through a joined regulation of 14-3-3γ with AMP-activated protein kinase (AMPK), one of the master regulators of cellular energy homeostasis. In the absence of growth factors and nutrients, PI3K-C2β translocates to late endosomes/lysosomes, where it produces PtdIns(3,4)P_2. This PtdIns(3,4)P_2 production recruits 14-3-3γ proteins to the organelle, and AMPK, which had been activated by the low energy levels that correlate with starvation, phosphorylates RAPTOR. These phosphorylation events provide binding sites for 14-3-3γ, causing mTORC1 inhibition. To further maintain this inhibition, PI3K-C2β lipid production contributes to lysosome perinuclear localisation (Fig. 1.5). The order in which these events occur is currently unknown [1, 21]. This retrograde transport takes place through Rab7 small GTPase binding to RILP to dynein motors [21].

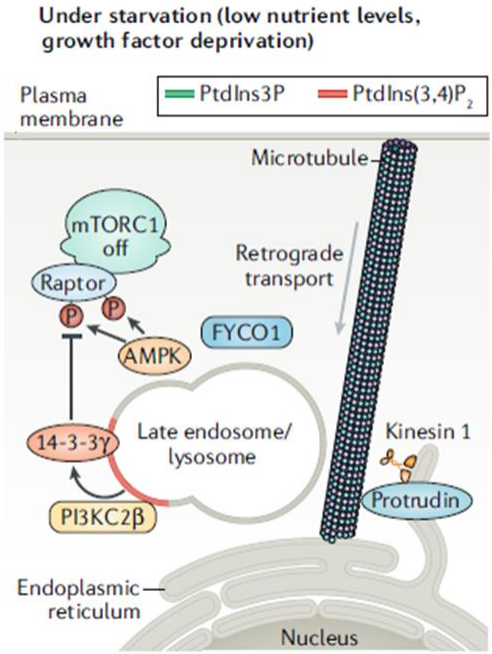

Fig. 1.5. Scheme showing retrograde transport of lysosomes from the periphery to the perinuclear region. To be fully activated mTORC1 needs to be localised on lysosomal membranes. PI3K-C2β intervene is this dynamic by providing the lipid products that serves as a signalling platform for the rest of the players. For further detail, please see above. Image taken from Bilanges et al. (2019) [1].

Other mechanism by which mTORC1 may be activated is by PI3K-C2α. PI3K-C2α produces PtdIns3P, which it is further phosphorylated by PIKFyve to PtdIns(3,5)P_2. This PtdIns(3,5)P_2 binds the PROPPIN domain in Raptor and allows mTORC1 activation [35].

1.2.4 Class III PI3K

Class III PI3K comprises a unique member, VPS34, which is the most ancient PI3K, and it is evolutionary conserved from yeast to mammals. In contrast to the other PI3Ks, VPS34 has a lipid-substrate specificity limited to PtdIns, generating PtdIns3P exclusively [1, 7].

VPS34 plays important roles in endocytic trafficking, macroautophagy, phagocytosis and nutrient sensing [1, 3, 7, 19, 36]. By synthesising PtdIns3P, VPS34 is involved in the recruitment of proteins containing PtdIns3P binding domains to intracellular membranes [7, 37]. These PtdIns3P -binding domains are FYVE (Fab 1, YOTB, Vac 1, EEA1 (proteins where it was found)), PX (Phox homology) and PROPPIN (*β*-propellers that bind polyphosphoinositide, also called WD40 often terminating in a Trp-Asp (W-D) dipeptide) domains [1, 7].

VPS34 will be developed in the following sections.

1.3 VPS34

VPS34 was discovered in budding yeast as the product of a gene required for the correct sorting of vacuolar hydrolases from the late Golgi to the vacuole [38]. This was the first indication that PI3K could regulate membrane trafficking [39]. In mammals, VPS34 is localised in different subcellular compartments [7] and has been shown to be ubiquitously expressed along the tissues in humans (Fig. 1.6) [40, 41].

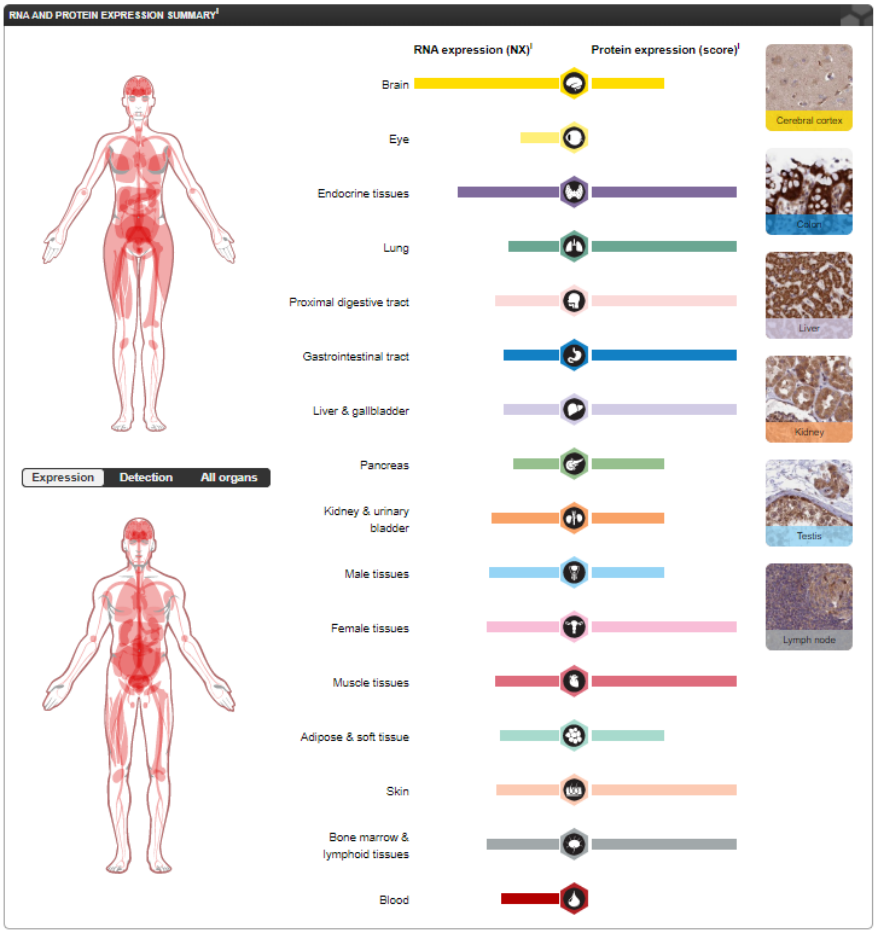

Fig. 1.6. RNA & protein expression of VPS34 in different human organs. Image taken from The Human Protein Atlas.

1.3.1 VPS34, and VPS34 main binding partners structure

VPS34 is divided into three domains (Fig. 1.7). In the N-terminal, there is a C2 domain, which interacts with the other three components of the complex, is subjected to modifications by 5' AMP –dependent kinase (AMPK), Cdk1 and 5 in its Ser/Thr-rich loop. C2 domains usually interact with membranes, but in the case of VPS34, it is unlikely. This domain in VPS34 is separated from the rest [42]. A helical domain that has two conserved residues responsible for VPS34 stabilisation upon poly-ubiquitination (which increases autophagosome maturation) follows the C2 domain. The kinase domain is at the C-terminal end. This domain can be subjected to phosphorylation and acetylation [43].

Vacuolar protein sorting 15 (VPS15) function is not entirely clear. Some authors describe it as VPS34 regulatory subunit and others as a pseudokinase coupled with VPS34. What is known is that VPS34 stability highly relies on VPS15. VPS15 is divided into a N-terminal kinase domain

devoid of active-site motifs conserved in kinases, a helical domain, a linker region, and a WD40 domain that is responsible for the recruitment of VPS34 to the complex once VPS15 binds to activated Rab5A (Fig. 1.7). Just before the kinase domain, there is a typical myristoylation signal that seems to allow further binding to the membrane. A more recent study has reported a VPS34 complex-independent role of VPS15 at the Golgi, where VPS15 forms a complex with the Golgi protein GM130 free of VPS34. This complex formation seems to facilitate Intraflagellar Transport (IFT20)-dependent sorting and transport of membrane proteins from the cis-Golgi to the primary cilium [7, 44].

Beclin 1 (vps30 in yeast) was the first autophagy gene being characterised. It is divided in four domains; a BH3 domain, two coiled-coil domains (CC1 and CC2) and a BARA domain (Fig. 1.7). Post-translational modifications (PTMs) in these domains regulate Beclin 1 function. Modifications in the N-terminal BH3 domain are mostly associated with autophagy promotion, while PTMs in the other regions cause autophagy inhibition [43]. Some examples are phosphorylation of S15 by the Unc-51 Like Autophagy Activating Kinase 1 (ULK1) or S93/S96 by AMPK, both of which activate complex I and II, respectively, or phosphorylation by the death-associated protein kinase (DAPK) at T119. This last phosphorylation prevents Beclin 1 binding to VPS34 complexes by disrupting Beclin 1 binding to B-cell lymphoma 2 protein (Bcl2) or B-cell lymphoma-extra large protein (Bcl-XL) by its Bcl-2 homology 3 (BH3) domain. These proteins prevent the binding of Beclin 1 to VPS34 complexes [45]. The CC domains and the BARA domain are important for the dimerization of the complex [46].

Autophagy related 14 like (ATG14L) (also known as Barkor, apg14 in yeast) is the distinctive member of complex I and was primarily identified in co-immunoprecipitation study in yeast vps34 [47]. Further studies confirmed the exclusive presence of ATG14L in VPS34 complex I but not in complex II and its co-localisation with LC3, Atg16L1 and the ER marker Calnexin, indicating that ATG14L is bound to autophagic structures at the ER [12, 48, 49]. ATG14L is divided in three coil-coiled domains, a shorter one at the N-terminal (CC1), where the residues responsible for its ER localisation reside, followed by two larger ones (CC2 and CC3). The last two domains are a C-terminal, and the Barkor/ATG14L autophagosome targeting sequence (BATS) domain, accountable for its membrane binding through the hydrophobic surface of an intrinsic amphipathic alpha

helix [43] (Fig. 1.7). ATG14L binds the omegasome thanks to its BATS domain, which possess the ALTS motif imperative for complex I selectivity to high curvature membranes [50] Interestingly, the BATS domain also binds to PtdIns(4,5)P_2, a feature that allows its interaction with VPS34 and Beclin 1 [51]. Phosphorylations at S29 by Autophagy related 13 (Atg13) and FAK family kinase-interacting protein of 200 KDa (FIP200) collaborates in complex I activation upon amino acid and glucose starvation [52]. Complex I activity inhibition occurs upon phosphorylation at its C-terminal region [53].

Ultra violet radiation resistance associated gene (UVRAG, vps38 in yeast) was originally identified as part of a genetic screen for UV-irradiation sensitivity in Xeroderma pigmentosum cells [54]. It is the fourth member of complex II. It has a role in endocytic trafficking [55], and possibly, at early and late stages of autophagy [56, 57]. It has been found to co-localise with Rab5 (early endosome marker), Rab7 (late endosome marker) and Rab9 (a marker for the TGN and late endosome transport) [12]. It is divided in five different domains (Fig. 1.7); an N-terminal proline-rich region; a C2 domain able to bind either PtdIns3P, PtdIns4P or PtdIns5P; two coil-coiled domains (a short CC1 and a longer CC2); a BARA2 domain similar to the one of Beclin 1; and a C-terminal domain [43]. Truncated version of UVRAG harbouring C2 and CC1 domains only displays defective autophagy and augmented tumorigenesis [43]. Many phosphorylation sites have been identified in its C-terminal region, which could modify its membrane binding. mTORC1 phosphorylates three sites, S498, which could increase association with the negative regulator RUN domain and cysteine-rich domain containing Beclin-1-interacting protein (RUBICON) [56], and S550 and S571, which activates complex II under amino acid rich conditions [58].

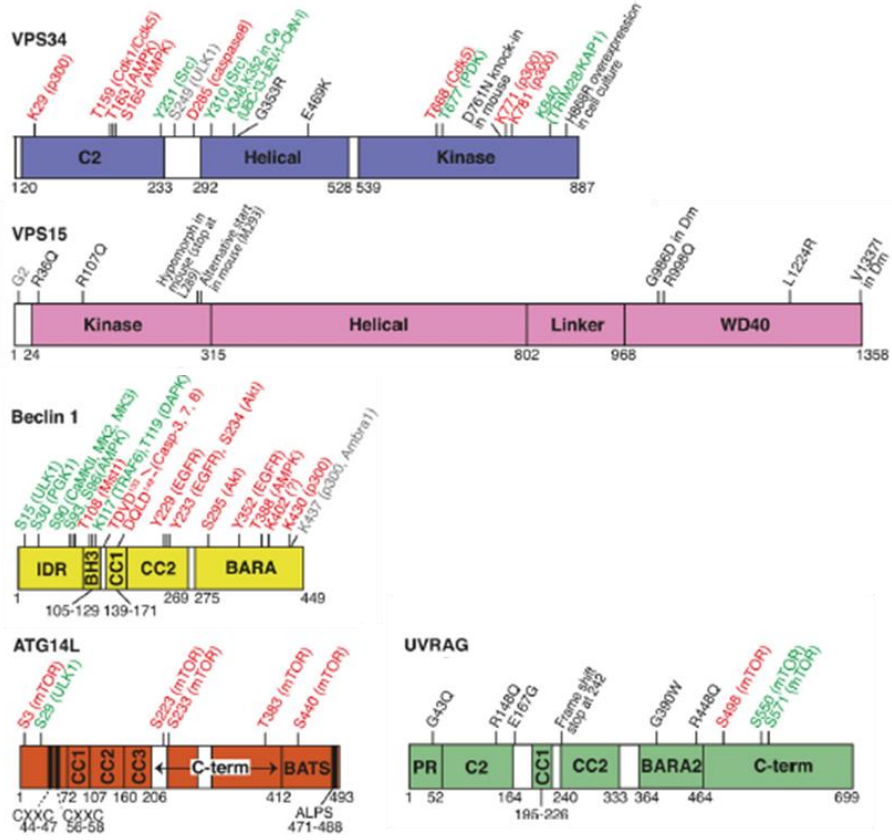

Fig. 1.7. Structure of VPS34 and its partners Beclin 1, ATG14L and UVRAG. Posttranslational modifications and somatic mutations (in black) are annotated. Grey=no effect, red=inhibitory, green=activating. Taken from Ohashi et al. (2019) [43].

1.3.2 VPS34 complexes

VPS34 functions in multiple protein complexes. The core complex contains VPS34, VPS15 and Beclin 1. Additional subunits bind in a mutually exclusive manner this core to form specific complex such that Atg14L binding will form VPS34 complex I and UVRAG will form VPS34 complex II). In addition, other accessory subunits, listed in Table 1.2, can also bind these core complexes depending on context and cell lines. Few lines of evidences suggest that a Beclin 1-free complex containing VPS34-VPS15 complex exist, however its function has not been characterised.

Recent reports have extensively studied the involvement of these specific VPS34 complexes. Complex I functions in autophagy, whereas complex II takes part in endocytic sorting and late stages of autophagy [7, 13]. The relative amount of these different complexes varies depending on the cell line. However, assessment of the lipid kinase activity of VPS34 from

glucose-starved cells showed that this is higher in complex I or II than in the VPS34, VPS15 and Beclin 1 complex [13].

Table 1.2 Summary table with VPS34 complex binders. Complex I comprises VPS34, VPS15, Beclin 1 and ATG14L, while Complex II shares the core proteins but instead of ATG14L, it contains UVRAG. Additionally, depending of the cellular and stress context, the complexes can be found interacting with accessory proteins that modulate their activity. All references showed in the table represent the first papers where the interaction was observed.

	VPS34 COMPLEX I				
Core proteins	**VPS34 [59]**	**VPS15** [60, 61]	**BECLIN 1** [62]		
Distinctive member of the complex	**ATG14L** [12, 49]				
Accessory proteins	**NRBF2** [63-65]	**PAQR3** [66]	**AMBRA 1** [67, 68]	**Dapper1** [69]	**RACK I** [70]

	VPS34 COMPLEX II			
Core proteins	**VPS34** [59]	**VPS15** [60, 61]	**BECLIN 1** [62]	
Distinctive member of the complex	**UVRAG** [12]			
Accessory proteins	**RUBICON** [48, 71]	**BIF-1** [57]	**AMBRA 1** [67, 68]	**Pacer** [72]

The group of R. Williams, in Cambridge, resolved the three-dimensional (3D) structure of yeast and human VPS34 and complex II [42, 73]. Both complexes have a V-shape-like 3D structure around the core complex formed of VPS15, Beclin 1, and VPS34 (Fig. 1.8). Complex I and II differ in their membrane affinity. BATS domain, located in the C-terminal region of ATG14L is implicated in targeting complex I to highly curved membranes, such as autophagosome [7]; while complex II binds much bigger vesicles with low curvature membranes.

The structure of human complex I has been defined [26], while complex II has been studied in yeast [42]. In both cases VPS34 together with VPS15 interact closely to one side of the V shape, each domain of VPS15 interacting with one domain of VPS34. VPS15 integrity is dependent on VPS34 and membrane binding, and VPS34 kinase activity rely on VPS15.

In contrast with class I PI3K, the C2 domain of VPS34 does not interact with the helical or kinase domain of the protein, it sits in the middle of the V shape. VPS34 kinase domain is one of the sites of contact with the membranes. On the other arm, Beclin 1 interacts with ATG14L/UVRAG through BARA-BARA2 domains or BARA-BATS at the tip of the arm, respectively (Fig. 1.8). They both interact with membrane binding. To this regard, the BATS domain in ATG14L is especially important. As previously mentioned, it harbours an amphipathic helix that targets the complex to highly curved membranes, such as those of the phagophore. In contrast to complex I, complex II binds to low curvature membranes (like endosomes), precisely, thanks to the flexibility of their domains [1, 42]. At the bottom of the structure sits the HEAT repeats of VPS34 and the N-terminal region of Beclin 1-UVRAG or Beclin 1-ATG14L, depending on the complex. The other arm of the ”V” is accountable of the VPS34-mediated phosphorylation of PtdIns at the membrane as the kinase domain of VPS34 is located and exposed at the tips of this arm [7, 42].

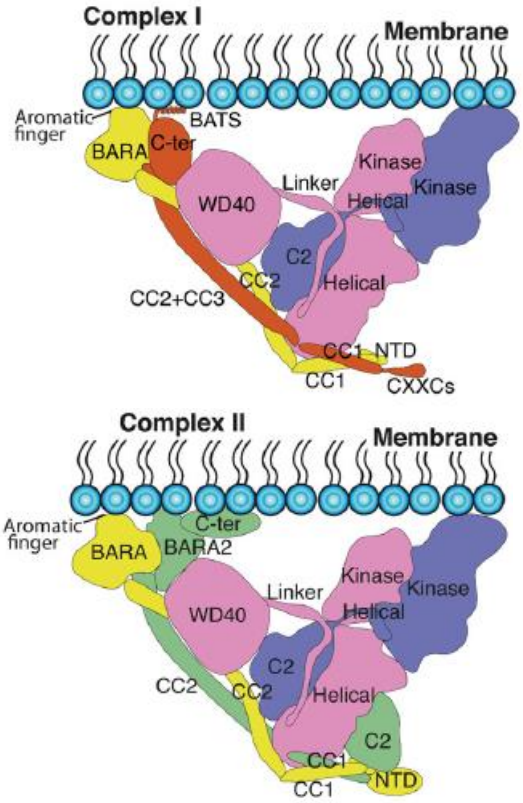

Fig. 1.8. Structures of VPS34 Complex I and II. VPS34 is displayed in purple, VPS15 in pink, Beclin 1 in yellow, ATG14L in orange and UVRAG in green. Image taken from Ohashi et al. (2019) [43].

This structural feature has provided a model by which each complex is regulated by membrane curvature (Fig. 1.8). This flexibility and adaptation

to membrane curvature explain how VPS34 complex I preferentially binds highly curved membranes such as autophagosomes and complex II functions in more flat membranes such as endosomes [1].

These structures are dynamic and can be placed in an open or closed conformation, which affects the catalytic activity of VPS34. In an unbound state, the helical and kinase domain of VPS34 bend inward and adopt a closed conformation, which blocks the ATP binding site. Upon membrane binding, the kinase domain flips out to expose the ATP binding site for hydrolysis to occur [74].

Importantly, the VPS34 accessory subunits have also a role independent of VPS34 complexes. For instance, ATG14L interacts with snapin, a Soluble NSF Attachment Protein REceptor (SNARE) binding protein, to manage the fusion of endocytic vesicles and liposomes. UVRAG interacts with the HOPS complex to regulate the maturation of early endosomes, and with the RINT1-ZW10-NAG complex to govern the retrograde traffic from the Golgi to the ER, although the absence of VPS34 involvement in this last function is controversial [7].

Apart from the main binding partners cited above, other proteins are able to regulate the activation or stabilisation of the complexes under certain conditions, some of which are still poorly understood (Table 1.2). The best-characterised proteins are the Nuclear Receptor Binding Factor 2 (NRBF2), RUBICON, ATG14L activating molecule in Beclin 1-regulated autophagy protein 1 (Ambra1), Bax-interacting factor 1/endophilin B1 (BIF-1), and progestin and adipoQ receptor family member III (PAQR3).

NBRF2 (atg38 in yeast) binds with high affinity to complex I, more precisely to VPS15 [64] or ATG14L [63]. It has an N-terminal MIT (microtubule interacting and trafficking) domain. Originally identified with nuclear functions as a binder of certain nuclear receptors, it plays an important role in the induction of autophagy in serum-starved/stressed cells, by allowing the binding of the members of the complex, and thus, activating VPS34 lipid kinase activity [7, 63, 64]. It has been found that NRBF2 sits at the base of the V-shaped complex, where it is interacting with the N-terminal region of ATG14 and Beclin 1. Because NRBF2 can exist as a homodimer, it can promote the dimerization of complex I, forming large heterotetramers [75]. It was also reported to be an interactor

of ULK1, and upon mTOR phosphorylation, it triggers inhibition of complex I activity [65, 76].

PAQR3 is a Golgi-resident transmembrane protein that stabilises complex I under normal conditions. It increases complex I activity not only by acting as a scaffold protein, but also by supplying phosphorylation sites for AMPK. Upon glucose starvation, PAQR3 is phosphorylated by AMPK, subsequently its localisation changes and is no longer located at the Golgi [7, 43, 66].

RUBICON binds a subset of complex II proteins specifically, localised at the late endosomes/lysosomes [48, 77]. It is a negative regulator of autophagy and endocytosis and interacts with the small GTPase Rab7 [78]. It exerts its inhibiting action by binding to Beclin 1. Recruitment of RUBICON is promoted by acetylation of Beclin 1 by p300 [79].

AMBRA1 is only transiently bound to either complex I or II. It has a WD40 domain and activates VPS34 activity upon Beclin 1 binding. This binding is avoided by the interaction of AMBRA1 and Bcl2, which involves AMBRA1 in mitochondrial dynamics [43, 67, 80, 81].

BIF-1 was shown to localise to autophagosomal structures, as well as to mitochondria, where it activates Bax and Bak in apoptosis, or to the Golgi [57]. It possesses an N-terminal BAR domain important for membrane curvature and a SH3 domain required to bind UVRAG. It promotes VPS34 activity [57, 78]. Thorensen et al. (2010) showed that it interacts with complex II, specifically, it is responsible for endocytic receptor trafficking (at least of epidermal growth factor receptor (EGFR) and cytokinesis [55].

The tight regulation of these complexes is intriguing, since the same stimulus can produce a different outcome. For instance, glucose starvation increases lipid kinase activity of complex I and II but decreases the activity in bulk PtdIns3P pool [13], while insulin stimulation activates only complex II activity [36].

1.4 VPS34 functions

As previously mentioned, VPS34 complexes are involved in many vesicular trafficking events. The precise mechanism behind these processes is just starting to be uncovered. The best characterised function of VPS34 are in autophagy, endocytic traffic and phagocytosis.

More recently, emerging evidences have involved VPS34 in cytokinesis, suggesting a new role of VPS34 during mitosis. I will describe in the next paragraphs the main role of VPS34 in autophagy, endocytic traffic and cytokinesis, while phagocytosis is beyond the scope of this study.

1.4.1 VPS34 in autophagy

Autophagy is the process by which cellular content is degraded at the lysosome after being engulfed in vesicles, called autophagosomes. It is a critical event to maintain cell homeostasis in basal conditions and it is promoted under stress conditions, such as nutrient deficiency situations to adapt to energy demand. In conditions where nutrients are scarce, cells rely on autophagy by degrading cytoplasmic materials to provide enough nutrients for their survival for a certain period of time. Dysregulation of autophagy is involved in many human pathologies, such as neurodegenerative diseases, cancer, aging or resistance to pathogens [14, 82, 83]. There are three forms of autophagy; macroautophagy, microautophagy and chaperone mediated autophagy (CMA). Microautophagy refers to the direct engulfment of the autophagic substrates by the lysosome; while, CMA consist in the degradation of tagged proteins with a specific sequence motif that binds to chaperone HSP70 and is, thus, transported and internalised in the lysosome [84]. Macroautophagy is the most widely studied form of autophagy and the focus of my study. For simplicity, it will be hereafter referred to as autophagy. In mammals, the initiation of autophagy is induced upon a stress signal such as nutrient depletion and involves the formation of double-membrane vesicles, called autophagosomes, from the phagophore (also called isolation membranes), which enlarge and close around a portion of cytoplasm including damaged organelles and/or misfolded protein or aggregates. These autophagosomes ultimately fuse with lysosomes, resulting in degradation of their contents. Therefore, autophagy could be divided into different steps; a) initiation, formation and closure of the autophagosome; b) maturation of the autophagosome and fusion with the lysosome, which permits lysosomal degradation; and c) autophagosome-lysosome reformation (Fig. 1.9). Depending on the context and the cytoplasmic material that is engulfed, we can distinguish between non-selective autophagy and selective autophagy. Selective autophagy consist on the degradation of particular organelles or content such as mitochondria, ER, aggregates, Golgi, etc. These processes have

been named according to the organelle engulfed (mitophagy, ER-phagy, aggrephagy, Golgi-phagy…).

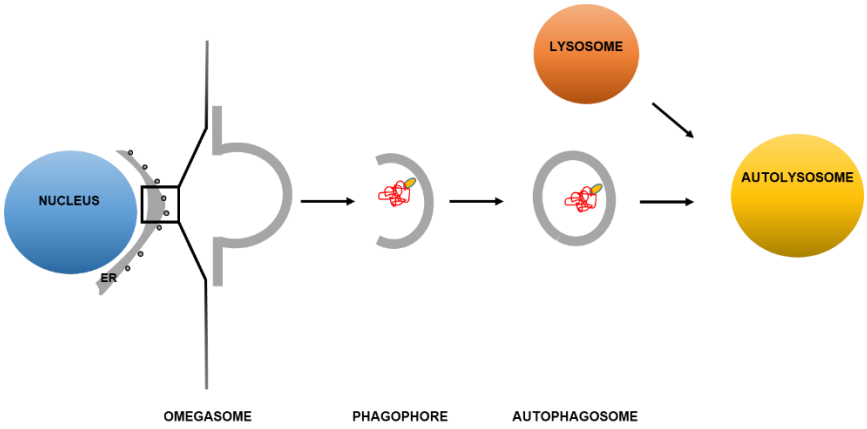

Fig. 1.9. Representation of the autophagic pathway. The future autophagosome originates from a PtdIns3P -enriched part of the ER called the omegasome. This region is enlarged and, eventually, splits from the ER to form the isolation membrane or phagophore, which will engulf different content. Once it closes, the autophagosome starts the delivery of its cargo to the lysosome, to eventually fuse and deliver its content. At the lysosome, this content will be degraded. The autophagosome can also fuse, prior to the lysosome fusion, with late endosomes. When this occurs, they are denominated amphisomes.

PtdIns3P has been considered the major player in autophagy since genetic studies from yeast, flies and mammals suggested that PtdIns3P production by class III PI3K is required for autophagosome formation. Several PtdIns3P binding proteins have been identified to play a role in autophagosome biogenesis, such as (double FYVE-containing protein 1 [DFCP1] or the WD-repeat protein interacting with phosphoinositide [WIPI1-2]) [85, 86]. However, alternative pathways can also take part in this process as it has been reported that other lipids, and in particular PtdIns4P and PtdIns5P, could be involved in autophagosome formation [87-90].

1.4.1.1 Induction of autophagy, formation and closure of the autophagosome

Autophagy is one of the cellular processes that maintains cellular homeostasis, and it is upregulated by stress signals (nutrient starvation, growth factor deprivation, hypoxia, ER stress, pathogen infection…). The master regulators that integrate this signalling to modulate autophagy activation are mTORC1 and AMPK. mTORC1 is critical to direct the balance of catabolic and anaerobic activities. Upon nutrient rich

conditions, mTORC1 is activated and phosphorylates its substrates S6K1 and 4E-BP1, which trigger the synthesis of proteins, lipids, nucleotides. In addition, it phosphorylates UNC51-like Ser/Thr kinase (ULK1), in charge of the initiation of autophagy [91], and the transcription factor EB (TFEB), which triggers transcription of genes involved in lysosome biogenesis. In summary, activated mTORC1 represses autophagy [92] (Fig. 1.10). AMPK senses the imbalance in the cell energy by raises in the level of AMP, indicative of cellular stress. AMPK is activated by a low ratio of ATP/AMP, and the depletion of glucose (which drops the ATP/AMP ratio) by phosphorylation via liver kinase B1 (LKB1) [93]. Once activated, AMPK phosphorylates and activates the TSC2 complex, which inhibits mTORC1. Moreover, AMPK can directly phosphorylate Raptor, the regulatory member of mTORC1 complex at S863 [94], and in addition to this, it can directly activate ULK1 by phosphorylation [95, 96]. Therefore, activated AMPK positively regulates autophagy.

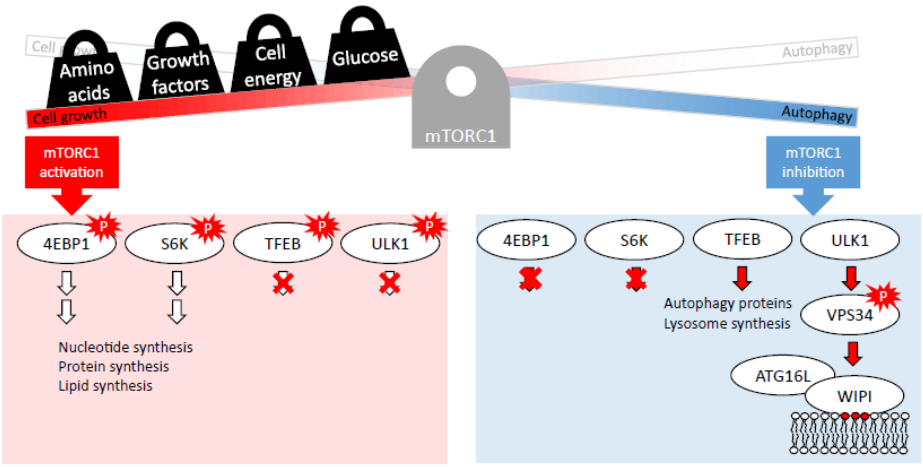

Fig. 1.10. mTORC1 control in cell growth and autophagy. Figure taken from Walker and Ktistakis (2020) [92].

After induction of autophagy, ULK1 complex, formed by ULK1, FIP200, Atg13 and Atg101, activates and translocates from the cytoplasm to the omegasome until completion of the phagophore (Fig. 1.11). ULK1 is crucial to gather the rest of the machinery required for autophagosome formation. It recruits and positively regulates VPS34 activity by phosphorylating Beclin 1 at S14 [97] and S30 [98], ATG14L at S29 upon direct binding of Atg14L with Atg13 [52] (this phosphorylation does not take place in Huntington's disease [99]), and by directly binding to VPS34 complex I by ATG101 [100]. This recruitment might also be induced by phosphorylation of AMBRA1 in S465 and S635 by ULK1 [101, 102].

ULK1 is the target of multiple phosphorylations that regulates its functions and it phosphorylates mTOR and AMPK among others [76]. By phosphorylating Raptor at multiple sites [103], ULK1 provokes mTORC1 inhibition while nutrients are scarce, by preventing Raptor binding to mTORC1 substrates.

Another ULK1 functions is to regulate Atg9 trafficking, a transmembrane protein that travels from the Golgi, endosomes or Atg9 positive membranes, to autophagic structures (omegasome, phagophores and autophagosomes). Several membranes (plasma membrane, mitochondria, recycling endosomes and TGN), contribute to the elongation of the autophagosome membrane by providing membrane material. Atg9 function is still unclear but it has been suggested to deliver components to its recruitment localisations and participate in membrane scaffolding [104].

The Golgi complex has an indirect role in recruiting ULK1 to the omegasome. WAC and GM130 proteins, both resident in the Golgi apparatus, regulate a pool of GABARAP (members of the Atg8 family, explained below) that traffics to the centrosome. The non-lipidated centrosomal GABARAP binds then the omegasome, where it recruits ULK1 by its LC3 interacting region (LIR) domain [85].

Besides VPS34 complex I recruitment to the omegasome by ULK1, there are other mechanisms of recruitment of VPS34 complex I to the ER. However, it is not clear yet whether they are essential or if this is cell context dependent. These include the potential involvement of PtdIns(4,5)P_2 produced by PIPKIγi5, which regulates the assembly and stabilisation of the complex by binding ATG14L [51] or Vacuole Membrane Protein 1 (VMP1), which binds Beclin 1, facilitating the formation of VPS34 complex I.

Upon ULK1 recruitment and activation at the omegasome, VPS34 produces PtdIns3P that in turn recruits FYVE and PROPPIN domain containing proteins, such as double FYVE domain containing protein 1 (DFCP1) or WIPI2. WIPI2 directly binds Atg16L1 [105] and this step is critical to promote the autophagic flux [76]. The actin-capping protein CapZ and the actin nucleation-promoting factor WHAMM create an actin network assembled in the phagophore, which is suggested to help with autophagosome biogenesis [106]. Other nucleation-promoting factor,

JMY, is recruited via its LIR motif to promote actin nucleation, which plays a role in autophagosome formation and maturation [85] (Fig. 1.11).

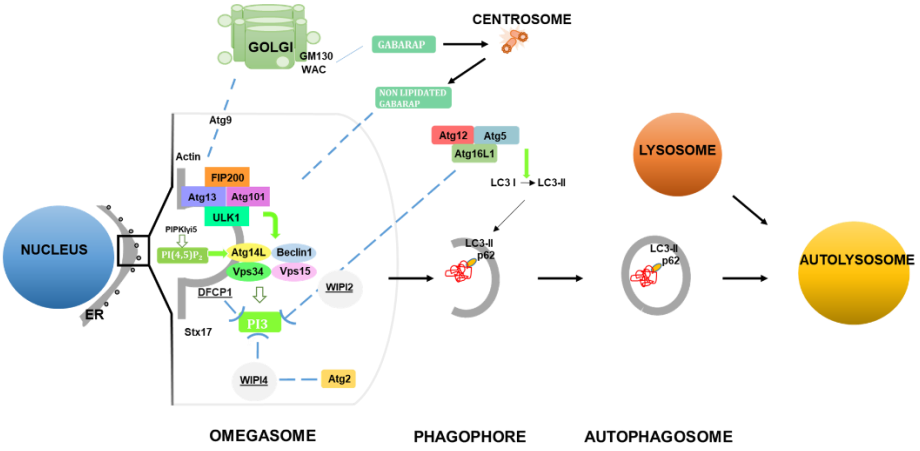

Fig. 1.11. Sequence of events in the initiation of autophagy. ULK1 complex is recruited to the omegasome, as well as Atg9. ULK1 triggers recruitment of VPS34 complex I to the omegasome, where it produces PtdIns3P, which in turn, recruits PtdIns3P-binding proteins, such as DFCP1 or the WIPI family. WIPI2 recruits the Atg16L1-Atg5-Atg2 system, which allows lipidation of LC3 proteins. LC3-II contributes to the scaffolding of the membrane and allows binding of selective autophagy receptors (SARs), such as p62, or other protein complexes (ULK1, VPS34, ATG14L, Beclin 1, Atg4 or Atg12-Atg5, not shown). Finally, closure of autophagosome occurs and fusion with the lysosome takes place.

The elongation of the phagophore relies on two ubiquitin-like conjugation systems, whose schematic view is presented in Fig. 1.12. Atg8 family (LC3/GABARAP) is found as cytosolic precursors that are cleaved by Atg4, a cysteine protease that exposes a Gly residue at the C-terminal region of Atg8. This is activated by Atg7 (E1-like enzyme), transferred to Atg3 (E2-like enzyme) and conjugated to phosphatidylethanolamine (PE), its membrane-bound form, thanks to the Atg12-Atg5-Atg16L1 system (which act as a E3-like enzyme). This process can be reversed by Atg4 cleavage by PE [16, 107]. The second system is the Atg12-Atg5-Atg16L1 complex, previously mentioned. The formation of the ATG16L1 complex start with Atg12's last Gly being activated by Atg7 to form a thioester bond, which gives rise to an Atg12-Atg7 intermediate complex. Atg12 is then transferred to form another thioester bond with Atg10 (E2-like enzyme). Atg5 has an acceptor Lys, where Atg12 is finally conjugated via an isopeptide bond. Finally, two sets of the Atg12-Atg5 complex binds to Atg16L1 [107, 108].

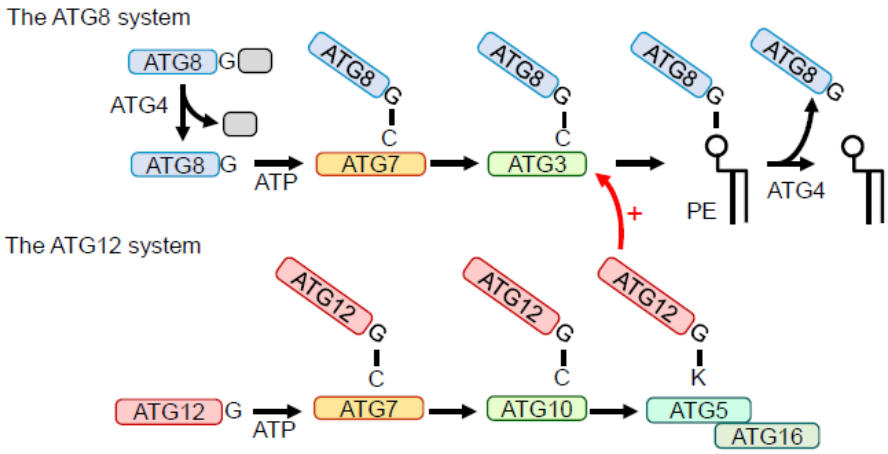

Fig. 1.12. Atg8 and Atg12 systems. They function as ubiquitin-like systems, where consecutive transient interactions and modifications give rise to LC3 lipidation. Taken from Mizushima (2019) [107].

Importantly, the presence of Atg16L1 in phagophore membranes indicates the site of Atg8 lipidation [107]. In mammals, Atg8 family comprises Microtubule-associated protein 1A/1B-light chain proteins (MAP1LC3, more commonly known as LC3), whose more characterised member is LC3B, and GABARAP. LC3 proteins take part mainly in autophagosome generation, while GABARAPs are mostly involved in the maturation step. The nomenclature used for the different forms of LC3 changes upon their state i.e. LC3 with their Gly residue exposed is named I and lipidated forms II (e.g. LC3-I vs LC3-II). Lipidated members of LC3 family are crucial for the expansion and closure of the phagophore. They associate with protein membranes acting as a scaffold, and allow the attachment of cargo receptors (SARs) such as p62 via their LIR domain. This domain also serve to recruit other proteins like ULK1, VPS34, ATG14L, Beclin 1, Atg4 or Atg12-Atg5 to autophagic membranes. They also play roles in the transport of the autophagosomes and their interaction with the lysosome [85, 109].

Engulfment of cellular material occurs thanks to certain SARs, such as p62, that interact with the cargo and the LC3 family of proteins at the inner membrane of the phagophore [109]. Later steps of the autophagic process comprise fusion of the autophagosome with the lysosome forming the autolysosome, where its intracellular content is degraded by lysosomal enzymes and/or recycled [85, 110].

It has recently been shown that the LIR domain in ATG14L, VPS34 and VPS15 preferentially bind GABARAP, GABARAPL1 and LC3C [111]. VPS34 and VPS15 binding to GABARAP depends on ATG14L LIR interaction. Some of the effects of disrupting this interaction is that the phosphorylation by ULK1 in ATG14L S29 is reduced (which reduces VPS34 activity), complex I does no longer co-localise with LC3B (defective autophagy), p62 is not efficiently transported to lysosomal structures (defective degradation), and there is an impairment of mitophagy [111]. GABARAPs are mostly known to be essential for autophagosome-lysosome fusion by their involvement in PtdIns4P production by recruitment of PI4KIIα to the autophagosomes [112]. Altogether, this finding highlights the importance of the LIR interaction in ATG14L protein for initiation, expansion and closure of the autophagosome; and what is more, raises the question of whether VPS34 complex I plays unknown functions at late stages of autophagy.

Besides recruiting LC3, Atg16L1 binds to FIP200, member of the ULK1 complex. This acts as a feedback loop to increase VPS34 activity and assure a correct PtdIns3P production. Once the autophagosome is formed, it is transported by a microtubule network to the lysosome, where it fuses and delivers its content for degradation [85].

1.4.1.2 Maturation of the autophagosome and fusion with the lysosome

The initiation, nucleation and expansion steps of autophagy are followed by the maturation of the autophagosome and fusion with the lysosome, critical for degradation of the engulfed materials. These late steps engage a set of proteins that are part of the late endosome/lysosome system. Autophagolysosomal fusion requires changes in lysosomal pH, tethering factors such as the HOPS complex and RAB7, some cytoskeleton motor proteins such as dynein, certain phospholipids such as PtdIns(3,5)P_2, the SNARE complex, and LC3 [1].

Fusion of autophagosome-lysosome also requires VPS34 complex II, but it remains controversial. Liang et al. (2008) showed that complex II bound to RUBICON interacts with HOPS complex [113]. HOPS complex is required for vesicle tethering and comprises VPS11, VPS16, VPS18, VPS33, VPS39 and VPS41. VPS39 is involved in the recruitment and activation of the small GTPase Rab7.

Under nutrient-rich conditions, UVRAG is phosphorylated by mTORC1, which promotes RUBICON binding and decreases VPS34 activity; besides, it impairs UVRAG-HOPS complex interaction [56] (Fig. 1.13). In contrast, under nutrient depleted conditions, mTORC1 is no longer active (a condition promoted when autophagy is active), to phosphorylate UVRAG and impairs its interaction with HOPS complex. This interaction promotes Rab7 activation, and interaction with effectors, such as the Rab-interacting lysosomal protein (RILP), required for transport to lysosomes, is enhanced. Autophagosome maturation and lysosomal degradation would be increased. However, Jiang et al. (2014) results suggested that UVRAG did not form a complex with HOPS complex in autophagy but it did in endocytosis [114]. Instead involving complex II, they found that HOPS complex binds to the SNARE protein Syntaxin17 (Stx17) and, probably, promotes the assembling of the Stx17-Snap29 (Synaptosomal-associated protein 29) and the vesicle-associated membrane protein 8 (VAMP8) for autophagosome-lysosome fusion (Fig. 1.13).

Interestingly, ATG14L has been found to interact with Stx17 in a different context than the one described at the omegasome. ATG14L was found in mature autophagosomes, where it forms a complex together with Stx17 and Snap29 to promote autophagosome-lysosome fusion by the interaction with VAMP8 at lysosomal membrane [115]. There is no direct evidence of whether ATG14L functions alone or in association with VPS34 complex I, but very recent work by Takáts et al. (2020) has suggested that complex I is an effector of Rab18, and that this would maintain Rab7 late endosomes/lysosome compartments stability and promote lysosome fusion and maturation [116].

Recently, Cheng et al. (2017-2019) contributed to clarify the outlook introducing a new partner to the equation [72, 117]. They found that PACER (protein associated with UVRAG as autophagy enhancer), a protein with 23% similarity with RUBICON that associated with mature autophagic structures and that is mostly found bound to these membranes, competes with RUBICON in binding to complex II, enhancing VPS34 activity, and is required for autophagosome maturation (Fig. 1.13). The authors reported that VPS34 complex II activity is directed to the autophagosome by binding to PACER. PACER also interacts with the HOPS complex, independently of UVRAG, and brings the complex to the autophagosome. Lastly, the authors found that PACER was able to bind Stx17 and this binding was suggested to be the trigger for PACER

localisation at autophagosomes. Altogether, these data indicate a role for complex II in autophagosome maturation that is followed by ATG14L (or complex I), and Stx17-Snap19-Vamp8 association to mediate autophagosome-lysosome fusion. A summary of the process is presented in Fig. 1.13.

Once that the outer autophagosomal membrane fuses with the lysosomal membrane, lysosomal content degrades the inner membrane of the autophagosome, creating the autolysosome, which will degrade the engulfed material/organelles using lysosomal hydrolases and export the resulting amino acid, nucleic acids… to the cytoplasm [92].

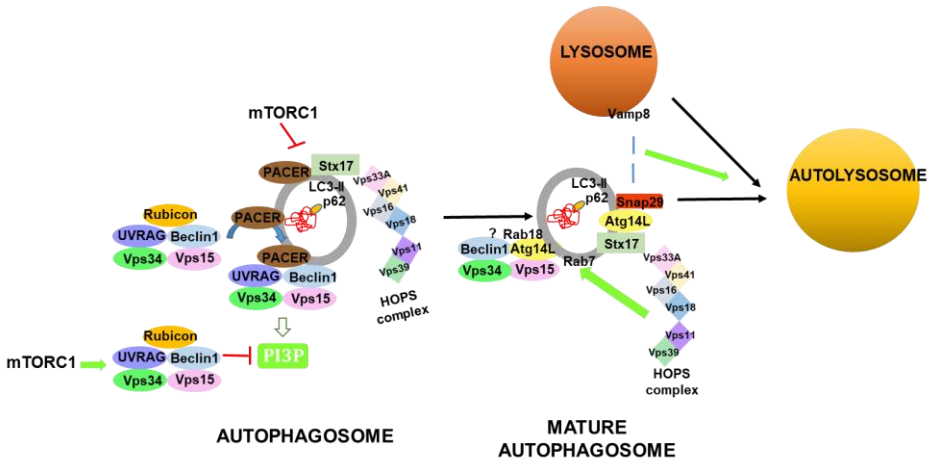

Fig. 1.13. Model of autophagosome maturation and lysosome fusion. Under nutrient-rich conditions, where autophagy is inhibited, mTORC1 phosphorylates UVRAG. This phosphorylation promotes RUBICON binding to VPS34 complex II and prevents VPS34 activity. When autophagy is stimulated, mTORC1 is inhibited and PACER competes with RUBICON, increasing VPS34 activity and promoting autophagosome maturation. PACER localisation to the autophagosome is determined by its binding to Stx17. Later, HOPS complex binds to Stx17 promoting Snap29 and Vamp8 binding to ATG14L, or complex I, to promote autophagosome-lysosome binding.

1.4.1.3 Autophagosome-lysosome reformation

To be able to maintain their structure and identity, lysosomes undergo autophagosome-lysosome reformation (ALR), a process that co-exist with a weakening of autophagic activity. mTORC1 is inhibited at the initiation of autophagy but becomes activated at the lysosome upon sufficient release of amino acids from lysosomal degradation [7, 58].

Although it was first reported to occur during prolong macroautophagy [118], ALR seems to take place under basal conditions as well [58]. Nevertheless, it is exacerbated upon starvation, and consist on the scission of the autolysosomal tubules to regenerate lysosomes [58, 118]. VPS34 complex II is partially responsible of this process. Phosphorylation of UVRAG at S550 and S571 (within VPS34 complex II) by mTORC1 increases VPS34 activity and produces a lysosomal PtdIns3P pool important for the separation of the autolysosomal tubules (Fig. 1.14).

Interestingly, UVRAG depletion mimics VPS34 inhibition using the VPS34 inhibitor IN1, causing a reduction in lysosome punctae and increased in size. VPS34 complex II is thus crucial for this process. Importantly, abrogation of ALR causes cell death [58, 119], which exemplifies the critical role of this process.

In Fig. 1.14 a summary of the process can be found. PtdIns4P and PtdIns(4,5)P_2 orchestrate the induction of the autolysosome tubulation [120, 121], and in addition, PtdIns4P provide the substrate for PIP5K1A kinase, which drives tubule scission together with VPS34 complex II. Microtubules are necessary for ALR [118], and Dynamin2, a GTPase that mediates scission of cellular membranes and that can be activated by PtdIns3P, PtdIns4P or PtdIns (3,4)P_2, is involved in the process of tubule scission [122].

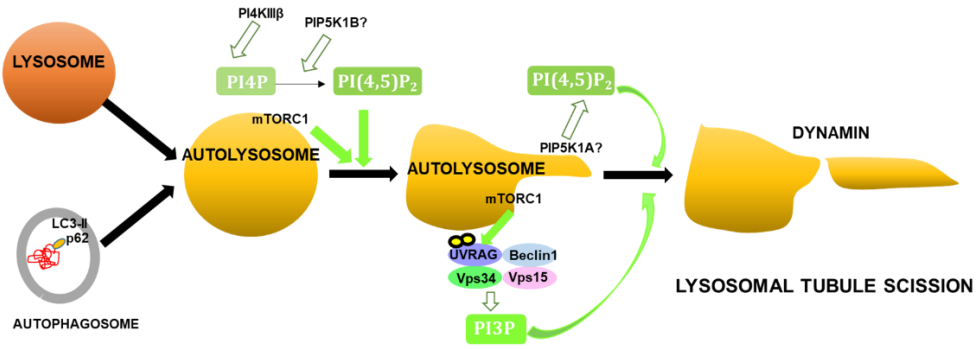

Fig. 1.14. Model for autophagosome-lysosome reformation (ALR). Autolysosomes tubulate thanks to the coordinated action of mTORC1, PI4KIIIβ and PIP5K1B. After the tubule is formed, mTORC1 phosphorylates UVRAG and increases PtdIns3P activity, which promotes lysosomal tubule scission.

1.4.1.4 Practical considerations on how to monitor autophagy

Many reviews have tackled what has been proved a tricky determination and complete guidelines have been published to not only make sure the autophagic assays are interpreted correctly, but also to provide update on new techniques to assess many aspects of the autophagy pathways [123-126].

Autophagy is a highly dynamic process and several complementary assays are required to draw definitive conclusions. Broadly, there are two ways to monitor autophagy: assessing the absence/upregulation of certain related proteins or structures, or quantifying the degradation rate of autophagic substrates.

As previously explained, the autophagic structures are the omegasome, which emerges from the ER, the isolation membrane or phagophore, autophagosome, and autolysosome/lysosome. Some typical markers to assess initiation of autophagy are omegasome markers, such as any of the members of ULK1 complex, Atg9, or VPS34 complex I. Absence of any of these members prevents autophagy initiation, and accumulation of some substrates like p62, damaged mitochondria or ferritin occurs [124]. The presence of DFCP1 is also a widely used marker [86].

ULK1 and VPS34 complex can be present as well at the phagophore. Proteins such as WIPI1/2 [127], Atg5 or LC3 are also used for visualization [124]. Other recently discovered marker is Atg16L1 [128]. All these complexes, but LC3, detach once the autophagosome is closed.

To mark autophagosomes, the most standard markers are LC3B and p62. p62 (also called SQSMT1) is a cargo receptor that is degraded by autophagy. LC3 is necessary for the formation of the autophagosome; it can be detected in two different forms (LC3-I, the cleaved form with a terminal Gly; and LC3-II, already conjugated with PE) depending on the autophagic activity, and is degraded in the lysosome, as well as p62. They are widely used to assess the autophagic flux, which measures autophagic degradation. STX17 can also be used in this case, with some precautions since it also stains ER and mitochondria [124].

Finally, lysosomes can be marked using lysosomal-associated membrane protein 1/2 (LAMP1/2) markers or lysotracker.

			Results			
	Assays	Mehods	Basal	Induction	Early step suppression	Late step suppression
Autophagosomes	Number of LC3 positive puncta	IHC	→	↑↑	↓	↑↑
	LC3-II level	WB	→	↑↑	↓	↑↑
Morphology	AP/AL detection	TEM	AP →	AP ↑	AP ↓	AP ↑↑
			AL →	AL ↑	AL ↓	AL ↓
Autophagic flux	LC3 turnover	WB	→	↑↑	↓	↓
	P62 level	IHC/WB	→	↓	↑	↑
	mCherry-GFP-LC3	IHC/FM	Red →	Red ↑	Red ↓	Red ↓
			Yellow →	Yellow ↑	Yellow ↓	Yellow ↑↑
	Long lived protein degradation	IR	→	↑↑	↓	↓

Fig. 1.15. Summary on ways of monitoring autophagosome and autophagic flux. AP, Autophagosome; AL, Autolysosome; IHC, Immunohistochemistry; IR, Isotope release; FM, Flow cytometry; TEM, Transmission electron microscopy; WB, Western blotting; Early step suppression refers to impairments in autophagosome formation or maturation; Late step suppression refers to impairments in the fusion and degradation steps. Taken from Zhang et al. (2013) [129].

All these structures are routinely visualised using confocal microscopy-immunofluorescence (IF). Its absence/overexpression can be measured by western blot (WB) (see Fig. 1.15). An important consideration to take is that all these measures are point quantifications and proper controls need to be taken.

In addition to confocal microscopy and WB, electron microscopy has traditionally been used and it was actually the method by which autophagy was discovered. Autophagosomes are visualised like double-membrane structures with undigested content that have not fused with the lysosome [123]. Though autolysosomes have a single membrane, they are slightly more difficult to visualise since they have shared characteristic with both lysosomes and autophagosomes [130].

The most common mistake and best example to explain the dynamic nature of autophagy is the assumption that more autophagy structures represent a higher rate of autophagy. Autophagy is a degradative pathway. Structures are formed and then, either fuse with others, or degrade. A high number of autophagosomes could reflect either a high rate of autophagy, or a blockage in the autophagic flux that would hamper fusion of the autophagosome with the lysosome. To distinguish between the two interpretations, inhibitors are broadly used. To simplify, there are three ways of modulating autophagy (Fig. 1.16A). The first one is by activating autophagy using stimuli that enhance the autophagic response, such as starvation, e.g. removal of amino acid or serum, or

pharmacological inhibition of mTORC1. Broadly, the second one consist on inhibition of the first step of autophagy, i.e. the formation of the autophagosome. IN1, the specific VPS34 inhibitor is part of this category. Lastly, the third category of inhibitors of autophagy include the ones that prevent fusion of the autophagosome with the lysosome. The most used inhibitors in this category include Bafilomycin A1 and Chloroquine.

Regarding interpretation of autophagic flux, a summary of the different outcomes and their meaning can be easily explained using Fig. 1.16B [124]. As previously explained, LC3 is present in the cytoplasm in its uncleaved form. Atg4 then cleaves its C-terminal region, and exposes a Gly residue. This form is known as LC3-I. However, LC3 needs to be lipidated to be part of the phagophore and autophagosome. LC3-I is conjugated with PE and becomes LC3-II. Based on this notion, under basal conditions where only basal autophagy is present, there should be either equal quantity of LC3-I (upper band, Fig. 1.16B) and LC3-II or almost no LC3-II. There is a different level of basal autophagy depending on the cell type, for instance, HeLa cells have a high rate of autophagy, and in basal conditions have a higher quantity of LC3-II than other cell types [123]. If autophagy is stimulated, there is a higher rated of LC3-I conversion to LC3-II (Fig. 1.16). Regarding p62, this protein is bound to LC3 and degraded within the lysosome. If we compared basal conditions to conditions where autophagy is increased (Fig. 1.16), we would see a decrease of p62, because this protein is already being degraded.

Coming back to the misinterpretation discussed above, the notions just presented only give a static picture of what is occurring. To be able to properly assess the autophagic flux, another component needs to be added to the equation. Autophagosomes are being formed as they are being degraded, so if an inhibitor that prevent autophagosome degradation is used, the number of autophagosomes that have been produced can be measured. In the previous example of treated cells having higher number of autophagosomes, and not knowing whether this represents a high rate of autophagy or a blockage in autophagy, if an inhibitor such as Bafilomycin A1 was present, the expected amount of LC3 would be either the same amount of LC3-II, in the case of autophagy inhibition, or higher LC3-II in the case of autophagy induction. p62 would be higher as well.

In Fig. 1.16B there is an example of how to interpret changes in autophagic flux in treated cells. Group A represents cells with higher autophagic flux and group B cells where autophagy is impaired. By looking at LC3-II quantity in normal conditions in all three groups (control, A and B) there is almost no difference, but upon inhibition with Bafilomycin A1, the outcome is clear (as predicted above). Group C shows under normal conditions higher level of LC3-II than the control group. This could be interpreted as higher autophagic flux but comparing -/+ Bafilomycin A1 in group C, LC3-II does not increase. If there is high autophagic flux, there should be more autophagosomes accumulating. This implies that these cells have a defect in autophagosome degradation, so it is rather a decrease in autophagic flux than an enhancement.

Finally, Fig. 1.16B.3 also shows the interpretation of autophagic flux by IF. The groups represent the same autophagy activity that the previously explained example for WB, as well as the same principle. LC3 antibodies do not have high affinity for LC3-I, so the observed LC3 punctae are LC3-II recruited to autophagic structures [124]. By IF, they appear like punctae that increase or decrease depending on the autophagic flux.

Other way to visualise LC3 by confocal microscopy or live imaging is by the mRFP-GFP-LC3 tandem protein [131]. The principle behind this mechanism is based on the acidic pH of the lysosome, which will quench the green fluorescent protein (GFP) (with a pKa=5.9) but not the red fluorescent protein (mRFP) (pKa=4.5). Autophagosomes would be seen as yellow, while internalization of LC3 and degradation at the lysosome would cause red signal.

A)

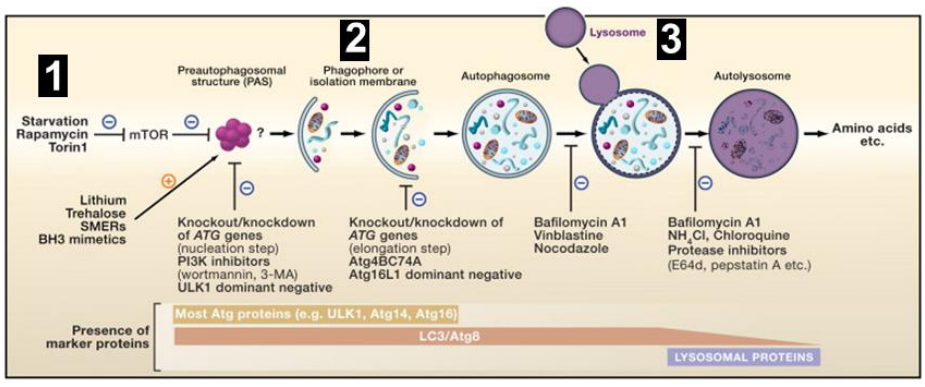

B)

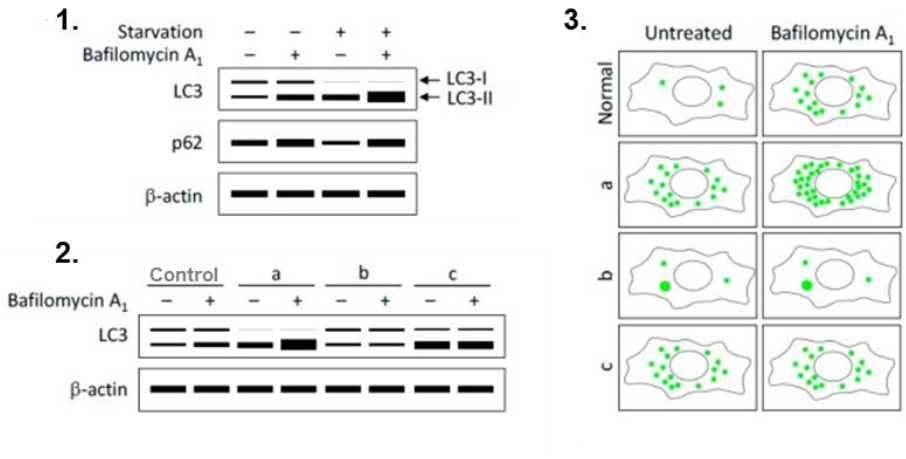

Fig. 1.16. Practical principles on how to monitor autophagy. A) Schematic representation of the autophagic pathway. The target of different inhibitors, and the impairment occurring in Atg knock out (KO)s are depicted. Modified from Mizushima et al. (2010) [123]. B) LC3 and p62 changes upon autophagy inhibition/activation. On the left a summary of expected results from WB determination, and on the right, expected results from IF determination. For further explanation, please see text above. Taken from Yoshii et al. (2017) [124].

1.4.2 VPS34 in endocytic trafficking

Endocytosis is a key process for many cellular functions. It consist on the internalization of macromolecules and surface proteins from the plasma membrane through different routes, such as the ones involving clathrin, caveolae, or clathrin-independent pathways. These cargos are transported and arranged in different vesicles, called endosomes (Fig. 1.17), that fuse one to another along the way to reach diverse destinations; they can either be degraded in the lysosome, recycled back to the plasma membrane or, in polarised cells, become part of the transcytosis traffic (Fig. 1.17).

The fate of the cargoes rely on the fact that not all endosomes are equal. Endosomes endure different states of maturation in which they change their pH to become more acidic and their PIs lipid composition to contribute to the directional flow of the traffic. Changing their PIs lipid composition along the route entails having a distinct identity and recruiting different binding partners, many of which belong to the Rab family of GTPases, and that will contribute to the fate of the cargoes [132]. Different lipid phosphatases and kinases are distributed to these compartments to acquire the adequate lipid identity. For instance, PtdIns(4,5)P_2 is enriched at the plasma membrane recruiting proteins belonging to the clathrin-

mediated endocytosis (CME) pathway; PtdIns3P is present at early endosomes and intraluminal vesicles (ILVs) and recruits proteins with a FYVE or PX domain such as EEA1 or HRS (Fig. 1.17).

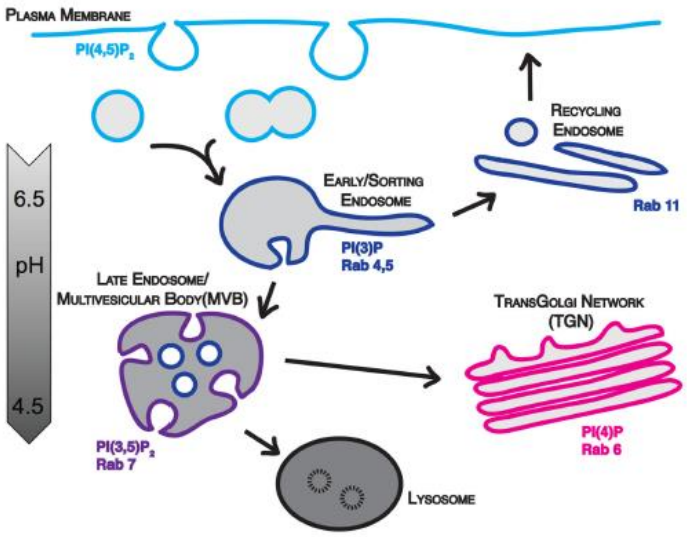

Fig. 1.17. Different fates of endocytic vesicles. Maturation of vesicles occurs through fusion, acidification of their lumen and change of phospholipid membrane identity, which provokes an exchange of effector proteins. Taken from Elkin et al. (2016) [132].

PI3K raised an early interest in this field after it was noticed in 1995 that Wortmannin, a pan class I/III PI3K inhibitor (see section 1.7) prevented homotypic endosome fusion *in vitro* [133], and unsurprisingly, many of the proteins that play a role in endocytic traffic tight regulation were shown to possess PtdIns3P-binding domains [132]. Subsequent studies in yeast and mammals indicated that VPS34 was the main player in the endosomal trafficking and it was assumed for many years to be the main source of this PtdIns3P in these compartments. Emerging evidences proved that it is not the case. The less understood Class II PI3K isoforms come to play in this process and bring a fine-tuning regulation of this pathway at different levels. For instance, class II PI3K-C2α plays a prominent role in CME producing PtdIns(3,4)P_2 [134], and in cargo recycling to the plasma membrane, synthesising PtdIns3P. It is also responsible of Rab11 activation through the generation of an early endosomal PtdIns3P pool, promoting the recycling of vesicles to the plasma membrane [1]. Class II PI3K-C2β has a pivotal importance at the late endosome state, as explained in section 1.2., and it seems to be implicated in the maturation on APPL1 endosomes (very early endosomes) [28].

Despite the fact that VPS34 is no longer thought to be the main producer of PtdIns3P at the endosome, it is still a fine regulator of the endosomal sorting with a predominant role in the late steps of endocytosis. VPS34 complex II localise to Rab9 (found in late endosome involved in retrograde transport), Rab7 (found in late endosome) and Rab5 (early endosome marker) positive endosomes [12].

Localised production of PtdIns3P at the early and late endosome contributes to the recruitment of PtdIns3P binding protein effectors. At the early endosome, mutual binding to VPS34 complex and Rab5 tethers early endosome antigen 1 (EEA1) to the endosome [135, 136] (Fig. 1.19). Other FYVE domain-containing proteins that function in regulation of cargo transport towards the vesicle and promote endosome fusion are rabenosyn-5 [137] and rabankyrin-5 [138]. Rabankyrin-5 might operate principally in micropinocytosis (a type of endocytosis where vesicles are very small~0.1µm).

The transition from early to late endosomes is a dynamic process that takes place by changing the small GTPases Rab identity and the activation status (activated (bound to GTP) or inactivated (bound to GDP)) at the endosome. Early endosomes, characterised by the presence of Rab5, swap Rab5 to Rab7 as they mature to late endosome. This process is partially regulated by VPS34. As small GTPases, Rab5 and Rab7 need GAP and GEFs to modulate their activity [139]. VPS15 binds to the activated form of Rab5 [140, 141], which consequently recruits VPS34 complex. Production of PtdIns3P recruits different protein effectors, such as GAP TBC-2/Armus (mammalian homolog of TBC-2). TBC-2 acts as a switch to turn Rab5 activity off and promote endosome maturation in *C.elegans* [142]. In addition to Rab5 binding, VPS34 is also able to interact with Rab7 through VPS15 [143], and recruit Armus (in a similar fashion to its recruitment at the early endosome) to repress Rab7 activation in mammals [144]. Moreover, VPS34 seems to play an additional PtdIns3P -independent role regarding Armus localisation to the endosome, but this remains unclear [145]. A schematic representation is presented in Fig. 1.18.

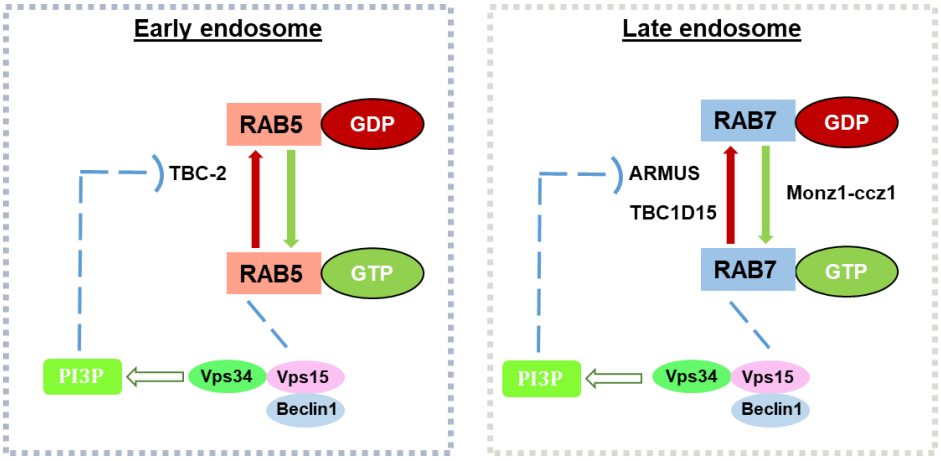

Fig. 1.18. Model of Rab regulation at the early and late endosome in *C.elegans* and mammals, respectively.

As previously mentioned, VPS34 first known function was in the endosome to lysosome pathway [38]. PtdIns3P production recruits the endosomal sorting complex required for transport (ESCRT)-0 subunit HRS, which functions in the degradative [146-148] and recycling [149] endosomal pathway. Furthermore, PtdIns3P interacts with VPS36, a subunit from the ESCRT-II complex. The ESCRT complex plays a role in the cargo sorting and the intraluminal vesicle (ILV) biogenesis. It is formed by four sub-complexes. The ESCRT-0 sequesters transmembrane cargo proteins by recognition of ubiquitin tags. ESCRT-I and II have ubiquitin-binding domains and receive the cargo from the ESCRT-0. Finally, ESCRT-III is recruited to excise forming ILVs from the limiting membrane of the endosome [150].

Lastly, PIKfyve uses PtdIns3P produced by VPS34 to synthesise PtdIns(3,5)P_2 which regulate in turn intraluminal vesicle formation and endosome size [87]. Altogether, this places VPS34 as an important regulator for intraluminal vesicle formation and cargo sorting, recruiting important factors and providing PIKfyve substrate [150].

VPS34 is also implicated in endocytic recycling and endosome motility from endosomes to the plasma membrane, a trafficking event that can regulate cell surface components and receptor signalling events. Tubular regions of the endosomes are involved in the two subcategories of endocytic recycling and endosome motility. The slow recycling process consist on the delivery along the microtubules, from the early endosome towards the periocentriolar endosome (recycling endosome) by the interaction between the PtdIns3P binders SNX4 and KIBRA. The

movement from the recycling endosome to the plasma membrane is mediated by KIF16B, a microtubule motor protein that directly binds to PtdIns3P by its PX domain to promote PtdIns3P-containing vesicles transport [150].

Such VPS34-mediated transport of vesicles is also seen in retrograde trafficking from endosomes to the trans-Golgi Network (TGN) using a similar mechanism [150]. Retrograde transport to the TGN is fundamental for receptor recycling that will transfer newly synthesized proteins to other localisations such as endosomes or the plasma membrane [150, 151]. The retromer complex is the most studied of these complexes and it is recruited to endosome membranes via binding of two of its subunits to PtdIns3P [150].

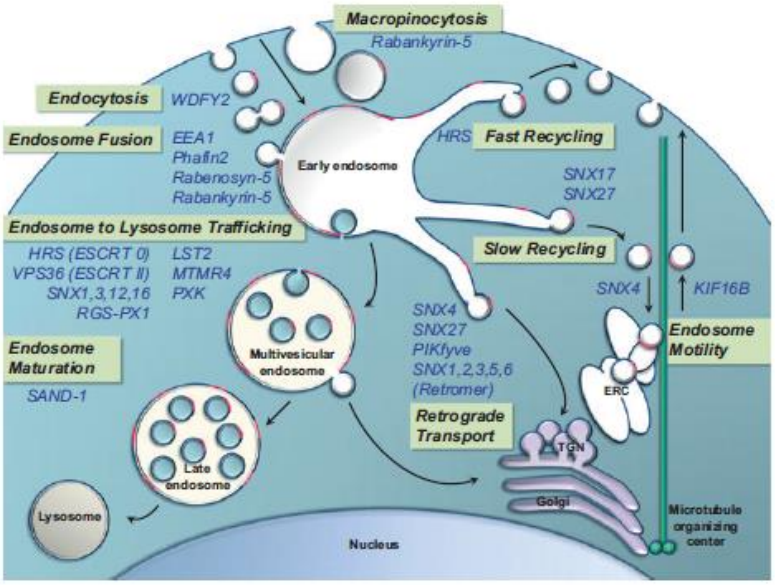

Fig. 1.19. Representation of the different aspects of endocytic traffic. Relevant proteins that take part in every step of endocytic transport are shown in blue. ERC, endocytic recycling compartment. Taken from Raiborg et al. (2013) [150].

1.4.3 VPS34 in cytokinesis

Recent work has highlighted an unexpected role of VPS34 in cytokinesis. Cytokinesis is the last step of the mitosis. It consists on the separation of two daughter cells by abscission of an intracellular bridge, the midbody [152]. Both endocytosis and autophagy play an important role in it. Recycling endosomes (Rab11, FIP3 or Rab35 endosomes) contribute to the complete abscission of the intracellular bridge by recruitment of

specific proteins such as septin2 or ESCRT-III [153] (Fig. 1.20), while autophagy is in charge of eliminating the cytokinetic machinery.

VPS34 involvement in cytokinesis was reported by Sagona et al. (2010) [154]. They showed that PtdIns3P mediates the translocalisation of FYVE-CENT, a protein required for proper cytokinesis, from the centrosome to the midbody by the microtubule-depend motor protein Kinesin-like protein KIF13A. This process involves Tetratricopeptide Repeat Domain 19 (TTC19), a FYVE-CENT binder (Fig. 1.20). It acts upstream of the ESCRT-II member Charged Multivesicular Body Protein 4B (CHMP4B) and may control its function. ESCRT-III machinery has been proposed to mediate midbody abscission.

VPS34 is localised at the midbody, and siRNA knockdown of VPS34 and Beclin 1 drove more cells in cytokinesis and increased the number of binucleated and multinucleated cells. Thoresen et al. (2010) [55] showed that knockdown of UVRAG and BIF-1 but not ATG14L mimicked VPS34 or Beclin 1 knockdown effect in cytokinesis (more cells in cytokinesis than in control group); and thus, suggested that VPS34 complex II was responsible for the PtdIns3P production at the midbody.

The role of autophagy in mitosis is a controverted issue. While some proteins from the cytokinesis machinery are degraded by the proteasome, some are degraded in a p62 dependent manner [155]. It is still not clear which complex is involved, but autophagy plays a vital role, since depletion of autophagy genes such as *Atg7* or *Atg5* impair cytokinesis and produces aneuploidy [155]. Some examples of autophagy substrates are the small GTPase RhoA (which regulates cell shape and completion of cytokinesis) and Cyclin A2 (a partner of cyclin dependent kinase CDK1). Furthermore, the midbody ring can also be degraded by selective autophagy. LC3 and p62 associate with the midbody remains during abscission and together with other autophagic proteins orchestrate the degradation of this structures [155]. On the other hand, it has recently been reported that autophagy is inhibited by the CDK-1 during early stages of mitosis [156].

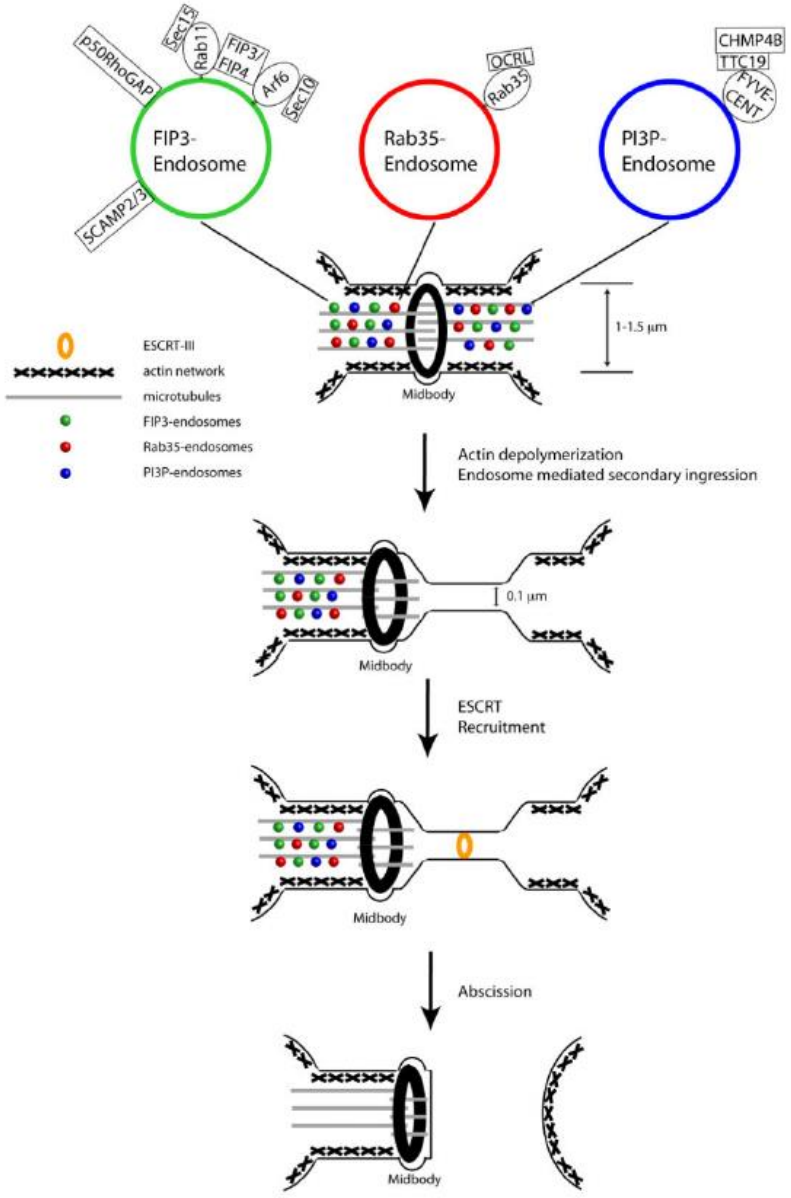

Fig. 1.20. Model for intracellular bridge abscission. The three different types of endosomes mentioned are required to be localises at the midbody. They mediate actin depolymerisation and the secondary ingression to reduce intracellular bridge width. Once the bridge reaches around 100nm, scission occurs. Taken from Schiel and Prekeris (2013) [153].

1.5 VPS34 regulation

VPS34 activity can be regulated by several inputs. External stimuli such as insulin, glucose or amino acids can modulate VPS34 activity. Downstream of these, VPS34 is also regulated by multiple posttranslational modifications (PTM) such as phosphorylation, acetylation, SUMOylation or ubiquitination [7, 43]. These PTMs are mainly mediated by enzymes involved in the energy sensing pathway, such as

ULK1, mTORC1 or AMPK. VPS34 activity can also be regulated by protein interaction (developed in section 1.3), or by spatial restriction whereby selective sequestration of the complexes in unwanted intracellular compartments affect its activity [7]. A recent study has also suggested that intracellular pH changes can also modify activity of VPS34 complexes in particular settings such as phagocytosis of filamentous bacteria [157]. Whether or not this is a more general phenomenon needs to be determined.

1.5.1 VPS34 regulators

1.5.1.1 Nutrient availability

As mentioned above, VPS34 activity is regulated by the nutritional or energy status of the cell. Extracellular nutrient availability such as glucose or amino acids, differentially affect VPS34 activity based on the nature of the VPS34 complex (VPS34-VPS15; VPS34-VPS15-Beclin 1; complex I; or complex II) [13, 158]. While the activity of VPS34-VPS15 dimer and VPS34-VPS15-Beclin 1 decreases under amino acid or glucose starvation, the activity of VPS34 increases when found in complex I. In contrast, when associated to complex II, the activity of VPS34 is enhanced upon insulin stimulation [36].

Glucose-starvation induces AMPK activation, which prevents mTORC1 activity. AMPK activation triggers Beclin 1 phosphorylation at S91/94 when found in complex I, and complex II, increasing the activity of these complexes [13]. Furthermore, PAQR3, one of the complex I binder, is also phosphorylated at T32 by AMPK, inducing activation [66]. On the other side, AMPK can also decrease VPS34 lipid kinase activity by phosphorylating VPS34 at T163 and S165 when found in the dimer VPS34-VPS15 or the VPS34-VPS15-Beclin 1 complex [13].

In amino acid deprived conditions, ULK 1 is activated and phosphorylates Beclin 1 at S14 in VPS34 complex I or II, thereby increasing their lipid kinase activity. Furthermore, the direct binding of UVRAG or ATG14L to ULK1 enhance their regulation by ULK 1 [97]. Amino acid depletion also induces the phosphorylation of Beclin 1 by AMPK [7].

The first hint about the involvement of VPS34 in the insulin pathway was suggested by Byfield et al. [158], who showed that VPS34 is required for

insulin-dependent activation of S6K1 (by T389 phosphorylation) and 4EBP1 (by phosphorylation at S65) through mTORC1.

Some further studies suggested that upon insulin stimulation, VPS34 translocates to the plasma membrane and is activated by Src-mediated phosphorylations at Y231 and Y310, which contributes to VPS34 activation, production of PtdIns3P, and generation of lamellipodia. This phosphorylation is required for mTORC1 translocation to lamellipodia and activation of mTOR substrate S6K1 [159, 160]. The VPS34 complex mediating this process is still unknown.

Nemazanyy et al. [36] , using hepatocytes derived from VPS15 cKO mouse, showed that VPS34 complex II perturbance negatively affects insulin receptor (IR) degradation and insulin signalling. IR is endocytosed and degraded at the lysosome, a process where VPS34 complex II plays an important role. Upon VPS15 depletion, the IR kinetics in endocytic traffic decrease. VPS15 KO mice showed an increased insulin sensitivity. In addition, this study showed that insulin stimulation can activate the VPS34 complex II by relieving the inhibitory interaction of RUBICON with UVRAG. Whether this phenomenon is seen only in hepatocytes remains to be determined. Moreover, it is not entirely clear if the effects observed in this study are due to VPS34 inactivation itself or results from the loss of expression of the VPS34 binding partners often seen in KO studies [161].

This question is indeed of importance, as VPS34 inhibitors do not seem to have an impact on AKT signalling in primary hepatocytes [162]. IR interaction with UVRAG, and RUBICON release from the complex was uncovered. Lastly, Bilanges et al. [162] shed some lights into the mechanism of regulation of VPS34 with the characterisation of a heterozygous VPS34 kinase dead mouse model whose phenotype can be phenocopied using a VPS34 specific inhibitor on WT mice. These mice showed enhanced insulin sensitivity and glucose tolerance. The mechanism underlying these phenotypes was unrelated to insulin receptor trafficking, but instead involved a mild autophagy impairment provoking a reduction of anaplerotic metabolite necessary to feed into the TCA cycle. As a consequence, mitochondria respiration was reduced, causing a drop in ATP level upregulating AMPK pathways and its downstream effects such as inhibition of hepatic gluconeogenesis and enhancement of glucose uptake in the muscle. Altogether, these studies

suggest that VPS34 inhibition could be used as a new therapeutic opportunity to treat insulin resistance-associated diseases.

1.5.1.2 PTMs

Besides being controlled by nutrients and growth factors, VPS34 activity is also affected by nutrient sensing master regulators such as AMPK, ULK1 or mTORC1. ULK1 and AMPK have been explained in section 1.4.1. VPS34 and mTORC1 pathways are strongly interconnected in the different functions that VPS34 executes and the influence of VPS34 in mTORC1 will be discuss in section 1.5.2.1.

mTORC1 activity changes by the depletion or excess of amino acids, glucose, or growth factors [30], and its inhibition reduces non complex I or II PtdIns3P pools [53, 97, 158].

In the context of ALR, mTORC1, whose activation depends on lysosome-derived amino acids, regulates many steps (see section 1.4.1.3.). Importantly, Munson et al. (2015) discovered that mTORC1 was directly regulating this PtdIns3P pool by the phosphorylation of two Ser-residues in UVRAG (S550 and S571), which in turn, increased VPS34 activity and produced a PtdIns3P pool at the lysosome, important for the separation of the autolysosomal tubules [58, 119].

Other mTORC1 substrates are also important for autophagy. The transcription factor TFEB is phosphorylated and inhibited by mTORC1. This prevents TFEB translocation to the nucleus and thus expression of genes that promote lysosome biogenesis [163].

Interestingly, Ma et al. (2017) [164] recently showed that NRBF2 is subjected to spatial regulation by mTORC1. In the presence of nutrients, mTORC1 is activated, and it phosphorylates NRBF2, which promotes NRBF2 binding to VPS34 or VPS15. However, in conditions were mTORC1 is inhibited, this phosphorylation does not take place. NRBF2 changes its binding to Beclin 1/ATG14L and this increases VPS34 lipid kinase activity and autophagy.

Moreover, VPS34 activity can be modulated by proteins like CDK1 or CDK5 as well, which inhibit its kinase activity during the early stages of mitosis through direct phosphorylation [165], or MAPKAPK2 or MAPKAPK3, which phosphorylate Beclin 1 and indirectly contribute to

complex I induction in the presence of amino acids [166]. Other PTMs can directly regulate VPS34. Acetylation of VPS34 residues in its kinase domain by p300 decreases its activity, diminishing the affinity of VPS34 for its substrate, an approach that Bilanges et al used for creating kinase dead VPS34 mice [162]. Indirect ubiquitination of Beclin 1 increases VPS34 complex I activity, and sumoylation of VPS34 increases VPS34 lipid kinase activity in vitro [7].

1.5.2 VPS34 regulates downstream signalling

1.5.2.1 Regulation of mTORC1 by VPS34

Although growth factors and hormones activate mTORC1 by the class I PI3K signalling cascade explained in section 1.2.2 (via AKT and Rheb), studies by Byfield et al. (2005) [158] and Nobukuni et al. (2005) [167] showed that mTORC1 activation by amino acids is not regulated by class I PI3K, but by VPS34. Gulati et al. (2008) [168] showed that amino acids stimulation triggers an increase in Ca^{2+}, which promotes the binding of Calmodulin to VPS34 and in turn activates mTORC1 activity.

Glucose and amino acid deprivation decreases VPS34 levels. However, in the presence of amino acids, VPS34 is activated, and through mTOR, allows for S6K1 phosphorylation at T389 [167] . VPS34 is also required for the phosphorylation of S6 and 4E-BP1 mTORC1's substrates in insulin-stimulated cells [158].

At the lysosome, upon amino acid stimulation, VPS34 is activated and produces a pool of PtdIns3P that promotes recruitment of the phospholipase PLD1 to the lysosome (Fig. 1.21). PLD1 produces phosphatidic acid, which dissociates the inhibitory subunit Deptor from mTORC1. It additionally promotes the recruitment of FYCO1 protein for anterograde transport of the lysosome from the perinuclear region to the plasma membrane, where mTORC1 is further activated [1, 21, 169, 170].

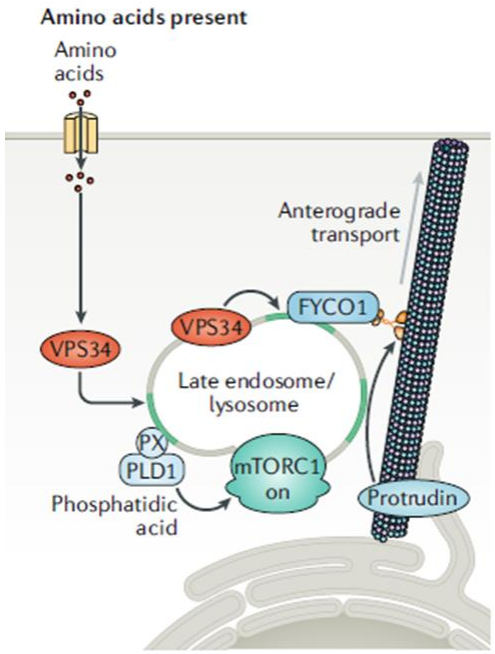

Fig. 1.21. Activation of mTORC1 by VPS34 at the lysosome. Recruitment of PLD1 to the lysosome by VPS34 triggers Deptor dissociation of mTORC1 and promotes its activation. Taken from Bilanges et al. (2019) [1].

1.5.2.2 Crosstalk between VPS34 and class I PI3K

Serum- and glucocorticoid-regulated kinase-3 (SGK3) is a Ser/Thr kinase belonging to the AGC kinase family, highly related to AKT that is recruited to endosomal membranes. It contains a PX domain, by which it binds PtdIns3P [171]. Several studies from D. Alessi's group reported that treatment with the VPS34 inhibitor IN1 induced a rapid decrease of SGK3 activity and its downstream effectors (such as NDRG1). The authors reported that PtdIns3P recruits SGK3 to the endosomes via its PX domain, a crucial step for PDK1 to further increase SGK3 activity [172]. Further studies showed that after prolonged treatment with class I PI3K or AKT inhibitors in breast cancer cells, SGK3 expression and activity was upregulated replacing the role of AKT in mTORC1 activation, presenting thus a new mechanism for cells to bypass long treatment inhibition. In this model, the authors presented evidences that PtdIns3P synthesised by VPS34 controls SGK3 phosphorylation and activation [171, 173]. In addition, the authors showed that SGK3 activity is stimulated by growth factors, namely Insulin-like growth factor 1 (IGF1), EGF and insulin, via two different mechanisms, one involving Class I PI3K and SHIP-2 to produce PIP_3 which would be dephosporylated to form PtdIns3P, and the other one including the VPS34-mediated PtdIns3P production [173].

Further experiments demonstrate that the PtdIns3P pool involved in SGK3 activation is mediated by VPS34 complex II.

Interestingly, p110β was a hit in the same screen as VPS34 when Christoforidis et al. (1999) were looking for Rab5 effectors [140]. Authors showed that p110β interacts with Rab5 and is responsible for a slightly bigger amount of the PI3K activity at the Rab5 positive membranes. Rab5 has a role in endocytosis, but Ravikumar et al. (2008) [174] showed that Rab5 also plays a role in the formation of the autophagosome. Dou et al. (2010) decided to study the relationship between PI3K and autophagy, and reported that p110β depletion impairs autophagy in MEFs, liver and heart. They showed that p110β KO MEFs did not produce formation of autophagosomes upon serum starvation nor PtdIns3P, they had defective mitochondria, and accumulation of aggregates. In addition, their results suggest that p110β kinase activity is not required to regulate autophagy and its role in autophagy is independent of the canonical PI3K pathway through AKT. The authors propose a model where p110β associates with VPS34 complex I through binding to Rab5, and via p110β scaffolding role, enhances autophagy by promoting VPS34 catalytic activity upon growth receptor depletion [175, 176]. Remarkably, the binding sites of Rab5 and p110β have been very recently reported [177], which opens new opportunities to modulate this binding. Very recently as well, Cui et al (2020) reported the involvement of the 110β-VPS34 pathway in non-small cell lung cancer, which highlights the potential importance of this unexplored axis in cancer development.

1.6 VPS34 at the organismal level

VPS34 inactivation mouse models have been created using different strategies to try to uncover VPS34 functions. These different strategies revealed several *in vivo* phenotypes that have helped to elucidate the organismal roles of VPS34 and its related complexes. These phenotypes are summarized in the Table 5.1.

Not only these models highlighted the importance of VPS34 in tissue homeostasis but also validated the VPS34-mediated biological processes such as endocytosis, endosome fusion, endosome motility, endosome maturation [144], cargo sorting to lysosomes, initiation of autophagy [161, 178], phagosome maturation and neutrophil oxidase complex function [85, 150], in primary cells. Furthermore new roles have also been

identified such as its role in maintenance of naïve T cells, and promoting T lymphocyte survival [179, 180], rod cells survival [181], neuronal integrity and survival, and insulin sensitization [162]. Some of these phenotypes have been attributed to the drastic defects in the endo-lysosomal pathways observed upon VPS34 deletion [182].

However, most of these models used a KO approach which has limitations. As part of huge protein complexes, VPS34 has undoubtedly a scaffolding function, as well as kinase function. In most of these KO studies, the expression of VPS34 binding partners (Beclin 1, VPS15, ATG14…) is dampened upon VPS34 deletion [161]. Therefore, it is not clear whether the phenotypes observed in these studies are due to the dampening expression of the binding partners or to VPS34 itself.

To circumvent this problem, Bart Vanhaesebroeck's laboratory pioneered the use of a genetic kinase 'knock-in'(KI) strategy in which a single inactivating point-mutation into the VPS34-encoding *Pik3c3* gene creates an inactive VPS34 kinase activity while preserving its structural function. The mutation consists of mutating the crucial kinase motif (DFG motif) present in the kinase domain into an AFG motif abrogating the kinase activity of VPS34 without affecting its expression and therefore maintaining the VPS34 complexes integrity. Importantly, this model has the further advantage that mimics the effects of a selective VPS34 inhibitor at the organismal level. While the VPS34 homozygous KI mice are embryonically lethal, the VPS34 heterozygous KI mice are healthy and viable and display an improved metabolic phenotype [162]

1.7 Pharmacological inhibition of VPS34

Prior to the recent discovery of VPS34 selective inhibitors in 2014, most of the studies used the very unselective and poorly characterised compound 3-methyladenine (3-MA) and the class I and class III PI3K inhibitor Wortmannin to uncover the functions of VPS34. Although both of these inhibitors block autophagy [183, 184], they are highly unselective for VPS34.

3-MA is a pan-PI3K inhibitor [185, 186]. Due to its off-targets effects, 3-MA based studies should be analysed carefully. It shows higher selectivity for the class III PI3K probably thanks to a hydrophobic ring distinctive of

VPS34. The ATP binding pocket is narrower than that of PI3K, which allows a better binding of 3-MA [73].

Wortmannin is a fungal metabolite that acts as an irreversible inhibitor for PI3K [187]. It has been shown to have a similar *in vitro* efficacy in inhibiting all PI3K but PI3K-C2α. It also has the added drawback of inhibiting related kinases such as mTOR [186, 188].

To avoid the use of 3-MA or Wortmannin, and prior to the discovery of selective VPS34 inhibitors, some studies used the microinjection of VPS34 antibodies that targeted the C-terminus of the protein, inhibiting its activity. One successful example of this application comes from Byfield et al. (2005) [158].

In 2010, a breakthrough study from Roger Williams lab solved the crystal structure of VPS34 and identified unique characteristics that allowed the creation of selective inhibitors [73]. The most striking feature of VPS34 is its ordered catalytic domain (consisting on the P-loop, activation loop and catalytic loop), which appears entirely disordered in the rest of the PI3Ks. A conserved signature of the PI3K is the function of its amphipatic C-terminal helix, which acts as a lid to avoid catalytic activity when substrate is not present, its apo structure. In fact, deletion of the last 10 residues in this helix dampens VPS34 lipid kinase activity in the presence of substrate, while it enhances it in absence of this substrate. In addition to these features, the C-terminal helix also accounts for membrane binding [73, 189].

Since 2014, both *in vivo* and *in vitro* selective VPS34 inhibitors became available. Compound 19 or SAR405 were found to selectively inhibit VPS34 *in vivo*, while PIK-III and IN1 were shown to be *in vitro* inhibitors [172, 190-192].

SAR405 was one of the first described VPS34 selective inhibitors [190]. It binds the ATP-binding pocket and shows disruption in late endosome/lysosome functions and blockage of induced autophagy, but no effect in early endosomes. In addition, antiproliferative activity in renal cancer cell lines after using combination therapy of SAR405 and everolimus, an mTOR inhibitor (a rapamycin homolog) was reported.

PIK-III was the first in vitro selective VPS34 inhibitor [191]. It was shown to block autophagy and contributed to the discovery of various autophagy

substrates, such as NCOA4, a selective autophagy receptor that binds iron-containing ferritin complexes, sequesters them into LC3 positives autophagosomes, and further degrades them, resulting in the release of bioavailable iron. This study identified a new role of VPS34 in maintaining iron homeostasis.

Compound 19 is a derivative of PIK-III inhibitor that can be used orally in *in vivo* models [192]. Compound 19 is extremely selective and it is able to block autophagy both *in vitro* and *in vivo*.

IN1 is a highly selective, permeable and very potent inhibitor with 25nM IC_{50} [172]. Importantly, it does not inhibit any other PI3K or relevant kinase (340 tested in total). Treatment of cells with 1µM of IN1 is able to decrease PtdIns3P levels in endosomes in one minute. Interestingly, Munson et al. (2015) used 1µM of IN1 and 5 µM of IN1 and performed a PX domain staining [58]. They observed that while 1µM of IN1 reduced 60% of the PtdIns3P staining, 5µM achieved a decrease of 90%, showing that different pools of PtdIns3P might be more tightly regulated. Related to this observation, Dowdle et al. (2014) showed that at least 90% of VPS34 activity needs to be reduced in order to block autophagy [191], which correlates with the observation in Bilanges et al. (2017) [162], where heterozygous KI mice, which maintained 50% of VPS34 activity, did not have a complete block in autophagy.

These inhibitors allow repression of total VPS34 activity in a dose dependent manner and paved the way to investigate the impact of modulating VPS34 activity level required to achieve a response either on PtdIns3P, or a biological response, such as in the case of autophagy. A summary of the IC50 activities of the different inhibitors is shown in Table 1.3.

Table 1.3. Summary of autophagy inhibitors and their IC_{50} activity. IC_{50} activity is shown in nM. Asterisk (*) show putative compounds whose inhibitory activity has not been demonstrated. Taken from Pasquier (2016) [193].

Compounds	Biochemical assays						Cellular assays	
	VPS34	PI3K Class I				mTOR	GFP-FYVE	GFP-LC3
		α	β	δ	γ			
3-MA	25,713	145,600	225,900	-	60,671	-	616,000	~1,000,000
Wortmannin	2	28	86	31	78	-	6	1
LY294002	4,216	5,475	>10,000	3,300	>10,000	>3,000		~1,000
PT210*	450	-	-	-	4,428	-	-	-
GSK-2126458*	3	1	2	1	1	6	349	-
Spautin-1	-	-	-	-	-	-	740	-
SAR405	1.2	>10,000	>10,000	>10,000	>10,000	>10,000	27	419
Compound 31	2	2,703	4,489	2,530	>10,000	>10,000	82	204
VPS34-IN1	25	8,036	21,440	1,896	2,685	-	-	-
PIK-III	18	3,960	>9,100	1,200	3,040	>9,100	55	-

1.8 Modulators of VPS34 and inducers of autophagy

Emerging evidences suggest that disturbance of autophagy is a hallmark in certain illnesses and diseases such as in cancer, infections, ageing or neurodegenerative and immune diseases [16, 194].

Inhibition or activation of autophagy can take place depending on the disease context. For instance, while at the start of the tumorigenesis autophagy plays a cytoprotective role, activation of autophagy in an advance cancer such as pancreatic cancer is a common feature that contributes to cancer cell resistance to various stress, such as survival in an environment with low nutrients (e.g. at the core of the tumour) [195]. In addition, many cancer therapies increase autophagy, probably as a way for the cancer cells to develop a resistance mechanism, and it has been suggested that a combinational therapy with an autophagy inhibitor would improve the effectiveness of the therapy. Lastly, in certain conditions related to immunogenic cell death, activation of autophagy would be a combination therapy of choice [16, 195-199].

In order to modulate autophagy, different approaches have been taken over the years tackling autophagy at different stages (for a summary of the available autophagy inhibitors, see Fig. 1.22). VPS34 is one of the most relevant players in the initiation of autophagy, and as such, VPS34 complex I has been the target of many of these attempts.

One of such approaches was Tat–beclin 1, an autophagy inducer drug peptide-derived from this protein [200]. Shoji-Kawata et al. (2013) showed that this peptide efficiently enhances autophagy. However, reports showed co-localisation of Beclin 1 with early endosomes, suggesting that this peptide could be affecting the endocytic pathway as well and therefore question which pathway is involved in. Importantly, treatment with Tat–beclin 1 reduce viral titres in a mice model of neonatal infection with CHIKV and WNV and enhances survival. Besides this approach, in 2018, two different papers came out, both of them targeting Beclin 1 interactions. Wu et al. (2018) [201] investigated the coiled-coil interaction between Beclin 1 and UVRAG. They uncovered its crystal structure and designed peptides that aimed to avoid Beclin 1 homodimerisation and thus promote its interaction with ATG14L or UVRAG. Successfully, one peptide (called Tat-SP4) was found to increase UVRAG binding to Beclin 1 and trigger autophagy and endolysosomal trafficking. Chiang et al. (2018) [202] developed two high throughput screening approaches and found three compounds that disturb Beclin 1-Bcl2 binding and thus, promote formation of VPS34 complexes without enhancing apoptosis. These reagents increased autophagic flux but the authors did not perform any assay to test endocytosis modulation. Very recently, Zachari et al. (2020) [203] performed a drug screening to identify ULK1 and VPS34 specific inhibitors, from which they obtained two ULK1 specific inhibitors and three VPS34 inhibitors.

The main challenge regarding the development of new modulators of VPS34 activity comes from its complex nature. During the preparation of this thesis, a very recent report by Pavlinov et al. (2020) showed a new disrupter of VPS34-ATG14L, obtained from a curated library of protein-protein interaction inhibition molecules, that specifically targets VPS34 complex I, interfering in Beclin 1 and Atg14L binding, and disrupts autophagy without apparent effect in vesicular trafficking [204].

The aim of my project was to undertake the challenge to find VPS34 complex specific binders using nanobodies in order to identify VPS34 complex specific modulators.

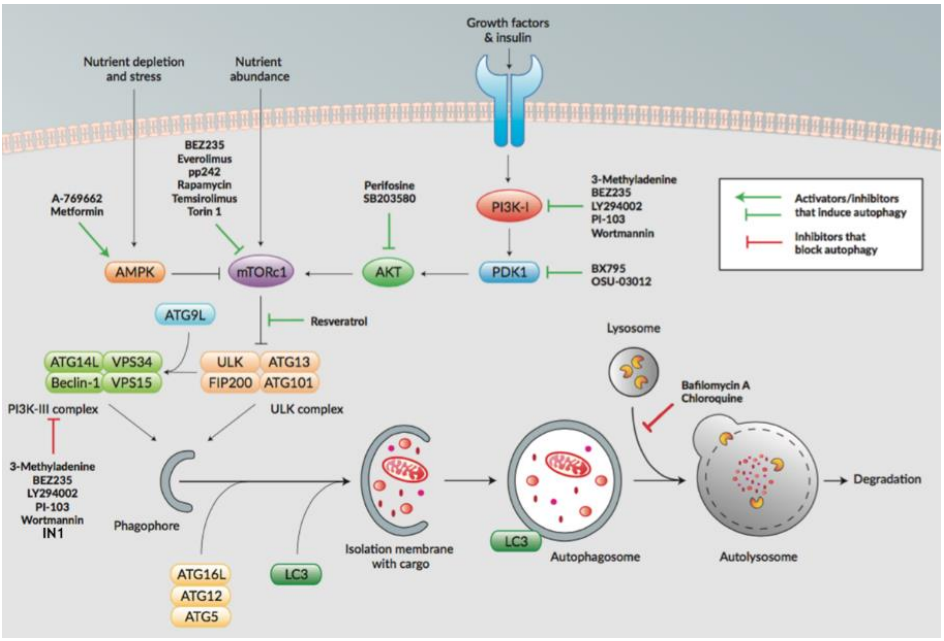

Fig. 1.22. Schematic representation of available autophagy inhibitors. Modified from Invivogen website (https://www.invivogen.com/autophagy-inhibitors).

1.9 Nanobodies

Antibodies are soluble effector proteins who come from the cell surface of antigen (Ag) receptors on B cells (Immunoglobulins, Ig) and that have been secreted as response towards Ag stimulation. They are Y-shaped molecules formed by heavy and light chains divided in variable and constant regions [205].

Antibodies comprise two fragments, fragment antigen binding (Fab) and fragment crystallizable (Fc), which in turn consist of light and heavy chains bound by disulphide bonds. Fab serves for the specific binding of the antibody to the antigen. Its N-terminal end is composed by both light and heavy variable domains. These encompass a broad range of differing amino acids that vary between antibodies and are termed the hypervariable region. They are responsible for the binding specificity. The Fc region is essential for the effector functions of the antibody such as the recruitment of macrophages and natural killer cells or the complement activation. Its function is to engage the antigen binding side to these effector functions [205] (Fig. 1.23).

The characteristics of antibodies have been thoroughly used. These comprise uses in detection or isolation of proteins, as well as inducers of

immunity. However, there are still some limitations to their use. Here is where nanobodies come into play.

The first mention of nanobodies goes back to 1993 [206], when it was described that camels owned heavy chain-only antibodies, besides their natural set of antibodies. These heavy chain-only antibodies have single variable domains that harbour all the full binding capacity to the antigen (see Fig. 1.23) and occur naturally in the *Tylopoda* suborder and sharks [207].

Nanobodies possess many advantages over conventional antibodies that make them especially interesting for certain applications. They are smaller than conventional antibodies (~15 KDa *vs.* 150 KDa) and more stable than them, which allows nanobodies to access to parts unavailable to conventional antibodies, as well as binding to multiprotein complexes. In addition, they are very specific in their binding to conformational epitopes; they have high affinity for folded proteins [208].

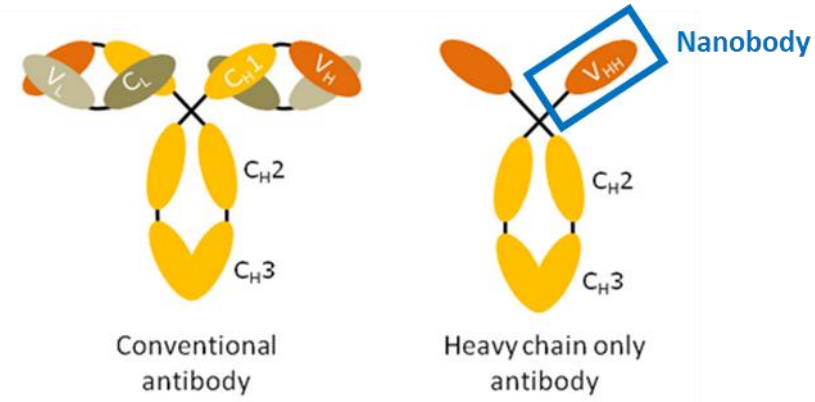

Fig. 1.23. Representation of conventional antibody and heavy chain-only antibody. Nanobodies are small fragments of these heavy chain-only antibodies. Modified from Steyaert Lab website**.**

Over the years, nanobodies have been used mainly in structural biology as chaperones to stabilise proteins in particular conformational states [42, 209, 210]. For instance, several studies used these particular properties to stabilise proteins or protein complexes in active or inactive conformations, or bound to specific ligands [211-213]. Moreover, nanobodies have been used for other important applications outside of crystallography field [214]. For instance, as biosensors to follow the dynamics of specific proteins or their conformational changes [215, 216], to target a protein of interest to degradation [217], as a tool to isolate or visualize different proteins (ex. commercialised GFP-trap by Chromotek,

[218] [219]) or even to find new molecules with a therapeutic potential [220, 221].

1.10 Aims of the study

This study was focused on the class III PI3K (VPS34), and aimed to develop new ways of modulating and tracking VPS34.

This ancestral lipid kinase is part of multiprotein complexes that have different roles in autophagy, endocytic traffic, phagocytosis, and signalling [7]. The current involvement of VPS34 in the biology of these distinct processes have mostly been obtained using depletion approaches that do not keep the scaffolding function of VPS34, and therefore dampen the expression of the rest of its binding partners [161], convoluting the interpretation of the different phenotypes.

To circumvent this problem, the host laboratory used a conditional knock-in strategy in mice to inactivate VPS34 activity, while preserving its scaffolding role, by deleting exon21 of VPS34. This would give rise to a kinase dead allele. This strategy has been previously reported in different conditional mouse models without being fully characterised [8-11]. The first goal of this study was to characterise this truncated protein *in vitro* using HeLa and HEK293 cells.

The second aim of this project was to use nanobodies as a new approach to modulate and track VPS34 complex-specific activity, taking advantage of the properties of the nanobodies to stabilise protein complexes in a specific conformation. Although specific VPS34 inhibitors are available, they decrease global VPS34 activity and therefore, the implication of the different complexes in certain setting is challenging to assess. To date, no specific VPS34 activators have been reported. Importantly, the contact site of these nanobodies could be utilised to develop allosteric small molecule inhibitors or activators of each complex, which would be crucial for modulating autophagy in disease content.

2 Material and Methods

2.1 Materials

2.1.1 Reagents

2.1.1.1 General reagents

Table 2.1 List of general reagents

Reagents	Supplier	Catalogue#
Ammonium chloride	Sigma Aldrich	a4514-100g
ATP	Sigma	A2383
Avidin	IBA	2-0204-015
Bafilomycin A1	Sigma Aldrich	SML1661-.1ML
Bradford protein assay dye	Bio-Rad	5000006
Carbonyl cyanide 3-chlorophenylhydrazone (CCCP)	Sigma	C2759-250MG
Coverslips	VWR	631-0150P
Deuterium oxide (D20)	Acros Organics	AC351430075
Digitonin	Sigma	D141-100MG
Dimethyl sulfoxide (DMSO)	Sigma	D2650
Dulbecco's modified Eagle's Medium, Medium-high glucose (4500 mg/L glucose) (DMEM)	Sigma	D6429-500ML
DMEM/F-12, no phenol red	Gibco	21041025
Protein A Dynabeads	Invitrogen	10001D
Protein G Dynabeads	Invitrogen	10003D
Earle's Balanced Salt Solution	Thermo Fisher Scientific	24010043
ECL Western Blotting Substrate	Promega	W1001
EDTA-free protease inhibitor	Roche	05056489001
Fetal Bovine Serum (FBS)	PAN-Biotech	P30-8500

Reagents	Supplier	Catalogue#
FluoroBrite DMEM	Gibco	A1896701
Formic acid	Sigma	F0507-500ML
Fugene HD transfection reagent	Promega	E2311/2
Gigaprep kit	Qiagen	12991
Guanidine hydrochloride (Gu-HCl)	Sigma	50950-2.5KG
Hepes solution	Sigma	H0887-100mL
Luminata Forte ECL reagent	Millipore	WBLUF0500
6x Massruler DNA loading Dye	Thermo Fisher Scientific	R0621
MassRuler DNA Ladder, High Range	Thermo Fisher Scientific	SM0393
MassRuler DNA Ladder, Low Range	Thermo Fisher Scientific	SM0383
Matrigel basement membrane matrix	Corning	354234
Maxisorp 96-well Immunoplates	Nunc	439454
Menadione	Sigma	M5625-25G
Mitotracker deep red FM	Invitrogen	M22426
OneShot TOP10 chemically competent *E. coli*	Invitrogen	C4040-10
OptiMEM	Gibco	31985070
Dulbecco's Phosphate Buffered Saline (DPBS)	Sigma	D8537-500ML
PEFA	Melford	MB2003
Penicillin-streptomycin	Sigma	P4333-100ML
Phosphatidylinositol	Sigma	P2517-5MG
Premo Autophagy Sensors (LC3-FP) BacMam 2.0	Invitrogen	P36235
ProLong™ Gold Antifade Mountant with DAPI	Thermo Fisher Scientific	P10144

Reagents	Supplier	Catalogue#
Propidium iodide	Sigma	P4170-25M
Protease Inhibitor Cocktail set I	Merck Millipore	535142
Phosphatase Inhibitor Cocktail set II	Merck Millipore	524625
PVDF membranes Immobilion-P membranes	Millipore	IPVH00010
Radioactive labelled γ-ATP (^{32}P)	Hartmann	SRP401
Saponin	Sigma	47036-250G-F
Strep-Tactin conjugated to horse radish peroxidase	IBA	2-1502-001
Strep-Tactin superflow high capacity	IBA	2-1208-002
TCEP	Soltec Ventures	M115
Torin1	Adooq biosciences	A11587
Transit-LT1	Mirus	MIR2300
Trypsin-EDTA	Sigma	59418c-100ML
Tunicamycin	Bioworld	42010020-1
UPLC grade H2O	Romil	H949
Z-VAD (Ome)-FMK	Santa Cruz	SC-311561

2.1.1.2 Molecular Biology reagents

Table 2.2 List of Molecular Biology reagents

Reagents	Supplier	Catalogue#
CIP enzyme	NEB	M0290
dNTPs	Thermo Scientific	R0242
Fermentas FastDigest™ AfeI	Fermentas	FD0324

Reagents	Supplier	Catalogue#
Fermentas FastDigest™ EcoRI	Fermentas	FD0274
Fermentas FastDigest™ KSPAI	Fermentas	FD1034
Fermentas FastDigest™ NotI	Fermentas	FD0594
GFP-Trap_MA	Chromotek	Gtma-200
Gigaprep	Qiagen	12991
In-Fusion HD Cloning plus kit	Takara Bio	638909
Maxiprep Kit	Qiagen	12165
Miniprep Kit	Qiagen	12123
Nuclease-free water	Ambion	AM9937
Phusion High-Fidelity DNA Polymerase	Thermo Fisher Scientific	F530L
Q5® Site-Directed Mutagenesis Kit	NEB	E0554S
QiAquick gel extraction kit	Qiagen	28706
QiAquick PCR Purification kit	Qiagen	28104
T4 ligase	NEB	M0202S
RNaseA	Sigma	83834
KDEL-red plasmid	Kind gift from M. Krauß	-
pEGF N2- nanobodies Plasmids	Kind gift from Y. Ohashi	-
5/6xHIS-EIPA-2xStrep-tagII tagged pcnd4TO plasmids- nanobodies	Kind gift from Y. Ohashi	-

2.1.2 Antibodies

2.1.2.1 Primary antibodies

Table 2.3 List of primary antibodies

Antibody target protein	Origin	Dilution	MW(kDa) of target protein or fixation method	Supplier	Catalogue#	Assay
β-Actin	Mouse	1:10000	40	Sigma	A-5441	WB

Antibody target protein	Origin	Dilution	MW(kDa) of target protein or fixation method	Supplier	Catalogue#	Assay
Atg14	Rabbit	1:1000	55	ProteinTech	19491	WB/ IP
Atg14	Rabbit	1:1000	55	MBL	PD026	WB/ IP
Atg14	Rabbit	1:1000	55-60	CST	96752	WB
phospho-Atg14 (Ser29)	Rabbit	1:1000	65	CST	92340	WB
phospho - ATG16L1 (S278)	Rabbit	1:100	1 min PFA+10 min ice-cold Methanol	Abcam	ab195242	IF
Beclin 1	Rabbit	1:1000	50-60	CST	3738	WB/ IP
Phospho-Beclin (Thr119)	Rabbit	1:1000	55-60	Sigma-Aldrich	ABC118	WB
Calnexin	Rabbit	1:100	Methanol	CST	2433S	IF
Calreticulin-647	Rabbit	1:100	Methanol	Abcam	Ab196159	IF
Caveolin	Rabbit	1:100	1 min PFA+10 min ice-cold Methanol	Santa Cruz	SC894	IF
Cleaved caspase 3	Rabbit	1:100	4%PFA	CST	9664S	IF
EEA1	Rabbit	1:400	1 min PFA+10 min ice-cold Methanol	CST	3288	IF
Mono- and polyubiquitinylated conjugates monoclonal antibody (FK2)	Mouse	1:100	1 min PFA+10 min ice-cold Methanol	Enzo	BML-PW8805	IF
β-galactosidase	Mouse	1:5000	110	Promega	Z3781	WB
GFP	Chicken	1:1000	-	Abcam	ab13970	IF
GFP	Mouse	1:2000	27	Clontech	632381	WB/ IP

Antibody target protein	Origin	Dilution	MW(kDa) of target protein or fixation method	Supplier	Catalogue#	Assay
GM130	Mouse	1:100	1 min PFA+10 min ice-cold Methanol	BD transduction laboratories	610822	IF
HA	Rabbit	1:4000	-	Abcam	Ab9110	WB/ IP
HA	Mouse	1:100	-	Covance	901501	IF
HA	Mouse	1:250	-	Santa cruz	sc-7392	IF
LAMP1	Mouse	1:100	1 min PFA+10 min ice-cold Methanol	BD Biosciences	555798	IF
LC3	Rabbit	1:1000	14-16	CST	2775	WB
LC3	Mouse	1:100	Methanol	Nanotools	0260-100/LC3-2G6	IF
MYC	Rabbit	1:1000	3.7%FA	Homemade	-	WB/ IP
NRBF2	Rabbit	1:1000	35-37	Proteintech	24858-1-AP	WB
P62	Guinea pig	1:300	Methanol	Progen	GP62-C	IF
TOM20	Rabbit	1:300	1 min PFA+10 min ice-cold Methanol	Santa Cruz	sc-11415	IF
α-Tubulin	Mouse	1:5000	52	Sigma	T6074	WB
Vinculin	Mouse	1:5000	130	Sigma	9131	WB
VPS15	Rabbit	1:1000	150	Abcam	Ab124817	WB
VPS34	Rabbit	1:1000	100	Cell signalling Technology (CST)	3811S	WB
VPS34	Rabbit	1:1000	N/A	CST	4263S	IP
UVRAG	Mouse	1:1000	78	MBL	M160-3	WB
WIPI2	Mouse	1:500	Methanol	Homemade-S.Tooze	-	IF

* WB: Western Blot; IF: Immunofluorescence; IP: immunoprecipitation assay

2.1.2.2 Secondary antibodies

Table 2.4 List of secondary antibodies

Antibody	Origin	Dilution	Supplier	Catalogue #	Assay
Amersham ECL Anti-rabbit IgG Horseradish Peroxidase-Linked Species-specific Whole antibody	Donkey	1:5000	GE Healthcare	NA934	WB
Amersham ECL Anti-mouse IgG Horseradish Peroxidase-Linked Species-specific Whole antibody	Sheep	1:5000	Ge healthcare	NXA931	WB
Alexa-Fluor 488 α-chicken	Donkey	1:1000	Jackson Immuno Research	703-545-155	IF
Alexa-Fluor 488 α-rabbit	Goat	1:400	Invitrogen	A32731	IF
Alexa-Fluor 568 α-rabbit	Goat	1:400	Invitrogen	A-11011	IF
Alexa-Fluor 568 α-mouse	Goat	1:400	Invitrogen	A-11004	IF
Alexa Fluor 647 α-guinea pig	Donkey	1:400	Jackson Immuno Research	706-605-148	IF

* WB: Western Blot; IF: Immunofluorescence; IP: immunoprecipitation assay

2.1.3 Primers

Table 2.5 List of primers

Primer ID	Sequence
mVPS34^{WT} (F)	AGTCGAATTCATGGGGGAGGCGGAGAAGTTCC
mVPS34^{WT} (R)	AGTCGCGGCCGCTCATTTTCTCCAGTACTGGGCAAACTTATGG
mVPS34-ex22F	GCAAACTCTTCCATATAGATTT
mVPS34-ex20R	CACAGCTTTTAACGTAAGTGT

Primer ID	Sequence
pLVX-[ATG+CA12560] (F)	TAGAGCGATCGCTAGCGCTATGCAGGTGC AGCTG GTGGAGTCT
pLVX-[ATG+CA12560]-HA (R)	GTAAGGGTAGCAGAATTGACTGGAGACGG TGACCTGGGT
pLVX-[ATG+CA12560+tags]-HA (R)	GTAAGGGTAGCAGAATTGGGCTTCAGGTT CGTGATGGTGATGGT
pLVX-[ATG+CA12560]-GFP (R)	CCCTTGCTGGCGGCCGCACTGGAGACGGT GACCTGGGT
pLVX-[ATG+CA12560+tags]-GFP (R)	CCCTTGCTGGCGGCCGCGGCTTCAGGTTC GTGATGGTGATGGT
pLVX-[ATG+CA12560]-3xFLAG (R)	CTTGTAATCGCAGAATTCACTGGAGACGGT GACCTGGGT
pLVX-[ATG+CA12560+tags]-3xFLAG ®	CTTGTAATCGCAGAATTCGGCTTCAGGTTC GTGATGGTGATGGT
p-LVX-[ATG+CA12560+TGA]-PURO	GTCGACTGCAGAATTCTCAACTGGAGACG GTGACCTGGGT
p-LVX-[ATG+CA12560+tags+TGA]-PURO	GTCGACTGCAGAATTCTCAGGCTTCAGGTT CGTGATGGTGATGGT
CALL001	GTCCTGGCTGCTCTTCTACAAGG
CALL002	GGTACGTGCTGTTGAACTGTTCC
VHH-Back	GATGTGCAGCTGCAGGAGTCTGGRGGAGG
VHH-For	CTAGTGCGGCCGCTGGAGACGGTGACCTG GGT

* F: Forward; R: Reverse

2.1.4 Cell lines

Table 2.6 List of cell lines

Cell line	Derived from	Origin
HeLa	Epithelial adenocarcinoma	ATCC
Hepa 1.6	Murine hepatoma	ATCC
HEK293	Human embryonic kidney	ATCC

Cell line	Derived from	Origin
MEFs	Embryonic day 13.5 mouse embryos	WT mice
U2OS	Osteosarcoma	Gift from P. Rodriguez-Viciana' Laboratory
HCT116 WT	Colorectal carcinoma	Gift from H. Walczak Laboratory
HCT116 Bax^{-}/Bak^{-}	Colorectal carcinoma	Gift from H. Walczak Laboratory

* ATCC: American Type Culture Collection

2.1.5 Buffers

Table 2.7 List of Buffers

Buffer	Composition
Buffer A	20 mM Pipes pH 6.8 137mM NaCl 2.7mM KCl H_2O
Buffer for solid-phase coating (nanobody synthesis)	NaHCO3 buffer pH8.2 0.5mM TCEP
Cantley's Lysis Buffer (CLB)	50mM Tris-HCl pH7.4 150mM NaCl 10% Glycerol 1mM CaCl2 1mM MgCl2 1% Triton X-100 1:1000 Phosphatase inhibitors* 1:1000 Protease inhibitors*
Deuterated Buffer (D2O)	20mM HEPES pH 8.0 150 mM NaCl 0.5 mM TCEP 94.9% D20
FACS medium	1% BSA PBS 1mM EDTA

Buffer	Composition
Gel filtration buffer	20 mM HEPES pH 8.0 150 mM NaCl 0.5 mM TCEP
Kinase Buffer	20 mM Tris pH 7 67mM NaCl 10mM $MnCl_2$ 0.02% (w/v) NP40
Lysis Buffer	50mM Tris-HCl pH 7.4 100mM NaCl 50mM NaF 5mM EDTA 2Mm EGTA 1%Triton X-100 H_2O 1:1000 Phosphatase inhibitors* 1:1000 Protease inhibitors*
Lysis Buffer used for HDX-MS	50mM HEPES pH 8.0 150mM NaCl 0.5mM TCEP 12% glycerol 2mM $MgCl_2$ EDTA-free protease inhibitor 0.5mM PFA 1% triton
MOPS running buffer	50mM MOPS 50mM Tris Base 0.1% SDS 1mM EDTA pH 7.7
Non deuterated Buffer	20mM HEPES pH 8.0 150mM NaCl 0.5mM TCEP
Pepsin-A buffer	0.1% Formic acid
Pepsin-B buffer	0.1% Formic acid 99.9 % Acetonitrile
Quenching buffer	5M Gu-HCl

Buffer	Composition
	8.4% Formic acid 15mM TCEP UPLC grade H_2O
10x Running buffer for homemade gels	1.9M Glycine 249.3 mM Tris 34.7mM SDS 1L distilled H_2O
4x sample buffer	200mM Tris pH 6.8 400mM DTT** 8% SDS Bromophenol Blue 40% Glycerol
Selection and screening buffer for complex I (nanobody synthesis)	20mM Hepes pH8.0 200mM NaCl 0.5mM TCEP
Selection and screening buffer for complex II(nanobody synthesis)	20mM Hepes pH8.0 300mM NaCl 0.5mM TCEP
Sorting medium	1% FBS 1mM EDTA 25mM Hepes pH7-7.4 PBS
TE buffer	10mM Tris-HCl pH 8.0 1mM EDTA H_2O
TEV buffer used for HDX-MS	50mM HEPES pH 8.0 150mM NaCl 0.5mM TCEP
10x Transfer buffer for WB	1.9M Glycine 247.6mM Tris 1L distilled H_2O
1x Transfer buffer	1:2:7 of 10x Transfer Buffer: Methanol, and H_2O, respectively
Wash buffer used for HDX-MS	50mM HEPES pH 8.0 150 mM NaCl

Buffer	Composition
	0.5mM TCEP 50mM $MgCl_2$ 0.1% Triton 5mM ATP pH8.0 0.5mg/mL RNaseA

* Freshly added before use.

** DTT is dissolved in the buffer and aliquots of the buffer are frozen at -20ºC to contribute to DTT stability.

2.2 Methods

2.2.1 Molecular cloning

2.2.1.1 PCR (Polymerase chain reaction)

PCR assays to clone mVsp34 protein into different plasmids and mutate the mVsp34 WT protein were performed using a PeqSTAR thermocycler from VWR (732-2773). Phusion reaction $mVsp34^{WT}$ was performed in order to clone the protein; Q5 Site-Directed Mutagenesis to mutate the protein; and In Fusion Reaction for cloning of the nanobodies. The different PCR conditions used for these different assays are specified in the table below.

Table 2.8 Summary of PCR conditions used for the different experiments performed.

Phusion reaction ($mVPS34^{WT}$)	Q5 Site-Directed Mutagenesis ($mVPS34^{DEL21}$)	In Fusion reaction (nbs)
Heat lid to 110°C 98°C 30” 30xCycle: 98°C 5” 55.4°C 20” 72°C 15” 72°C 7’	Heat lid to 110°C 98°C 30” 25xCycle: 98°C 10” 60°C 20” 72°C 3’ 16” *	Heat lid to 110°C 98°C 30” 35xCycle: 98°C 10” 56°C 15” 72°C 2’

* For 6xMyc tagged plasmids. For GFP tagged, this step was performed for 3 min 30 secs and for HA tagged, for 3min 8secs

2.2.1.2 mVPS34^{WT} Cloning

Full-length mVPS34 was amplified by PCR technique using mVPS34^{WT}-pCMV S6 plasmid (a kind gift from J. Backer) as a template. Amplified full length mVPS34^{WT} was then cloned into N-terminal HA-tagged pCMV S6 (HA-pCMV S6) plasmid, 6xMyc-tagged pCMV S6 (6xMyc-pCMV S6), and GFP-tagged pCMV S6 (GFP-pCMV S6) plasmid. mVPS34^{WT} (F) and mVPS34^{WT} (R) primers (see Table 2.5) were designed using Oligocalc online primer design tool (http://biotools.nubic.northwestern.edu/OligoCalc.html) and were synthesised by Eurofins Genetics. The designing criteria of each primer were to have a melting temperature of around 58^{o}C, a GC content higher than 50%, a primer length of around 40 nucleotides, and no self-complementarity (or the least possible). In addition, the sequence AGTC was included at the start of each primer in order to promote polymerase attachment. Besides, each sequence ends in G, C or double G/C. Finally, an *EcoRI* restriction site was added to mVPS34^{WT} forward primer and a *NotI* restriction site was added to mVPS34^{WT} reverse primer.

The PCR conditions used are specified in Table 2.8 while PCR reagents and material volumes are specified in the table below (Table 2.9).

Table 2.9 PCR reagents volumes

PCR reagents	Concentration
DNA	20ng
5x Buffer	10µL
R-Primer (10µM)	2.5µL
F-Primer (10µM)	2.5µL
dNTPs (2mM)	5µL
Phusion Polymerase (2U/µL)	0.5µL
Nuclease free water	Up to 50 µL

PCR reactions were performed in a 50 µL final volume with 20 µg of DNA, 10 µL of 5xBuffer, 2.5 µL of each primer at 10 µM, 5 µL of dNTPs and 0.5 µL of Phusion polymerase.

Once the gene was amplified, the 2664bp PCR product was run on a 1% agarose gel, extracted and purified using the corresponding Qiagen kits

following manufacturer's instructions (Table 2.2). Subsequently, restriction enzyme (*EcoRI* and *NotI*) digestions were performed; followed by a ligation step and transformation into TOP10 strain of *E. coli*. Finally, positive clones were selected using restriction analysis with *EcoRI/NotI* enzymes and sequenced by Eurofins Genomics using the Sanger method. Sequencing results were analysed using Serial Cloner software.

2.2.1.3 Site-Directed Mutagenesis (SDM)

SDM to delete exon 21 was performed on the positive clones for the three different tagged mVPS34^{WT} constructs, was performed using NEB kit Q5® Site-Directed Mutagenesis Kit following manufacturer's instructions. The PCR conditions used are specified in Table 2.8. Cloning and analysis of the resulting plasmids were performed as described in section 2.2.1.2.

2.2.1.4 Gel extraction and PCR product purification

Agarose gel bands were visualised by short exposure to UV light and corresponding bands were excised from the gel. Extraction of DNA and PCR purification were performed using the specific Qiagen kits (Table 2.2), and In-Fusion (Takara) kit following manufactures' instructions.

2.2.1.5 Restriction enzyme analysis for mVP34^{WT} and mVPS34^{DEL21}

The digestion reaction experiment was performed using Fermentas FastDigest™ *EcoRI and NotI* enzymes and Fermentas 10x Buffer from Thermo Fisher. Purified products were incubated for 45min at 37°C with the restriction enzymes and specific buffer. Reagents and corresponding concentrations are specified in the following table (Table 2.10).

Table 2.10 Restriction enzyme analysis reagents concentration

Reagents	Concentrations
DNA	1µg plasmid DNA/10µL PCR product
10x Buffer	2µL
NotI*	1µL
EcoRI*	1µL
Nuclease free water	Up to 20µL

* FastDigest enzymes' concentration is proprietary information. Their enzyme activity is measured by FastDigest unit (FDU), which states that 1 µL of enzyme (1 FDU) cleaves 1 µg of DNA substrate in 5-15 min at 37 degrees C in 20 µL of 1X FastDigest buffer.

Digestion product (1µg plasmid DNA or 10µL PCR product) was purified using Qiagen kit (QiAquick PCR Purification kit) according to manufacturer's instructions. Results were analysed using Serial Cloner software.

2.2.1.6 Ligation

Ligation of the digested products were performed using T4 ligase enzyme from NEB, at a 1:3 ratio of plasmid:insert, incubated overnight at 16°C.

2.2.1.7 Transformation of competent cells

One Shot *TOP10* chemically competent *E. coli* cells (specified in Table 2.1) were used for the transformation of plasmids. Vials were incubated on ice for 30' and then cells were heat-shocked for 30" at 42°C without shaking. The vials were then placed on ice for 2'. Aseptically, 300µL of pre-warmed S.O.C. (Super Optimal Broth) medium was added to each vial and incubated at 37°C for 1 hour shaking at 225 rpm horizontally. Bacteria was then spun down for 30", supernatant was removed and the pellet was suspended in the remaining medium. The suspended pellet was spread on a pre-warmed selective agar plate and incubated overnight at 37°C.

2.2.1.8 Cloning of nanobodies

Nanobodies contained within the bacterial expression vector pMEsy4, were kindly provided by our collaborator, Prof. R. Williams. To clone the nanobodies into mammalian expression vectors, the In-Fusion system (Takara) was used following manufacturers' instructions. In summary, this involves the use of forward and reverse primers, which share the 15 nucleotides with the host plasmid. Single-stranded 5' overhangs are created at the end of the cloning insert and the linearized cloning vector, which are then annealed.

To make stable cell lines, nanobodies were cloned into four C-terminal tagged viral vectors: HA-pLVX; 3xFlag-pLVX; GFP-pLVX; and un-tagged pLVX In addition, two versions of the nanobodies were cloned: the

nanobody sequence, and the nanobody sequence C-terminal tagged with 6xHis and EPEA.

Cloning was performed following manufacturer's instructions using 1ng DNA starting material, primers designed with SnapGene software (see section 2.1.3), and the PCR programme described in section 2.2.1.1. The correctly sized insert was checked by running 2 µL of the PCR on a 1% agarose gel. Once size was confirmed, the remainder of the PCR reaction was run on a 1% agarose gel. In parallel, linearization of the pLVX plasmid using *AfeI* and *EcoRI* for plasmids HA/3xFlag/no tag, and *AfeI* and *NotI* for GFP-tagged pLVX plasmid was performed. Inserts / linearized plasmids were visualised using ultraviolet light and bands were excised. The remainder of the cloning was performed as explained in 2.2.1.2. DNA extraction and purification was performed using the In-Fusion kit. Minipreps, maxipreps and sequencing were carried out as described in 2.2.1.2. Analysis of the results was performed using SnapGene software.

2.2.2 Cell culture techniques

Cells were cultured in a humidified incubator at 37°C and 5% CO2, and maintained in DMEM supplemented with 10% FBS, 50 U/mL penicillin/streptomycin. For the live-imaging carried out in the Nikon Biostation, cells were maintained in DMEM/F-12 medium, with no phenol red, supplemented with 10%FBS. FluoroBrite DMEM was used for live cell imaging using the spinning disk confocal.

Amino acid starvation was achieved by washing cells three times with EBSS and then incubating them for 1-2H. Cells in complete medium that were part of the same experiment were washed three times with complete medium.

2.2.3 Cell Transfection

Transfections were carried out using Fugene HD (Promega) at a ratio 1:3 (Fugene:DNA) according to manufacturer's specifications. Cells were seeded at a confluence of 60-70% the previous day to transfection. Briefly, DNA was mixed with OptiMEM by pipetting, then Fugene reagent was added, mixed by pipetting again and brieftly spun down. Samples were then incubated for between 10-15 min and then the complex was added to the cells and mixed. Cells were transfected for 17-20h.

2.2.4 Preparation of lentiviruses and lentiviral infection

$16x10^6$ HEK293Lenti-X cells were seeded on 15 cm dishes in 20mL medium (DMEM+10%FBS). The next day, cells were transfected with two packaging vectors (pCMV-VSVG and pCMV- d8.9R) and a target vector (pLVX) encoding the gene of interest. To do so, 2µL of Transit LT1 transfection reagent/µg of DNA was mixed with 500 µL OptiMEM/dish and incubated at room temperature for 5min. Then, 4 µg of each packaging vector and 8 µg of the pLVX vectors (one version of the pLVX vectors per dish) were mixed with 500 µL OptiMEM/dish. Finally the DNA was mixed with the transit LT1 dilution and incubated at room temperature for 20-30 min. 1mL of the mix was added to each dish and mixed by gently swirling. The dishes were incubated at 37°C overnight.

The following morning, 500µl of 0.5M sodium butyrate solution was added to each dish, to achieve a final concentration of 10-12.5mM, and mixed by gently swirling. The dishes were left in the incubator for 6h after which the cells were washed with warm PBS, and 15mL of fresh medium was added. Cells were returned to the incubator for an additional 24h. In parallel, HeLa cells at passage 4 (recipient cells) were seeded in 6 well-plates at a density of $2x10^5$ cells/well. The next day, supernatant from Lenti X cells was collected and filtered through a 0.45µm filter. Filtered supernatant was mixed with polybrene (to a final concentration of 8µg/mL) and was added to the HeLa cells. These were incubated for 24h, after which medium was removed and fresh medium was added. 24h later, medium was replaced with 2µg/mL puromycin DMEM 10% FBS for selection. Once selected, cells were maintained with 1µg/mL puromycin in their medium.

2.2.5 Western blot (WB)

Two types of gels were used in this study, homemade and precast gels. The homemade gels were used for the characterisation of $mVPS34^{DEL21}$ and the CI60 stable cell line (section 3.1.2 and 3.2.3.3), while the precast gels were used for the characterisation of nanobodies (section 3.2.3).

In both cases, cells were lysed by scraping the wells with previously cooled lysis buffer, and incubated on ice for 10 min (for 6-well plates) or 20 min (for 10 cm dishes). To remove cell debris, lysates were spun at

13,000 rpm for 20-30 min at 4°C and the supernatant fraction recovered. Protein concentration was determined by colorimetric assay (Bradford assay, Biorad).

10-30 µg of extracted protein was loaded onto the gels. Gels were run at 100V for 1H30, after which they were transferred to PVDF membranes by wet transfer, performed at 100V for 1H30 at 4°C.

For homemade precast gels the used running buffer was explain in table tal; while for precast gels MOPS running buffer was used.

Membranes were blocked in 5%milk/TBST for 1H at room temperature on a shacking platform. Membranes were then quickly washed with TBST and incubated overnight at 4°C with the corresponding antibodies in 3%BSA (see Table 2.3 List of primary antibodies). The following day, antibodies were recovered for future reuse (three times maximum, stored in 2mM sodium azide). Membranes were washed three times for 10 min with TBST and incubated with the corresponding secondary antibody (see Table 2.4 List of secondary antibodies). Antigen-specific binding of antibodies was visualised using ECL (Promega) or Luminata Forte (Millipore) in the ImageQuant LAS 4000 system. Visualisation and preparation of images was performed using Imagequant software (GE Healthcare) and QuantityOne software (BioRad) was used for signal quantification.

2.2.6 Immunoprecipitation (IP)

2.2.6.1 IP to be followed by kinase assay

Protein G Dynabeads magnetic-agarose beads were used for immunoprecipitation of Myc and HA-tagged proteins. Protein A sepharose beads were used with p85 antibody. Slurry was washed once with PBS before coupling with HA/Myc antibody overnight at 4°C. 3 µg of antibody were used in 20 µL of slurry.

Cells were lysed in CLB buffer and incubated for 25 min on ice. They were spun at 15,000G for ten minutes at 4°C. Protein concentration was determined by colorimetric assay (Bradford assay, Biorad).

Beads were washed once with CLB buffer and incubated with 1mg of HEK293 cellular extract overnight at 4°C on a rotator. Samples were

washed three times with ice-cold lysis buffer (Table 2.7) containing 0.1% Triton, separated in two, one for kinase assay and the other one eluted in 50 µL of 1x sample buffer and boiled for 5 minutes.

2.2.6.2 IP to assess binding of nanobodies

Protein G or A magnetic-agarose beads were used depending on the antibody for the pull down (α-rabbit or α-mouse). Coupling of the antibody to the beads was performed using 15 µL Dynabeads slurry per sample. Samples were washed in 1x PBS by spinning them down and separating them in a magnetic rack. Antibodies were prepared in 300 µl of PBS/sample with 0.1% Triton (and 3% BSA for UVRAG). The antibodies were added to the beads and incubated overnight at 4°C on a rotator.

The following day, cell lysis was performed as described for WB (see section2.2.5), but for the UVRAG IP, the NaCl concentration was increased to 300 mM. IPs from pLVX transiently transfected cells was performed in 15cm plates, while 10cm plates were used for all other transfections. Bradford assay was performed as described in section 2.2.5. The beads coupled to the antibody were collected and washed twice in lysis buffer.

3.5-5µg/µL protein in 300 µL was used as input (50µL from input was reserved and mixed with 4x sample buffer for WB) and added to the beads coupled with the antibody of choice. Samples were incubated overnight at 4°C on a rotator. The next day, beads were recovered from the incubation and separated using the magnetic rack. 50µL were taken and mixed with 4x sample buffer to assess the efficiency of the IP by WB. The rest was removed and three washes were performed using cold lysis buffer (5x washes for UVRAG IP). Beads were eluted in 25µL and mixed with 1x sample buffer (diluted from 4x sample buffer with lysis buffer) and boiled for 10min. Input, supernatant and IPs were stored at -20°C until WB was performed.

IPs were performed slightly differently for cells transfected with Strep-tagged plasmids, as explained below. Once input was collected, 10µg of avidin/sample was added and extracts were incubated for 30 min at 4°C on a rotator. Samples were then centrifuged at 4°C for 5min at 20,817g and supernatant was recovered. 50µL from the supernatant was taken as input and mixed with 4x sample buffer for WB. The remainder was added to 10µL of StrepTactin superflow high-capacity resin (previously washed

three times with lysis buffer) and incubated overnight at 4°C on a rotator. The next day, the resin was spun down at 4°C for 5min at 1000g, and 50 µL of supernatant was retained and mixed with 4x sample buffer. The resin was washed five times with cold lysis buffer by spinning the resin down. After the last wash, elution was performed in 1x sample buffer.

2.2.7 Lipid kinase assay

Immunoprecipitated protein was incubated with 25 µL of kinase buffer to perform a kinase assay. Radioactive labelled γ-ATP (^{32}P) was used to quantify radioactive PtdIns3P by thin layer chromatography (TLC), as previously described [222]. PtdIns was diluted in kinase buffer at a concentration of 1 µg/µL. 10 µL of PtdIns per reaction was then added to 25 µL of IP. A master mix of 100 µM cold ATP per sample for 50µL total volume reactions was prepared in kinase buffer. Once in the radioactive room, 0.1 µCi/µL of radiolabelled ^{32}P-ATP /per reaction was added to the master mix. 15 µL of the master mix was then added in a staggered manner to each sample and samples were incubated for 30 min at 37°C. Reactions were stopped by adding 100 µL of 1N HCL and inversion of the tubes. Once each reaction had been stopped, they were mixed vigorously for 2 min, after which 200 µL MeOH:CHCl3 (1:1) was added to each sample and then mixed again for a further minute. Samples were then centrifuged at 2,500 rpm for 5 min and the lipid phase was collected. 80 µL of MeOH: 0.1N HCl (1:1) was added to the samples and they were vortexed and spun at 2,500 rpm for 5min. The lipid fraction was again collected and spotted onto a TLC plate, previously treated with 1% K-oxalate in MeOH:H2O 2:3 + 2 mM EDTA and 'baked' for more than 45 min at ~124°C. Once the lipids were spotted, the plate was placed in a glass chamber (properly sealed) containing 97.5mLpropanol-1, 46.5mL water and 6mL Acetic acid (100%) for about 3 hours. Prior to the experiment, the chamber had been previously stored in that buffer for a week. Once the TLC had run, the plate was dried in a fume hood, wrapped in cling film and placed on a phosphoscreen. The screen was analysed the following day using a Typhoon trio + phosphorimager (GE Healthcare Life Sciences).

2.2.8 Immunofluorescence (IF)

Coverslips were placed in 6-well plates (3 coverslips per well) or in 12 well-plates and coated with matrigel (500µL/well in 6-well plates, 250

µL/well for 12 well-plates) for 30 min. Matrigel was recovered for re-use and wells were washed three times with PBS. After the last wash, cells were seeded in these wells to 70% confluence. The next day, cells were transfected for 15-20h as explained in section and then washed once with PBS and fixed. Fixation was performed in two different procedures. Fixation method 1; 4% PFA for 1 minute, then 100% ice-cold methanol for 10 min. Fixation method 2; methanol for 10 min (see Crossref). Wells were washed three times with PBS and cells were incubated with blocking solution (3% BSA/PBS) for 1H. Following this, coverslips were incubated with primary antibody diluted in 3% BSA/PBS for 1H 30'. Coverslips were then washed three times in PBS, and incubated with the corresponding secondary antibody, coupled to an alexa fluorophore (488, 568 or 647) for 1H at room temperature. For primary antibodies already coupled to fluorophores, these were added during the secondary antibody incubation. Following this last incubation, three 10min PBS washes were performed and coverslips were mounted onto slides using mounting media with DAPI (Prolong gold).

For PtdIns3P staining the protocol was adapted from [223]. After washing once with PBS to remove the medium from the cells, cells were fixed for 15 min at room temperature with 2% PFA/PBS, after which they were washed three times with 50 mM NH4Cl/PBS. Cells were permeabilized with 20µM digitonin diluted in Buffer A for 5 min, washed three times with Buffer A and blocked with GFP-2xFYVE probe (a kind gift from V.Haucke) diluted to a final concentration of 0.055µg/mL in 50mM NH4Cl/ 5% goat serum for 1H. Once blocking was over, coverslips were washed twice with Buffer A for 5min, and coverslips were incubated with the primary antibody diluted in 5% goat serum/Buffer A for 1H at room temperature. Then, coverslips were washed twice with Buffer A and incubated with the secondary antibody diluted in 5% goat serum/Buffer A (the secondary antibody was spun down at 13,000 rpm for approximately 5min at 4°C before use). After this last incubation time, coverslips were washed 4 times with buffer A and a post-fixation step using 2%PFA/PBS for 5-10min took place, after which coverslips were washed three times with 50 mM NH4Cl/PBS for 5min, and then two washes with PBS. Cells on coverslips were mounted onto slides using DAPI mounting media (Prolong gold).

2.2.9 Live imaging

2.2.9.1 Using Nikon Biostation

Cells were seeded 24 hours before in 6-well plates or 12-well plates to a confluence of around 70% for transfection with CI60-GFP- pLVX, NC59-GFP- pLVX and GFP control (GFP-pLVX empty vector). When inhibitors were added, these were added directly after transfection. Images were taken around 2-3 h post transfection every 10 or 15 min.

2.2.9.2 Using Spinning disk confocal

U2OS/HeLa cells were seeded in a 96 well plate at a confluence of 15,000 cells / well, then transfected the following morning (see 2.2.3). The 3i Spinning Disk Confocal was used to live image cells for 24h, at 37°C and 5% CO2.

2.2.10 Sorting

10 million cells/mL in sorting media were used for sorting. Cells were stained with the cell death marker propidium iodide (1:500). Subsequently, cells were sorted using a BD FACS Aria III Cell Sorter.

2.2.11 Flow cytometry

HeLa, U2OS, HCT116 WT and HCT116 Bax-/Bak- cells were seeded in 48-well plates, 24hr prior to transfection, at 60% confluence. Cells were transfected using either pLVX or pEGF N2 constructs (specified in results) for 12, 24 or 48H. When inhibitors were used, these were added 5h after transfection. At the indicated time point, the supernatant from the wells was collected into FACS tubes. Cells were washed once with 500 µL PBS, collected into the original FACS tube, and trypsinized in 300 µL. Cells were then suspended and pooled in FACS tubes. Tubes were centrifuged at 300 x g at 4°C, for 5min. All subsequent steps were performed on ice.

Four compensation controls are used for each experiment: non stained samples, GFP transfected cells (single GFP channel), dead cells only stained with propidium iodide (treated with 100ng/mL hTNF-α and 25µg/mL cyclohexamine, or 20 µM digitonin in the case of HCT116 cells) and cells only stained with mitotracker deep red. Supernatant was aspirated and cells were suspended in either FACS medium for

compensation controls (except mitotracker control) or 50nM mitotracker deep red/FACS medium (HCT116 were stained with 100 nM mitotracker deep red) for 30 min. After incubation, every sample and dead cell control were washed with FACS medium and stained with 1:500 PI/ FACS medium in 350 µL total volume, while the rest of compensation controls were suspended in FACS medium.

Following propidium iodide staining, samples were analysed using a BD Fortessa X20 Flow Cytometer. Analysis was performed on GFP positive cells.

2.2.12 Nanobody synthesis

Complex I and II purification was carried out in R. Williams's Lab. The protein purification protocol was identical to that described below in the HDX-MS section (2.2.13), albeit some slight differences for complex I: VPS15, Beclin 1 and ATG14L had been tagged with proteinA (ZZ), which was cleaved after purification. The heterodimer Beclin 1-ATG14L was in excess. In the HDX-MS, only VPS15 was tagged and the resulting complex I was mono-disperse.

Nanobody synthesis was performed by the VIB. A total of 1 mg of protein was used for immunisation and nanobody selection. 700 µg were used for immunisation and 300 µg were used for nanobody selection, identification and characterisation. Every aspect of the synthesis of the nanobodies is detailed in [208] and was performed at the VIB centre. Specifications for this project are found below.

Immunisation of the Llamas took place according to European animal welfare legislation in the VIB facilities. Before immunisation there was at least one week of acclimatisation. Injections were subcutaneous, in the proximity of the neck base of the llama, near the bow lymph node. Llamas were injected every week. Injections consisted in immunogen and adjuvant in a 1:1 ratio, in the first, second, third and fifth week. The third and sixth week the immunogen was injected first and the adjuvant later at 5cm from the first injection. GERBU LQ was used as adjuvant.

Four days after the last injection, 100 mL of blood from immunised llamas was obtained to clone the set of nanobodies, and isolation of peripheral blood lymphocytes was performed. RNA was purified and cDNA was synthesised. Two-step nested PCR was carried out to amplify the

nanobody encoding ORFs using CALL001, CALL002, VHH-Back and VHH-For primers.

Following PCR, cloning into phage display vector pMESy4 was performed and phage display selections were carried out employing cross-linked (performed by mixing Complex I with CovalX K200 (CovalX AG, Switzerland) by R. Williams Lab) and non cross-linked complexes that were solid-phase coated in 96 well plates. Selections and screenings were performed using the same conditions. Two rounds of panning were necessary.

To further characterise the nanobodies, an additional ELISA was performed using non cross-linked complex I / complex II (solid phase coated in the same buffer used for the phage-display). The buffer used in the ELISA was the same as for the selection and screening for complex II.

2.2.13 Hydrogen Deuterium eXchange-Mass Spectrometry (HDX-MS)

Every step of HDX-MS was performed at R Williams' Lab by Y. Ohashi.

2.2.13.1 Complex I purification

In order to perform Hydrogen Deuterium eXchange-Mass Spectrometry (HDX-MS), human complex I and nanobody CA12560 (CI60) were purified separately. Transfection of complex I was carried out in Expi293f cells, which were grown in 4 L of Expi293 Expression medium (Thermo Fisher A1435101). They were transfected with 12 mg PEI (4 mg/L; Polysciences 24765) at a cell density of around 2.0-2.5 x10^6 with 4.4 mg of plasmid DNA (1.1 mg/L). These were incubated at 37˚C, 8% CO2, 125 rpm shaking for 48 hours. Cells were harvested at 3,000 g for 25 min, flash-frozen in liquid nitrogen, and stored at -80˚C until use. To purify complex I, the cell pellet was dissolved in 120 mL lysis buffer (no sonication or shaking). It was then centrifuged at 142,000 x g for 30 min using Type45 Ti (Beckman). The supernatant was recovered and 4 mL bed volume of IgG beads (IgG Sepharose 6 Fast Flow, GE Healthcare), which had been equilibrated with lysis buffer, were added. Supernatant and beads were rotated at 8 rpm at 4˚C for 3.5 hours and then centrifuged for 800 x g for 8 min. Supernatant was removed and the beads/lysate were transferred to an empty gravity flow column, drained, and washed

with 200 mL wash buffer. After this, it was washed with 100 mL TEV buffer. 10 mL tev buffer and 50 µL of TEV (3 mg/mL, homemade) was added and the column was set horizontally at 4˚C overnight. The flow-through was later collected using 5 mL tev buffer+0.1% CHAPS without TEV. This process was repeated 3 more times (4 times of 5 mL elution with TEV buffer + 0.1% CHAPS). The fractions were combined, and the protein was passed through a 0.45 µm syringe filter, concentrated down to 500 µL using a 100 k cut-off concentrator (Amicon Ultra, Millipore: UFC910024) and gel filtration was performed with a S200 10/30 column.

2.2.13.2 Deuteration step

Samples were run in triplicate and at 4 deuteration timepoints were measured at 3000, 300, 30 and 3 seconds.

Complex I +/- CI60 samples were incubated in solution with deuterium oxide, denatured and digested. Five non-deuteration samples were used as controls.

Protein was diluted with gel filtration buffer to a final concentration for complex I of 7µM and for CI60, 28µM. After dilution, samples were incubated for 15 minutes on ice to allow CI60 to bind to the complex.

The deuteration step took place at room temperature. Samples were added to 40 µL of D_2O buffer (to make a final concentration of 75% D_2O) and quenched at every time point with 20 µL of quenching buffer. Once the time course was complete, samples were immediately frozen and stored at -80˚C.

2.2.13.3 HDX-MS

Rapidly-thawed samples were injected onto an ultra performance liquid chromatography (UPLC) system (M-class UPLC, Waters) which had been previously cooled. To digest the deuterated sample, an Enzymate Pepsin “Trap” Column (Waters) was used. Temperature was maintained at 15˚C for two minutes. Elution of the peptides was performed into an equilibrated column (Acquity 1.7 µm particle, 100 mm × 1 mm C18 UPLC column , Waters) for 20 minutes. Equilibration was performed with Pepsin A buffer in a gradient of 5-36% of pepsin B buffer. The Waters Synapt G2 Si (Waters) system was used to gather peptide data in High-Definition MS^e

data acquisition mode fitted with an ESI source in a range over 50 to 2000 *m/z.*

Identification of the peptides was performed from five non-deuterated samples for complex I, by using the ProteinLynx Global Server (PLGS, Waters, U.K.) using the parameters previously mentioned. The DynamX 3.0 software (Waters, U.K.) was used to analyse deuterated peptides. The criteria of peptide inclusion was as follows:

Minimum score: 6.4

Minimum consecutive products: 1

Minimum products per amino acid: 0.3

Maximum MH+ error: 5ppm

The software performed an initial automated spectral processing step and then individual peptides were manually examined for quality assurance. The HDX analysis complies with the community agreed guidelines.

2.2.14 IF quantification and statistics

Criteria to quantify IF signal of GFP cells and to measure of particles was performed using Fiji software, with the limit of 0-4 µm in size particle and 0-1 circularity. The threshold used was RenyiEntropy for LC3, p62 and PtdIns3P staining, Moments for TOM20 staining and Intermodes for WIPI2 staining. pAtg16L1 IFs were processed with despeckle and smooth to eliminate noise and unspecific local maxima. The find maxima function in Fiji/ImageJ was then employed using a prominence of 5000. Intensity was measured at these points for the intensity measurement. The macro was based on Rodriguez-Berriguete et al. (2018) [224].

Experiments were performed twice, unless stated otherwise in the results part. Z-stacks were used in every IF experiment but for the pATG16L1 staining, and maximum intensity projections were created using Zen software to analyse the images. The number of cells quantified varied depending on the experiments, due to the difficulty of the experimental settings, which are explained in the Results chapter. For HeLa cells, in LC3 and p62 experiments, a total of 155±40 cells was used for every condition of the DMSO treated cells; 125±31 cells in WIPI2 experiments; and 71±6 cells in TOM20 experiments. An average of 35 cells/condition

were quantified in the preliminary experiment using the antibody WIPI2 in cells treated with Bafilomycin A1; 79±10 cells/condition in the stable cell lines using GFP-2xFYVE^{Hrs}, and 61±8 cells/condition in the transient transfection using GFP-2xFYVE^{Hrs}. 44±6 cells/condition were quantified in the pATG16L1 preliminary experiment. Lastly, in U2OS cells, due to technical difficulties, ~30 cells were quantified per condition. Distribution of the samples was tested and non-parametric tests were used to assess the significance of the data. GraphPad Prism 6 was used for the statistical analysis. The type of analysis performed appears in the figure legend. $*p < 0.05$, $**p < 0.01$, $***p < 0.001$.

3 Results

3.1 Characterisation of a novel conditional mVPS34 mouse allele

3.1.1 Cloning of mouse wild type VPS34 (mVPS34^{WT}) and DEL21 mutant VPS34 (mVPS34^{DEL21}) into mammalian expression vectors.

To gain insight in the organismal function of VPS34 kinase activity, our laboratory generated a mouse line in which VPS34 was expected to be conditionally kinase-dead. This was done by a gene targeting strategy whereby exon 21 located in the kinase domain was flanked by loxP sites, which can be excised by Cre-mediated recombination (see Fig. 3.1 A for structure). This exon encodes a region of the kinase domain, which is expected to be critical for the kinase reaction. Given that this exon encodes 75 nucleotides, Cre-mediated excision is expected to maintain the open reading frame creating truncated version of VPS34 protein lacking 25 amino acids. This strategy was originally designed to create a kinase-inactive protein that is still expressed, which differs from gene knock out (KO) strategies whereby protein expression is lost (Fig. 3.1B). The experiments below were aimed to experimentally validate this hypothesis.

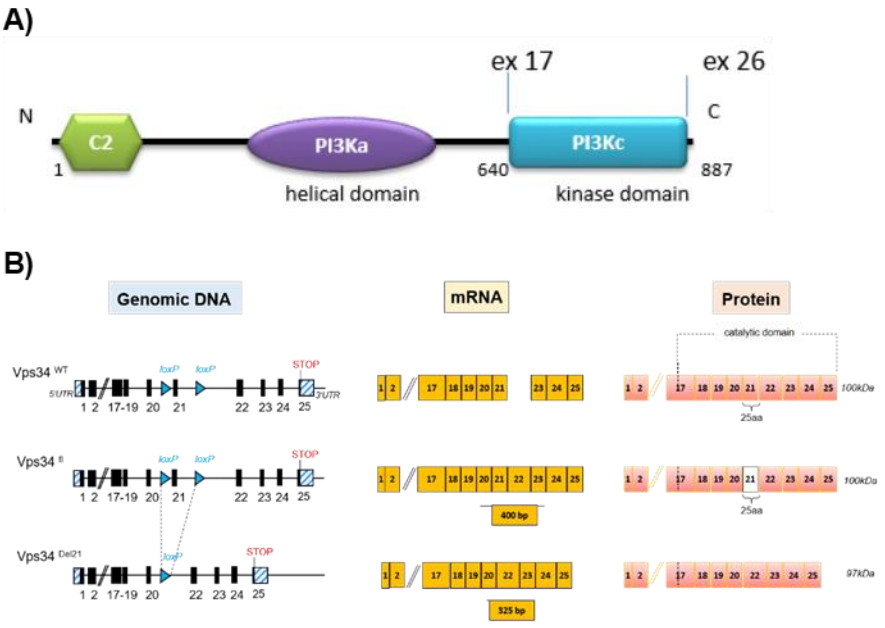

Fig. 3.1. VPS34 structure and targeting strategy. A) VPS34 domain structure. Three structural domains are found in VPS34, namely an N-terminal C2 domain (which engages all subunits of the VPS34 complex), a helical domain and a C-terminal the kinase domain. B) Mouse gene-targeting strategy. Exon21 (located

in the kinase domain) of mouse VPS34 was flanked with LoxP sites. 'Floxing out' this gene segment using Cre recombinase is expected to result in deletion of 75 nucleotides without changing in the reading frame, giving rise to a truncated VPS34 protein 25 amino acids shorter and inactive.

In order to characterise this allele *in vitro*, and to assess if this deletion would indeed lead to kinase inactivation of VPS34, mammalian expression plasmids encoding mouse VPS34^{WT} and VPS34^{DEL21} mutant were generated. An overview of the cloning strategy is presented in Fig. 3.2. Because I planned to perform immunoprecipitation (IP), western blotting (WB) and immunofluorescence (IF) experiments, mouse VPS34 (mVPS34) was subcloned in vectors that allowed to add an N-terminal tag namely HA, 6xMyc or GFP. Firstly, mVPS34^{WT} was subcloned in the N-terminal tagged plasmids (Fig. 3.2) as explained in M&M. A PCR from the VPS34 pCMV-S6 plasmid was performed, to amplify mVPS34 and add the *EcoRI* and *NotI* sites to both ends of the fragment. The restriction sites EcoRI and NotI in the pCMV S6 were used to subclone this into the GFP/HA/6xMyc N-terminal tagged pCMV S6 plasmids.

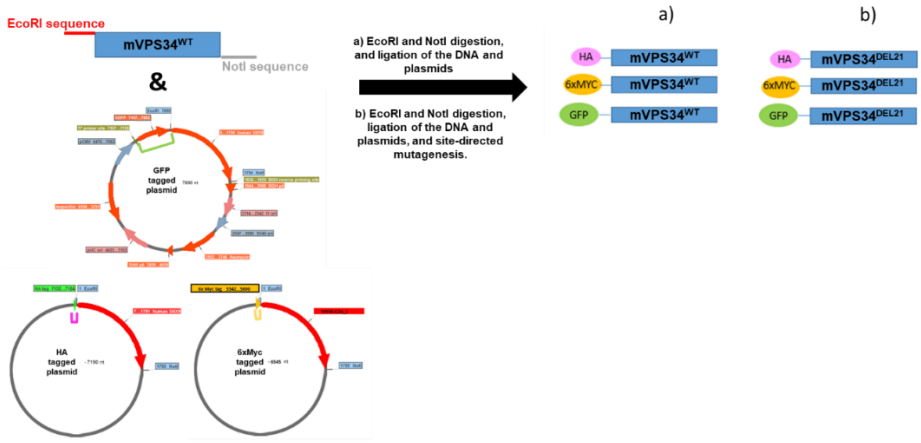

Fig. 3.2. Overview of the cloning of N-terminally-tagged mVPS34^{WT} and mVPS34^{DEL21}.

Positive clones were selected by restriction enzyme analysis (Fig. 3.3A) followed by DNA sequencing. Then, site directed mutagenesis was performed in the positive clones to obtain the VPS34^{DEL21} mutant, following the strategy presented in Fig. 3.3B.

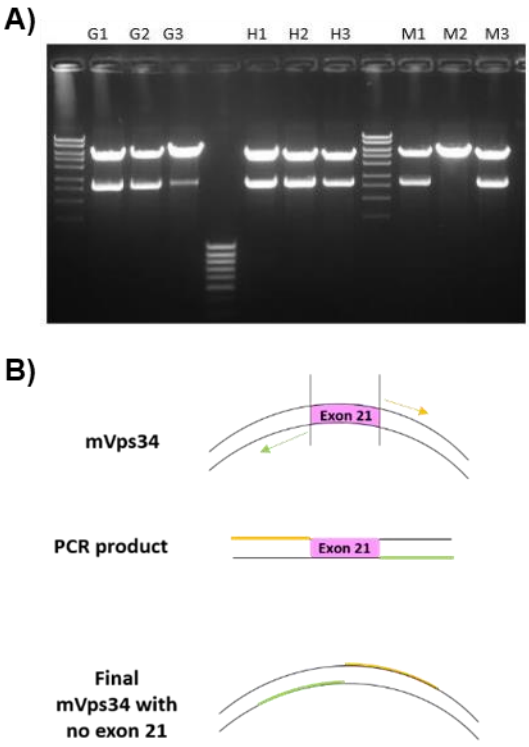

Fig. 3.3 mVPS34 ^{WT} and mVPS34 ^{DEL21} cloning overview. A). Agarose gel from the restriction analysis. EcoRI and NotI enzymes used in GFP-mVPS34 ^{WT} (G), HA-mVPS34^{WT} (H) and 6xMyc-mVPS34^{WT} (M). Minipreps from three clones per construct were analysed and one positive clone per construct was selected and sequenced. B) Site-directed mutagenesis strategy to delete exon21. The arrows represent the primers flanking the exon 21.

3.1.2 Functional characterisation of a VPS34^{DEL21} in transiently transfected cell lines

3.1.2.1 Expression of VPS34^{DEL21} mutant

In a first attempt to characterise the VPS34^{DEL21}mutant, the hepatoma cell line Hepa1.6 and immortalized mouse embryonic fibroblast (MEFs) cells were transfected for 24h with the following tagged version of mVPS34: GFP-mVPS34^{WT}, HA-mVPS34^{WT}, 6xMyc-mVPS34^{WT}, GFP-mVPS34^{DEL21}, HA-mVPS34^{DEL21}, 6xMyc-mVPS34^{DEL21} (Fig. 3.4). The different versions of the construct were distinguished because of the difference in the molecular weight of the VPS34 signal, due to the GFP/HA/6xMyc tags. It is also possible to appreciate the band shift between the VPS34^{WT} and VPS34^{DEL21}, due to the ablation of the 25 amino acids encoded by exon 21.

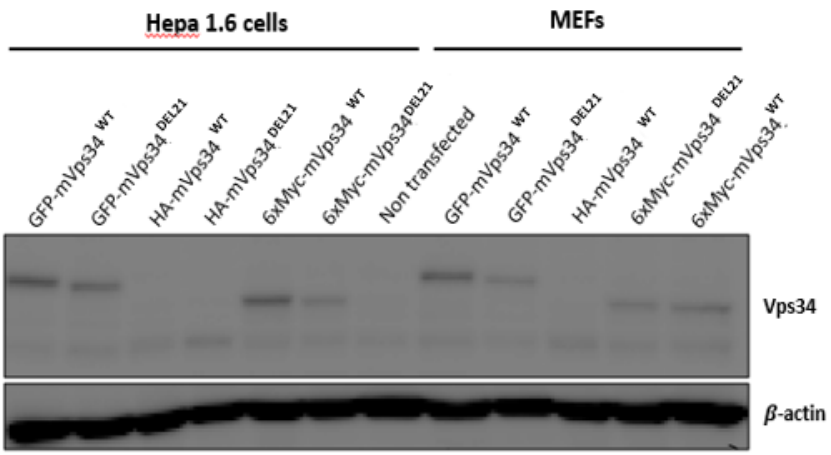

Fig. 3.4 Expression of VPS34 in Hepa 1.6 and MEFs. Cells were transfected with different N-tagged version of mVPS34 for 24h followed by immunoblotting using an antibody to VPS34**.**

I was able to confirm that the DEL21 mutant was expressed in truncated form in both cell lines.

To assess whether there was any phenotypic difference induced by these VPS34 mutants, HeLa cells were transfected with either mVPS34^{WT} or mVPS34^{DEL21} as GFP-tagged versions. HeLa cells have a higher transfection efficiency than MEFs and are bigger and flatter than Hepa 1.6. These characteristics that have made them a widely used cell line for imaging. The cells were transfected for 24h and treated after transfection for 1H or 6h with either DMSO, the specific VPS34 inhibitor IN1 (5 µM), or starved with EBSS to check phenotypic changes not only under normal conditions but also in conditions where VPS34 would be inhibited or activated (Fig. 3.5).

The first observation in complete medium (control treated with the vehicle, DMSO) was that while mVPS34^{WT} has a largely cytoplasmic expression, where vesicles are occasionally noticeable (see Fig. 3.5); mVPS34^{DEL21} was mostly present in punctae (Fig. 3.5). In DMSO, mVPS34^{WT} and mVPS34^{DEL21} did not lead to further phenotypical differences. However, in mVPS34^{WT} cells incubated with IN1 for 6 h I can observe a slight increase in the number and size of vacuoles compared to mVPS34^{DEL21} cells. In addition, some vacuolization can be observed in EBSS condition in the mVPS34^{DEL21} cells, which is not present in the same condition in mVPS34^{WT} cells. Vacuolization is a major feature observed in cells treated with the VPS34-specific inhibitor IN1, and in VPS34 KO/KI.

The level of expression of the different constructs is shown in Fig. 3.5. GFP-mVPS34^{WT} has a better transfection efficiency than GFP-mVPS34^{DEL21}.

Regarding the EBSS condition I hardly observed any change compared to the complete medium control (DMSO), although in some cases I noticed that around 2% of the cells showed an increase in cell size (Fig. 3.5C, right)

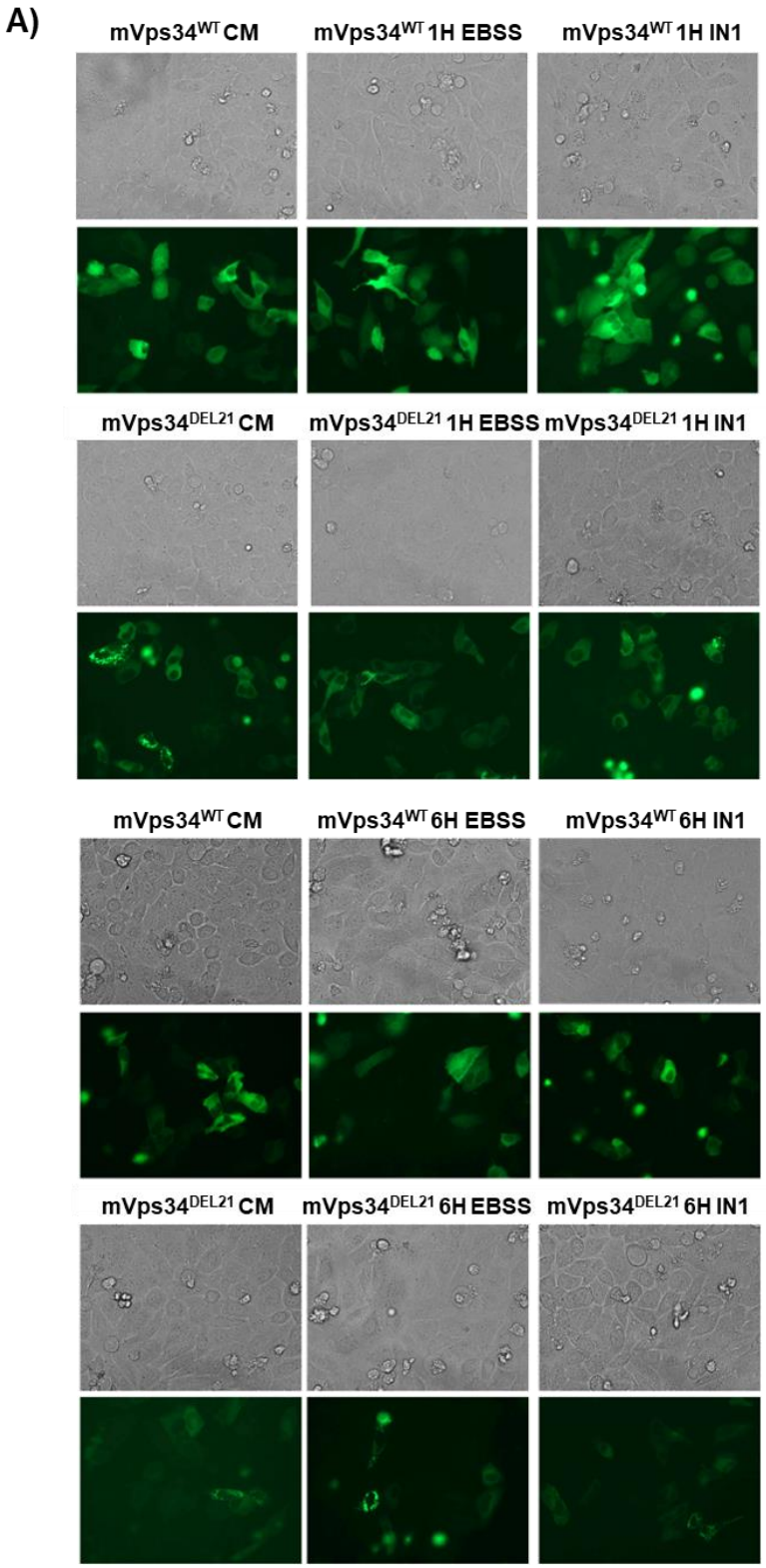

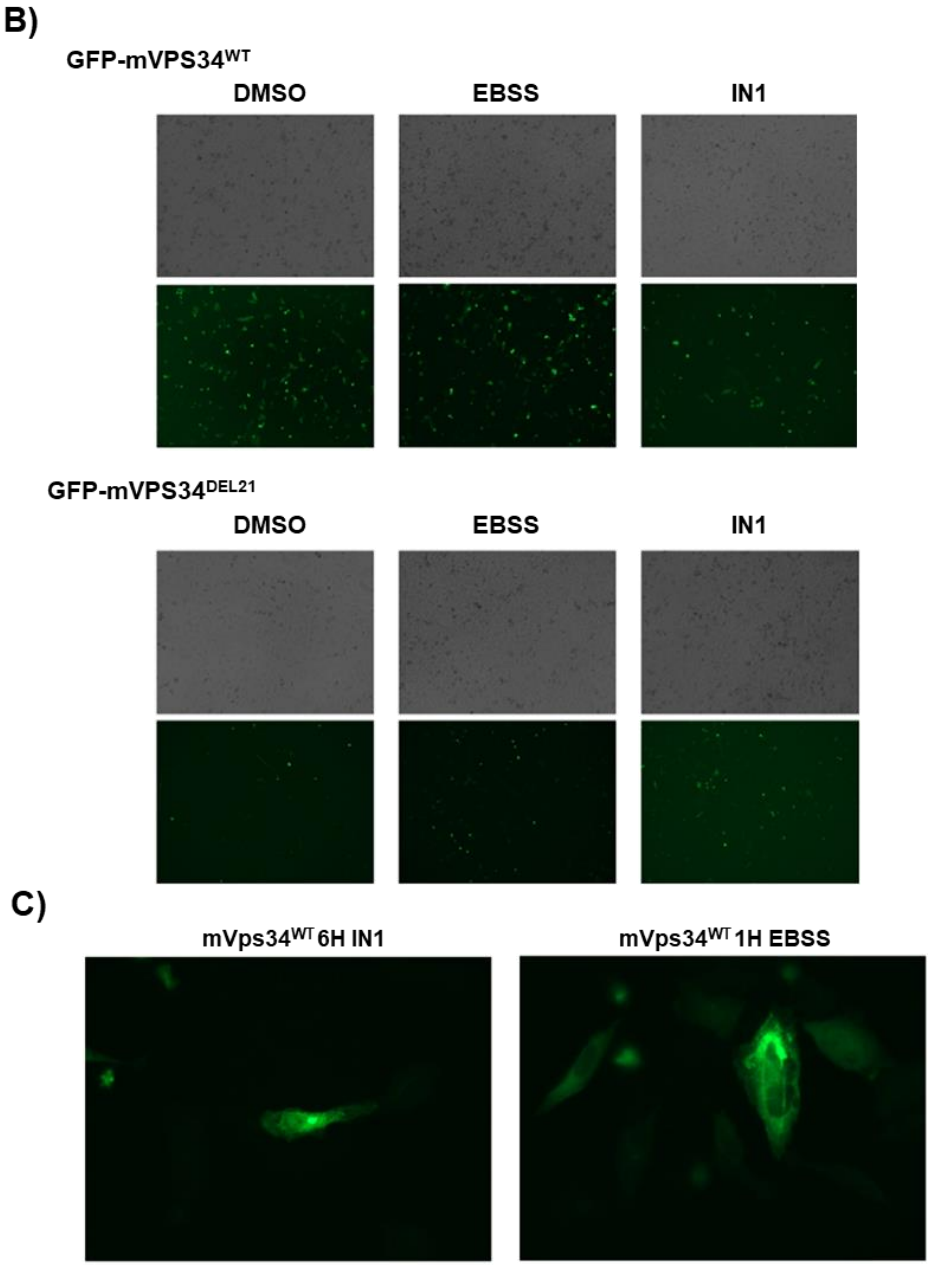

Fig. 3.5 Comparison of GFP-mVPS34^{WT} and GFP-mVPS34^{DEL21} phenotype. HeLa cells transiently transfected with GFP-mVPS34^{WT} or GFP-mVPS34^{DEL21} for 24 h. Images where taken with Epifluorescent microscope, EvosFL Auto. A) 1H or 6h treatment with CM (DMSO), IN1 or incubation in EBSS after 24h transient transfection. B) Expression level of GFP-mVPS34^{WT} or GFP-mVPS34^{DEL21} in the different conditions. C) GFP-mVPS34^{WT} transiently transfected cells treated with IN1 for 6h (left) or EBSS for 1H (right).

3.1.2.2 Lipid kinase activity of mVPS34^{WT} and mVPS34^{DEL21}

Next, the ability of mVPS34^{DEL21} to phosphorylate phosphatidylinositol (PtdIns) into phosphatidylinositol 3-phosphate (PtdIns3P) was assessed. To show that the mVPS34^{DEL21} mutant was kinase dead, a total of three

in vitro lipid kinase assay were performed using PtdIns as a substrate on either HA-tagged-VPS34 or 6xMyc-tagged VPS34 IPs.

A summary of the kinase assay is shown in Fig. 3.6. Transfection of the cells was carried out with the HA- and 6xMyc-tagged mVPS34 plasmids in duplicates, cells were lysed 24 h post-transfection and protein was extracted. To isolate HA/6xMyc-mVPS34 $^{WT/DEL21}$, HA- or Myc- IP was performed from 1 mg of total protein. A kinase assay was carried out on VPS34 IPs. This assay employs radioactive labelled ATP to quantify radioactive PtdIns3P ran on a thin layer chromatography (TLC).

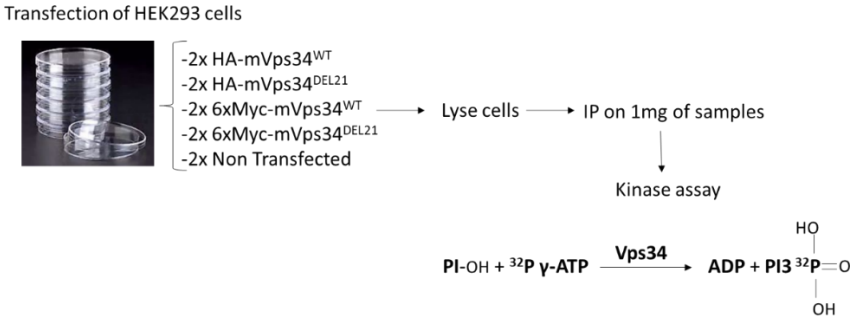

Fig. 3.6. Kinase assay layout.

HEK293 cells were transiently transfected in replicates for 24h with the HA and 6xMyc tagged mVPS34 plasmids. Kinase assays were carried out on HA- or Myc- IP.

The data are displayed in Fig. 3.7. Control IPs and WB showed the efficacy of the IPs on the tagged VPS34 version. In the bottom panel the kinase assay clearly shows a complete reduction of mVPS34 kinase activity in the mutant relative to the WT counterpart. (Fig. 3.7A and B).

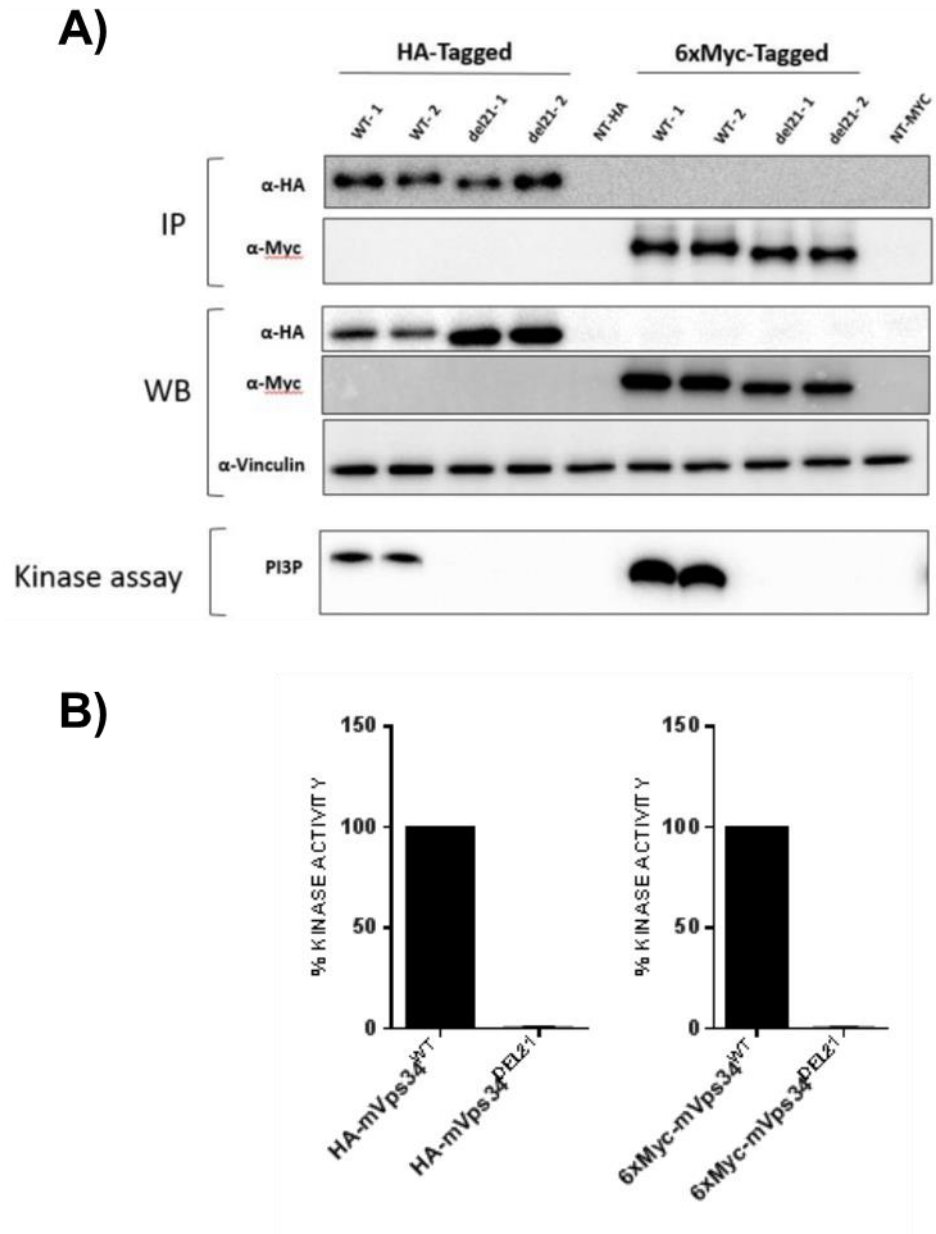

Fig. 3.7. *In vitro* characterisation of the VPS34^{DEL21}. A) IP, WB, and *in vitro* kinase assay of tagged version of the truncated (VPS34^{DEL21}) and wild-type (VPS34^{WT}) VPS34 allele in transiently transfected HEK293 cells. WT stands for mVPS34^{WT}, and DEL21 for mVPS34^{DEL21}. NT corresponds to the non-transfected controls. HEK293 were transiently transfected in duplicates (1, 2). Each lane represents a replicate. Representative data of three independent experiments is shown with two replicates per experiments (labelled as WT-1, WT-2, DEL21-1, DEL21-2). B) Bar graphs showing the percentage of kinase activity in both mVPS34^{WT} and mVPS34^{DEL21} proteins (HA tagged on the left panel and 6xMyc-tagged on the right).

3.1.2.3 VPS34 complex integrity

As detailed in the introduction, at least two VPS34 complexes exist in cells which share a core complex composed of VPS34, VPS15, and Beclin 1

but differ in fourth component which is either ATG14L (complex I) or UVRAG/VPS38 (complex II). These two partners are mutually exclusive. CI is required for autophagy, whereas CII is implicated in both autophagic and endocytic pathways (Fig. 3.8).

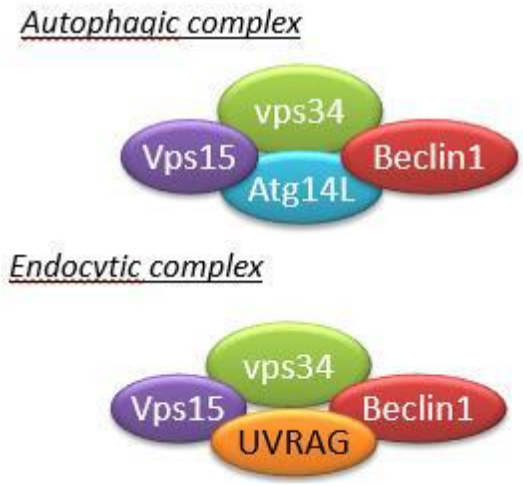

Fig. 3.8. CI (left) and CII (right) VPS34 complexes.

In order to address whether mVPS34^{DEL21} mutant is able to associate with its binding partners co-IP experiments in HEK293 transfected cells were performed.

The outcome of these co-IPs was however more challenging to interpret. As shown in Fig. 3.9 while anti-HA IPs brought down exogenous WT and mutant VPS34, almost no VPS34 associated partners were found in these IPs. Anti-Myc IPs however seemed to be more efficient as small amount of Beclin 1, VPS15 and UVRAG were found associated with VPS34. In contrast, IP using binding partner specific antibody (such as UVRAG) or VPS34 antibody, allowed the detection of associated exogenous and endogenous VPS34, Beclin 1, UVRAG and VPS15. Only ATG14L was not found in these anti-UVRAG IPs, confirming the exclusive association of UVRAG in the VPS34 complex II.

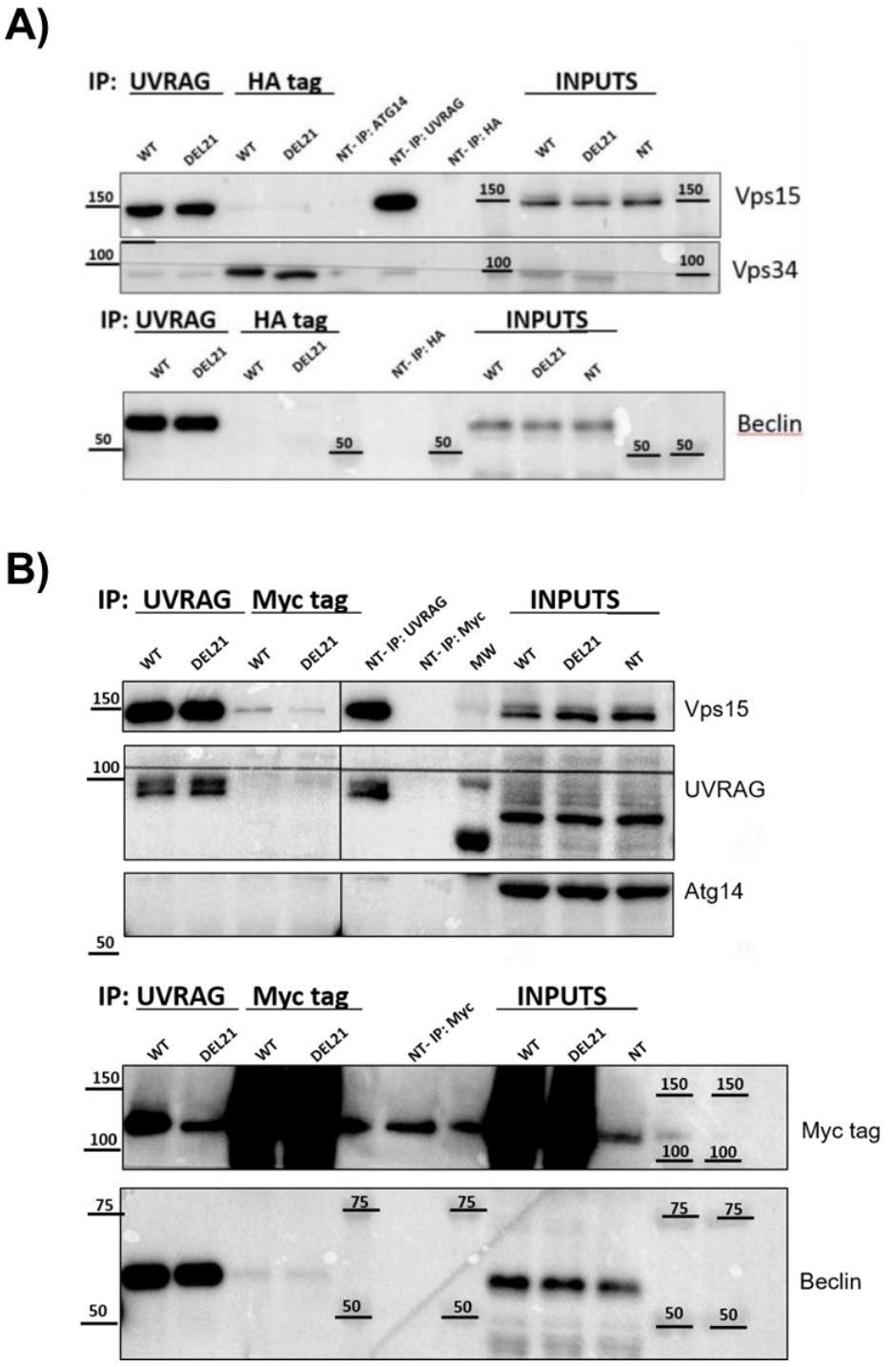

Fig. 3.9. mVPS34^{DEL21} maintains the complex integrity. UVRAG and tag (Myc or HA) IPs. A) HA-tagged constructs. B) 6xMyc-tagged constructs. WT stands for mVPS34^{WT}, and DEL21 for mVPS34^{DEL21}.

One of the reasons to have poor binding with the members of the complex is that the N-terminal tag might prevent the interaction with the members of the complex. There is as well some evidence in the literature [12] showing that C-terminal GFP tagged VPS34 is observed in punctae while N-terminal VPS34 localisation is diffuse, which highlights possible outcomes derived from the use of tags at different ends of the protein.

At the same time that these assays were performed, our collaborators from Okkenhaug's laboratory carried out a proteomic profiling using label-free high-resolution mass spectrometry to compare mVPS34^{WT} and mVPS34^{DEL21} in a conditional mice model (Fig. 3.10).

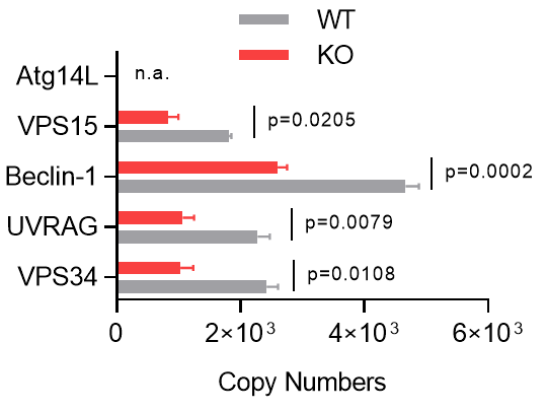

Fig. 3.10. mVPS34^{DEL21} expression presents a 2-fold decrease in regulatory T cells (Treg) accompanied by the decrease of the rest of the members of the complex. Estimated copy numbers from each protein after proteome profiling performed in mVPS34^{WT} and mVPS34^{DEL21} Treg cells by C.J.F. Courrèges are showed. Data represents three biological replicates. The bar shows SD. Student's t-test was used for the statistical analysis.

mVPS34^{DEL21} protein expression decreased 50% compared to mVPS34^{WT}. Accordingly, protein levels of VPS15, Beclin 1 and UVRAG dropped as well in the mVPS34^{DEL21} samples. ATG14L was not detectable either in WT nor DEL21 samples. Altogether, this results show that the 25 amino acid truncation in mVPS34^{DEL21} renders the protein unstable in these cells and highlights the relevance of the scaffolding role played by VPS34.

These results resembled those obtained from my IP assays, where a difference in relative amount of VPS15 in IP: myc is already seen (Fig. 3.9B).

Taken together, the results suggest that mVPS34^{DEL21} protein expression may vary between cell lines. In those where it is expressed, like in the cell models used in this study, its kinase activity is completely abolished. IP results show a weaken binding towards the members of the different VPS34 complexes, which could be motivated by the use of an N-terminal tag.

3.2 Modulation of VPS34 activity using nanobodies

For decades, researchers were limited to use aspecific or poorly characterised VPS34 inhibitors (such as Wortmannin or 3-MA) to investigate VPS34 function in cells. The recent discovery and characterisation of highly specific VPS34 inhibitors has now opened new avenues and these compounds have been proven to be powerful tools to dissect the roles of the catalytic activity of VPS34 in cells and in disease. However, these inhibitors do not allow to discern between complex I or II VPS34 activity or the VPS34-dependent autophagy and endocytic pathways. Inhibiting a pathway over the other might be more effective and less toxic if some off-target activity against one of the complex can be avoided.

Therefore, I aimed to selectively modulate one complex over the other by a specific targeting strategy. For this, the stabilizing properties of nanobodies, small single domain antibodies, were used to bind to, and modulate the specific VPS34 complexes.

3.2.1 Obtention of nanobodies from llamas.

The nanobodies raised against the VPS34 complexes were obtained as part of a collaboration with R.Williams' group and the VIB facility in Belgium.

To do so, llamas from the VIB facility were immunized with either recombinant complex I or II, which had been previously purified in the R.Williams' lab. The whole procedure is illustrated in Fig. 3.11. Briefly, purified RNA from peripheral blood lymphocytes were used to synthesise cDNA. Nanobody encoding ORFs were amplified using a two-step nested PCR and then cloned into phage display vector pMESy4. Two rounds of panning were carried out using cross-linked and non-cross linked complex I/complex II. For characterisation, an extra ELISA was executed using non cross-linked complex I or II.

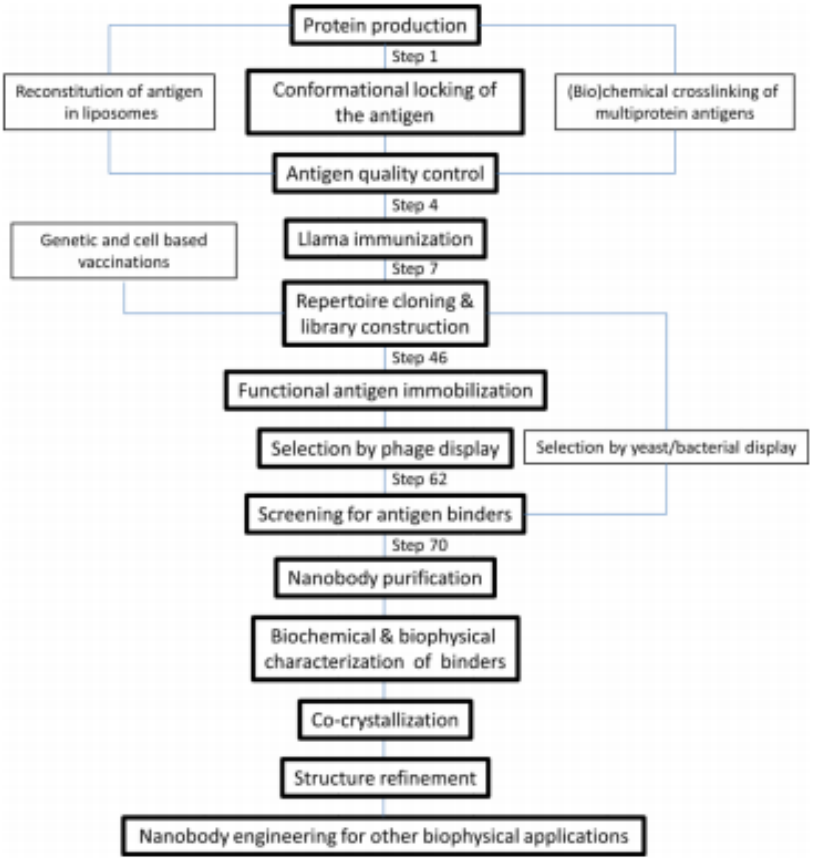

Fig. 3.11. Schematic view of the nanobody production process. Taken from Pardon et al. (2014) [208]

3.2.2 *In vitro* characterisation of the nanobody candidates

Forty-five nanobodies were identified (shown in Table 3.1). Primary screening assays revealed 4 nanobodies that exclusively bind to complex I and six to complex II .A secondary ELISA assay narrowed down the number of nanobody binding specifically to either of the complexes such that three were binding with high affinity to complex I (CA12560, CA12561 and CA12582) and two to complex II (CA12599 and CA12570).

Table 3.1. List of the nanobodies obtained from the screen. The first table shows nanobodies specific to complex I and the second table nanobodies specific to complex II. The reference number indicates the plasmid name from the VIB. Family is a group of nanobodies that share high similarity in their complementarity determining region (CDR3) region (it is considered that they bind to the same epitope). The occurrence indicates the amount of times that a family has been found after sequence analysis and ELISA. Data from VIB.

Reference No.	Family	Occurrence	Selection conditions in which this family of Nanobodies is found		Extra ELISA on solid phase coated material	
			solid phase coated		non cross-linked	
			Cross-linked H. sapiens Complex I	Non cross- linked H. sapiens Complex I	H. sapiens Complex I	H. sapiens Complex II
CA12579	1	13	X	X	-	-
CA12580					-	-
CA12581					-	-
CA12568	2	12	X	X	-	-
CA12569					-	-
CA12570					-	
CA12571						
CA12572					-	-
CA12573						
CA12564	3	9	X	X		
CA12565						
CA12566						
CA12560	4	3	X	X		-
CA12561						-
CA12562	5	3	X	X	-	-
CA12557	6	4	X		-	
CA12558						
CA12567	7	1	X		-	-
CA12576	8	1	X		-	-
CA12577	9	1	X		-	
CA12578	10	1	X			
CA12582	11	1	X			-
CA12559	12	1		X	-	-
CA12563	13	1		X	-	
CA12574	14	1		X		-
CA12575	15	1		X		

Reference No.	Family	Occurrence	Selection conditions in which this family of Nanobodies is found		Extra ELISA on solid phase coated material	
			solid phase coated		non cross-linked	
			Cross-linked H. sapiens Complex II	Non cross- linked H. sapiens Complex II	H. sapiens Complex I	H. sapiens Complex II
CA12585	1	11	X	X	-	-
CA12586					-	
CA12589	2	4	X	X		
CA12588	3	3	X	X	-	-
CA12587	4	8	X		-	-
CA12590	5	4	X			
CA12591	6	1	X		-	-
CA12592	7	1	X		-	-
CA12593	8	2	X			
CA12594	9	1	X		-	-
CA12595	10	1	X		-	-
CA12596	11	1	X		-	-
CA12597	12	1	X		-	-
CA12598	13	1	X		-	-
CA12599	14	1	X		-	
CA12600	15	1	X		-	-
CA12601	16	1	X		-	-
CA12583	17	5		X	-	-
CA12584						

Colors refer to the ratios seen in ELISA (specific signals to background signals)

- considered negative as ratio is <1,5
- ratio >2,5
- 2,5 > ratio >2
- 2 > ratio >1,5

Some of these nanobodies were further characterised in *in vitro* assays in R.Williams' laboratory to confirm the preliminary results from VIB (see Table 3.2). Recombinant Nanobodies and VPS34 complexes were purified to perform pull downs and ADP glo assay to measure the binding specificity and VPS34 kinase activity on Giant Unilamellar Vesicles (GUVs), respectively. GUVs are artificial membrane systems that allow measuring more accurately VPS34 activity (since complex I and II are more active when bound to membranes [42]). Several nanobodies (CA12557, 65, 71, 75, 81 and 88) were found to bind both complexes, while CA12560, 61 and 82 showed exclusive specificity to complex I; and CA12585 to complex II. (See Table 3.2). Kinase activity relative to complex I (CI) and II (CII) in the presence of the different nanobodies was measured, and results are summarised in Table 3.2. The values (+ or – signs) report presence or absence of complex I or II activity relative to

activity of those complexes devoid of nanobody. *In vitro* kinase assays showed that two complex I and II binders (CA12571 and 75) inhibit complex I and II activity. Interestingly, these nanobodies are not members of the same family, which means that they bind different epitopes. Intriguingly, other two nanobodies (CA12565 and 81) that belonged as well to different families and that bind to both complexes, inhibit exclusively complex II activity with no effect on complex I.

Altogether, this suggests that our nanobody screening (1) identified nanobodies that can bind and modulate the activity of one or both complex at different epitopes for each nanobody and (2) identified some nanobodies that can bind without having any modulatory effect on any of the complexes.

The table below summarizes these results:

Table 3.2. Summary of the binding affinity and kinase activity of the nanobodies. C1 stands for complex I and C2 for complex II. The (+) sign indicates that the complex still has kinase activity i.e. ++ means that the kinase activity measured after addition of the nanobody was the same as the kinase activity of the complex in the absence of the nanobody while the (–) sign indicates inhibition of the kinase activity. Data kindly provided by Y. Ohashi (R.Williams' lab).

	Binding affinity			Kinase activity	
	C1	C2	antigen	C1	C2
CA12557	+	+	C1	+	-+
CA12559	-	-			
CA12561	+	-		NO DATA	
CA12562	-	-			
CA12563	-	-			
CA12565	+	+		++	-+
CA12560	+	-		++	++
CA12571	+	+		-+	-
CA12575	+	+		-+	-
CA12576	-	-		NO DATA	
CA12581	+	+		++	-+
CA12582	+	-		++	++
12583	-	-	C2	NO DATA	
12585	-	+		++	+
12588	+	+		++	++
12590	-	-			
12593	-	-		NO DATA	
12594	-	-			
12598	-	-			
12601	-	-			

C1 and C2
C1 only
C2 only

A more in depth *in vitro* characterization was performed on the CI60 nanobody using Hydrogen Deuterium eXchange Mass Spectrometry (HDX-MS) approach to map the contact site with the VPS34 complex I and will be presented in section 3.2.4.

3.2.3 Cellular expression of nanobodies

To further characterise the nanobodies, I decided to express them into a mammalian cellular system. Because the *in vitro* assays using recombinant proteins (section 3.2.1 and 3.2.2) do not take into account potential intracellular cofactors (for instance additional binding partners or post-translational modifications) that could affect the interaction between the nanobody and the specific complexes, I decided to express these nanobody into HeLa, U2OS or HCT116 cells.

HeLa cells were chosen for cellular studies mainly because of their high efficiency transfection capacity and their overall spread morphology, which is an advantage for cell imaging. In addition, they are also of special interest because of their high rate of autophagy [123]. U2OS cells have been previously used to study VPS34 complex [13, 58]. They have a more balanced amount of complex I *versus* complex II, and are as well a good model for cell imaging. In contrast, HCT116 cell lines carry a premature stop codon in UVRAG cDNA truncating the protein and reducing its expression level suggesting that this cell line could be a good model to assess the VPS34 complex II *versus* complex I contribution in the nanobody-expressing cells.

3.2.3.1 Cell based validation: identification of complex specific binder nanobodies in cells.

First, HeLa cells were transfected for 24h with plasmids encoding different nanobodies. Using IPs and WB assays, the expression and binding specificity of each nanobody was monitored in normal growing condition (complete media) or under stress conditions (1H of starvation using EBSS media). Each nanobody was tagged with a Strep-tag II system, which has a 100 higher affinity to Strep-Tactin (a derivative of streptavidin) than to streptavidin. To perform the pull down, Strep-Tactin was used to immunoprecipitate the nanobodies.

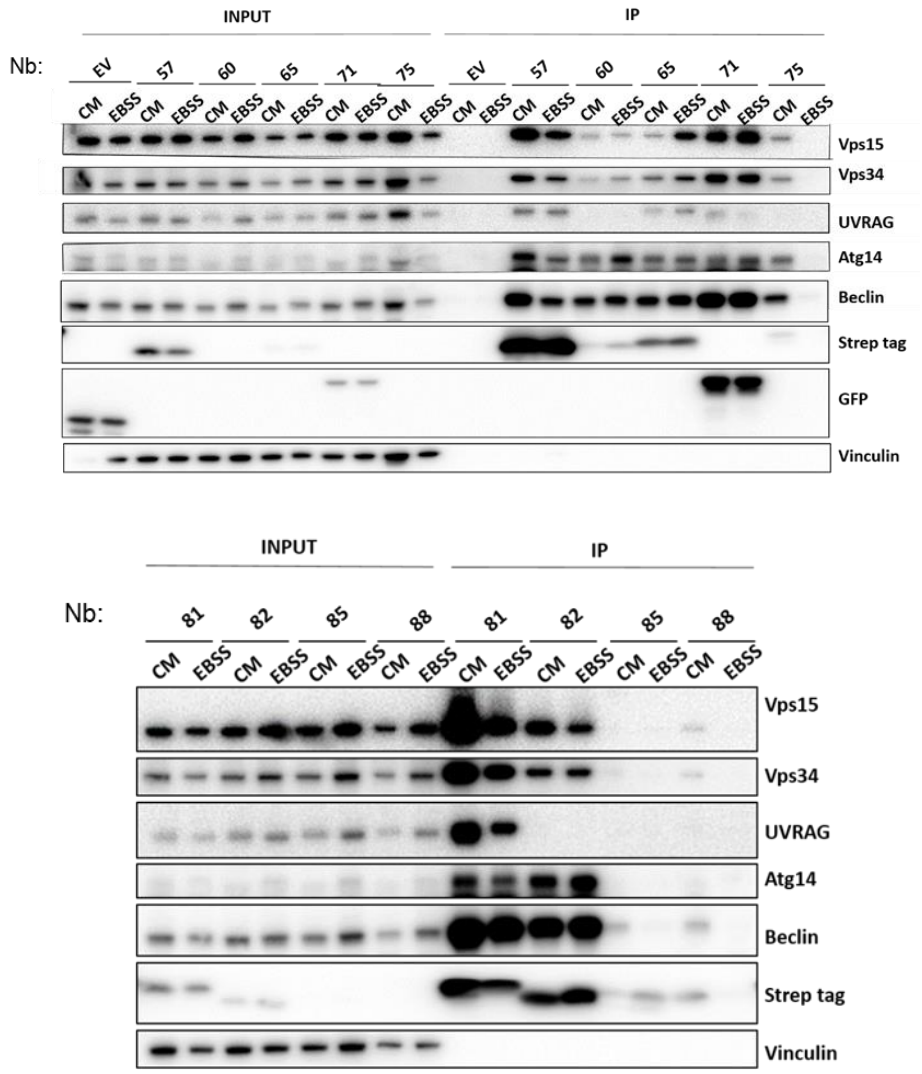

Fig. 3.12. Nanobodies have different binding specificities. Pull downs of total lysate of HeLa cells. Cells were transfected with 5/6xHIS-EIPA-2xStrep-tagII tag version of each nanobodies at the exception of Nb 71, which was tagged with GFP. EV: empty vector. Representative image of n=2. Each nanobody number corresponds to the last two digits numbers given by the nomenclature from VIB.

Expression of the nanobodies in HeLa cells was low in most of the cases as seen on the input lanes from Fig. 3.12, where the signal from nanobody expression band is only present in the pull down (for comparison, see input lanes and the pull down lanes). What is more, some nanobodies (CA12560, CA12575, CA12585 and CA12588) show very poor expression signal even after pulldowns. The possibility that this was the result of poor immunoprecipitation was dismissed since a very strong association of the VPS34 complex-associated proteins in the pulled downs was observed, suggesting that very little expression is enough to pull down members of VPS34 complex I.

Analysis of these pull downs assays confirmed that CA12560 and CA12582 are complex I specific binders. This is more evident with the CA12560 nanobody regarding the binding of the partners of complex I after starvation, in particular ATG14L. CA12582 expression was higher compared to CA12560, but the latter had a better binding affinity, since very little amount of nanobody was able to pull down all the members of VPS34 complex I. I also confirmed that CA12581 is an efficient binder of both complexes. No specific binder of complex II was found (Table 3.3).

Taking into account these last results, I stablished a new nomenclature using the last two digits of the original nomenclature and the acronym CI for complex I binders, CII for complex II binders, BC for binders of both complexes, NC for the non-binders and C for the nanobodies binding the complexes Core: VPS34, VPS15 and Beclin 1. e.g. CA12560 became CI60.

It is not possible to compare the stoichiometry of the ATG14L and UVRAG interaction with the nanobodies because the antibodies used for IPs may have different affinity, but it is remarkable to see that BC81 and BC57 are binders of both complexes and exert a similar activity towards complex II (see Table 3.2). It is also interesting to see that EBSS starvation seem to decrease the interaction of the nanobody BC57 with ATG14L. At this stage, I cannot explain this observation.

BC57 is not the only nanobody that behaves in a versatile way. Interestingly, there was an increase in VPS15 and VPS34 binding upon starvation in BC65 pull down.

In the presence of BC71 and C75, inhibition of both complexes was observed in vitro using GUVs. BC71 binds very little UVRAG and C75 does not bind UVRAG. In this case, it is tempting to interpret the absence of binding towards UVRAG as a possible interference of these nanobodies with UVRAG site of binding. However, it is dangerous to interpret the lack of binding of the members as the only cause for inhibition since BC65 and BC81 were the only nanobodies that showed specific inhibition of complex II, but they could bind both complexes.

Lastly, C85 and C88, which were very low expressed, show no binding to ATG14L or UVRAG. Despite showing such a poor binding specificity and expression in cells, there was a little effect on kinase activity (as assessed by GUVs assay) in complex II with C85.

Table 3.3. Summary of the binding of the nanobodies using different techniques. CI: complex I binders, CII: complex II binders, BC: binders of both complexes, NC: non-binders, C: for the nanobodies binding the complexes Core: VPS34, VPS15 and Beclin. The nanobodies that showed the same result in all the tests are highlighted in green.

NANOBODY ID	ELISA-IN VITRO	PULL DOWN-IN VITRO	IP-CELL ASSAY
CA12557	CII	BC	BC
CA12559	NC	NC	NC
CA12561	CI	CI	Not tested
CA12562	NC	NC	Not tested
CA12563	CII	NC	Not tested
CA12565	BC	BC	BC
CA12560	CI	CI	CI
CA12571	BC	BC	BC
CA12575	BC	BC	C
CA12576	NC	NC	Not tested
CA12581	NC	BC	BC
CA12582	CI	CI	CI
CA12583	NC	NC	Not tested
CA12585	NC	CII	C
CA12588	NC	BC	C
CA12590	BC	NC	Not tested
CA12593	BC	NC	Not tested
CA12594	NC	NC	Not tested
CA12598	NC	NC	Not tested
CA12601	NC	NC	Not tested

Altogether, these results indicate that *in vitro* non cell-based assays are not necessarily correlating with the cell-based experiments. This could be to different reasons that it will be developed in the discussion. Only five nanobodies out of ten tested were validated using the different assays (*in vitro* and cell-based) (in green in Table 3.3): two binders to both complexes, two binders of Complex I and one non-binder.

Based on the results shown above, I decided to focus on the nanobody CI60 as representative of complex I specific , BC71 for its capacity of binding and inhibiting both complexes and BC81 for its capacity of binding both complexes but inhibiting only complex II. NC59 was used as control as it is a non-binder. CII99 was very preliminary characterised for its capacity to bind strongly to complex II in the original screening assays. Unfortunately, *in vitro* binding and activity data for the CII99 are missing, as it could not be expressed in bacteria (only in mammalian cells).

3.2.3.2 Phenotypic characterisation of transiently transfected nanobodies

My aim was to observe whether there was any phenotypic difference between nanobodies with different binding specificity to the VPS34 complexes.

I transiently transfected GFP-tagged CI60, BC71, BC81, NC59 and CII99 in HeLa cells for 24h using an EVOS microscope. I could notice that while GFP control, NC59, BC71 and BC81 showed a cytoplasmic expression, CI60 and CII99 showed a punctate pattern. Besides, cells transfected with these two last nanobodies had a striking low efficiency transfection (Fig. 3.13).

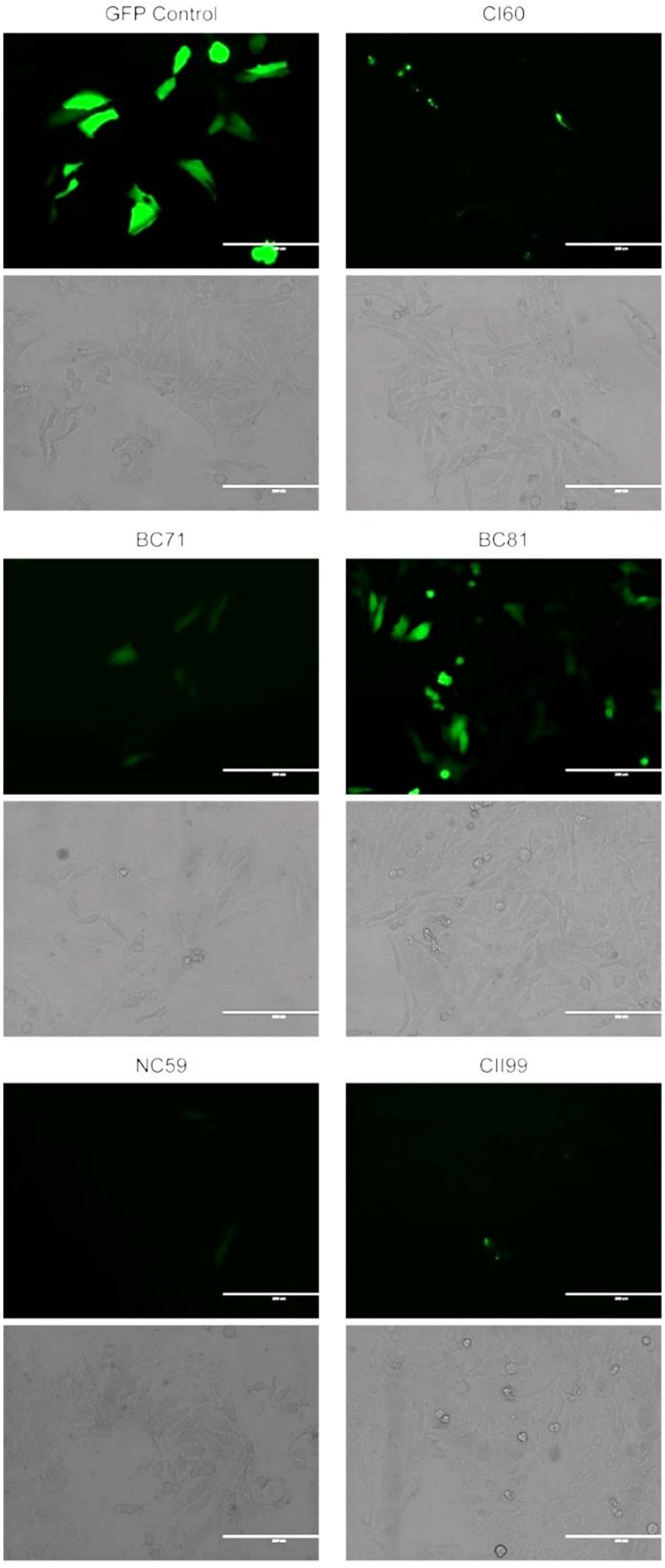
GFP Control
CI60
BC71
BC81
NC59
CII99

Fig. 3.13 CI60 and CII99 are observed in punctae while BC71, BC81 and NC59 appeared cytoplasmic. Expression of the GFP-tagged version of the nanobodies in HeLa cells after 24H transient transfection. Image were taken using a fluorescence microscope. pEGF N2 plasmids for CI60, BC71 and BC81, pLVX vectors for NC59 and CII99 and pmaxCloning™ Vector for the GFP positive control were used.

Complex I acts in the initiation of the autophagy, while complex II exerts its role in the maturation of the autophagosome, vesicular trafficking, cytokinesis, autolysosomal tubulation and LC3-associated phagocytosis [43] . Since CI60 displays a unique binding specificity on complex I and a punctate pattern when expressed in cells that suggest localisation to membranes, it was chosen for downstream characterisation.

CI60 subcellular localisation was addressed by immunofluorescence. Live imaging (Fig. 3.14.A) and IF in fixed cells (see Fig. 3.14B) was used to assess the formation of the punctate pattern. CI60 was interestingly expressed not only in punctae, but also in tubular forms after 15 min EBSS treatment (Fig. 3.14B).

A)

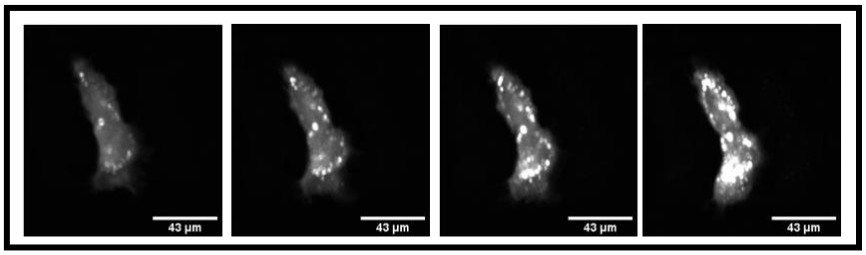

B)

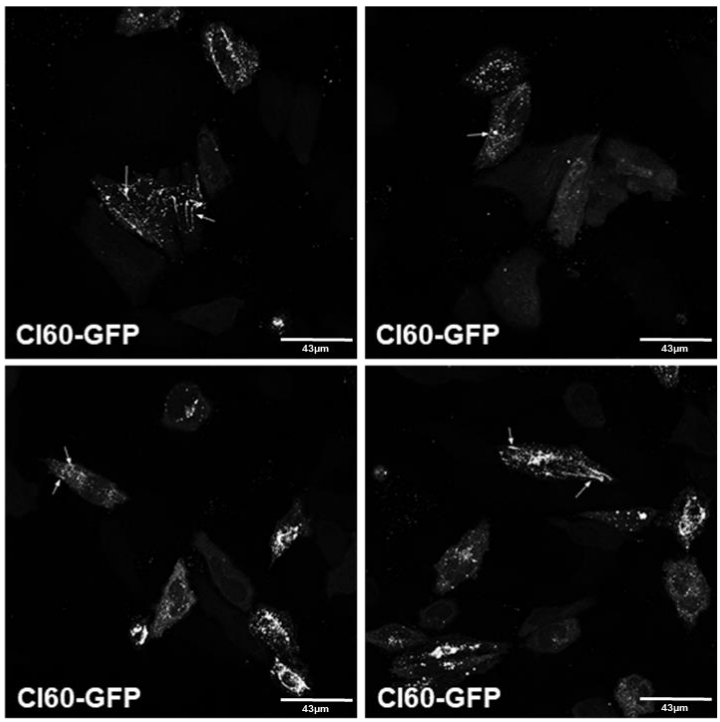

Fig. 3.14. CI60-GFP is also present in tubular structures. A) HeLa cells transiently transfected with CI60 6H posttransfection. Photos were taken every 20 min. Photos are frames #1, #2, #3 and #4. B) HeLa cells transfected with CI60-GFP after 15 min of EBSS starvation. The arrows point to the tubular structures marked with CI60.

I also confirmed the binding specificity results observed in HeLa cells in different cell lines such as U2OS (Fig. 3.15). Pull down experiments using specific antibodies against each of the VPS34 binding partners validated that nanobody CI60 is also a complex I binder in U2OS cells. I also was able to detect the binding of another binding partner called NRBF2 known to be a fifth subunit of the complex I [64].

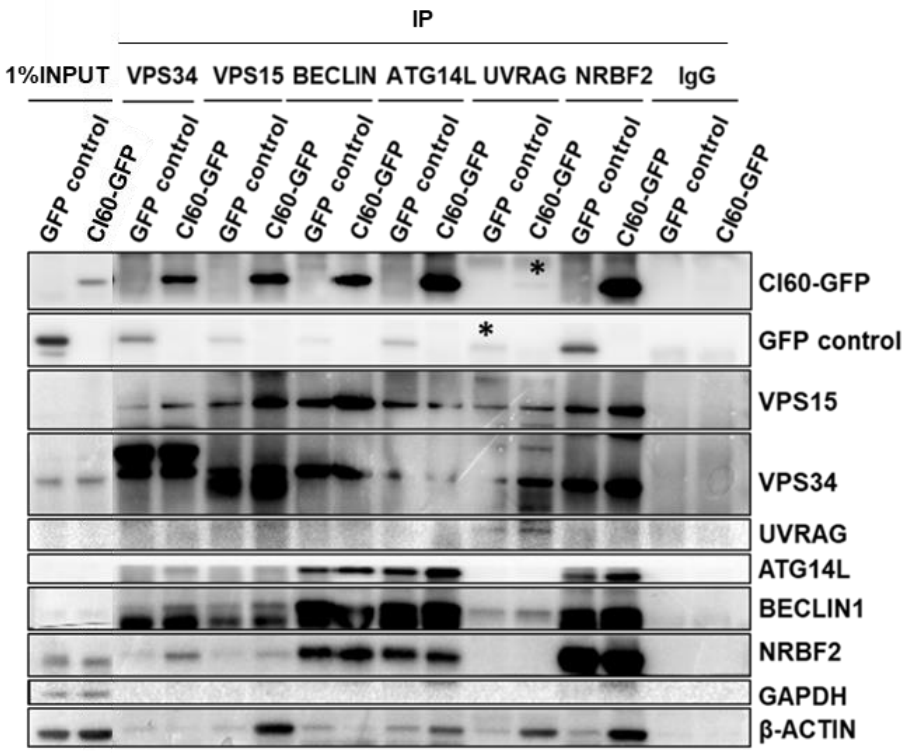

Fig. 3.15. CI60 is pulled down by the members of complex I in U2OS cells. IP from U2OS cell lysates. 1% of the input was loaded in the first two wells. Each antibody against the members of the complex (VPS34, VPS15, BECLIN 1, ATG14L, UVRAG or NRBF2) used for the pull down is indicated on the top of the figure. IgG was used as negative control. *: non specific band. Representative result from n=3.

3.2.3.3 Creation of stable CI60 HeLa cells.

In order to avoid multiple rounds of transfection and to have a higher number of cells with homogenous population, stable cell lines expressing CI60 were created. To facilitate biochemical assays as well as imaging approach, the nanobody was tagged using different tag versions.

HA tag, a ten- amino acid tag that could be used for immunocytochemistry studies, 3xFlag for biochemical studies and GFP tag for flow cytometry and live imaging experiments was chosen.

It should be noted that the nanobodies identified by the VIB were expressed as fusion proteins with their purification tag: 6/5xHis-EPEA. Since this form of the nanobody had been used for the preliminary results, I was unsure whether these additional amino acids would provide them further flexibility and/or stability. To avoid any interference from the original screen, I decided to clone a version with and without these extra original tags.

Below is a summary of the plasmids cloned and created with the different tag versions (Fig. 3.16).

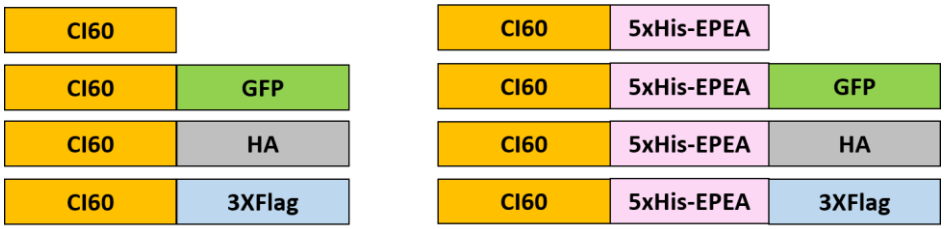

Fig. 3.16. Schematic view of CI60 pLVX lentiviral plasmids with the different tagged versions.

I created stable HeLa cell lines expressing each of these plasmids versions.

The first striking observation was that 50 to 90% of the cells infected with any of the tag version of the nanobody, died as compared to non-infected cells or the GFP empty vector expressing cells. The CI60 expressing cells also looked more stressed than the controls. Every stable line was maintained and recovered, except for the 5xHis-EPEA-3xFlag-CI60 tagged version expressing cell line, which did not survive. The GFP lines were assessed by imaging using an EVOS microscope and some cells showed a punctate pattern, but with a very low expression.

After 3 weeks of selection, I analysed the CI60 expression by WB. GFP and 3xFlag tagged nanobodies were detected, but not the HA tagged CI60 (Fig. 3.17). Expression of ATG14L was checked as well to assess whether there was any effect on the expression of complex I associated proteins along with p62, which is an indicator of autophagy, but no changes were observed (Fig. 3.17).

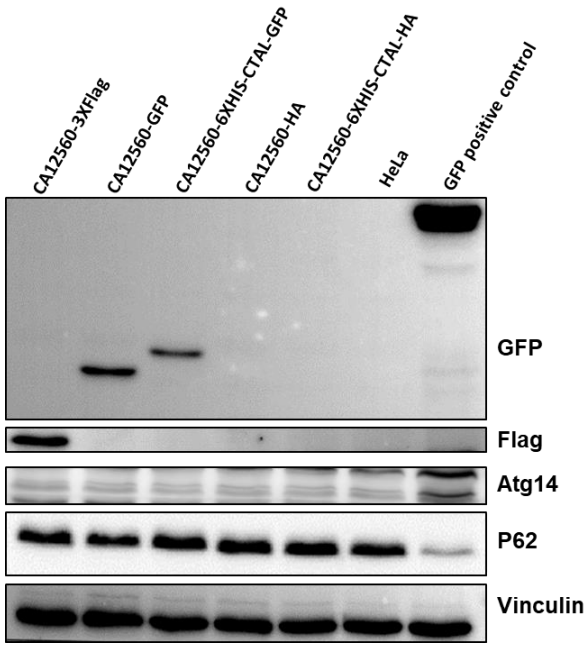

Fig. 3.17. CI60 is expressed in stable cell lines. Western blot showing CI60 nanobody expression in the stable cell lines.

I next checked for the specificity of the nanobody to bind complex I in the stable cell lines. To achieve this, the nanobody was pulled down using the equivalent tag for each version transduced and monitor the presence of some of the VPS34 complex I associated proteins. Similar to the transient transfected cell lines, CI60 was confirmed to be specific for complex I (see Fig. 3.18) and I was able to visualize HA-tagged nanobody by IP, whose expression was not strong enough to appear in the western blot in the input lane. Altogether, this data confirmed the transient transfection data showing that CI60 is a complex I specific binder.

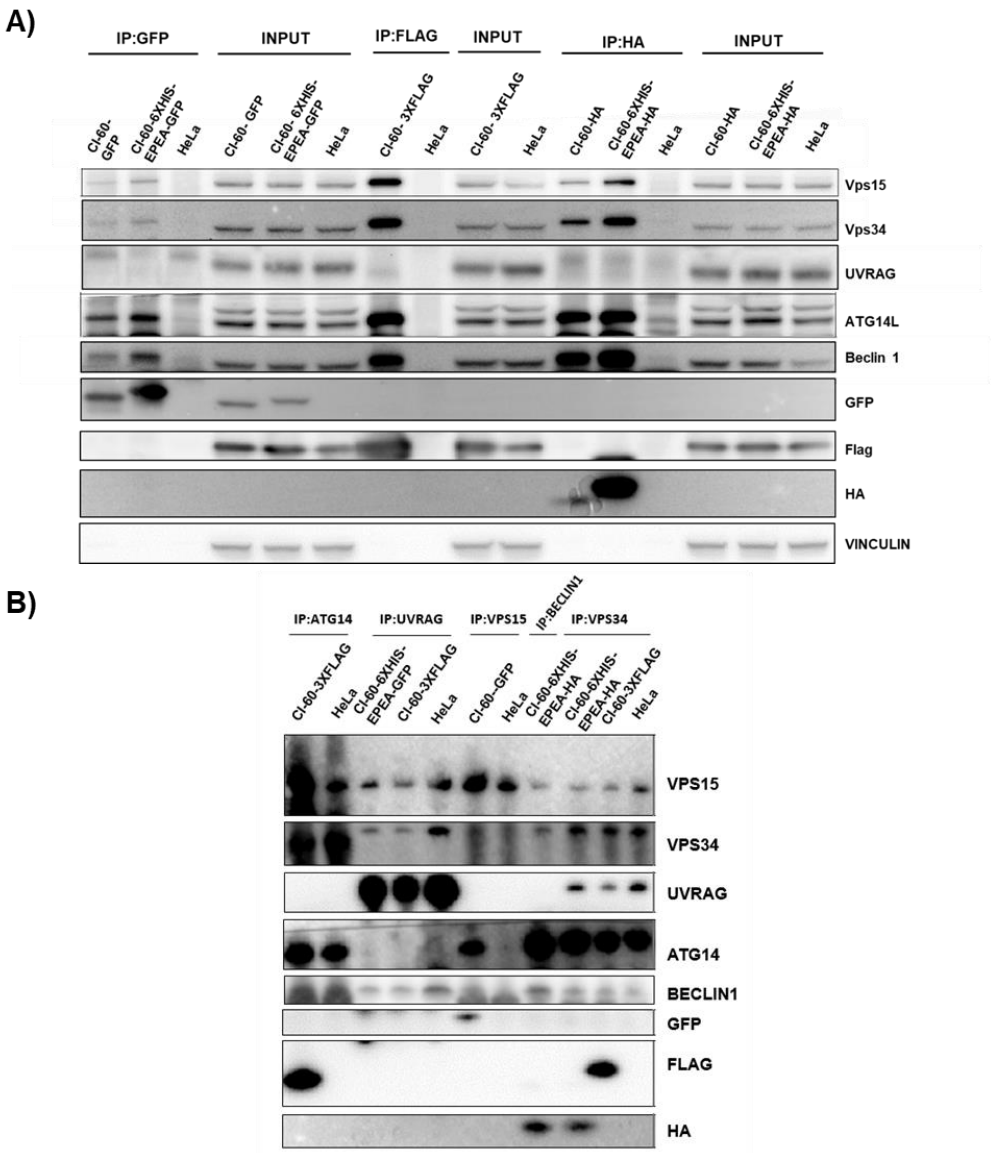

Fig. 3.18. CI60 is a specific complex-I binder. Western blot from the IP using stable HeLa cell lines. A) GFP/HA/3xFlag tags were used to pull down the members of VPS34 complex. B) Atg14L, UVRAG, VPS15, Beclin 1 and VPS34 were used for the IP.

To further characterise these nanobodies, their expression and subcellular localisation were monitored by immunofluorescence (IF). Surprisingly, instead of finding a homogenous subcellular pattern, I observed a variety of subcellular patterns as shown in Fig. 3.19. Around 70% of the cells showed cytoplasmic diffuse pattern as depicted on the Fig. 3.19A and B and the rest showed a punctate pattern as shown in Fig. 3.19C. It was also surprising to find that only around 40% of the cells in the stable cell line were expressing GFP, suggesting that most of the cells were expressing CI60 in a very low level.

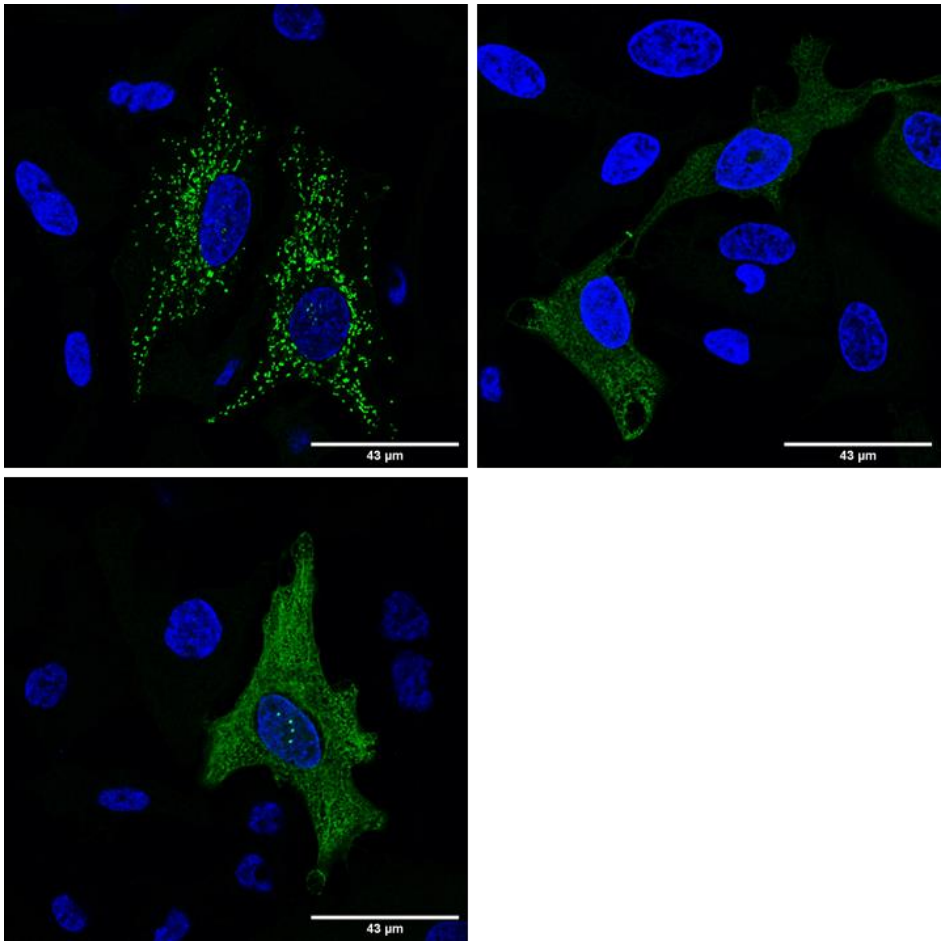

Fig. 3.19. Stable CI60 cell lines show different patterns. Stable CI60-GFP Hela cell lines grown in complete medium. Photos were taken with an x63 objective using a Zeiss LSM880 microscope.

To properly determine the level of GFP expressing nanobody, a flow cytometry based sorting was performed. I confirmed that the stable cell line showed a low percentage of cells that were highly expressing the CI60-GFP nanobody (7.4%). Of note, the level of expression in the “high” population was as high as the GFP empty vector control (Fig. 3.20)

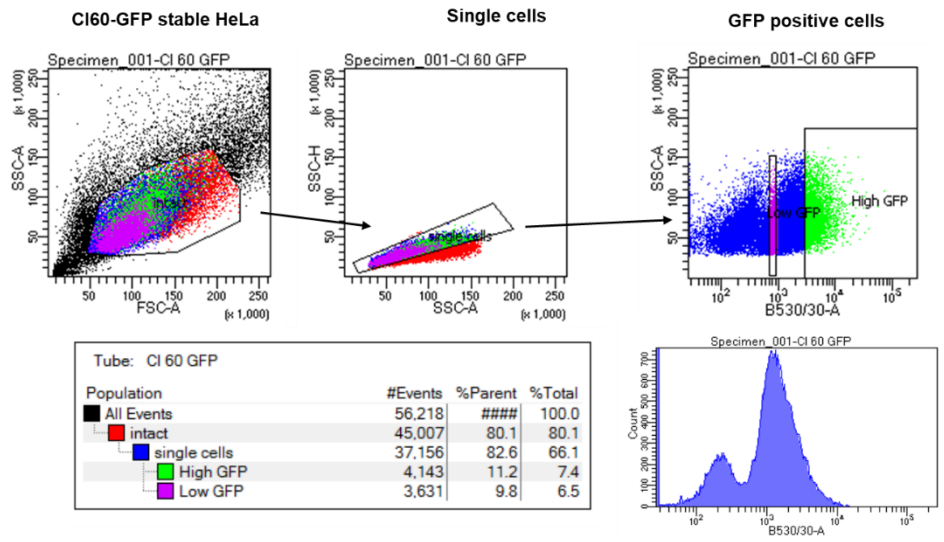

Fig. 3.20. Cell Sorting of stable CI60-GFP HeLa cell line. Approx. 40,000 cells were sorted and its level of expression of GFP was measured. Population was separated into two subpopulations, the “High GFP” which represents the maximum level of GFP in the cells, and “Low GFP” which marks the minimum GFP expression in the cells.

3.2.4 Mapping of the interaction regions with CI60 using Hydrogen Deuterium eXchange-Mass Spectrometry (HDX-MS)

We next addressed the question to which epitopes in complex I CI60 binds. To map the epitopes, we performed Hydrogen Deuterium eXchange-Mass spectrometry (HDX-MS). This powerful technique provides information about protein structure and conformation. It is based on the notion that hydrogen atoms within a protein can easily exchange with the labile protons of the surrounding solvent. If the solvent contains a different isotope of hydrogen such as deuterium, this exchange can be used to characterise protein structure and its dynamics through different methods including mass spectrometry (MS), which can distinguish the masses of the different isotopes. More specifically, amide hydrogens exchange with solvent at rates that are extremely sensitive to the presence of a secondary structure or protein structural changes caused by different perturbations (such as protein-protein interaction or aggregations). Amide hydrogens are involved in H bond in both α-helices and β-sheets and can only exchange when these bonds are transiently broken through protein motion [225]. In Fig. 3.21, a summary of this technique is presented. Samples consisted of the protein sample (apo samples), or the same proteins and their ligand. Non deuterated samples are used as controls. Proteins are incubated in deuteration buffer and different deuteration timepoints are taken, usually between 0.3s (short-term exposure) and 3000s (long-term exposure). Quenching is achieved by lowering the temperature and exposing the sample to an acidic pH. Protein unfolding takes place thanks to reducing agents or denaturants present in the buffer. After quenching, proteins are digested, usually using pepsin and the resulting samples are desalted and prepared to inject into the MS, where ionization takes place and their mass is measured. Comparison among the apo samples and the samples bound to their ligand is performed with the data obtained from the MS [226].

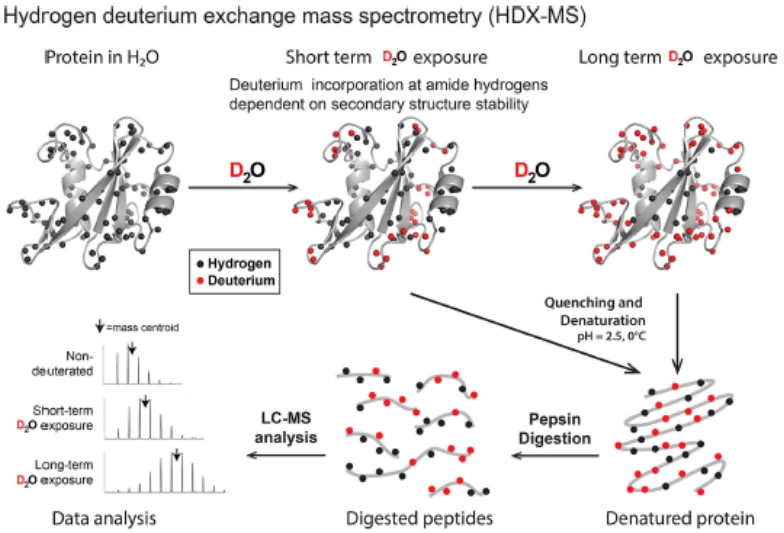

Fig. 3.21 HDX-MS workflow. Taken from Burke, 2019 [227].

MS analysis identifies peptides of regions that have been exposed or protected to the deuterium exchange. For instance, protein-protein interaction can provoke a change in conformation preventing deuterium incorporation and this region would then appear as “protected”. This protection can be interpreted as the region of interaction. However, caution needs to be taken when interpreting these results as certain regions can be protected not only because of the physical binding of the ligand and direct interaction on that specific region, but also because the ligand can potentially trigger indirect conformational changes caused by the direct interaction. In addition, an interaction can also result in conformational change “opening up” the surface of the protein and exposing that region to deuterium exchange.

The HDX-MS analysis was performed by Y. Ohashi as part of the collaboration with R. William’s lab.

The analysis of HDX-MS performed onto Complex I +/- CI60 revealed some regions that are protected in the linker region of complex I. More specifically, the protected regions identified were the linker between CC1 and CC2 domains of ATG14L (important for Beclin 1 binding [228]), the CBR1 loop of VPS34 (a region that in yeast complex II contacts UVRAG [42] and is within the C2 domain of VPS34 (which interacts with the other three proteins of the complex and is subject to phosphorylation by AMPK and Cdk1/5)), and the helical domain of VPS15 (involved in the interaction with VPS34). On the contrary, some regions were found exposed in VPS15 (WD40), ATG14L (CC1 domain) and Beclin 1 (CC1 domain). The WD40 region is especially important to bridge VPS34 and VPS15, as well

as Beclin 1 and UVRAG/ATG14L, and for VPS15 interaction with Rab5 in complex II [42, 43]. The CC1 of Beclin 1 is necessary for UVRAG/ATG14L interaction [229].

To further understand the relevance of this interaction map , I also compared it with the map of PTMs (such as phosphorylations, ubiquitinations, glycosylations) recently published in Ohashi et al. (2019) [43]. Analysis of each peptide did not reveal a potential alteration of any of these PTM (Fig. 3.22). A summary of the regions and sequences that are found protected or more exposed in each of the VPS34 complex I associated proteins is displayed in the same figure.

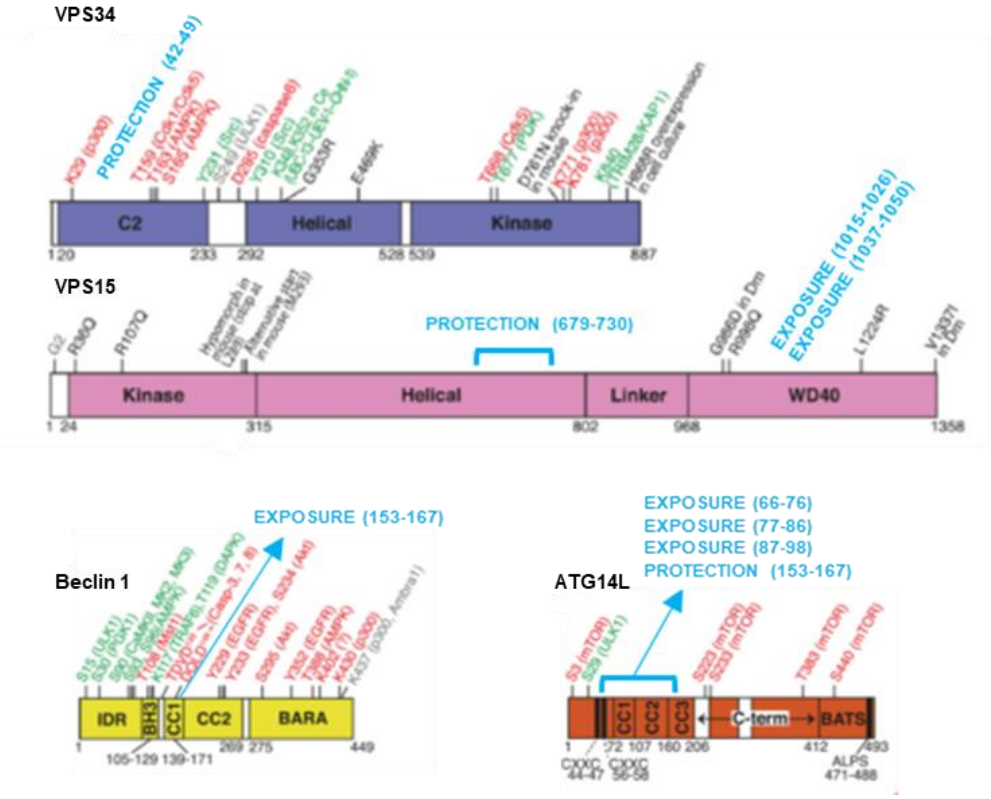

Fig. 3.22. Structural representation of complex I proteins. Modifications to include the HDX-MS data are shown in blue. Modified figure from Ohashi et al. (2019). [43].

As stated earlier, interpretation of HDS-MS data needs to be taken with caution. The protected regions are not necessarily the region of direct interaction and can be a result from a conformational change occurring in a different region.

After careful analysis, the HDX-MS analysis mapped a region located at the base of VPS34 complex I where the CBR1 of VPS34, Helical domain of VPS15, and the linker between CC1 and CC2 of ATG14L are gathered

(Fig. 3.23A and B). The most strongly protected region is the linker region situated between CC1 and CC2 of ATG14L (Fig. 3.23C). This region could act as a hinge that would affect the flexibility of the complex and its curvature depending binding. This might be the reason why this nanobody is complex I-specific. The nanobody binding to the hinge region also caused the disassembly of the CC1 domains of Beclin 1 and ATG14L [229].

Unfortunately, there was no peptide covered at the linker between CC1 and CC2 of Beclin 1 (Fig. 3.23D), so we cannot conclude that the nanobody does not bind to that region.

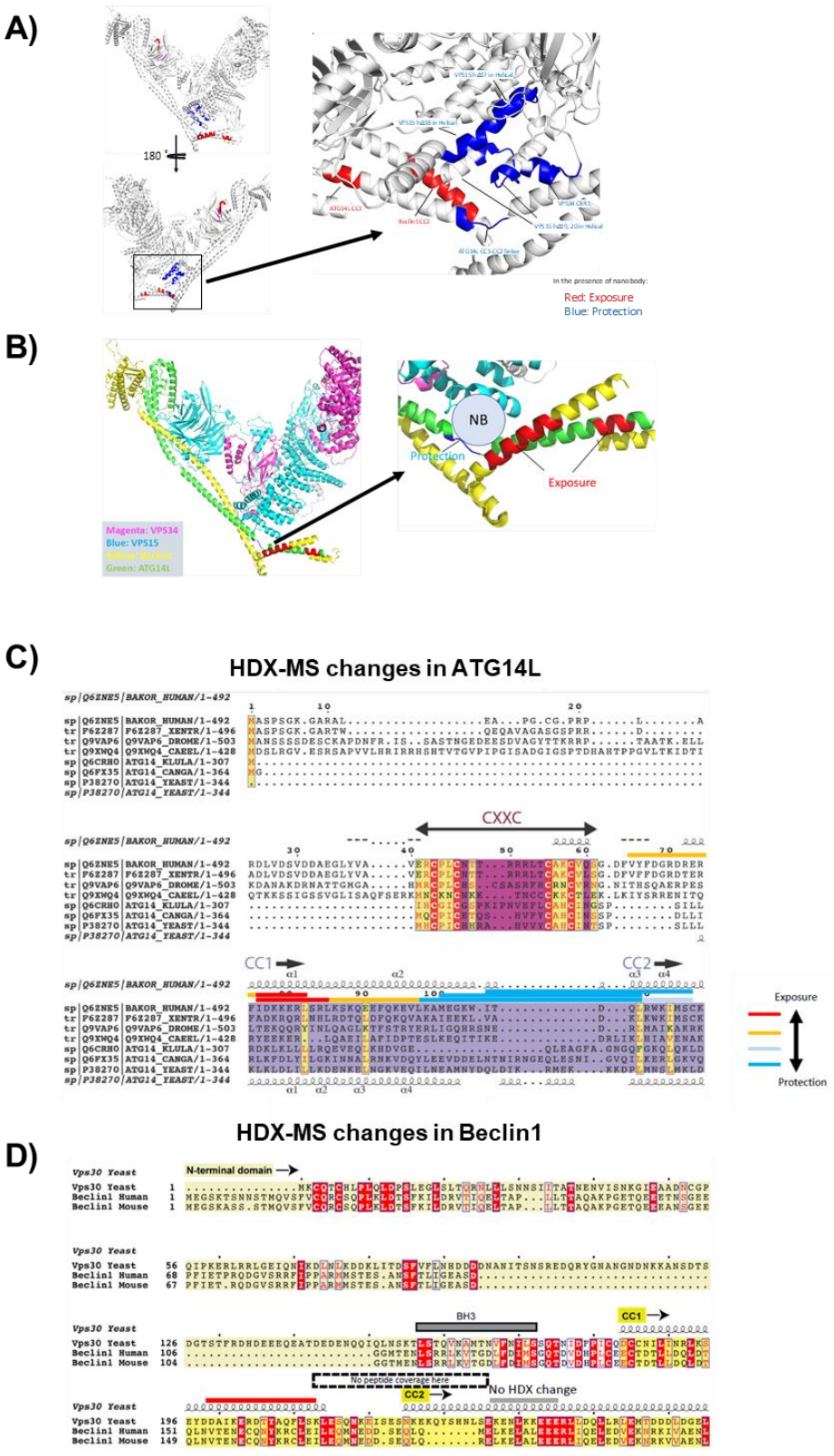

Fig. 3.23.Summary of the exposures/protected regions in the 3D structure of complex I. A) shows complex hinge with the specific regions protected (red) or exposed (blue). It appears that the nanobody is located at the hinge region of the complex, which also might have caused dissociation of the CC1 domains of ATG14L and Beclin 1. Performed by Y.Ohashi B) Shows VPS34 complex I members in different colours, and where we supposed the nanobody likely sits. The yeast complex II crystal structure (PDB: 5DFZ) was used as a model since

this is the highest resolution so far. Performed by Y.Ohashi C) Changes in ATG14L upon CI60 binding. Alignment performed by Y.Ohashi D) Changes in Beclin 1 upon CI60 binding. Alignment adapted by Y.Ohashi from Rostislavleva et al. (2015) [42].

3.2.5 Subcellular localisation of CI60

As stated previously, VPS34 complex I is a key player in the initiation of the autophagy, by producing a pool of PtdIns3P in regions of the ER named omegasomes that act as platforms for phagophore elongation. Considering this, CI60 should be localised in the proximity of this organelle. To check this hypothesis, IF using antibodies raised against ER proteins to label the ER. Moreover, two other organelles that have been suggested to provide a membrane source in the biogenesis of the autophagosomal membrane were examined: the mitochondria and the Golgi [85, 230].

3.2.5.1 CI60 at the ER

Calnexin and Calreticulin are transmembrane and luminal proteins, respectively, that act as chaperones and belongs to the ER quality control machinery. They are commonly used as a marker for ER along with the peptide sequence KDEL. KDEL is a peptide sequence that blocks the exit of proteins from the ER and is commonly used as ER marker when overexpressed in cells. [231, 232]. HeLa cells were transiently transfected with CI60 and maintained in nutrient rich (CM) or nutrient starvation (2H EBSS) conditions. Autophagy (where VPS34 complex I plays a crucial role) is induced by the latest, and therefore, assessing the different conditions was important. Staining or co-transfection with ER markers was performed.

3.2.5.1.1 Using KDEL marker

HeLa cells were co-transfected with CI60-GFP and a plasmid encoding dsRED-KDEL. The figure below shows that CI60-GFP partially co-localised or was at least in close proximity to the ER, represented by the ds-RED KDEL signal (Fig. 3.24 A).

ER is a specialized organelle that ensures control of the synthesis and the anterograde transport of proteins that are correctly folded and assembled. Because the GFP tag in the CI60-GFP-tagged version is the double in size of the nanobody, there was a concern regarding the possibility that

this might lead to the accumulation of unfolded or misfolded protein in the ER lumen, and therefore, mislead in the interpretation. To discard this possibility, HeLa cells were cotransfected with a plasmid expressing a shorter tagged version of the nanobody (CI60-HA) with the plasmid encoding dsRED-KDEL. Not only the nanobody was localised in close proximity to the KDEL positive compartments but the punctate pattern and overlapping features were detected in higher intensity in complete medium and EBSS (Fig. 3.24 B).

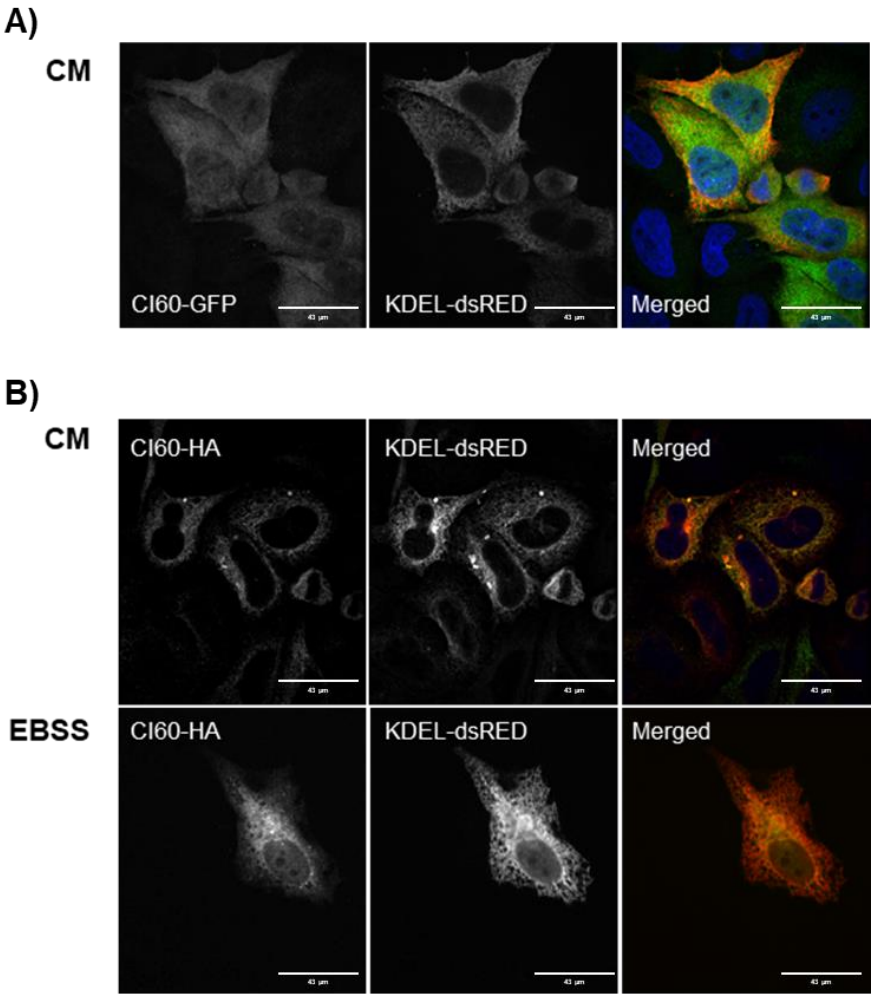

Fig. 3.24. CI60 co-localise with the ER marker KDEL. IF images of HeLa cells transiently cotransfected with dsRED-KDEL and CI60-GFP (A) or CI60-HA (B). After transfection, cells were kept on complete medium or starved with EBSS for 2h. Images were obtained with an x63 objective. GFP and HA markers were shown in green while KDEL signal was displayed in red.

3.2.5.1.2 Using Calreticulin

To rule out the potential artefactual effect produced by overexpressing KDEL protein CI60-GFP transfected HeLa cells were stained with an

antibody raised against the endogeneous ER protein Calreticulin (see Fig. 3.25).

I used a GFP tagged empty vector as control. The staining was not as clear as with the cotransfection with dsRED-KDEL but it seemingly confirmed the close proximity of the nanobody to the ER, as a reticular pattern is more evident in higher magnification (showed in Fig. 3.25 B).

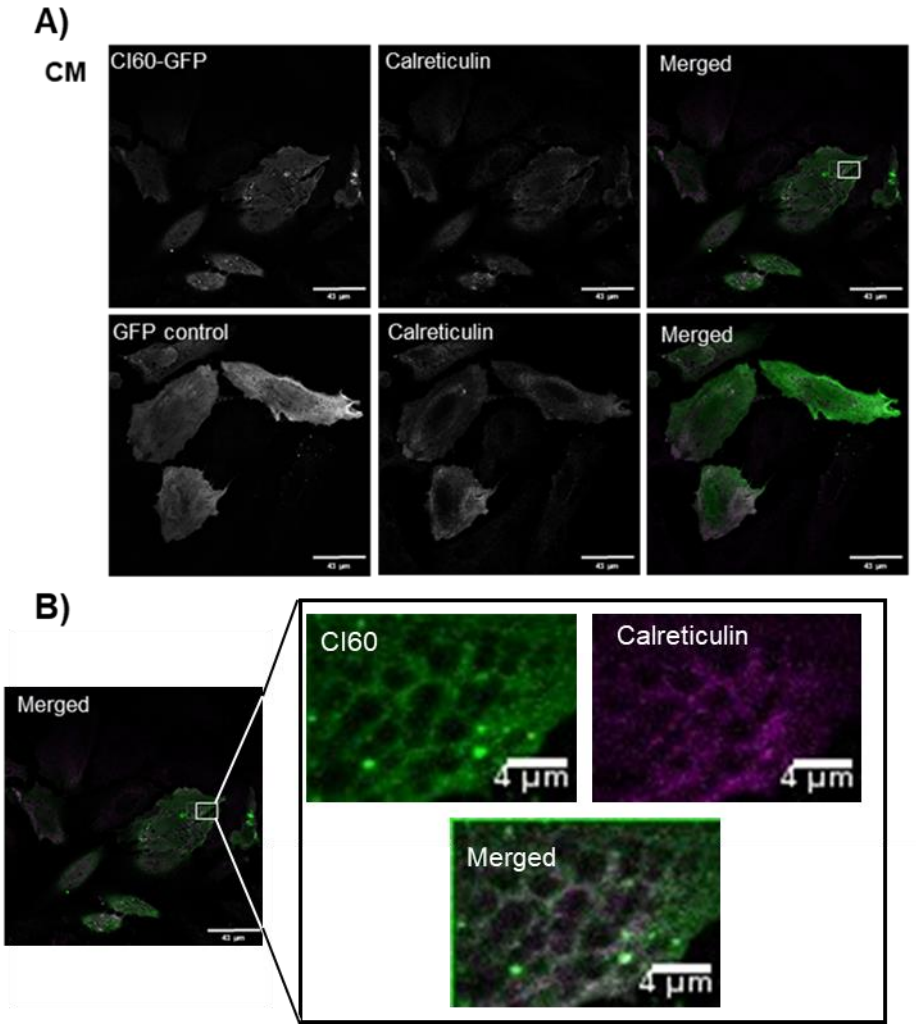

Fig. 3.25. CI60 co-localise with the ER marker Calreticulin. HeLa cells were transfected with CI60-GFP, fixed and stained with Calreticulin. Calreticulin was shown in magenta. A) Images were taken using a x40 objective. B) Magnification of a CI60-GFP transfected cell stained with Calreticulin.

3.2.5.1.3 Using Calnexin

To confirm the observations made using the Calreticulin staining, HeLa cells were transfected with CI60-GFP and then either maintained in complete medium or starved for 2h. Staining was performed using a specific antibody to detect endogeneous ER protein Calnexin. CI60 presented a reticular pattern that resembled that of the Calnexin staining,

in both complete medium and starved conditions. This was more apparent when the expression of the nanobody was higher with in some instance apparition of punctate pattern. Remarkably, the Calnexin staining was slightly thicker in the nanobody transfected cells, suggesting the presence of swollen ER, one of the hallmarks of ER stress [233]. Interestingly, a magnification picture of a maximum intensity projection of z-stack (showed in Fig. 3.26 B) showed a punctate pattern of the CI60 that seem to originate from the ER with a rounded structure very reminiscent of a nascent phagophores/autophagosomes.

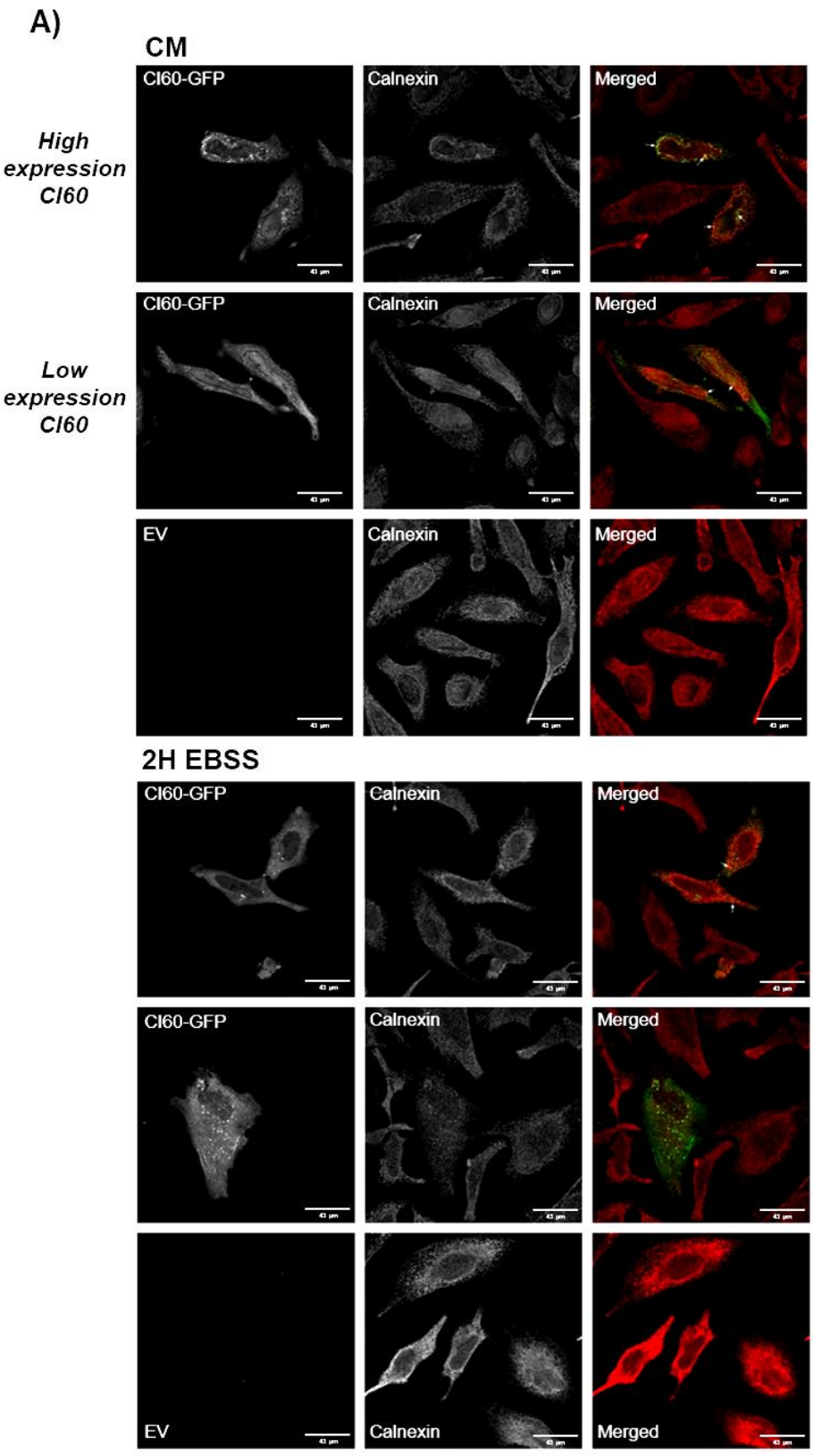
A)
CM
High expression CI60
Low expression CI60
CI60-GFP
Calnexin
Merged
EV
2H EBSS

B)

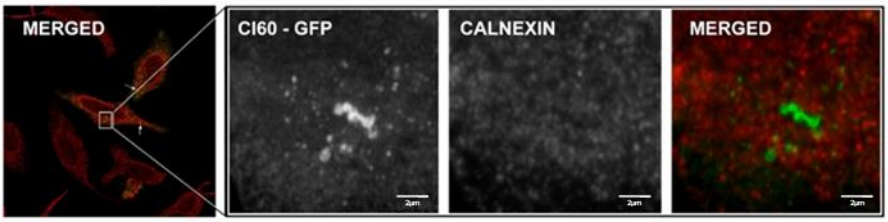

Fig. 3.26. CI60 co-localise with the ER marker Calnexin. Calnexin staining in HeLa cells transfected with CI60-GFP. A) CM (complete medium) High expression nanobody was showed in the upper picture, and lower expression nanobody was showed in the lower panel. The white arrows in the pictures point to the sites where the proximity to the Calnexin staining was more obvious; 2h EBSS starvation: HeLa cells expressing different amounts of nanobody. **B)** Magnification of a maximum intensity projection of a z-stack of the 2h EBSS condition.

To end the study on CI60's localisation at the ER, I checked that there was not signal peptide in the sequence of the nanobody that could be responsible for this co-localisation. The sequence of the nanobody was used as the input in the platforms SignalIP, DeepLoc 1.0, Predotar and Phobius and every of them showed no presence of a signal peptide, reinforcing the veracity of the results.

3.2.5.2 CI60 at the mitochondria

Mitochondria have been shown to have a role in the formation of the autophagosomal membrane [230]. These organelles are highly dynamic, are able to undergo mitophagy (a selective form of autophagy) and are a very good indicator of the cell health state. Their morphology, and indeed their distribution varies enormously among cell types (for instance in fibroblasts, they are more elongated while in hepatocytes, they are more rounded).

TOM20 is a mitochondrial protein that belongs to the translocators of outer membrane complex and recognizes mitochondrial targeting signals. This mitochondrial complex is in charge of transporting proteins from the cytoplasm to the mitochondria [234]. For this reason, antibodies raised against this protein are commonly used as mitochondria markers. The potential localisation of CI60 at this organelle was therefore examined using TOM20 staining. Moreover, any perturbations of the mitochondria dynamic/morphology can also be detected using this antibody and could

correlate with the possible impact in cell viability observed upon CI60-GFP expression (section 3.2.10) or the ER stress previously suggested.

HeLa cells were transfected, with CI60-GFP for 20h and kept in complete medium or starved for 2h. Then, cells were fixed and stained for endogenous TOM20.

Overall, the nanobody transfected cells appeared to be more stressed than the control (untransfected cells or empty vector expressing GFP cells), they were more elongated and lost their original wide flat shape. In complete medium, mitochondria in CI60 transfected cells looked more disorganized, less numerous and presented a morphology distinct from the control samples, sometimes creating chains. After two hours of starvation, mitochondria had a tendency to accumulate in the perinuclear region in the CI60 transfected cells (an effect not seen in complete medium) whereas the mitochondria in control cells seemed to be more spread out in the cytoplasm (see Fig. 3.27).

Mitochondria are highly dynamic organelles that are continuously passing through a fusion-fission state [235]. This could be the reason of the morphological heterogeneity observed in the photos (elongated vs. more rounded mitochondria).

Note that I could not find any co-localisation of CI60 with mitochondria (as assessed by TOM20 staining) but after EBSS starvation, some CI60 punctae appeared close to mitochondria (Fig. 3.27)

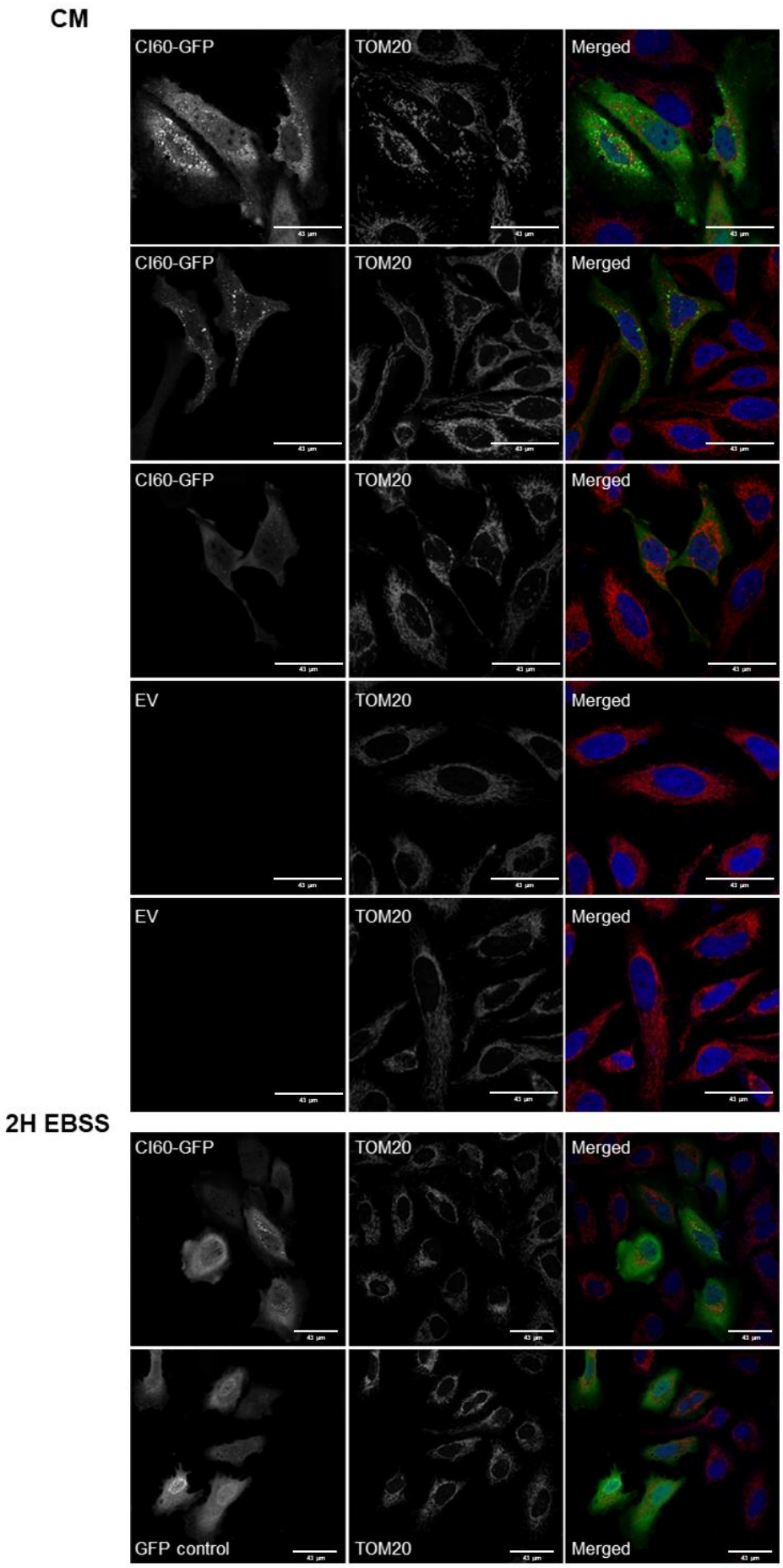
CM
CI60-GFP
TOM20
Merged
CI60-GFP
TOM20
Merged
CI60-GFP
TOM20
Merged
EV
TOM20
Merged
EV
TOM20
Merged
2H EBSS
CI60-GFP
TOM20
Merged
GFP control
TOM20
Merged

Fig. 3.27. CI60 has a negative effect in mitochondria. HeLa cells transfected with either GFP control or CI60-GFP and kept in complete medium or 2h EBSS starvation. TOM20 staining in red, DAPI in blue.

To confirm the observation that the mitochondria number decrease upon CI60 expression, TOM20 staining in transfected cells and controls was measured using Fiji software. Results are shown in Fig. 3.28. INTDEN (integrated density) measures the amount of the TOM20 positive elements in transfected cells, taking into account the area of the cell. Results show that surprisingly, TOM20 staining was higher in CI60 cells in complete medium than in controls, so rather that diminishing in number they were probably a bit more concentrated towards the perinuclear region already, as observed in starved CI60 transfected cells. After two hours EBSS starvation, control only decreased their INTDEN in a very subtle way, while INTDEN from mitochondrias from the CI60 transfected cells had a two-fold decrease, which could correlate with a decrease in the total number of mitochondria (see Fig. 3.28).

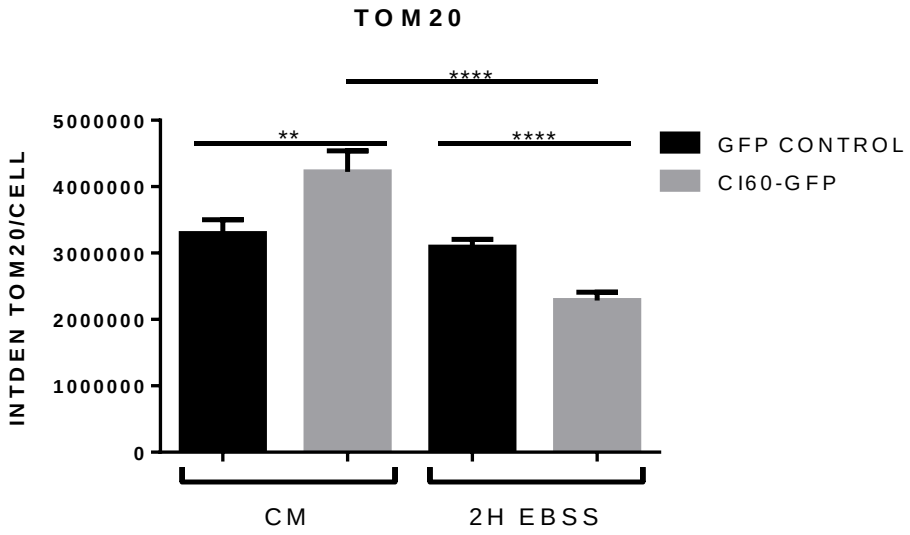

Fig. 3.28. Mitochondria decrease in CI60 treated cells after 2H EBSS treatment. Quantification of TOM20 staining. Integrated density was calculated in control cells vs. CI60-GFP transfected cells. Student t-test was used for statistics. Error bars shows the SEM. N=2

As mentioned above, it is difficult at this stage to make a final conclusion about the changes in mitochondria morphology upon CI60 expression mainly because mitochondria are highly dynamic organelles and are continuously passing through a fusion-fission state [235]. To better

delineate the effect of CI60 on mitochondria, mitochondria function was monitored by measuring its membrane potential.

The mitochondrial membrane potential (Ψm), indicates the mitochondria health state. I used a flow cytometry-based Mitotracker Deep Red FM (MTDR) staining to quantify Ψm in HeLa cells that had been previously transfected for 48h with the nanobody CI60-GFP. MTDR is a mitochondrial potential-dependent dye whose intensity is dependent upon membrane potential. Membrane depolarization by compounds such as CCCP, a mitochondria uncoupling agent, is quantified by the decrease in MTDR intensity whereas an increase in MTDR intensity reflects in increased membrane potential (an effect often seen upon nutrient starvation [236]. I also measured changes in Ψm under conditions of perturbation of VPS34 (using VPS34-IN1 inhibitor) or mTORC1 (using Torin1) pathways as well as inhibition of apoptosis (using ZVAD treatment),

I used different controls to a) show any difference between normal cells (GFP control transfected cells *versus* CI60), and b) show that if there is any effect, it is not a general effect cause by the introduction of nanobodies, but CI60 specifically (BC71-GFP and BC81-GFP transfected cells vs. CI60 transfected cells).

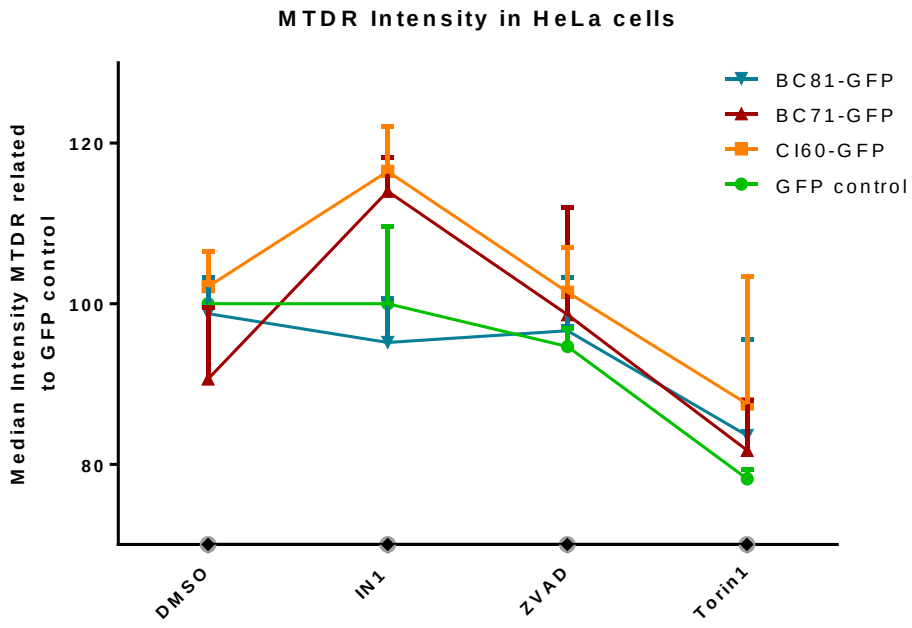

Fig. 3.29. CI60 treated cells do not show any changes in Ψm compared to control. Hela cells were transfected with GFP control, CI60-GFP, BC71-GFP or BC81-GFP, and treated with DMSO, IN1, ZVAD or Torin1 for 48h. Every sample was stained using 50 nM mitotracker red and analysed by flow cytometry. N=3.

Normalized flow cytometry analysis showed no significant differences in Ψm between samples (Fig. 3.29).

Altogether, these results suggest that CI60 expression cause subtle changes in mitochondria numbers without perturbing mitochondrial Ψm.

3.2.5.3 CI60 at the Cis Golgi

The Golgi apparatus is another organelle suggested to be a membrane source for the phagophore formation. My aim was to assess the localisation of CI60 around this organelle as well as its integrity, as previously reported [58], depletion of UVRAG provokes Golgi fragmentation and dispersion (as assessed by GM130, a Golgi marker specific to peripheral-Cis Golgi membrane protein). I hypothesised that, from these observations, CI60-specific association to complex I (UVRAG-free) should not affect the Golgi integrity and morphology, as CI60 is not expected to affect UVRAG-associated complex (complex II).

The Golgi apparatus changes its morphology and fragments at each every mitosis [237]. After cytokinesis, it condenses in a tight perinuclear structure that stays through all the interphase. This process has been extensively studied using HeLa cells.

To address the impact of CI60 on Golgi, CI60-GFP transfected HeLa cells were cultured either in complete medium or for one hour in EBSS starvation and immunofluorescence was performed using an antibody raised against endogenous GM130 [237].

Fig. 3.30 showed that CI60 was localised in a region close to the GM130 positive compartments, but there was no clear co-localisation. However, GM130 is a marker for the Cis-Golgi and I cannot discard that the nanobody may be localised in the TransGolgi Network or in recycling endosomes. This should be assessed with a trans-Golgi marker such as GP75 or TGN38.

Remarkably, while control cells had a heterogeneous Golgi morphologies, (as expected in an asynchronous cell culture) CI60-transfected cells showed homogenous Golgi morphologies, suggesting either an impact on Golgi dynamics or an indirect effect of CI60 on the cell cycle phases [90, 237-239]. Interestingly, CI60 transfected cells appear to be in either

interphase or the early stages of cytokinesis, when the Golgi has a more compact morphology. This effect is more obvious in the CM condition.

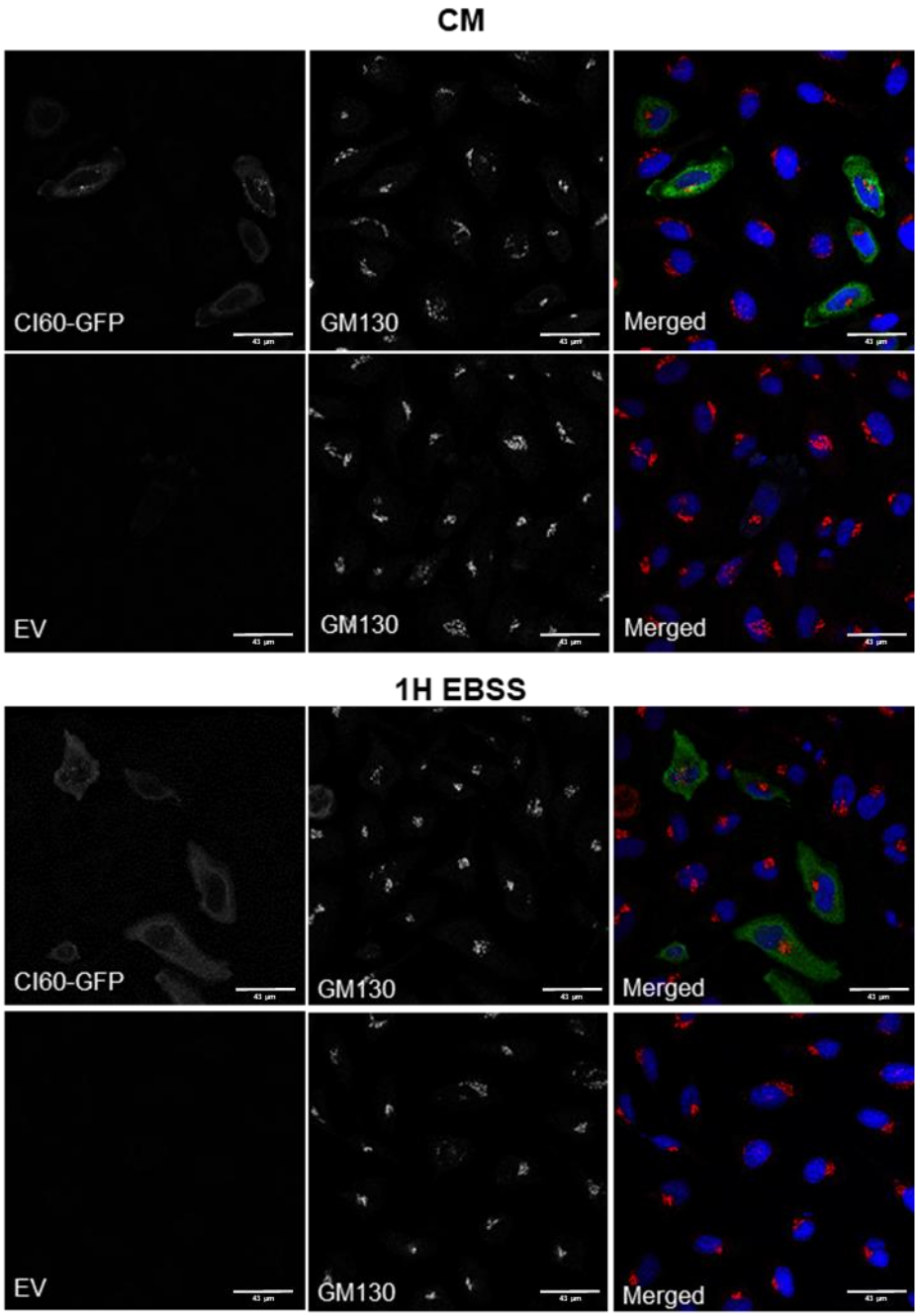

Fig. 3.30 Golgi morphology in CI60 transfected cells resembles control cells morphology upon EBSS treatment. HeLa cells transfected with CI60-GFP or empty vector (EV) maintained either in complete medium or in EBSS for 1H (starvation). GM130 is shown in red. E. Foxall took the images from one of the experiments.

3.2.6 Transient expression of CI60: Influence on Autophagy

3.2.6.1 Formation of autophagosomes is not impaired in CI60-GFP transfected

I next assessed the impact of CI60 on autophagy in order to determine whether this nanobody would affect VPS34 complex I activity. I first used immunofluorescence to quantify LC3 and p62 punctae/integrated density (INTDEN) as a way to measure autophagic activity [124]. Generally, in nutrient sufficient conditions, there is a low level of basal autophagy with very few number of autophagosomes being formed (marked by the lipidated form of LC3, termed LC3-II) and low levels of the autophagy substrate p62 being observed. In contrast, under nutrient starvation conditions, LC3 is lipidated and recruited to the nascent autophagosome, giving rise to a characteristic increase in intracellular punctate staining alongside with p62 (which binds LC3 via its LIR motif). In addition, because p62 is a selective autophagy receptor that sequesters ubiquitinated proteins into LC3 positive autophagosomes, p62 degradation is often used as a marker of autophagic clearance.

As stated in the introduction, VPS34 complex I is required for the formation of omegasomes [86], at the endoplasmic reticulum (ER) where several downstream components are recruited, leading to the expansion of the autophagosomal membrane.

Since my primary aim was to check for specific modulators of VPS34 activity, HeLa cells were transiently transfected with either CI60-GFP or GFP-empty vector control (EV) under conditions of complete medium or 1H of nutrient starvation (EBSS). LC3 and p62 punctae, INTDEN and average size of the positive compartments were measured. Besides this assessment, I also monitored the co-localisation of CI60-GFP with these autophagic markers as a way to confirm the specificity of the nanobody with complex I. According to literature [124], LC3 punctae in cells maintained in complete medium should increase in amino acid starvation conditions. In my experimental settings, the number of LC3 punctae was higher in the complete medium control compared to EBSS condition (Fig. 3.31A, bottom panel, B). These findings were indeed surprising but are consistent with the fact that HeLa cells are known to have a very high rate of autophagic flux and high basal autophagy [123]. This characteristic

property of HeLa cells were also confirmed by the decrease of autophagosome number in EBSS condition. This is in line with the observations summarised in the Guidelines for the use and interpretation of assays for monitoring autophagy in higher eukaryotes review, published in 2008, and Tanida et al. (2005) [240, 241].

In complete medium, CI60-GFP transfected cells (Fig. 3.31A, top panel, B) showed a 2-fold decrease in LC3 punctae. However, no differences in LC3 punctae number in CI60-GFP positive cells was observed under starvation. Interestingly, I observed that the number of LC3 punctae in CM treated CI60 positive cells reached the same level observed in starved control cells (where autophagy should be induced). (Fig. 3.31A, bottom panel and B). In addition, the integrated density (INTDEN) of the LC3 punctae and average size of the particles correlated with the LC3 punctae data in complete medium conditions, but under 1H EBSS starvation, the INTDEN of LC3 punctae and the average size of the particles were slightly decreased in CI60-GFP transfected cells (Fig. 3.31B). This could suggest that the amount of LC3 is actually slightly decreased in CI60 transfected cells after starvation.

Consistent with the data described above, CI60-GFP expressing cells showed a decrease in p62 punctae number in complete medium compared to control with no change upon EBSS starvation (Fig. 3.31A and B). Note that the number of p62 punctae decreased in control cells under starvation condition confirming that the autophagy induction induced by the nutrient starvation protocol is effective (Fig. 3.31)

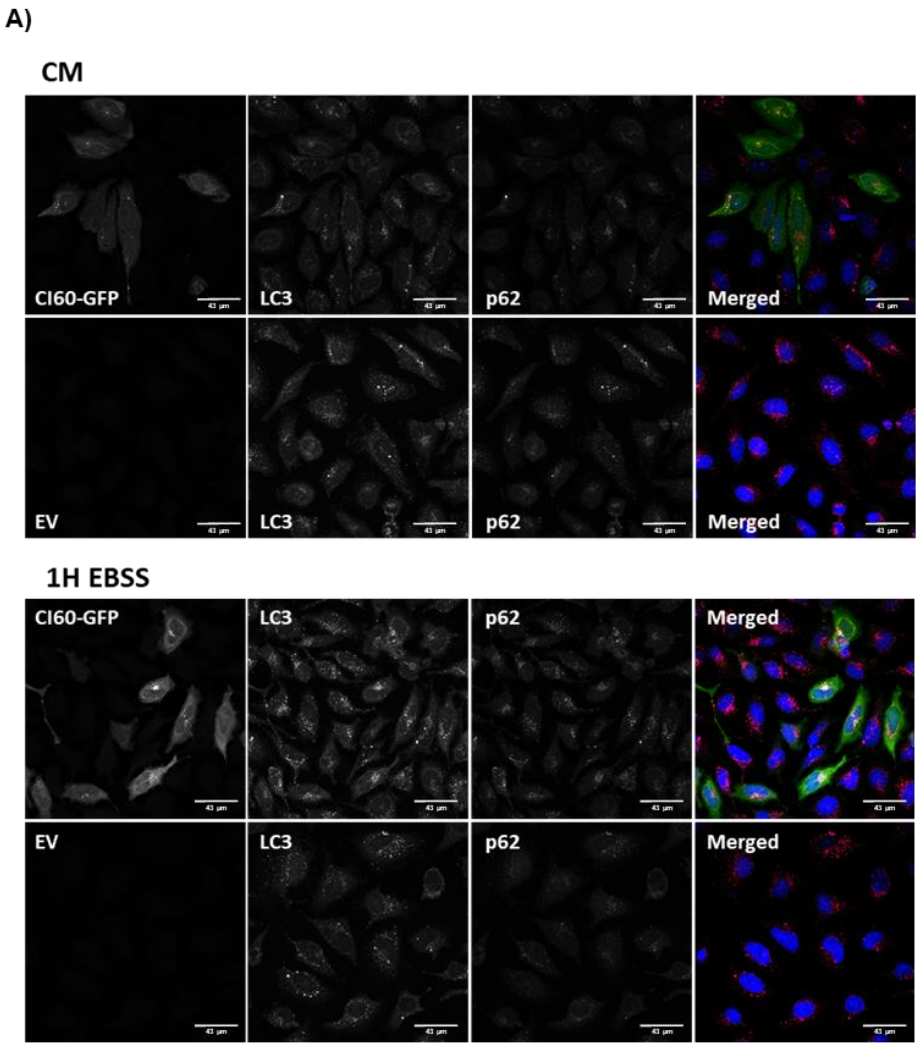
A)
CM
CI60-GFP
LC3
p62
Merged
EV
LC3
p62
Merged
1H EBSS
CI60-GFP
LC3
p62
Merged
EV
LC3
p62
Merged

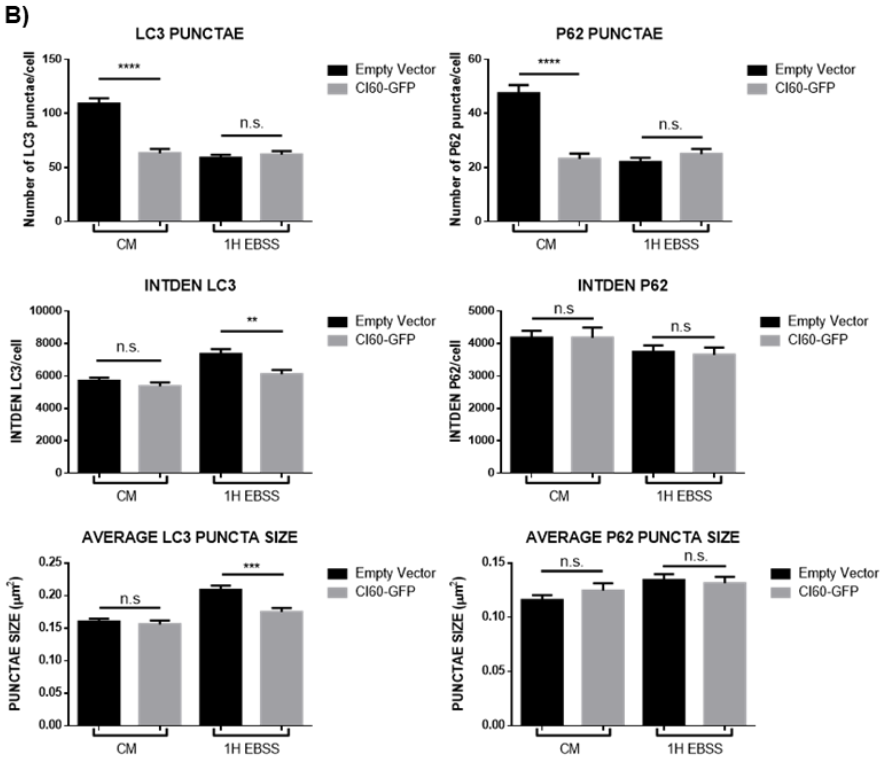
B)
LC3 PUNCTAE
Number of LC3 punctae/cell
****
n.s.
Empty Vector
CI60-GFP
CM
1H EBSS
P62 PUNCTAE
Number of P62 punctae/cell
****
n.s.
Empty Vector
CI60-GFP
CM
1H EBSS
INTDEN LC3
INTDEN LC3/cell
n.s.
**
Empty Vector
CI60-GFP
CM
1H EBSS
INTDEN P62
INTDEN P62/cell
n.s
n.s
Empty Vector
CI60-GFP
CM
1H EBSS
AVERAGE LC3 PUNCTA SIZE
PUNCTAE SIZE (μm²)
n.s
***
Empty Vector
CI60-GFP
CM
1H EBSS
AVERAGE P62 PUNCTA SIZE
PUNCTAE SIZE (μm²)
n.s.
n.s.
Empty Vector
CI60-GFP
CM
1H EBSS

Fig. 3.31. Formation of autophagosomes in CI60-GFP transfected HeLa cells in basal and starved conditions. LC3 (in red) and p62 (in magenta) punctae formation in CI60-expressing HeLa cells. Maximum intensity projection images from CI60-GFP transfected cells vs. empty vector transfected cells under complete medium (A) or nutrient starved for 1H (EBSS conditions) (B) and stained with LC3 and p62 antibodies Quantification of LC3 and p62 punctae, integrated density (INTDEN) and average size of LC3 and p62 stained particles. CM, n=2; 1H EBSS, n=3. Mann-Whitney test was performed: ** 0.0078, ***0.0003, ****<0.0001.

Altogether, the reduction of the LC3 and p62 punctae number observed in CI60-GFP positive cells could suggest two possible outcomes: (1) CI60 could either reduce the formation of autophagosomes, or (2) increase the autophagic rate and degradation. The fact that the decrease (two-fold decrease relative to control) observed in complete medium in CI60 samples of both punctae reached a level comparable to the EBSS-treated control samples (a condition of autophagy induction) points toward a model in which the CI-60 could act as an autophagy inducer rather than an autophagy inhibitor.

In addition to these observations, a strong co-localisation between CI60-GFP, LC3 and p62 was detected in each of the experiment performed (Fig. 3.32), validating a potential role of CI60 is in autophagy process.

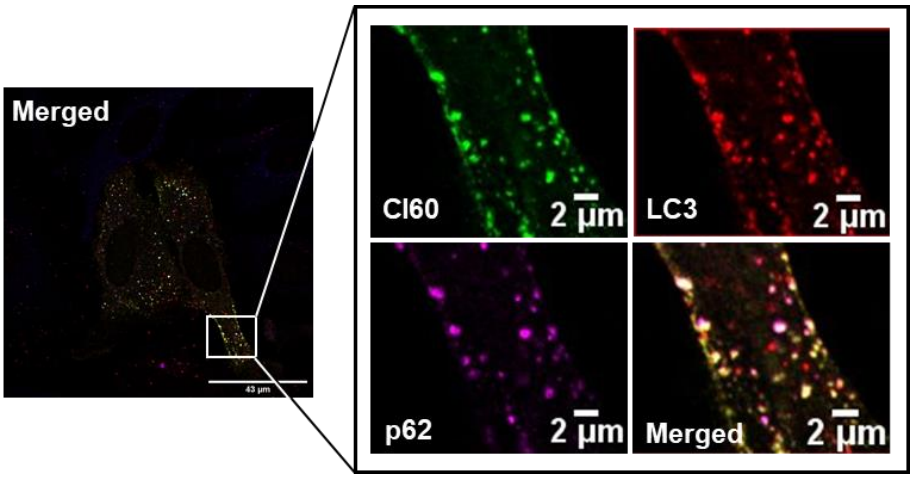

Fig. 3.32. CI60 co-localises with LC3 and p62. Co-localisation of LC3 (red) and p62 (magenta) with CI60 in transiently transfected HeLa cells in CM.

To properly assess which modulatory function CI60 plays on the autophagy process, the inhibitors of the autophagosome-lysosome fusion Bafilomycin A1, was used [124].

In normal cells, the number of LC3-positive punctae increases in the presence of Bafilomycin A1. Cells with activated autophagy have an increased number of LC3 punctae, which further increases with Bafilomycin A1 treatment. In contrast, cells that have impaired autophagy induction, show a small number of LC3 punctae in basal conditions, and this number does not increase upon Bafilomycin A1 treatment. Cells that have deficiency in lysosomal degradation (or impaired autophagic flux) have large number of LC3-positive punctae under basal conditions but this number does not further increase upon Bafilomycin A1 addition.

HeLa cells were amino acid starved for 1H in presence or absence of Bafilomycin A1. Preliminary results from Hela cells (n=1) are presented in Fig. 3.33.A and B. This experiment was repeated in U20S cells (Fig. 3.33C).

A)

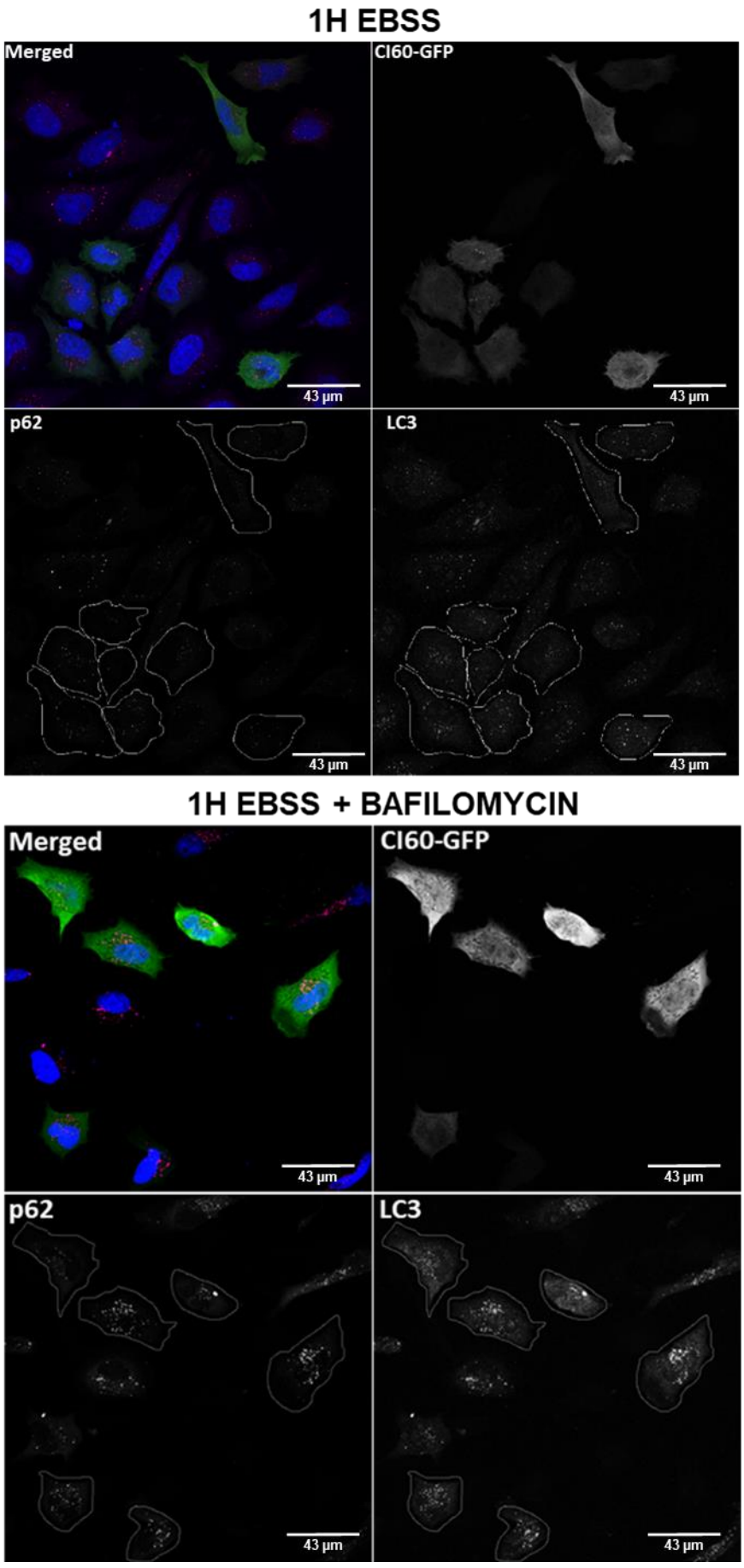
1H EBSS
Merged
CI60-GFP
43 µm
43 µm
p62
LC3
43 µm
43 µm
1H EBSS + BAFILOMYCIN
Merged
CI60-GFP
43 µm
43 µm
p62
LC3
43 µm
43 µm

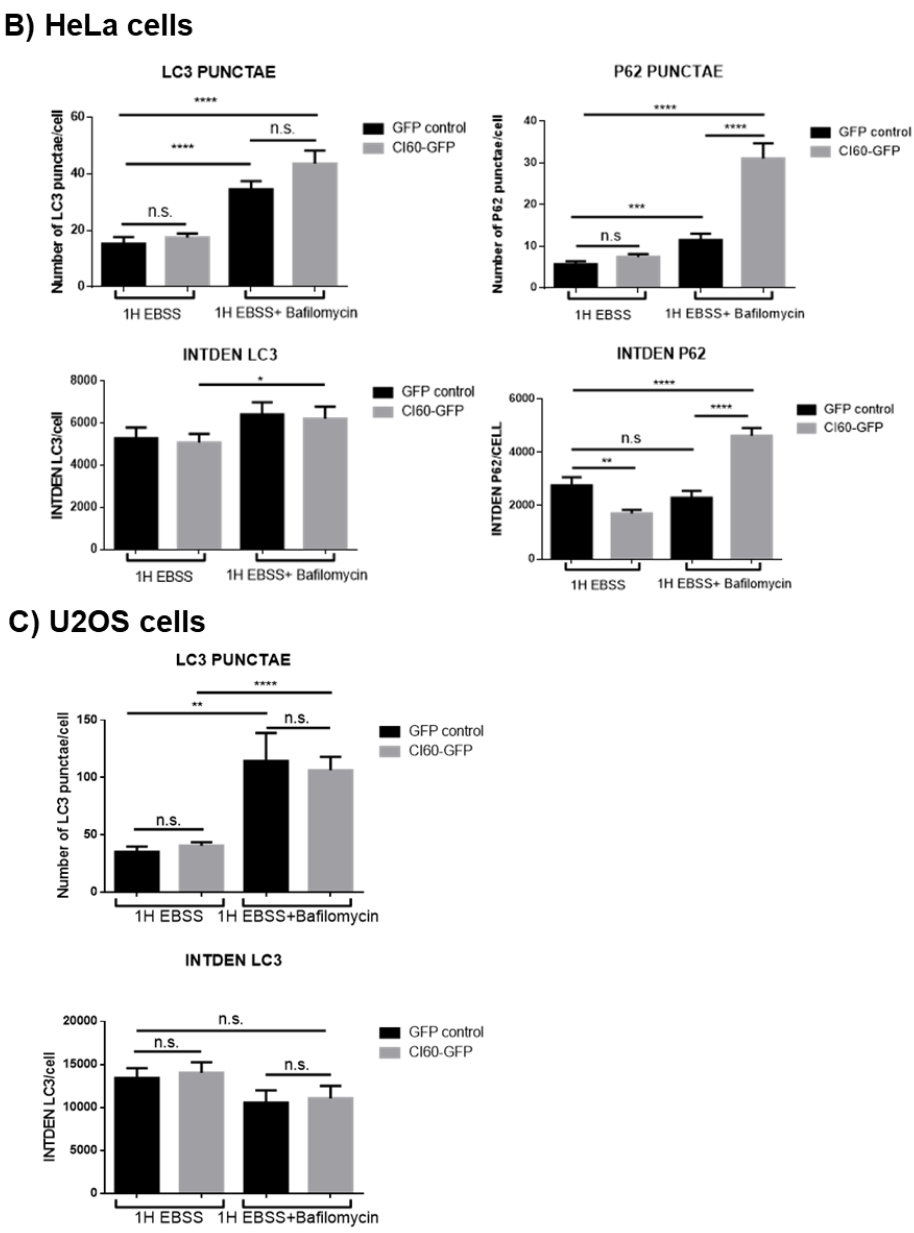

Fig. 3.33. CI60 does not inhibit formation of autophagosomes. HeLa and U2OS results from 1H EBSS treatment +/- Bafilomycin A1 A) HeLa cells treated for 1H in EBSS (nutrient starvation) in presence of 100nM Bafilomycin A1. B) Quantification of LC3 and p62 immunofluorescence shown in A. Kruskal-Wallis test was used to assess differences between control and treatments and Mann-Whitney test for the samples with the same treatment and those for which Kluskal-Wallis test was not powerful enough. n=1. C) Quantification of LC3 punctae number and INTDEN in U2OS cells under 1H amino acid starvation +/- 100nM Bafilomycin A1. Kruskal-Wallis test was used to assess differences between control and treatments. N=1

In control cells, the number of LC3 and p62 punctae is increased, as expected upon Bafilomycin A1 treatment, indicative of a block in autophagic flux. In CI60 transfected cells, a further increase in LC3 and

p62 puncae numbers was observed upon Bafilomycin A1 treatment, suggesting that the induction of autophagy was not impaired. If the autophagic flux was deficient, no differences in LC3 would have been observed (Fig. 3.33B). This observation will need to be validated by subsequent experiments to reach a n=3-4 independent experiments.

Taken together (with the caution that these experiments will need to be repeated), these results suggest that CI60 could act as a inducer of autophagy.

Lipidation assays were performed by WB but due to the low transfection efficiency it was impossible to assess the LC3 lipidation in whole cell extracts.

3.2.6.2 Autophagy activation is sustained longer in CI60 transfected cells

In the recent years, it has been shown that there are distinct pools of PtdIns3P produced by the different VPS34 complexes [13]. Various protein domains bind PtdIns3P produced by these complexes: FYVE, PX and PROPPINS [7, 25]. A commonly used method to measure the autophagic PtdIns3P pool is quantifying the number of WIPI2 punctae-positive cells and the number of WIPI2 punctae per cell by immunofluorescence [242]. WIPI2 is a PROPPIN-domain containing protein, which upon PtdIns3P binding generated by VPS34 complex I, recruits the ATG12-ATG5-ATG16L1 complex responsible for the LC3 lipidation process and expansion of the autophagosomes [127]. To assess whether CI60 nanobody would be a specific modulator of VPS34 complex I activity and whether it affects its autophagic function, IFs experiments using WIPI2 specific antibody were performed.

In this study, HeLa cells were transiently transfected with either CI60-GFP or GFP control, and maintained in either complete medium, or nutrient starved for 15 min or 1H. Immunostaining using WIPI2 antibody was performed on fixed cells to measure the PtdIns3P autophagic pool in CI60 expressing cells compared to control cells. In addition, cells were treated in presence or absence of 100nM Bafilomycin A1 for 30 min prior to incubations in each condition.

As shown in Fig. 3.34, the number of WIPI2 punctae was increased upon nutrient starvation, as expected. In CI60 transfected cells, the WIPI2

punctae number did not change when compared to control in DMSO conditions in CM. Note that in cells showing high level of CI60 expression, fewer WIPI2 punctae were observed compared to control in all starvation conditions. Although this is mostly noticeable after 15 min of starvation, as shown in Fig. 3.34 A-B, the overall effect within the two experiments is no longer apparent due to the low number of the “high” CI60-expressing cells. Interestingly, I observed that CI60 expressing cells have a larger size of WIPI2 punctae (INTEND and size) compared to control when the cells have been starved for a longer period (1H in EBSS), suggesting a potential higher activity of VPS34 complex I in CI60 expressing cells (Fig. 3.34C).

Bafilomycin A1 treatment should ,in principle, not affect the WIPI2 punctae formation. In these settings, WIPI2 punctae is increased in CM upon Bafilomycin A1 treatment in control cells, but not in CI60 transfected cells. This could imply that CI60 might inhibit the formation of autophagosome as no accumulation of WIPI2 positive autophagosomes is observed in CI60 upon Bafilomycin A1 treatment. However, upon 15 min starvation, the number of punctae in CI60 transfected cells increased compared to control and in a two-fold manner compared to CM condition. Because of the high variability of the CI60 expression encountered during the transient transfections, the use of cell lines stably expressing CI60 would be a better approach for further studies.

A)

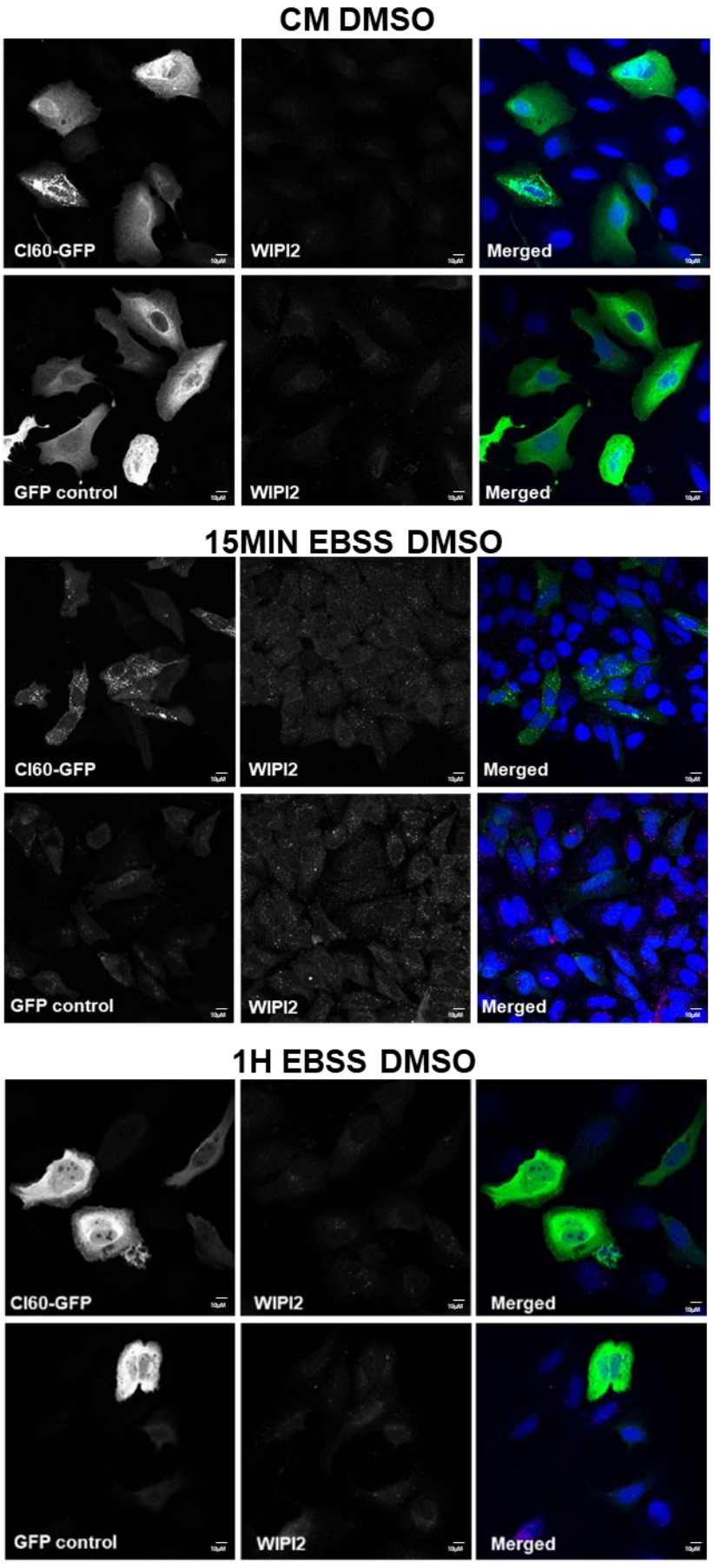
CM DMSO
CI60-GFP
WIPI2
Merged
GFP control
WIPI2
Merged
15MIN EBSS DMSO
CI60-GFP
WIPI2
Merged
GFP control
WIPI2
Merged
1H EBSS DMSO
CI60-GFP
WIPI2
Merged
GFP control
WIPI2
Merged

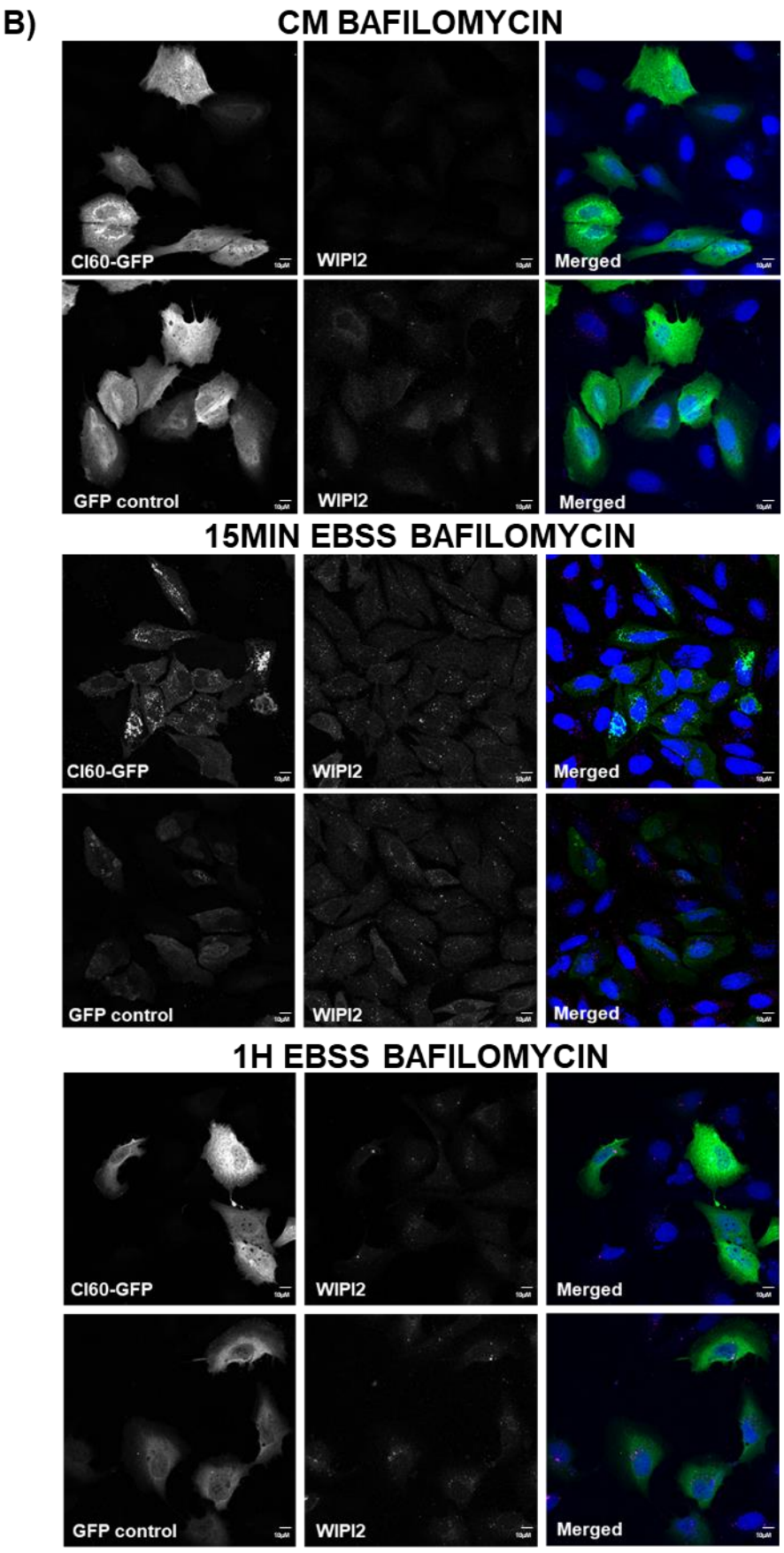
B)
CM BAFILOMYCIN
CI60-GFP
WIPI2
Merged
GFP control
WIPI2
Merged
15MIN EBSS BAFILOMYCIN
CI60-GFP
WIPI2
Merged
GFP control
WIPI2
Merged
1H EBSS BAFILOMYCIN
CI60-GFP
WIPI2
Merged
GFP control
WIPI2
Merged

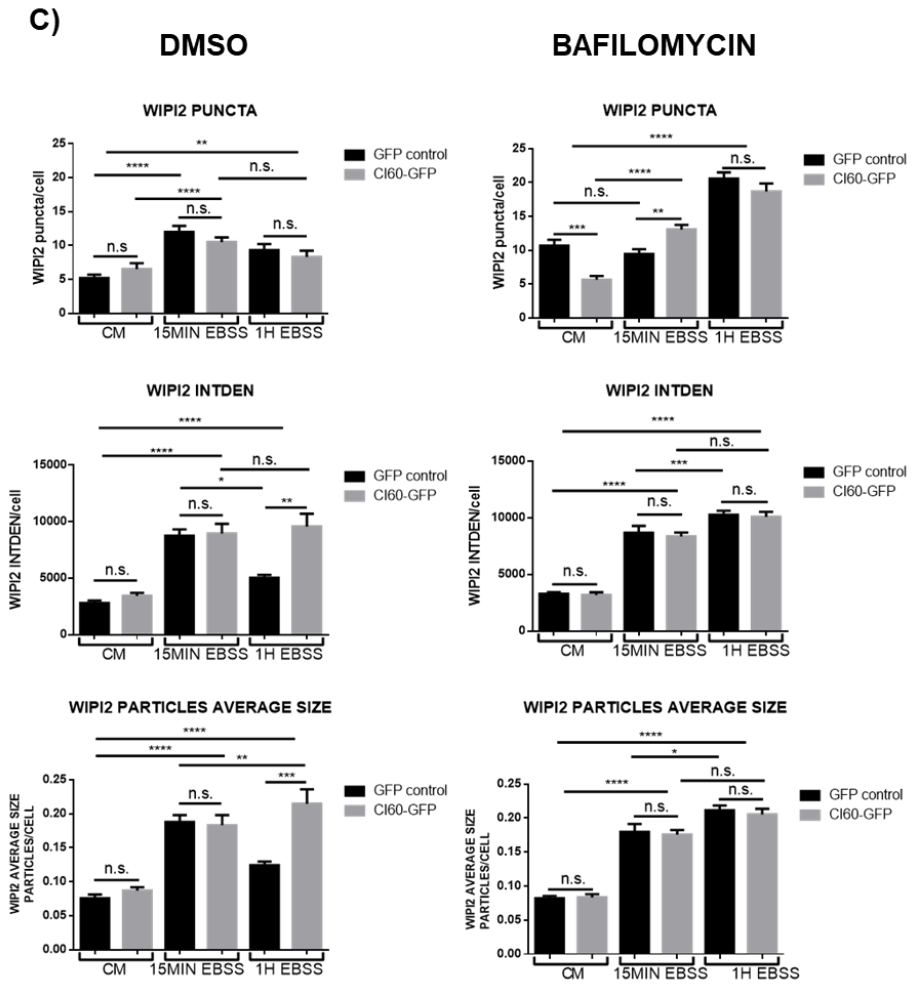

Fig. 3.34 CI60 transfected HeLa cells show high autophagy after 1H EBSS. A) Representative images of HeLa cells transfected with either CI60-GFP or GFP control and maintained in complete medium or amino acid starved for 15 min or 1H EBSS. WIPI2 staining is showed in magenta. All images are maximum intensity projection from z-stacks. B) Quantification of WIPI2 punctae in transiently transfected CI60-GFP or GFP control HeLa cells with (right graphs) and without (left graphs) Bafilomycin A1 treatment. Kruskal-Wallis test was used to assess differences between control and treatments. ****0.0001. n=2

To validate the above observations I performed a preliminary experiment (n=1) in U2OS cells that were transfected and treated using the same conditions as previously mentioned for HeLa cells. As shown in Fig. 3.35 the CI60-GFP transfected cells (in green) were compared to the untransfected cells in the three conditions (fed, and 15 min or 1H starved). Quantification of the IFs images showed first the difference in autophagic activity between HeLa and U2OS cells: HeLa cells displayed a peak of WIPI2 punctae formation 15min after starvation (Fig. 3.34) while U2OS reached theirs after 1H starvation (Fig. 3.35). This corroborates reports found in the literature that HeLa cells have high autophagic flux compared to most of cell lines (in particular U2OS here). This observation makes

U2OS a good model to test the nanobody in a more physiological context. More importantly, these preliminary results in U2OS showed WIPI2 punctae formation in CM condition (a condition where autophagy is normally low), and at 1H starvation timepoint in CI60 expressing cells. Unlike in HeLa cells, addition of Bafilomycin A1 does not reduce the number of WIPI2 puncta in CM, but instead dramatically increase it after 15 min of starvation.

Altogether, this preliminary data suggest that 1) U2OS could be a good model for cells that have a “normal” rate of autophagic flux, 2) the effect of the nanobody is probably cell-dependant, and 3) transfection of CI60 increases the number of WIPI2 punctae, in CM and after 1H of starvation. This implies that more PtdIns3P is generated, which points towards CI60 being an inducer of autophagy,

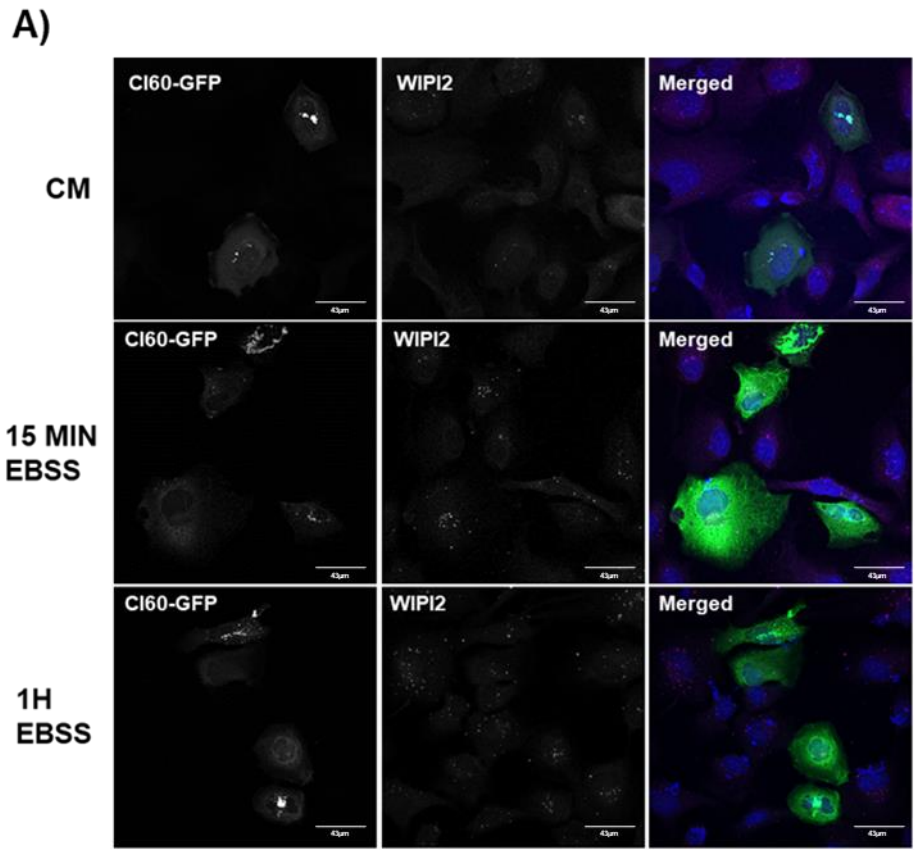

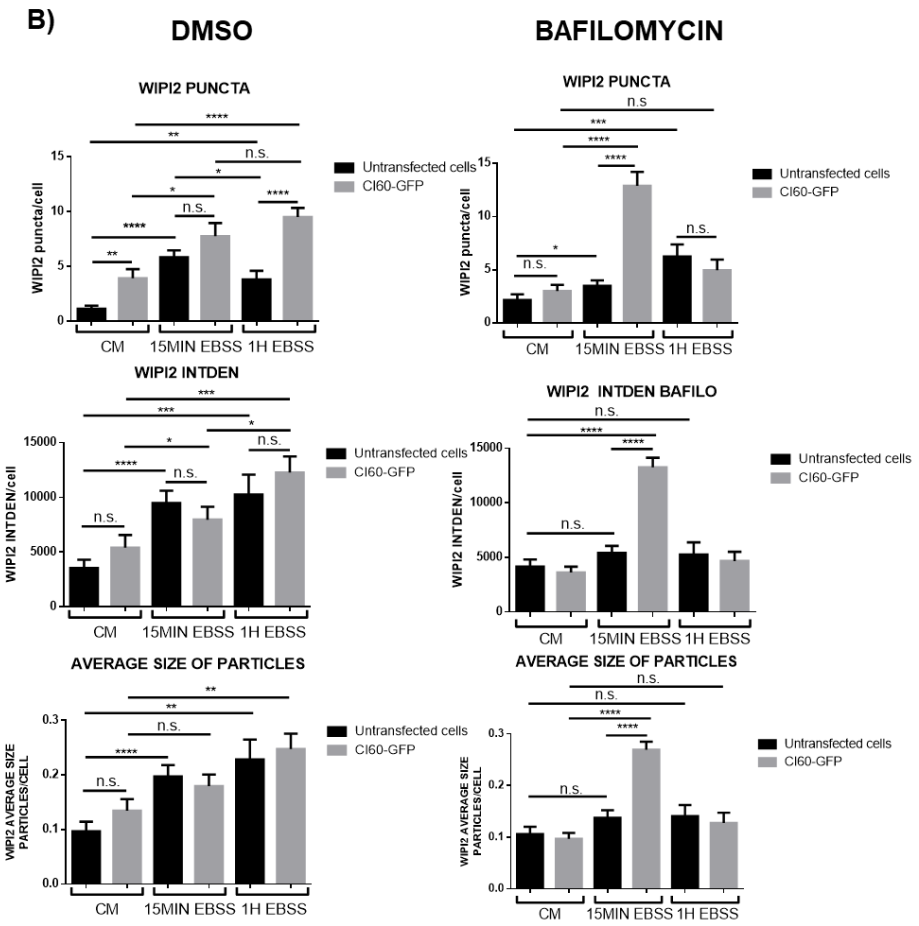

Fig. 3.35 CI60 increases autophagosome formation in U2OS cells. U2OS transiently transfected with CI60-GFP and stained with WIPI2 antibody. A) U2OS cells were maintained in complete medium or amino acid starved for 15 min or 1H. CI60-GFP transfected cells are shown in green. WIPI2 is shown in magenta. Untransfected cells from the same coverslips were taken as controls . Images are maximum intensity projections of z-stacks imaged using an x40 objective.B) Quantification of the images. Mann-Whitney was used for statistics.

In addition to the quantification of autophagic PtdIns3P pool produced upon CI60 expression, the potential co-localisation of WIPI2 and CI60-GFP by immunofluorescence was monitored. Fig. 3.36 shows that CI60 is localised at very close proximity to the WIPI2 positive compartments, suggesting that CI60 is localised closely to the site of production of the autophagic PtdIns3P pool, likely to the omegasome at the ER. Further experiments using markers of these specific sites, such as DFCP1 would be required to fully address this question.

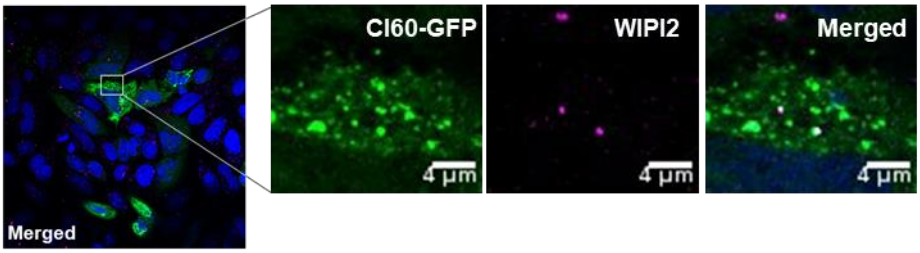

Fig. 3.36. CI60 co-localises with WIPI2. HeLa cells transiently transfected with CI60-GFP after 15min EBSS starvation. WIPI2 is shown in magenta**.**

3.2.6.3 Initiation of autophagy is upregulated in CI60 transfected cells

Atg16L1 has recently been reported to be a good marker to investigate the initiation of autophagy, in particular in its phosphorylated state [128]. Atg16L1 is recruited by WIPI2 to form a complex with Atg5 and Atg12. It recruits the complex to isolation membranes to allow the recruitment of LC3 to the nascent autophagosome membrane boosting the process of autophagosomes closure [105, 128, 243]. I therefore decided to use this marker to assess the possible modulation of the initiation of autophagy by CI60.

HeLa cells were transiently transfected with CI60-GFP or GFP control and maintained in complete medium (CM) or 1 H EBSS starvation (Fig. 3.37A). Under nutrient rich condition, low number of Atg16L1 punctae are expected compared to starvation condition.

Preliminary results showed the trend described for the controls. Moreover, an increase in pATG16L1 punctae and INTDEN was observed in CI60 transfected cells compared to control in CM and EBSS condition (Fig. 3.37B). This data corroborates that CI60 activates Vps34 complex I activity. However, independent experiments to n= 3-4 should be performed to validate this.

A)

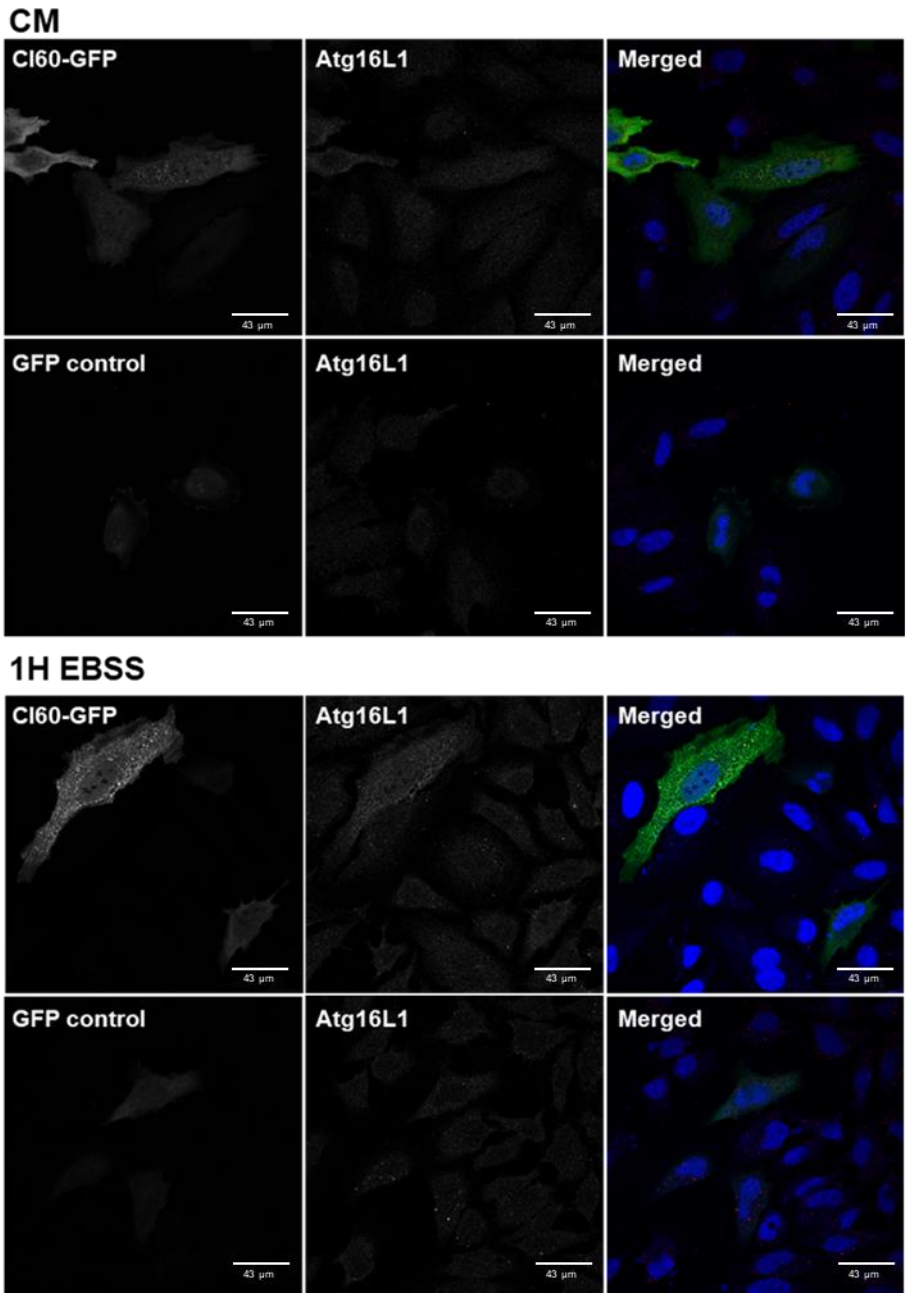
CM
Cl60-GFP
Atg16L1
Merged
GFP control
Atg16L1
Merged
1H EBSS
Cl60-GFP
Atg16L1
Merged
GFP control
Atg16L1
Merged
43 µm

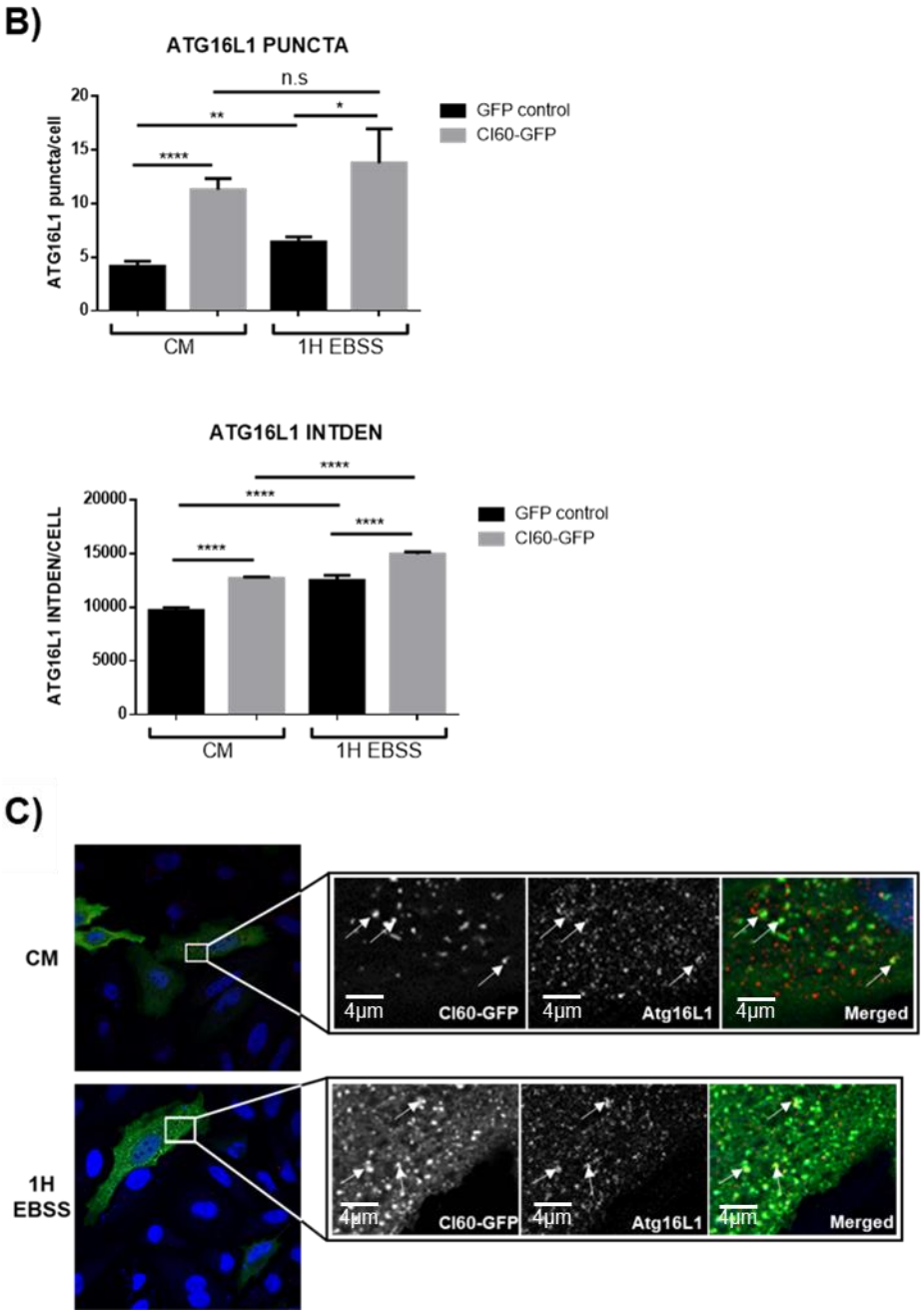

Fig. 3.37. pATG16L1 is upregulated in CI60 transfected cells. HeLa cells transiently transfected with CI60-GFP or GFP control and stained for ATG16L1 (in red). A) Hela cells were maintained in complete medium or amino acid starved for 1H. B) Quantification of ATG16L1 punctae, INTDEN and average size of the particles. T-test with Welch correction was used for statistics. N=1. Data was quantified by R.Wilson**.** C) Representative images of the CM and 1H EBSS conditions to exemplified the close proximity of CI60 and ATG16L1.The arrows indicate some of the points where colocalization can be observed.

I next assessed whether CI60 would co-localise with ATG16L. Fig. 3.37 C show that CI60 indeed localised in close vicinity to ATG16L in both fed and starved conditions (CM *versus* starvation).

3.2.6.4 CI60-GFP binds to VPS34 activated complex I

Based on the HDX-MS data identifying a putative contact site of CI60 at the hinge of the complex I , which changed the conformation of complex I and exposed some of the regions harbouring PTM prone sites (section 3.2.4), I wondered whether the phosphorylation sites on these proteins that participate in the complex activation would be compromised upon CI60 binding. Firstly, I asked whether the complex I bound to CI60 was able to be activated by the upstream complex ULK1, a signalling event critical for autophagy induction. ULK1 directly phosphorylates ATG14L on Ser29, which increases VPS34 activity [52]. Therefore, the phosphorylation status of ATG14L in CI60-GFP or GFP control transfected HeLa cells after 1H starvation (EBSS) or maintained in complete medium was assessed by WB (Fig. 3.38A) . Phosphorylation of ATG14L (pAtg14^{Ser29}) is upregulated upon starvation in both control and CI60-GFP transiently transfected cells input lines. Unfortunately, it is possible that the low transfection efficiency observed upon CI60 transfection might not be suitable to visualize an effect on pAtg14^{Ser29} and LC3 lipidation. Using GFP-trap IPs, I succeded to pull down GFP tagged CI60 along with pAtg14^{Ser29}. This suggested that the binding of CI60-GFP to VPS34-complex I does not affect the phosphorylation of ATG14 and probably,activation of the complex I. Interestingly, I noticed that, upon nutrient starvation (EBSS treatment), the amount of the binding partners increased in the CI60-associated complex. Moreover, the amount of pAtg14^{Ser29} in the supernatant (unbound protein) of the CI60 transfected cells is depleted, suggesting that most of the cellular phosphorylated form of ATG14 is present into the CI60-bound complex I.

Another site of phosphorylation that was of particular interest was Beclin 1 phosphorylation at pBeclin 1^{Thr119}. This site is located in the BH3 domain of Beclin 1, crucial for Beclin 1 binding to members of the Bcl2 family [45]. Dissociation of Bcl2 allows Beclin 1 to be recruited to complex I. This step is dependent on the phosphorylation of Beclin 1 at Thr119 by death-associated protein kinase (DAPK), a calcium/Calmodulin (CaM) Ser/Thr kinase [244].

The effects described above were confirmed using a different inducer of autophagy (Torin 1), and using Beclin 1 antibody for IPs (Fig. 3.38B). As controls, a GFP control and the NC59 nanobody (non-binder nanobody

from the same llama immunization to validate the binding specificity of CI60) were used.

Fig. 3.38B shows that pBeclin 1^{Thr119} increased in the GFP controls after autophagy induction (starvation condition). This has been previously reported in HeLa cells [245], but it may be different in other cell types [246]. Moreover, the association of CI60 seemed to upregulate Beclin 1 phosphorylation at this site, which suggest that phosphorylation of that site is not affected by the binding of CI60. However, to properly confirm the specific phosphorylation state of Beclin 1 in CI60-bound complex I, a GFP trap assay that would pull down CI60 should be performed.

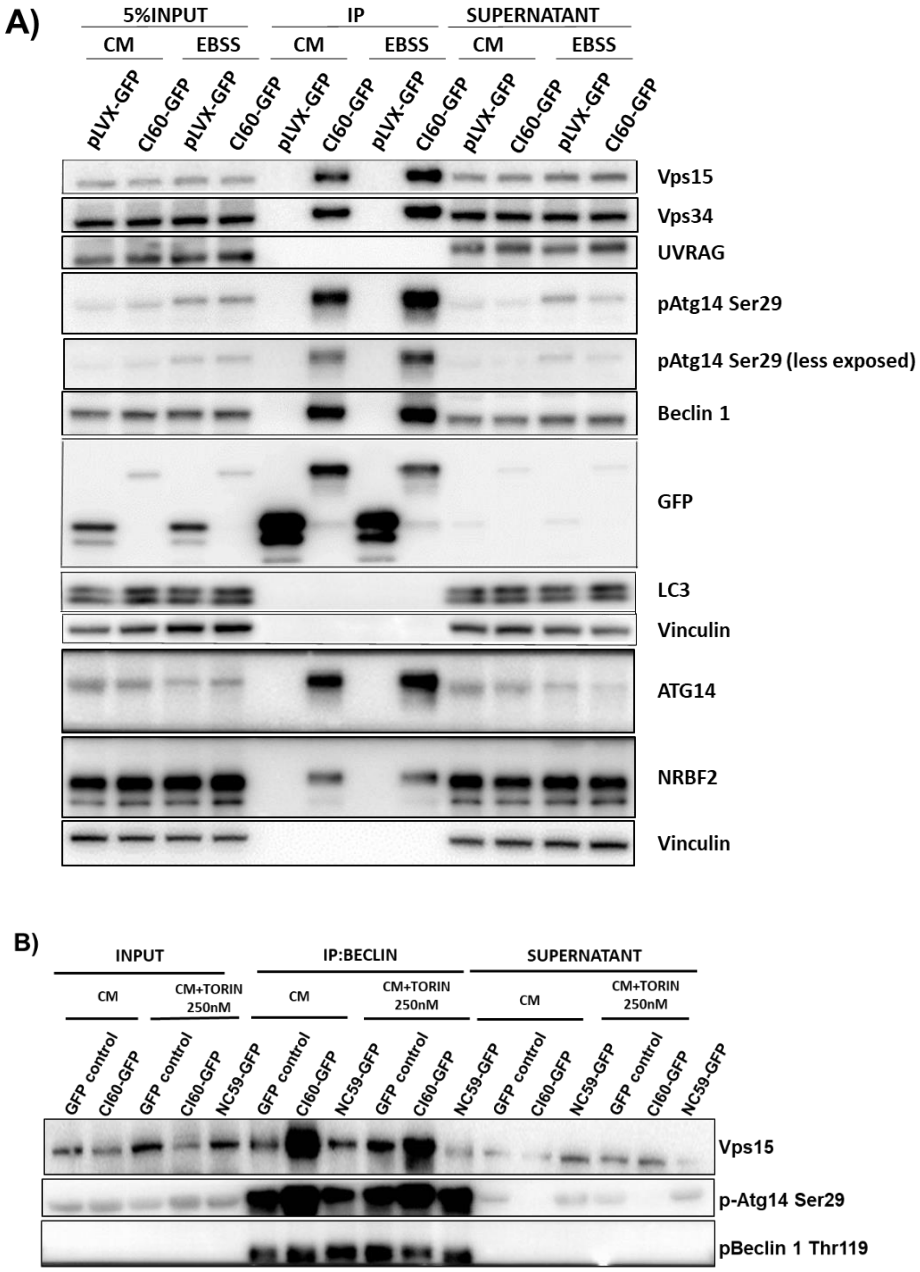

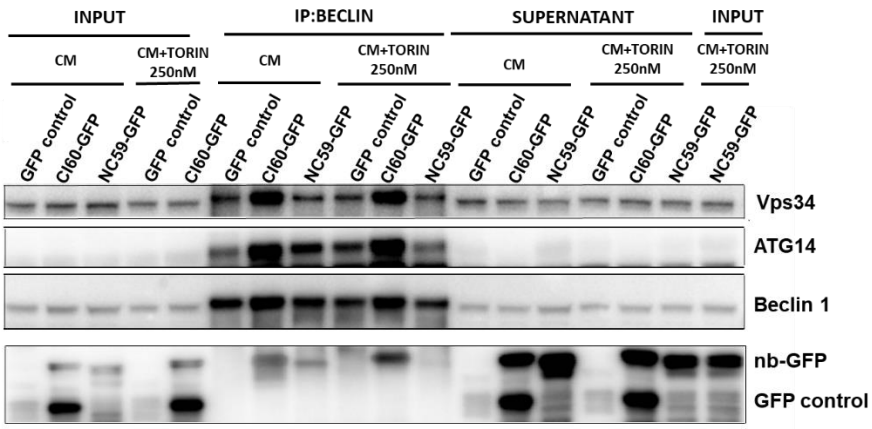

Fig. 3.38. Complex I pulls down pAtg14^{Ser29} and pBeclin 1^{Thr119}. IP from HeLa cells transiently transfected with A) CI60-GFP or GFP control and immunoprecipitated using GFP-trap. Cells were starved using EBSS for 1H. B) CI60-GFP, NC59-GFP or GFP control immunoprecipitated using a Beclin 1 antibody. Cells were treated with DMSO (CM) or 250nM Torin1 for 1H. E. López performed one of the WB from the IPs. N=2

Results show that pAtg14^{Ser29} was immunodepleted in the supernatant lines, confirming the results shown with the GFP-trap (Fig. 3.38A). Of note, pAtg14^{Ser29}, total ATG14, VPS15, VPS34 and Beclin 1 were pulled down with higher efficiency in cells transfected with CI60.

Overall, these findings suggest that the binding of CI60 to complex I does not affect the phosphorylation of pAtg14^{Ser29} and pBeclin 1^{Thr119} and further indicate that complex I is in its active conformation after CI60 binding. In addition, this data suggest that there may be a shift in the relative abundance of VPS34 complexes.

3.2.6.5 CI60 transfected cells tend to have swollen lysosomes

I next focused my attention on lysosomes, a further downstream organelle critical in the autophagic process. They degrade and “recycle” the sequestered cytoplasmic material coming from both autophagy and endocytic processes. Besides its degradative role, lysosome is also involved in autophagy regulation, primarily through its relationship with the master kinase complex, mTORC1 and its perinuclear localisation [32]. Any modification in the initiation of autophagosomes would result in modification of the lysosomal function [247]. Finally, it is possible that the lysosomal degradative pathway would be involved, to a certain extent, to the degradation of the nanobody CI60 if undesirable by the cells.

Under nutrient rich condition such as in complete medium, lysosome's distribution is closer to the plasma membrane while under nutrient starvation, lysosomes tend to move to a more perinuclear region. This localisation has been associated with less mTORC1 activity, formation of autophagosomes and facilitates autophagosome-lysosome fusion [247].

In this study, HeLa cells were transfected with either CI60-GFP or GFP control and then maintained in complete medium or starved for 1H (EBSS). Lysosomes were next examined using immunofluorescence with an antibody raised against Lamp1, a marker for lysosomes.

No difference in lysosome number was observed in complete medium, however the CI60 transfected cells showed a tendency to have enlarged lysosomes (Fig. 3.39).

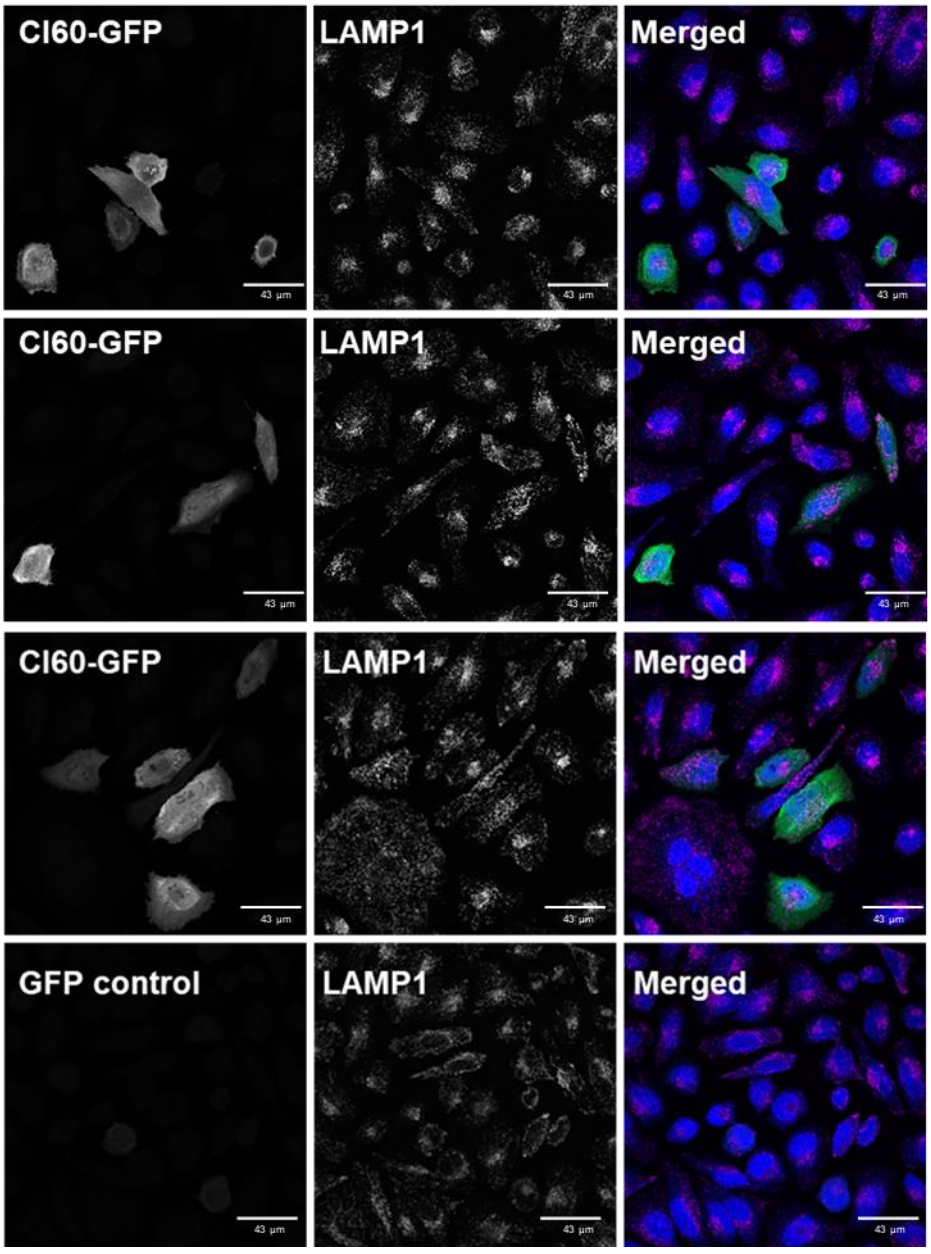

Fig. 3.39. Lysosomes are enlarged in CI60 transfected cells in complete medium. HeLa cells were transfected with CI60-GFP/ GFP control in complete medium and stained with LAMP1 (shown in magenta).

Under starvation condition (EBSS treatment), lysosomes tend to be more distributed in the perinuclear region as shown in the control cells, as previously published [32]. In the CI60 transfected cells, lysosomes seemed to be less numerous but larger, in particular in the “high” CI60 expressing cells (Fig. 3.40). Swollen lysosomes are usually associated with inhibition of autophagy [248], however, data showed that there was no impairment in the formation of the autophagosomes. To further investigate this, quantification on the size and number of lysosomes should be performed. Cathepsin D processing and EGFR degradation assays could be used as complementary assays. Interestingly, UVRAG deficiency causes reduction in the number of lysosomes [58].

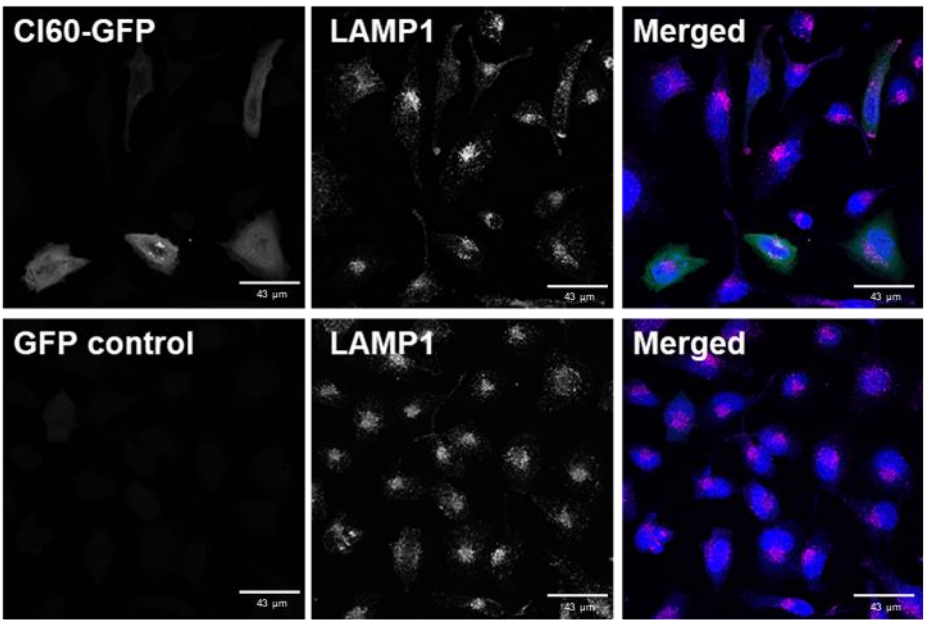

Fig. 3.40. CI60 transfected cells show enlarged lysosomes after 1H EBSS starvation. Transfected with either CI60-GFP or GFP control. LAMP1 is showed in magenta.

Importantly, I sometimes saw a co-localisation of CI60 with lysosomal markers LAMP1 suggesting that CI60 could be recruited to these compartments or degraded by the lysosomal degradative pathway. (Fig. 3.41). This could also point towards the role of complex I and/or CI60 in the autophagosome-lysosome fusion.

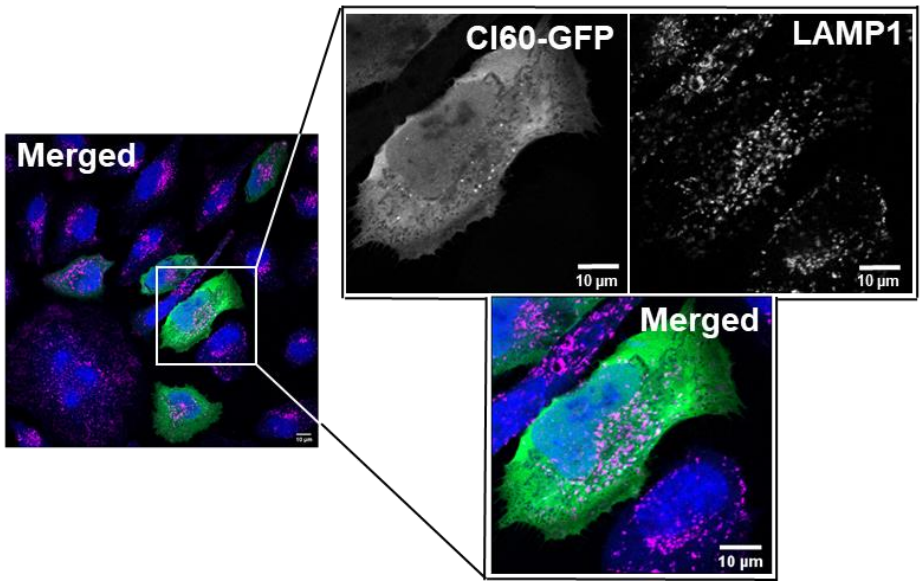

Fig. 3.41. CI60-GFP is only partially colocalising with the lysosome. Amplification of a CI60-GFP transfected cell stained with Lamp1. The little co-localisation of CI60 with the lysosome is observed as white dots**.**

3.2.7 Transient expression of CI60: Influence on Endocytosis

3.2.7.1 CI60 transfected cells display different total cellular PtdIns3P levels

Reagents to detect endogenous PtdIns3P in cells are very limited due their lack of sensitivity or specificity and often lead to misinterpretation due overexpression artefacts. To circumvent this problem, H.Stenmark developed a method using a recombinant GST or GFP fusion protein containing a double FYVE domain of HRS used on fixed cells in a similar way of the use of a primary antibody for IF. This method allowed several studies to monitor PtdIns3P membranes dynamics or stability [242], and the role to VPS34 in endocytic traffic. I aimed to assess whether expression of CI60 had any effect on endocytic PtdIns3P pools using a 2xFYVE^{HRS} probe, which in general do not co-localise with the PtdIns3P autophagic pools that are assessed with the specific markers mentioned above (DFCP1 or WIPI2). To do so, HeLa cells were transfected with either CI60-HA or HA expressing plasmid (referred to as EV) as control, and total cellular PtdIns3P pool were assessed using a GFP-2xFYVE^{Hrs}, and compared with a WIPI2 antibody on fixed cells (Fig. 3.42A). Lipid staining conditions are critical for 2xFYVE probe to properly work, and unfortunately are not adequate for the WIPI2 IF staining, therefore, WIPI2 punctae were less intense and background was higher in the co-staining experiments than in single WIPI2 staining. In nutrient rich conditions (CM)

very few WIPI2 punctae were detected, as expected. Nonetheless, the few WIPI2 punctae detected were in close proximity with the CI60 nanobody in CM condition (Fig. 3.42, top). In nutrient-depleted condition (EBSS), WIPI2 punctae number increased as described in section 3.2.6.2, and its co-localisation with CI60 nanobody was also more apparent (Fig. 3.42 and Fig. 3.34). Interestingly, the total cellular pool of PtdIns3P, detected by the FYVE probe mostly did not co-localise with the autophagic PtdIns3P pool (as assessed by WIPI2 staining) as previously published [86] confirming the specificity of detection of the different PtdIns3P pools using these tools (see Fig. 3.42B). In addition, I also found that some FYVE positive punctae co-localised with the nanobody and this was seen only under starvation condition (Fig. 3.42B).

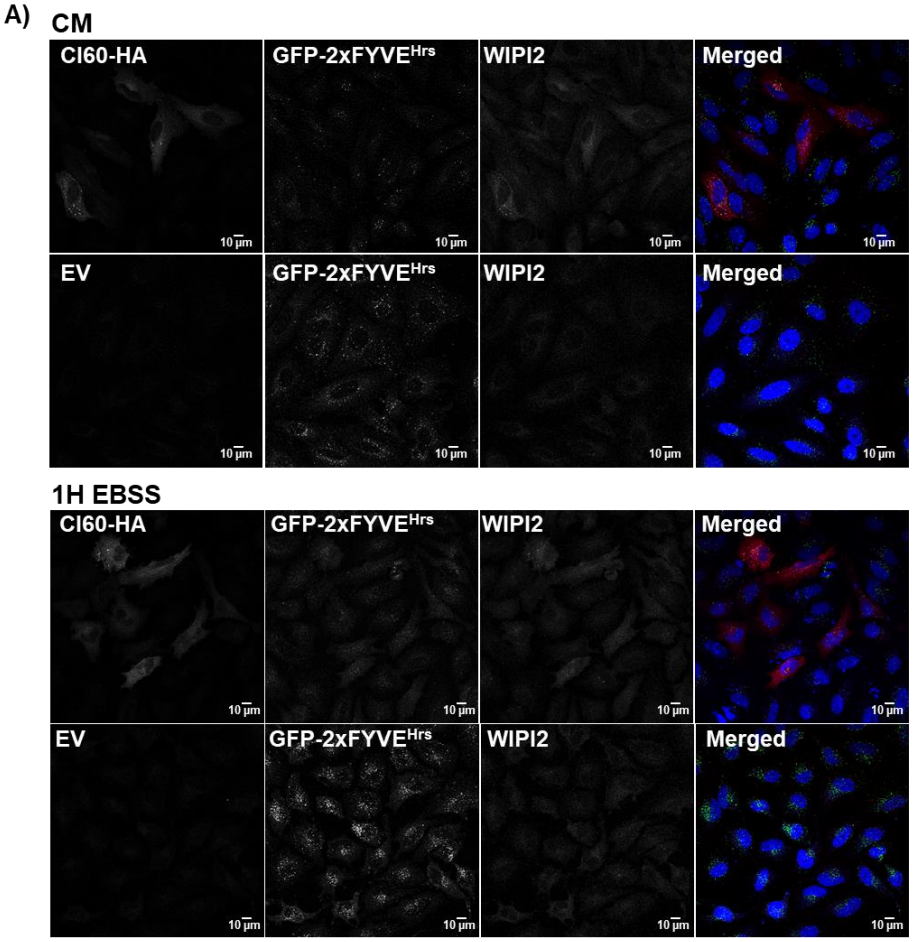

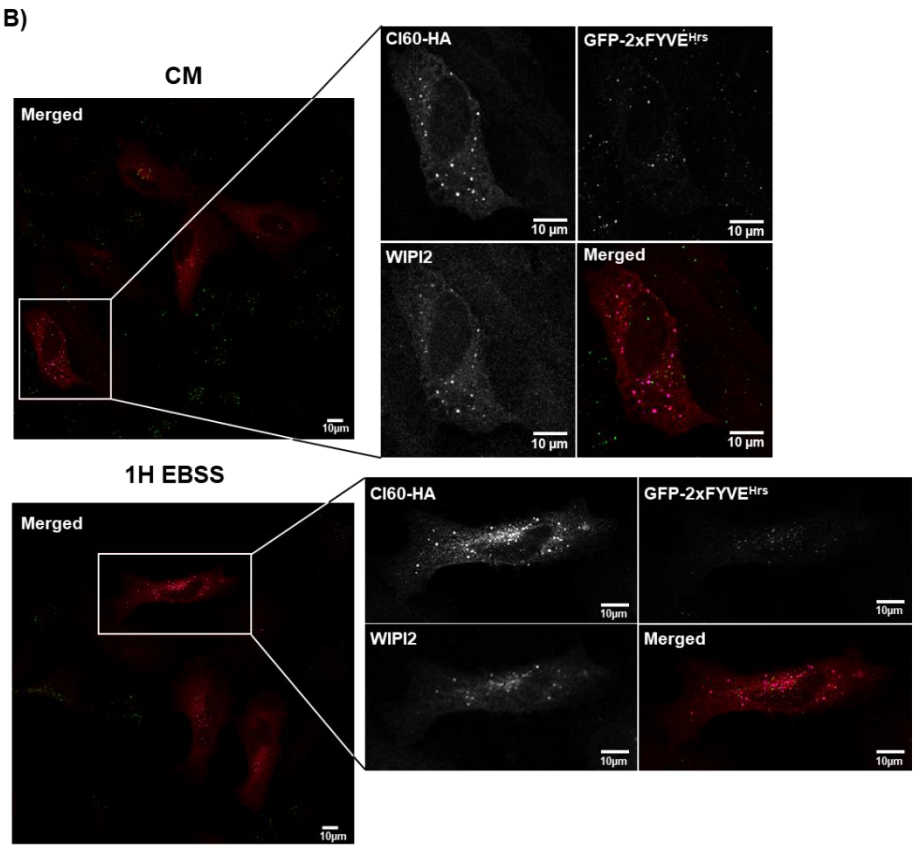

Fig. 3.42. CI60 shows little co-localisation with total PtdIns3P pools. GFP-2xFYVE^{Hrs} staining in transiently transfected HeLa cells. A) HeLa cells transiently transfected with CI60-HA or EV, fixed and stained with GFP-2xFYVE^{Hrs} and WIPI2 antibodies in CM or EBSS. N=1. HA tag (CI60-HA) is displayed in red, GFP-2xFYVE^{Hrs} in green and WIPI2 magenta B) Amplification of the CI60 transfected cells to show localisation of CI60, global PtdIns3P and WIPI2. N=1.

Quantification (Fig. 3.43A) of the HeLa cells presented in Fig. 3.42. showed that total cellular PtdIns3P pool (as assessed by the GFP-2xFYVE^{Hrs} punctae number) is reduced in CI60 transfected cells compared to control. This is reminiscent to the effect seen in the WIPI2 pools when CI60 nanobody was highly expressed. This reduction and marked difference with control was somehow unexpected, as most of the intracellular PtdIns3P pool should not be affected by the expression of CI60, suggesting that CI60 might have some role outside the autophagic complex. This particularity will be discussed more extensively in the discussion. I hypothesise that this reduction could be caused by the nanobody stabilizing complex I and not allowing the rest of the components to bind to UVRAG, which exerts its function in endocytic pathways. Of note, further experiments will be required to confirm these striking findings.

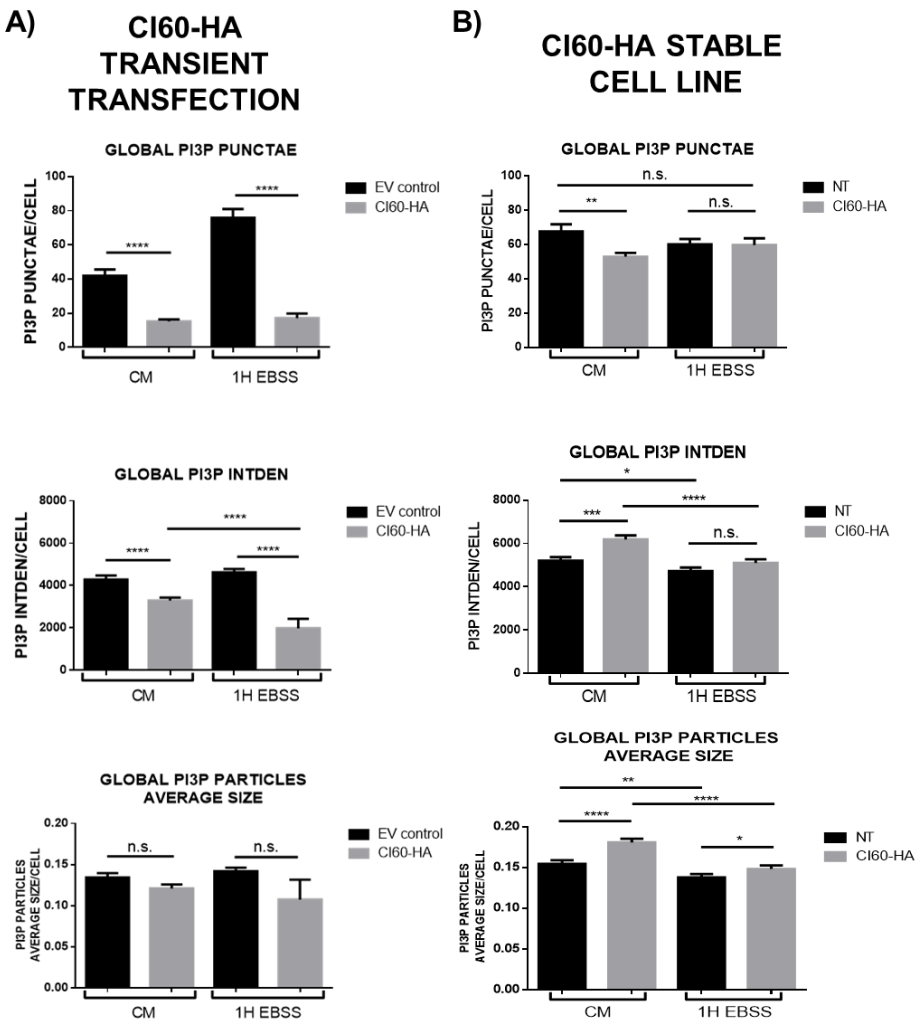

Fig. 3.43. Global PtdIns3P drops in CI60 transfected HeLa cells and CI60 stable HeLa cell line. Quantification of total cellular PtdIns3P, represented by GFP-2xFYVE^{Hrs}, from A) HeLa cells transiently transfected with CI60-HA B) CI60-HA stable expressing HeLa cell line and parental HeLa cell line. N=1. Error bars show the SEM, Mann-Whitney test was used for statistical analysis. EV: empty vector

This experiment was repeated in stably expressing CI60 HeLa cells lines and using parental HeLa cells as control (Fig. 3.43B). As observed in transient transfection experiments, CI60 expressing cells show a decrease in GFP-2xFYVE^{Hrs} punctae number in complete medium but not in EBSS. However, in contrast to transient transfection, the level of GFP-2xFYVE^{Hrs} INTDEN in complete medium is increased, with a similar trend (although at smaller extent) observed in EBSS condition (p=0.0527). In addition, the global size of the FYVE positive vesicles in CI60 stable cell lines was increased compared to the parental cells.

The difference in the results with the transient transfected cell line could be due to the huge heterogeneity of the CI60 nanobody expression. In

transient expression, CI60 expression was higher than in the stable cell line (probably due to the fact that the stable cell lines could only survive with a lower CI60 expression). Interestingly, although results are somehow opposite to the ones obtained in transient transfection, in both settings (transient transfection and stable cell line) global PtdIns3P punctae number in CM was decreased.

Overall, CI60 transiently transfected cells showed a tendency towards a lower total cellular PtdIns3P pool after starvation compared to controls, while the difference in CI60 stable expressing cells was less noticeable. Further experiments will be needed to confirm these preliminary results.

3.2.7.2 CI60 does not affect early endosomes

I showed here that CI60 binds specifically to VPS34 complex I. Because it does not bind complex II (UVRAG associated complex involved in endocytic pathway), CI60 should not affect any of the early endocytic routes. VPS34 localises to the early endosome, where it recruits PtdIns3P-binding proteins such as HRS or EEA1 via PX or FYVE domains [21]. EEA1 (early endosome autoantigen 1) is recruited by PtdIns3P promoting the fusion of early endosomes [249]. Changes in the PtdIns3P production from VPS34 complex II affect the endosomal pathway homeostasis. In order to address whether CI60 expression had an impact on the endocytic route, an immunofluorescence assay was performed in HeLa cells using an antibody raised against EEA1, one of the main endosomal marker. After transient transfection, CI60-GFP or GFP control transfected cells were kept in CM or starved in EBSS for 1H. No change in number or size of EEA1 punctae was observed in nutrient rich or nutrient depleted conditions suggesting that CI60 expression does not affect the early endocytic route as assessed by EEA1(Fig. 3.44).

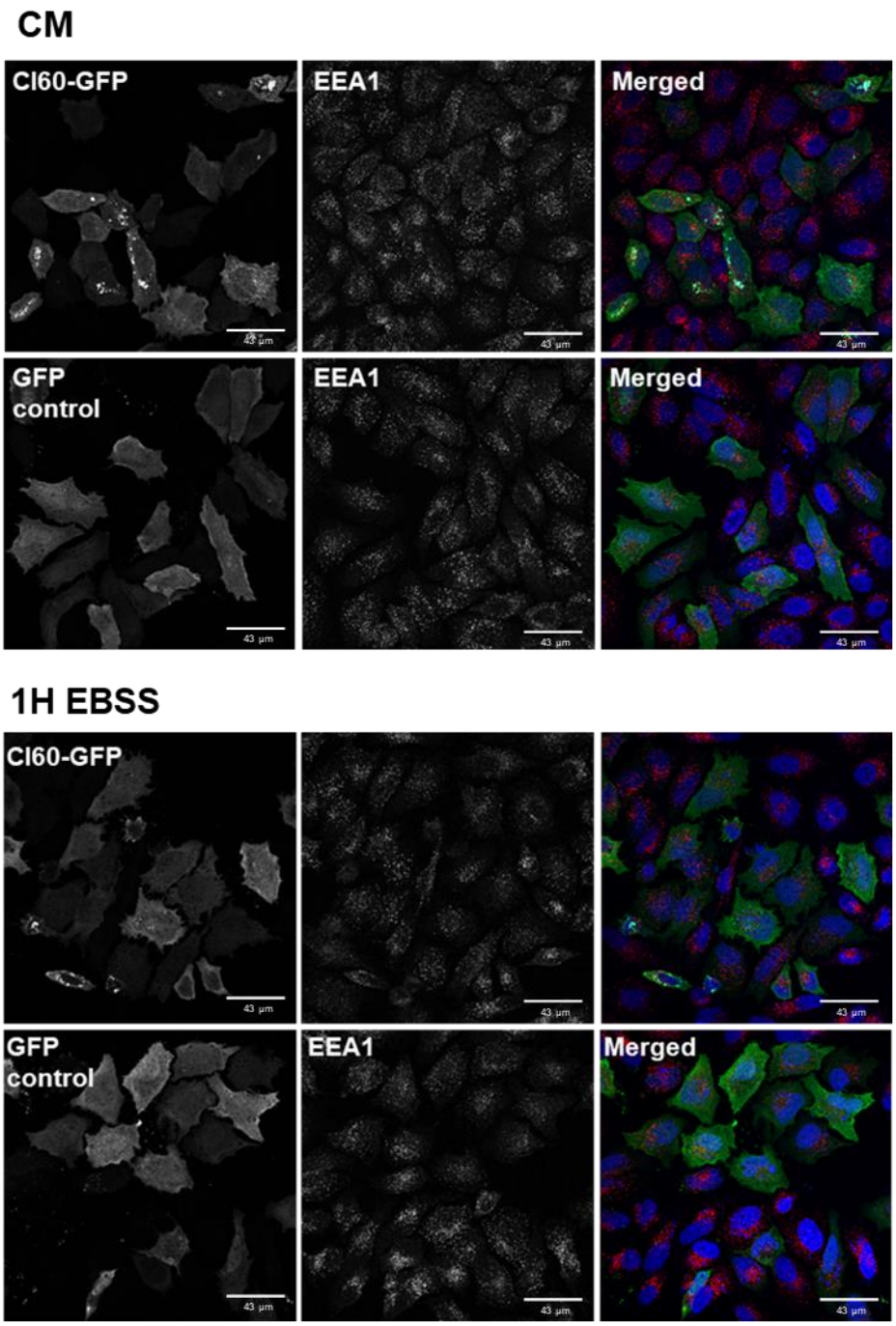

Fig. 3.44. CI60 does not affect early endosomes. HeLa cells transiently transfected with either CI60-GFP or GFP control and stained with EEA1.

Due to time limiting and the technical difficulties of low transient efficiency (where any effect measured by WB would not be noticed), I did not performed more assays. However, impact on endocytic routes should be further assess by creating an inducible model where expression of the nanobody could be homogeneous and EGFR degradation assay, transferrin uptake or processing of procathepsin D (which can be easily assessed by WB) could be performed.

3.2.8 Presence of CI60 in the cytokinetic bridge

During the IF experiments, I frequently noticed that CI60 nanobody, was localised in the midbody of cells that were in the late stage of cytokinesis (see Fig. 3.45). This was not necessarily surprising knowing that few studies reported a role of VPS34 in cytokinesis.

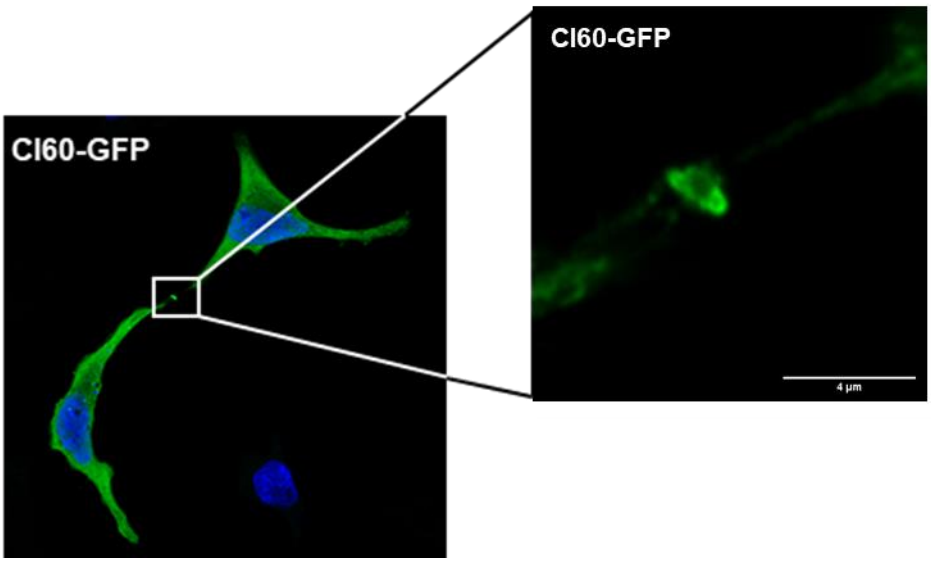

Fig. 3.45. CI60 localise to the midbody. HeLa cells transfected with CI60. The photo on the right shows a higher magnification of the cytokinesis bridge and the midbody, where the nanobody is localised.

Indeed, VPS34 has a known role in the control of cytokinesis, however, this has been attributed to VPS34 complex II [55, 154]. To confirm this finding, cells were transfected with CI60-GFP or NC59-GFP (a nanobody that does not bind any of the VPS34 complexes) as a control, starved for 1H with EBSS and subsequently stained with Aurora B antibody, a marker for the midbody, as shown in Fig. 3.46.

Interestingly, I also found some autophagy markers such as Atg16L1 (shown in Fig. 3.46B), LC3 and p62 (data not shown) localised to the midbody, confirming a role of the autophagy machinery in cytokinesis.

This was seen on two independent experiments, however, due to the low transfection efficiency of the nanobody and the difficulty of finding cells in cytokinesis in an asynchronous culture, more experiments would be required to properly confirm these findings. For instance, assessing the role of CI60 in synchronized culture using thymidine block on stable cell lines would be a way forward.

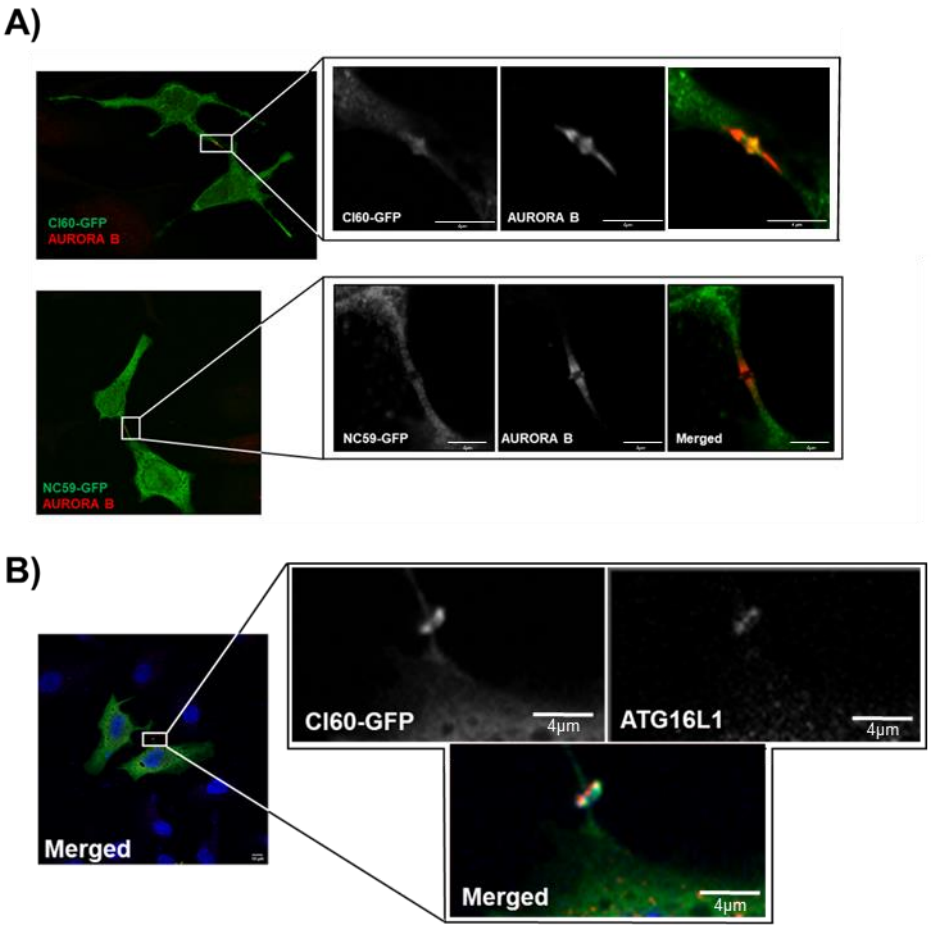

Fig. 3.46. CI60 and pATG16L1 are found at the midbody. Transfected HeLa cells were nutrient starved for 1H (EBSS) prior to fixation. Aurora B is displayed in red. Amplification shows the cytokinetic bridge. A) CI60-GFP and NC59-GFP (a non-binder nanobody) were transfected in HeLa cells B) HeLa cells transiently transfected with CI60-GFP and stained with Atg16L1. Atg16L1 is shown in red. Scale bar=4µm.

Altogether, the presence of CI60 and other autophagic markers (Atg16L1, LC3 and p62) suggest that not only complex II but also complex I could be implicated in some steps of the cytokinesis. Due to time constraint, this aspect of the study was unfortunately not followed but it would be interesting to confirm these data and further investigate the role of CI60 and complex I in cytokinesis.

3.2.9 CI60 is not degraded by autophagy

Co-localisation of CI60 with p62 (3.2.6.1) prompted to address the possibility that the nanobody could be targeted for clearance by the same cellular degradative pathway that it is being studied, i.e. the autophagy pathway. P62 cargoes are usually ubiquitinated and p62 binds them through its UBA (Ubiquitin-associated) domain. It brings them to

degradation by autophagy by its LIR domain, which binds LC3 to the phagophore [109, 250]. To my knowledge, no evidences showing nanobodies being degraded in this manner have been reported. However, I hypothesised that if it was the case, the nanobody would be transported by p62 and therefore should pull down p62 in the IP experiments. To check this, IPs from cell lysates of transfected HeLa cells were performed treated in absence or presence of puromycin, which induces the formation of large cytosolic bodies positive for p62 and polyubiquitinated proteins. I first monitored the presence of p62 and LC3 in the CI60-associated complex in pull down experiments. Neither p62 nor LC3 were detected in the CI60 pulled downs (see Fig. 3.47) suggesting that it is unlikely that CI60 nanobody was being degraded by the autophagy pathway.

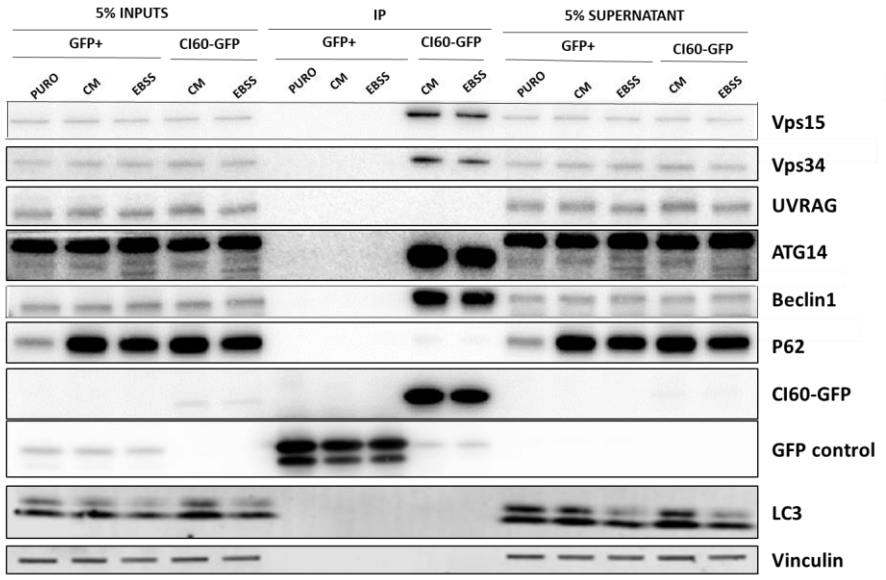

Fig. 3.47. CI60 does not pull down p62 or LC3. WB from the IP using GFP trap. 5% of the input, half of the IP and 5% of the supernatant were loaded. GFP+ stands for a GFP control. Puromycin control (named Puro) were HeLa cells transfected with GFP control and treated with puromycin (5µg/mL) for 2h to have a positive p62 line. LC3 was blotted to checked that induction of autophagy by 1H EBSS was effectively induced. n=2.

To further explore this possibility, IF assays were performed to investigate the presence of polyubiquitinated proteins in the vicinity of CI60. If CI60 was degraded by autophagy, it is likely that it would probably be ubiquitin-tagged, since P62 cargoes are usually ubiquitinated. HeLa cells were transfected with either CI60-GFP or an EV and then treated with puromycin for 8h (5µg/mL), to induce poyubiquitination or Hepes (as vehicle). Cells were stained using antibody (clone FK2) against the

different K29-, K48-, and K63-linked mono- and polyubiquitinylated proteins as reported in [251], and against p62.

As expected, in Hepes treated cells (see Fig. 3.48, top), EV control showed hardly any mono or polyubiquitinated proteins or p62 punctae, whereas after puromycin treatment (see Fig. 3.48, bottom) both punctae (FK2 and p62) were increased. Although in the CI60 transfected and vehicle treated cells, the number of polyubiquitinated proteins increased, their localisation was not at proximity of the CI60 positive punctae. Puromycin treatment seemed to increase the co-localisation of CI60 with FK2 antibody suggesting that CI60 might take part in the autophagy machinery to degrade the polyubiquitinated proteins and p62 bodies.

Overall, this data suggested that CI60 is most likely not being degraded by autophagy, since the co-localisation with the FK2 antibody was only present after the puromycin treatment.

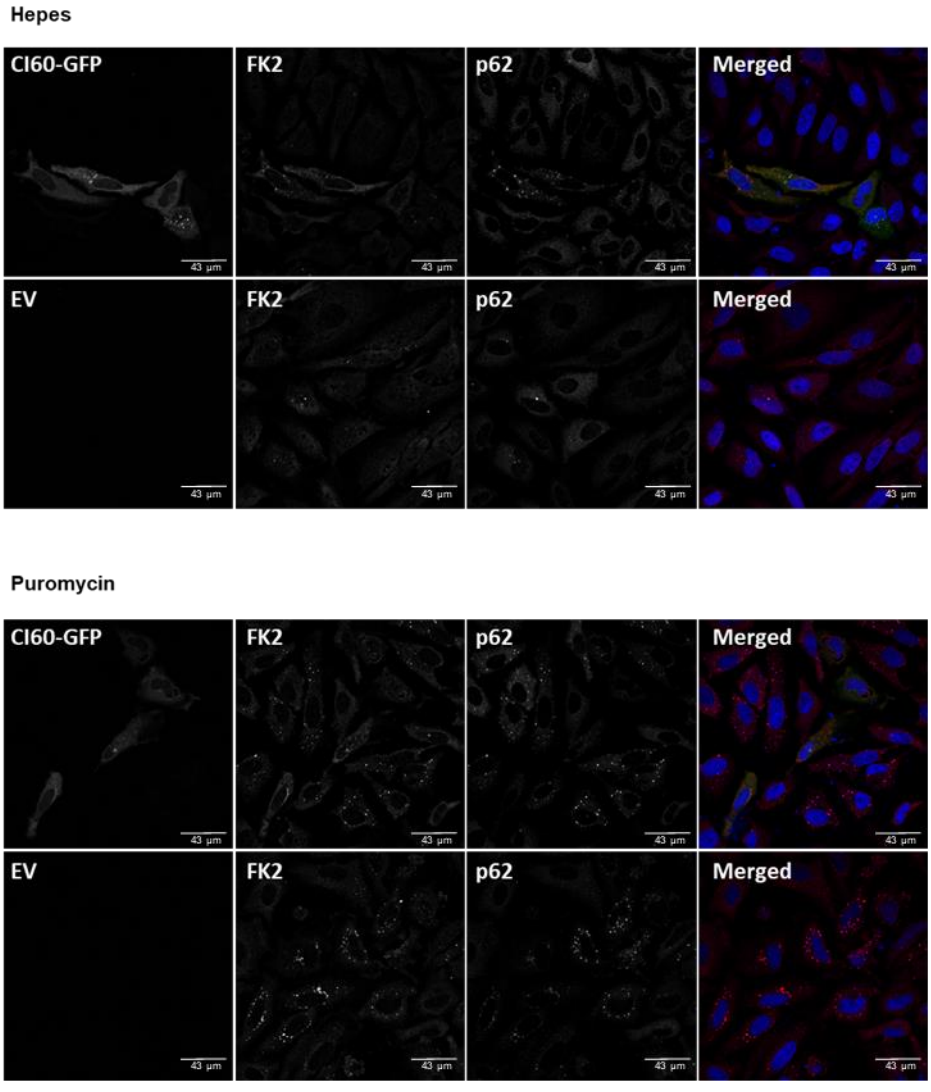

Fig. 3.48. CI60 is not degraded by autophagy. HeLa cells transiently transfected with CI60-GFP or with a pLVX empty vector, and treated for 8h with 5µg/mL puromycin or Hepes (vehicle). FK2 antibody is showed in red and p62 antibody in magenta. Images were taken using a x40 objective. N=2

3.2.10 CI60-GFP overexpression drives cell death

3.2.10.1 CI60 triggers cell death in HeLa and U2OS cells

Transient transfection experiments were challenging due to the low rate of transfection (after optimisation) and the high heterogeneity of CI60 expression in transient transfection. In an attempt to understand the reason behind this, a live experiment was set up. Cells were transfected with either CI60-GFP, NC59-GFP (non-binder nanobody from the same llama immunization) or GFP control, and then, imaged every 15 min for 24 h using an x20 objective. I first noticed that the CI60 nanobody showed an early phase of diffuse cytoplasmic expression just before becoming punctate. Surprisingly, I observed that as soon as CI60-GFP's expression was acquiring this punctate morphology (as assessed by GFP fluorescence), the cell started to die with characteristics of blebbing which is generally associated with apoptosis. This was particularly apparent in cells that were trying to complete cytokinesis. Neither NC59-GFP nor GFP control transfected cells were showing this pronounced cell death in such short time. Somewhat, this observation could explain the low transfection efficiency encountered after transient transfection of CI60, the very low expression of CI60 in stable cell lines, suggesting a counterselection process, and the variety in Ci60 expression patterns observed . Note that this striking effect was observed in complete medium suggesting that CI60 induced cell death might be independent of cellular stress (as of nutrient depletion).

Fig. 3.49 shows a representative summary on CI60 expression and cell death compared with the controls NC59 and GFP control. The medium panel of Fig. 3.49 shows a time frame in which CI60 already acquired its characteristic punctate appearance (2h post-transfection) in contrast to the GFP and NC59 control which showed a more diffuse cytoplasmic expression. The third panel of Fig. 3.49 shows the time frame when the cell start to die with some blebbling features in CI60 treated cells. In the same time frame, both NC59 and GFP control transfected cells were still alive. In HeLa cells the CI60-induced cell death happened at around 4h

after punctae formation. Note that in U2OS cell, this phenomenon was delayed by 3h after punctae formation (see Fig. 3.51). Interestingly, and as mentioned earlier, HeLa cells have a higher autophagic rate compared to U2OS [240]. I speculated that this difference in autophagy flux might explain the faster rate in cell death induction upon CI60 expression in HeLa cells and that the CI60-induced cell death could be related to its role in autophagy. Indeed it has been shown that both activation or inhibition of autophagy could be implicated in the cell death phenotype [252, 253] .

To further elucidate the mechanism of cell death, Z-VAD (a pan- caspase inhibitor of apoptosis), an inhibitor of autophagy induction (VPS34- IN1, a specific VPS34 inhibitor [172]); Bafilomycin A1, (the inhibitor of the lysosomal V-ATPase, which inhibits autophagosome fusion to lysosomes) and an activator of autophagy, Torin1 (an mTORC1 inhibitor), were used to try to rescue the phenotype. CI60-induced cell death was monitored by live imaging after treatment with the aforementioned inhibitors in HeLa and U2OS cells.

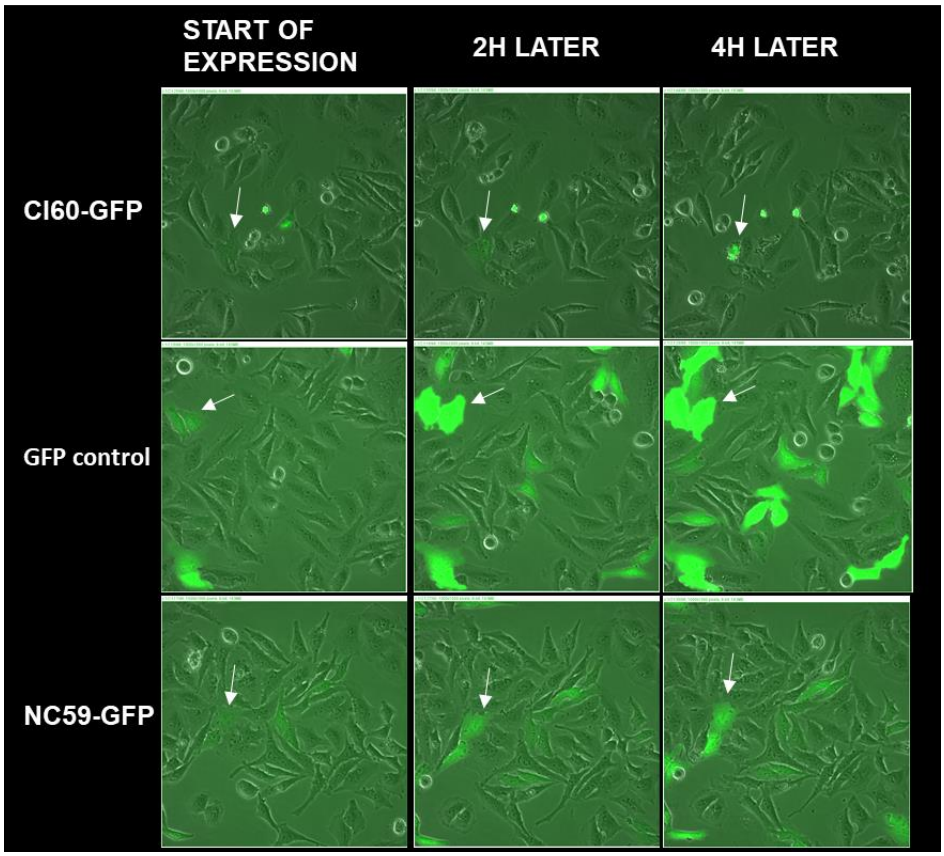

Fig. 3.49. CI60 transfected HeLa cells die within 4H of the onset of expression. HeLa cells transiently transfected with either CI60-GFP, GFP control, or NC59-GFP. Images were taken using a Nikon biostation. Objetive x20.n=3

Live imaging started 3h after transient transfection. Treatment with either IN1 or ZVAD showed a delay of CI60-induced cell death (of around 105 min for IN1, and a 90 min delay with Z-VAD) while no difference were observed in Bafilomycin A1 treated cells. This suggested that CI60 could probably be an activator of autophagy and that the cause of cell death could also be multifactorial, as apoptosis inhibitor can only partially rescue CI60-induced cell death.

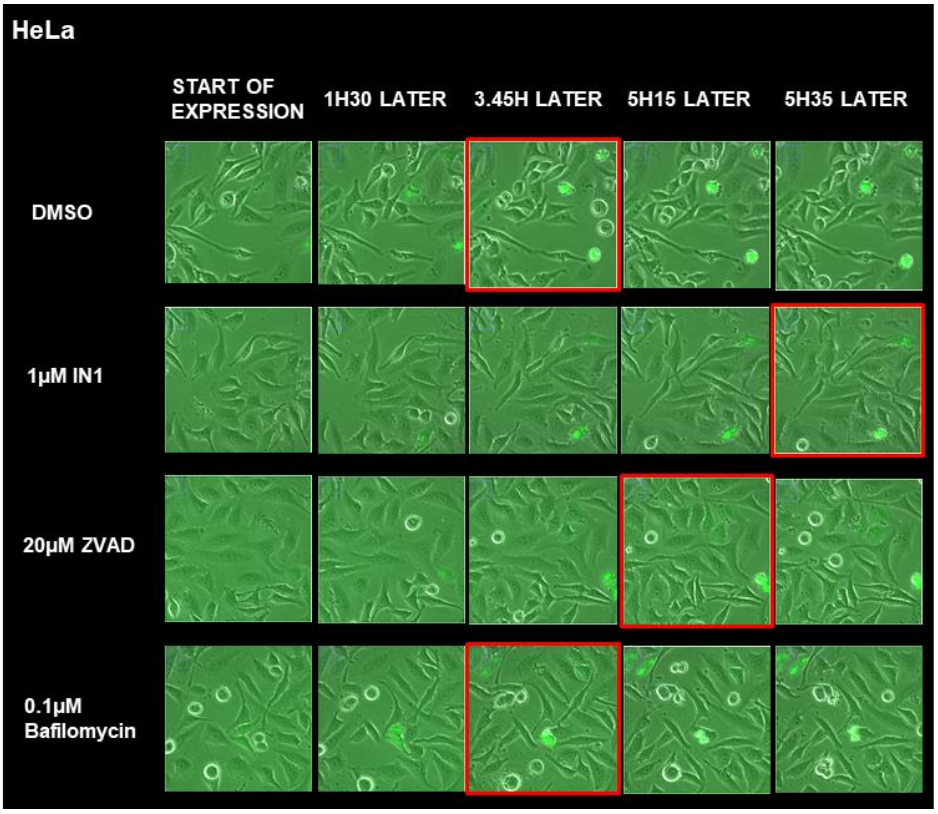

Fig. 3.50. Inhibiting autophagy and apoptosis delays CI60-induce cell death in HeLa cells. HeLa cells transfected with CI60-GFP and treated with different inhibitors at the concentrations indicated in the figure. The red squares mark the onset of cell death. The times above indicate the amount of time after the start of expression. Objective x20. Images were taken using a Nikon biostation.n=3

Similarly, all these rescue effects using the same panel of inhibitors were observed in U2OS cells with subtle differences (Fig. 3.51). Firstly, the rescue phenotype appeared to be stronger than in HeLa cells with a better recovery of all CI60 expressing cells. Secondly, unlike in HeLa cells, Torin1 and Bafilomycin A1 seemed to delay the CI60-induced cell death. This outcome will be discussed later on, but possible explanations may be the cell-specific characteristic of both cells. HeLa cells have a higher autophagic rate and the effect exerted by the inhibitors may be diluted. One of the drawbacks of this method is that it was not quantitative enough. I thus decided to explore the cell death phenotype using flow cytometry.

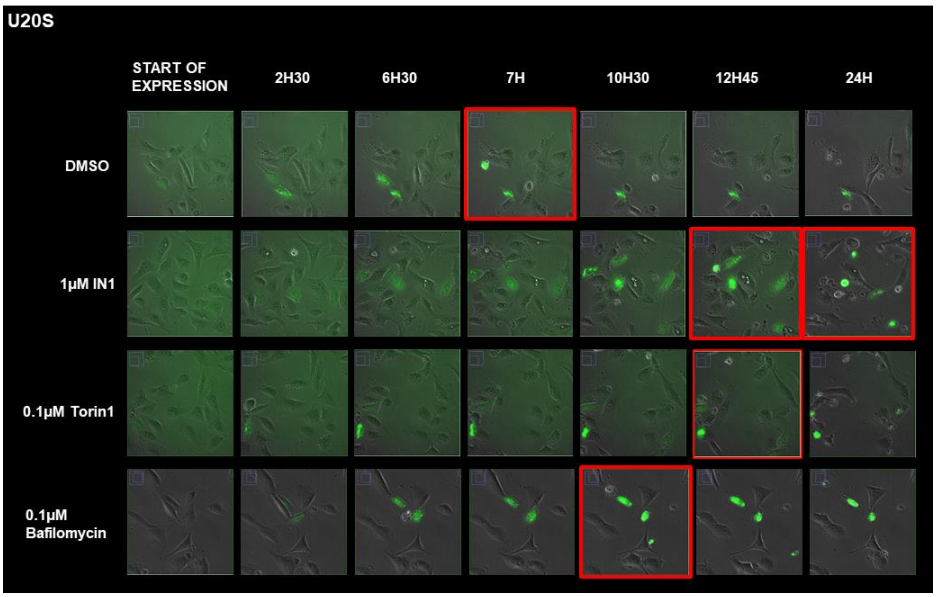

Fig. 3.51. CI60-induced cell death is delayed by 3H in U2OS, compared to HeLa cells. U2OS cells transiently transfected with CI60-GFP and treated with different inhibitors at the concentrations displayed in the figure. The red squares mark the time of death. The times above indicate the amount of time after the start of expression. Objective x20. Images were taken using a Nikon biostation for 24 H.n=3

3.2.10.2 CI60 showed a tendency to increase cell death

To confirm the live imaging observations, flow cytometry based propidium iodide staining was used. HeLa cells were transiently transfected for 12h, 24 and 48h with CI60-GFP or GFP control using pLVX vectors (Fig. 3.52). At different time points (12H,24H and 48H), dead and live cells were collected, stained with propidium iodide (PI), and PI positive (PI+) cells were quantified in the GFP positive population (GFP+). Propidium iodide is an intercalating agent that stain nucleic acids only in membrane-compromised cells, indicative of cell death. At 24H posttransfection, CI60 positive cells already showed a tendency toward increased cell death (p value = 0.0728). At 48H posttransfection, cell death was increased in CI60 transfected cells by almost three-fold compared to control cells.

.

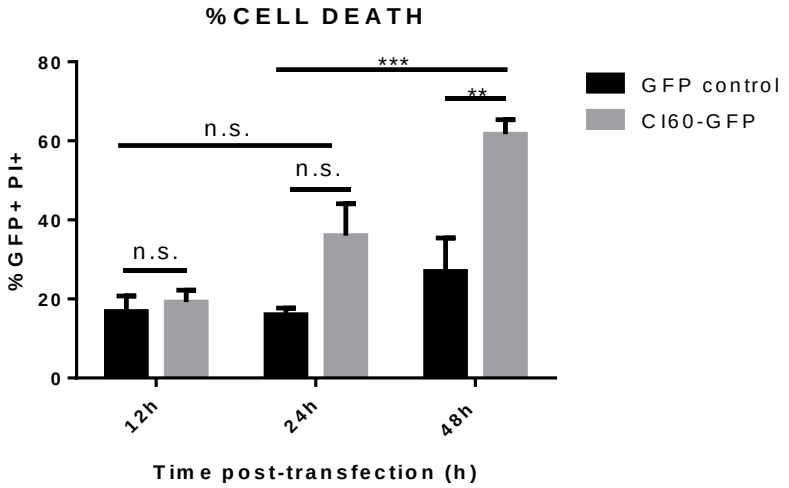

Fig. 3.52. CI60-induced cell death quantified using flow cytometry. HeLa cells were transfected with the pLVX constructs expressing either CI60-GFP or just GFP. Cell death was analysed by flow cytometry selecting GFP positive cells and measuring propidium iodide. n=3 independent experiments. 2-way anova was used to measure the statistical significance, ±SEM.

These results were confirmed using a pEGF N2 backbone plasmid (Fig. 3.53), a smaller size plasmid. BC71 and BC81 are nanobodies from the same llama immunization that CI60 that, as showed here, bind both VPS34 complexes. They were used as controls for two reasons, firstly, to show that this increase in cell death was not related to an overexpression artefact of nanobodies, and secondly, to compare with other VPS34-complex binders for a functional relevance. While these two nanobodies are binding both complexes, BC71 showed an inhibitory effect of both complexes in the *in vitro* characterisation performed by R. William's laboratory using GUVs, and BC81 showed a modest inhibition of only complex II with no effect on complex I. In addition, a BLAST search against ten of the identified nanobodies showed that BC81 contains the longest CDR3 region. I was interested on whether these characteristics had any possible implication in cell viability. Results showed that only CI60 showed an increase in cell death after 48H.

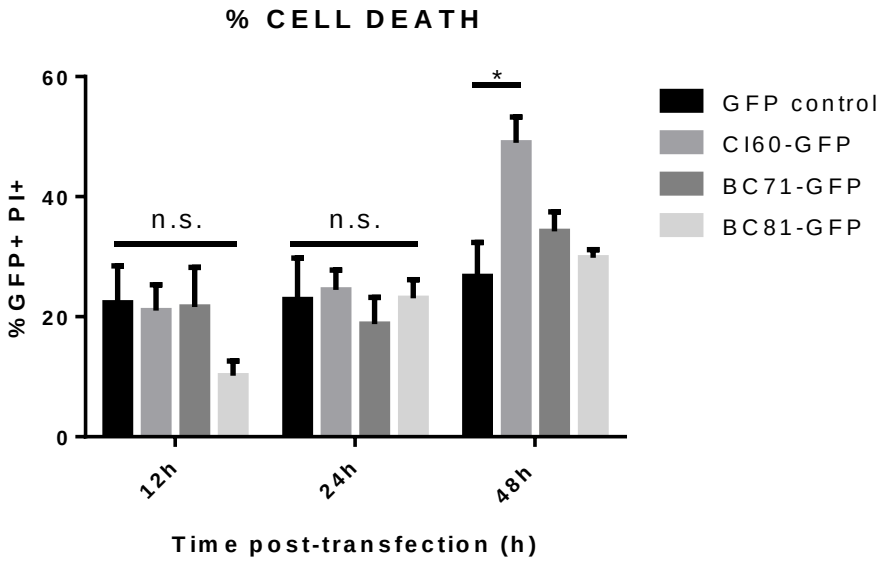

Fig. 3.53. CI60, but not BC71 or BC81, compromise cell survival in HeLa cells. HeLa cells were transfected using pEGF N2 constructs expressing either CI60-GFP, BC71-GFP or BC81-GFP. Cell death was analysed by flow cytometry selecting GFP positive cells and measuring propidium iodide. n=3 independent experiments were performed. 2-way anova was used to measure the statistical significance, ±SEM.

To confirm the results obtained in HeLa cells, I performed similar experiments on different cell types, U2OS (osteosarcoma cells), HCT116 WT (colon cells) and HCT 116 Bax^{-}/Bak^{-}, and U87MG (glioblastoma) cell lines (see Fig. 3.54). HCT116 Bax-/Bak- were used to further confirm the implication of apoptosis in this cell death, as they are defective in apoptosis [254].

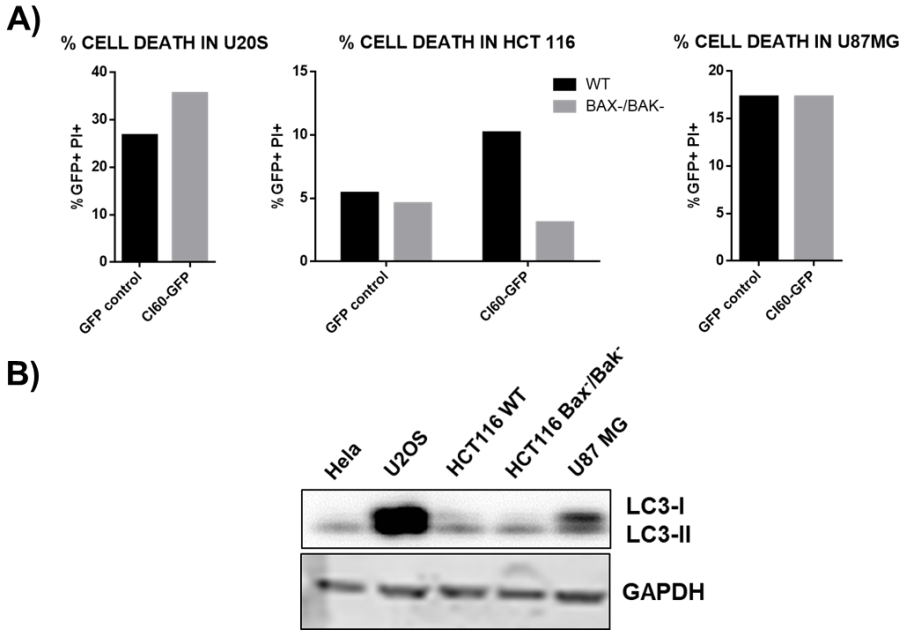

Fig. 3.54. Effect of CI60-induced cell death in different cell lines. A) U2OS, HCT116 WT and HCT 116 Bax^{-}/Bak^{-} and U87MG cells transiently transfected with pEGF N2 constructs expressing either GFP control or CI60-GFP nanobody for 48h. Cell death was analysed by flow cytometry selecting GFP positive cells and measuring propidium iodide. N=1 B) LC3 proportion in basal conditions from cell lysates of HeLa, U2OS, HCT116 WT and HCT 116 Bax^{-}/Bak^{-} and U87MG.

This preliminary experiment showed a differential cell death response to the CI60 expression across the cell types. In U2OS cells, CI60 expressing cells show a slight increase in cell death (to a lesser extent than in Hela cells), whereas in U87MG, there was no difference. More interestingly, HCT116 cells showed a 2-fold increase in cell death in CI60 expressing cells, which was abolished in the HCT116 Bax^{-}/Bak^{-} cells, suggesting that the type of cell death induced by CI60 is dependent of the apoptotic machinery, at least in this cell type. Due to technical problems, this experiment could not be repeated.

As described above, different inhibitors were used to explore the mechanism of cell death induced by CI60 either in the apoptotic process or autophagic process HeLa cells were treated with of IN1 (5µM), Torin1 (250nM), ZVAD (20µM) and Nec1 (50µM), an inhibitor of RIPK1 kinase-mediated necroptosis. At 6h post-transfections, inhibitors were added to the culture. At 48h endpoint, no major changes in cell death were detected upon inhibitor treatment in CI60 or BC81 transfected cells. These results are in sharp contrast with the live cell imaging data described above and will be discuss later (section 4.2.5). Interestingly, there was a small increase in cell death in BC71 transfected cells after IN1 treatment (Fig. 3.55).

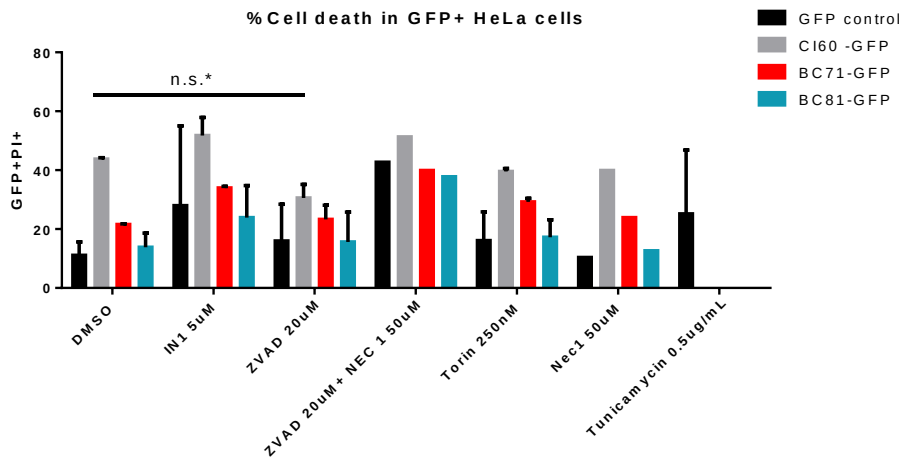

Fig. 3.55. CI60 cell death is only rescued by the pan-caspase inhibitor ZVAD. HeLa cells were transfected for 48h using pEGF N2 constructs expressing either CI60-GFP, BC71-GFP or BC81-GFP.n=2 independent experiments were performed. One-way anova was used to measure the statistical significance of the results. The error bar shows the SEM. Independent two-tail t-test N.s.*: p value=0.0562.

4 Discussion

The goal of this study was to gain further insight into new methods to modulate VPS34 activity. Although VPS34 was discovered 30 years ago, it is only now that we are starting to better understand its mechanism of action, and its biology. The challenges in assessing and manipulating VPS34 activity are mainly raised by two considerations. Firstly, VPS34 exerts its function as part of multiprotein complexes, suggesting that VPS34 has a key scaffolding role in addition of its lipid kinase activity. Secondly, VPS34 forms the core of these different complexes, which places VPS34 at the centre of many regulatory functions of the complexes to maintain cell homeostasis.

The first part of my project involved the cellular characterisation of mVPS34^{DEL21}, a new allele in which exon21 of VPS34 is deleted and that theoretically, gives rise to a truncated and kinase dead VPS34 protein. Characterisation comprised the assessment of the level of expression of this truncated VPS34 version and measuring its lipid kinase activity. The second part of my project was to create a tool to investigate the role of VPS34 within a specific complex. For this, I identified a complex-I specific nanobody from a panel of nanobodies obtained after immunization of llamas with recombinant VPS34 complex I or II. This nanobody, called hereafter CI60, was able to bind the members of complex I *in vitro* and in different cell lines. It also showed specific localisation at cellular sites where VPS34 complex I resides confirming the specificity of this nanobody to this complex. In an attempt to determine whether this nanobody could modulate VPS34-associated complex I activity, I used different means including functional assays that proved to be very challenging. One of the main reason is that this nanobody CI60 caused cell death in a relatively short time upon expression. However, extensive efforts led me to the conclusion that CI60 is a positive modulator of autophagy by activating VPS34 complex I. I investigated the mechanism of action of CI60-induced cell death which remains still elusive and further studies will indeed be required to fully address this question.

4.1 Characterisation of a novel conditional mVPS34 mouse allele

The understanding of VPS34 functions and dynamics has been provided by different studies, many of them in yeast, which depleted VPS34 protein

to understand its functional significance (see section 1.6). Although these studies have helped to gain a deeper insight into the roles of VPS34, they lacked the precision to separate the scaffolding from the kinase function of VPS34.

Depleting VPS34, either by RNAi silencing or by KO models, affects the stability of the different complexes, as loss of VPS34 often dampens the expression of the proteins associated to the complex [161]. This makes it impossible to distinguish whether or not the phenotype observed was due to the loss of VPS34 itself or to the loss of its binding partners. In addition, the deletion strategies would never allow separating the scaffolding role from the kinase function.

The discovery of highly specific VPS34 inhibitors in 2014 paved the way to address some of the above-mentioned issues (see section 1.7). Our laboratory has successfully used the so-called knock-in (KI) strategy for multiple PI3K isoforms [255] in which an inactivating point mutation in the mouse germline supresses kinase activity while preserving its scaffolding role. This approach has been proven successful for all the PI3K isoforms including VPS34. Not only this strategy has the obvious purpose to distinguish kinase *versus* scaffolding effects, but also to address the therapeutic potential of a VPS34 inhibitor. Using this approach, a constitutive VPS34 KI mouse with a mutation in the DFG sequence (a critical motif in the ATP-binding site of VPS34) was created [162]. The aim was to use this mouse model to distinguish kinase *versus* scaffolding effects, and to address the therapeutic potential of a VPS34 inhibitor. This study showed that homozygous KI mice were not viable, and that VPS34 heterozygous KI mice displayed enhanced insulin sensitivity and glucose tolerance, accompanied with a partial protection against hepatic steatosis. It identified VPS34 as a potential drug target for the treatment of metabolic disorders associated with insulin resistance, such as diabetes.

To overcome the use of heterozygous mice, a conditional mouse model was created in which exon21 (encoding a part of the kinase domain) was deleted (this exon was flanked with FloxP sites to allow tissues/conditional Cre-mediated deletion), producing a truncated protein lacking a functional kinase domain and hence kinase dead. This created an in-frame deletion of 25 amino acids of the protein producing a truncated enzyme which, in theory, should be expressed but would lack catalytic activity and thus be kinase dead. This strategy has been previously reported in different

conditional mouse models [8-11] without being fully characterised. The mouse model was characterised by others in the laboratory and collaborators, and this has been discussed later.

I carried out the *in vitro* characterisation of the mutant allele. In order to do so, I cloned the mVPS34^{WT} and mVPS34^{DEL21} deleted cDNA into vectors carrying different N-terminal tagged versions (GFP/HA/6xMyc). Antibodies directed towards the C-terminal end of PI3K inhibit their kinase activity and have been used before the specific inhibitors were available [158]. The preference for the N-terminal tags was thus to prevent an unintended inhibition of VPS34 kinase activity. Overexpression of the mVPS34^{DEL21} mutant in cells showed that the truncation did not affect VPS34 expression when compared to mVPS34^{WT}. Interestingly, live imaging experiments using the GFP-tagged version of mVPS34^{WT} and mVPS34^{DEL21} displayed some subtle differences such that the wild type protein was mostly cytoplasmic, while the truncated mVPS34^{DEL21} expression showed sometimes a punctate pattern.

In vitro kinase activity assays showed that the mVPS34^{DEL21} mutant has a completely abolished lipid kinase activity compared to mVPS34^{WT} confirming that exon 21 is critical for VPS34 activity. Importantly, it has been previously shown that VPS34 activity is higher when associated with complex I or II than when it is free or only bound to VPS15 and Beclin 1. To discard the fact that the inhibition of the kinase activity observed in the mVPS34^{DEL21} mutant was the result of inefficient binding to the members of the complex, I performed co-immunoprecipitation experiments. These studies showed that mVPS34^{DEL21} mutant is able to bind to the complex-associated proteins such as UVRAG, Beclin 1 or VPS15, suggesting that the integrity of the complexes is maintained. This finding also confirms the studies from Miller et al.(2010) and Rostislavleva et al. (2015) [42, 73], whose structural model on the VPS34 structure indicated that the exon21 did not seem to be in direct contact with any region of VPS15.

I further showed that when overexpressed in cells, the mVPS34^{DEL21} mutant displayed vacuolization compared to the mVPS34^{WT} overexpressing cells upon EBSS treatment, very reminiscent to the one treated with the VPS34 inhibitor (IN1) [162, 172]. Moreover, N-terminal tagged VPS34 usually presents a cytoplasmic expression [12], therefore, the big punctae observed in the mVPS34^{DEL21} could correlate with the

presence of larger autophagic structures or endosomes characteristic of an autophagic inhibition often observed in VPS34 deleted cells [248].

As previously mentioned, the KI mouse model expressing mVPS34^{DEL21} was characterised by others using a Cre recombinase under a tissue specific promoter. In all cases, conditional homozygous KI mice were viable regardless of the tissue targeted. The amount of protein expressed from this allele in the different tissues was very variable, ranging from complete loss to no loss. This was in contrast to my observations in HeLa and HEK293 cells where the mutant protein was robustly expressed. Analysis of tissues such as liver (B. Bilanges, unpublished data), kidney [8] , platelets [9], and thyroid [11] showed total or partial reduction of VPS34 expression. However, in pancreas, mVPS34^{DEL21} seems to be stable and expressed at the same level as the mVPS34^{WT} at both mRNA and protein level (F. Ramos-Delgado, unpublished data) and binds to every member of the complexes. As part of a collaborative work with K. Okkenhaug's laboratory who used this allele to generate a Treg specific mouse model (MS in preparation), a proteomic analysis revealed that mVPS34^{DEL21} mutant expression was reduced by 50% in Tregs, along with a reduction of VPS15, Beclin 1 and UVRAG (Courrèges et al. (manuscript in preparation).

This may be due to possible changes in stability of the protein in the different tissues as a consequence of their folding machinery. Tissues have regulatory elements for locus recombination that are not present in other cells and could affect the expression of the truncated protein. In addition, expression and activity of the overexpressed truncated protein was measured short time after transfection, while in tissues it is expressed for longer and the truncated version may be unstable, accounting for its loss of expression after time. This finding also highlights the importance of cell specificity and leaves a way open for VPS34 modulation.

This work will be part of a figure panel in a manuscript in preparation (Courrèges et al.).

4.2 Modulation of VPS34 activity by nanobodies

The second part of this study had two aims (1) to develop a tool to track the specific VPS34 complexes in cells using the high affinity binding

properties of nanobodies and (2) to identify and characterise nanobodies that could potentially act as inhibitors or activators of either complex I or II.

Nanobodies were first described in 1993 [206]. They harbour the full antigen-binding potential of conventional antibodies with the additional advantages of being much smaller (a conventional antibody is around 150 KDa while nanobodies are ~15 KDa), have a big stability, they are able to reach sites that conventional antibodies cannot bind and most importantly, they can bind conformational epitopes on folded proteins with high affinity [208]. Since nanobodies have been broadly used as strong stabilisers in structural biology, and some of them bind their complex of interest in an active conformation [215], it is reasonable to argue that they could as well be used to modulate a complex activity. In fact, this functionality has already been recently explored and let to the discovery of a highly selective inhibitor of the zinc-transporting P_{IB}-ATPase ZntA from *Shigella sonnei* [256].

By immunising llamas with recombinant VPS34 complexes, our aim was to isolate nanobodies that would be able to activate or inhibit the VPS34 associated complex activity. This modulation could be achieved by stabilizing the complex in a specific conformation (previously shown in [257]), or by binding to a particular pocket or binding site, that would eventually alter or favour post translational modifications that are important for the regulation of VPS34 associated complexes, or affect the interactions between the complex-associated proteins.

4.2.1 *In vitro* and cell-based primary screenings identified nanobodies with various binding specificities to the complexes

Nanobodies were produced by VIB and primary screenings indicated that four nanobodies were found to be specific to complex I and six to complex II. From this initial assessment, three different approaches were taken for further characterisation, narrowing down the nanobodies to three for complex I, and two for complex II. Additionally, co-immunoprecipitation experiments using recombinant proteins, and ADP glo assays using Giant Unilamellar Vesicles (GUVs – also called LUVs, L for large) were carried out at R. Williams laboratory to confirm the specificity of the nanobodies and assess whether they modulate the complexes kinase activity,

respectively. The ADP-glo assay measures kinase activity by converting ADP produced in the kinase reaction to ATP, which is measured using luminescence. Unilamellar vesicles are a good model to assess VPS34 activity, since complex I and II are more active when bound to membranes. There are two types of Unilamellar vesicles, SUVs (Small Unilamellar Vesicles) and GUVs. SUVs are around 15-30nm in diameter, while GUVs are low curvature membranes around 100nm. Although the yeast vps34 complex I is inactive on GUVs, the human counterparts have similar activities on GUVs when compared to complex II (personal communication from Y.Ohashi).

Results from the *in vitro* pull down using recombinant proteins confirmed the binding nature of 13 out of 20 nanobodies that were analysed and partially contradict those obtained by the VIB. This might be explained by the nature of the assays (ELISAs *versus* pull downs).

Although using GUVs are more accurate to assess VPS34 complex activity, *in vitro* assays do not take into account the intracellular environment. This means that cofactors or PTMs, which play an important role in the kinase activity of the complexes, are not present in the *in vitro* assays. To overcome this inherent problem of *in vitro* assays, nanobodies were expressed in HeLa cells. The most common methods to introduce nanobodies in cells vary from using purified recombinant proteins that are introduced in cells using charged surface mediated transduction [258], microinjection and electroporation [259], modified reporter proteins at the cell surface that transport them [216], using cyclic cell-penetrating peptides [259] or by transfection of plasmid vectors containing the DNA coding for the nanobody [260]. Transfection of plasmid DNA was an easy method, but to do so, nanobodies needed to be cloned in mammalian expression vectors. Nanobodies were cloned using different tags to evaluate if any of them would affect the binding of the nanobody to the complex. Strep-tag II fused to the nanobodies was used to first check for their expression level and binding affinity in transient transfection. Regarding their level of expression, I was also curious to see whether stress signals such as nutrient deprivation, known also to activate VPS34 activity, would affect the binding specificity and expression level of the nanobodies.

To simplify the nomenclature of the nanobodies, I have named binders to both complexes BC, Complex I-specific binders CI, Complex II-specific

binders CII, and binders to the core complex (VPS34, VPS15 and Beclin 1) C., followed by the last two digits of the VIB nomenclature. For instance, **CA12557** changed to **BC57**.

Both Complex binders (BC)

Four out of nine nanobodies showed binding to both complexes: **BC57**, **BC65, BC71 and BC81**. The fact that they are binders of both complexes would suggest that these nanobodies do not physically interact with UVRAG or ATG14L, nor a region of the complex relevant for the curvature recognition. From these nanobodies, only **BC65** and **BC71** coincide with the binding affinities obtained using non cell-based assays.

Upon EBSS treatment, **BC57** shows a decrease in expression and in its affinity to bind to the members of the complexes, except for UVRAG. It is tempting to speculate that this nanobody may bind with low affinity to a region that is bound by other cofactor or complementary member of complex I, and when a stress signal induces formation of complex I, the nanobody is displaced and degraded. It would also be interesting to know whether this nanobody could bind to pATG14L^{Ser29}, an indicator of activated complex I and thus give an indication on its ability to bind an active *versus* inactive complex I.

It seems that some of the other nanobodies can change their ability to interact with their partners depending on the cellular stress conditions. **BC65** shows higher binding affinity towards VPS15 and VPS34 after nutrient starvation. In this case, HDX-MS could be useful to determine whether these differences depend on their binding region. **BC71** Co-IP showed that after EBSS incubation, the nanobody shifted from being a binder to both complexes to a binder of complex I, as the interaction with ATG14L was stronger in EBSS treatment and lower with UVRAG.

In contrast, **BC81** expression does not change the expression of the complex-associated proteins neither change its ability to interact with specific complex in CM or EBSS. Intriguingly, a BLAST analysis of the sequence of all nanobodies revealed that **BC81** has a longer CDR3 region (hypervariable antigen-binding loops), compared to the rest of the nanobodies obtained from this immunization. The CDR3 loop is the most important antigen recognition region [261], and a longer CDR3 could imply that the recognition ability of this nanobody is higher. These

characteristics also make **BC81** a good candidate for tracking VPS34 complexes.

Complex I binders (CI)

Only two CI specific nanobodies were identified: **CI60** and **CI82**. **CI60** exhibit great affinity for the members of complex I. Interestingly, upon EBSS starvation, CI60 shows a stronger binding towards ATG14L while no changes were observed for **CI82,** suggesting that CI60 interaction responds to environmental stress or to the dynamic changes of the complex I upon starvation.

Complex II binders (CII) and core binders (C)

Nanobodies were raised from two different immunizations, one with purified VPS34 complex I, and the other with purified VPS34 complex II. Unexpectedly, no binders to complex II were found. This may be explained by the lack of flexibility of complex II compared to complex I, which could translate into less epitopes available for the nanobodies.

Surprisingly, two binders of the core VPS34-VPS15-Beclin 1 were discovered: **C85** and **C88**. They were expressed at very low levels in cells. **C85** had been previously shown to be a complex II binder but lack of binding to UVRAG in cell-based IPs ruled this out. Core binders could be interesting nanobodies to use as a biomarker to differentiate VPS34 pools and investigate functions unrelated to complex I and II.

Lastly, **CA12575** has shown different outcomes in the performed assays (binding affinity towards complex I or just the core) and would need further assessment to elucidate its binding affinity.

Assessment of kinase activity using GUVs

Nanobodies from the same immunization are classified into families, which are defined by similarity in their CDR3 region. Members of the same family bind to the same epitope, suggesting that they could, in theory, bind the same complex. If they had different binding affinities, they could have varying effects on the kinase activity of the complex.

Kinase assay were performed *in vitro* with recombinant proteins using GUVs. Members of the same family were not tested, which means that the nanobodies that were tested and have the same binding affinity do not

bind the same epitope, even if they modulate the complex kinase activity in a similar way. This explains the different binding affinities of **BC65** and **BC81**, which inhibit complex II specifically; or **BC71** and **CA12575**, which inhibit complex I and II activity. Intriguingly, **BC71** binds weakly to UVRAG while **CA12575** does not bind to UVRAG at all. In this case, it is tempting to speculate that the absence of binding towards UVRAG could be the outcome of a possible interference with the site of binding (**CA12575** could be competing with UVRAG). However, this is probably the less likely cause of inhibition. For instance, **BC65** and **BC81** were the only nanobodies that showed specific inhibition of complex II, and they could bind both complexes.

BC57 showed a weaker inhibition of both complexes compared to **BC71** and **CA12575,** and **C85** only a modest decrease in complex II specific activity**.** In summary, three inhibitors of complex II and three inhibitors of both complexes were found. It was striking to see that every nanobody that bound to both complexes exerted an inhibitory effect at least on one of the complexes.

Both CI binders showed no change in activity, suggesting that binding of the nanobody to the complex did not compromise structural conformation. They could be used a research tool to investigate/ track complex I in live cell imaging.

Due to time limitation, and the lack of a good control, I was not able to perform kinase assays from cell-based experiments. I found the selection of a good control for these experiments challenging. The most accurate control would have been a mutated CDR3 nanobody, given the CDR3 loop antigen recognition importance [261]. If it was mutated to Ala, the nanobody would not bind to its epitope and would allow to discern results dependent on just expressing nanobodies (in case cell stress was produced by overexpression of an exogenous protein for example) or by the binding to the epitope.

Kinase activity could be assessed by immunoprecipitating complex I (using ATG14L antibody) and complex II (using UVRAG antibody) from HeLa cells. Increasing amounts of recombinant nanobody could be added to the complex I/ complex II and kinase activity of the resulting complexes would be measured.

After this set of nanobodies was characterised, I focused on CI60 because it is a high affinity complex I- specific binder, and assessment and modulation of autophagy is highly relevant in cancer, neurodegenerative diseases and infection. In addition, it was one of the few nanobodies whose binding affinity was stable along the three different techniques by which it was measured, which suggested that it was a good binder. Moreover, upon EBSS treatment, it showed that its binding affinity to ATG14L increased, suggesting that its dynamics coincided with those of VPS34 complex I. Lastly, its binding affinity was further confirmed in stable cell lines, even at low concentrations.

4.2.2 Localisation and effect of CI60-GFP in subcellular compartments

The origin of the autophagosomal membrane has been a controversial issue. Many potential sources includes the ER [86], mitochondria[230], Golgi [262-264], or plasma membrane [265], all of them interacting dynamically with the ER [92]. Therefore, localisation of CI60 to these organelles was checked. Since autophagy is induced upon nutrient depletion, cells incubated in CM or EBSS were evaluated to check if the possible localisation or effects were already observed at basal conditions or depended on autophagy induction.

Localisation of CI60 at the ER was assessed using three different biomarkers for the ER (KDEL signal, Calreticulin and Calnexin). Data indicated that CI60 is localised within the ER, and that co-localisation seemed to increase under starvation conditions, which also increases formation of VPS34 complex I.

Importantly, database search for the presence of any ER signal peptide within the CI60 sequence was negative, dismissing the possibility that CI60 could be targeted to the ER independently of its association with VPS34 complex I. When CI60 localisation at the ER was examined, I noticed that on some occasions, there was a slight increase in the Calreticulin and Calnexin endogenous staining signal. Calreticulin and Calnexin assure the correct folding of proteins that leave the ER and then are transported to the Golgi. Expression and IP experiments would imply that CI60 is correctly folded because it was able to recognise epitopes in complex I (HDX-MS data). However, to rule out induction of ER stress caused by the nanobody, a preliminary experiment to assess expression

of IRE1, one of the three well-characterised stress sensors in the ER was performed. No upregulation of IRE1 by WB was seen (data not shown). However, to dismiss this hypothesis, expression of other ER stress markers such as GRP78, CHOP, XBP1,and ATF4 should be evaluated.

Next, mitochondria was assessed for two different reasons: its implication in the origin of the autophagosomal membrane, and its central role in the cellular metabolism.

No significant co-localisation of CI60 with TOM20 (mitochondria marker) was found, although some close proximity was found between mitochondria and CI60 punctae during starvation.

I observed that there was a noticeable difference between the mitochondria of CI60 transfected cells compared to control cells already at basal conditions. Mitochondria in CI60 transfected cells looked more disorganized (even in low CI60 expressing cells), and their morphology was different from control, varying from a rounder to an elongated/tubular shape. Under starvation conditions, mitochondria have been reported to become tubulated forming a network to avoid engulfment by autophagosomes and provide platforms to originate autophagosomes and maintaining energy homeostasis [266]. This adaptation mainly resulting from the fission/fusion dynamic of the mitochondria is crucial in order to produce the required ATP for maintaining cell survival during periods of stress. CI60 transfected cells under starvations conditions showed an increased perinuclear localisation of the mitochondria and a decrease in their number compared to control cells in EBSS. .

These observations in basal (nutrient rich) and nutrient depleted conditions were quantified using TOM20 staining /cell. Results showed that under complete medium conditions, there were more mitochondria in CI60 transfected cells. Images do not show this increase, but could be reflected by clustering of mitochondria. Upon starvation, there was a decrease in the number of mitochondria in the EBSS condition compared to CM. The relative decrease in EBSS was higher in CI60 transfected cells, where the amount of mitochondria dropped almost by half, compared to the CI60 transfected cells in CM. Decrease upon starvation can be explained by increased mitophagy (mitochondria selective autophagy degradation).

Based on the phenotypic differences observed on mitochondria content, it could be hypothesised that mitochondria may be experiencing higher degradation (mitophagy rate would be higher in those cells). This would explain their changes in morphology as fusion-fission state changes, critical in starvation to induce tubulation [266]. Until very recently, it was generally accepted that Dynamin-related Protein (Drp1) had a key role in this process [267]. However, Yamashita et al. (2016) [268] recently presented a new Drp1 independent model where mitochondrial division occurs concomitantly with autophagosome formation and requires upstream components of the autophagic pathway, such as the ULK1 complex or VPS34 complex I, and therefore could be directly modulated by a VPS34 complex binder.

Altogether, these data suggest that the changes in mitochondria morphology could be due to a higher rate of mitophagy, which would be higher already in complete medium conditions in CI60 transfected cells compared to control. This hypothesis could be further assessed by the use of the pH-sensitive fluorescent protein Keima used by Yamashita et al., (2016) [268] in a CI60-HA inducible model. In a neutral environment, Keima is excited at 440nm, but when present in an acidic environment such as in the autolysosome, it is no longer excited at 440nm but at 590nm. In addition, immunolabelling of CI60 for electron microscopy would help to elucidate whether CI60 affects mitochondria morphology.

To test whether mitochondria were healthy I measured the mitochondrial membrane potential. No changes between controls and CI60 transfected cells were seen, but I noticed a tendency for CI60 transfected cells to maintain polarization of mitochondria under conditions when VPS34 is inhibited with IN1. It is tempting to hypothesise that binding of CI60 to VPS34 complex I prevents the inhibiting action of IN1. The time point used was 48h post-transfection. The application of different time-points, alongside the use of an inducible system, and tetramethylrhodamine (TMRE), which labels active mitochondria, or measuring their respiration capacity and the ATP level could provide more information.

The Golgi apparatus is another possible source of membrane that give rise to the phagophores. Assessing the localisation of CI60 at this organelle had two aims (1) to assess whether complex I has a role at this organelle and (2) to discard potential “off-target” effects of CI60, as it has

been reported that UVRAG depletion triggers fragmentation and dispersion of the Golgi [58].

Confocal microscopy showed very close proximity between CI60 and GM130 (Cis-Golgi staining) without any significant co-localisation. It would be interesting to assess the TGN compartment, since proteins important for autophagy are transported from this compartment as well [269, 270]. In addition, I assessed the Golgi morphology since it dynamically changes depending on the cell cycle phase [237] (often observed in the asynchronized culture). Interestingly, upon starvation, the Golgi morphology in the control cells changed and adopted a compacted form that is usually seen in interphase. Intriguingly, CI60 transfected cells showed the same pattern of Golgi in both CM and EBSS starvation, which could imply that CI60 transfected cells experience a similar metabolic state in both CM and under starvation conditions. The final interpretation on the autophagic activity in CI60 expressing cells will shed some light into this matter (section 4.2.3). Notably, Gosavi et al. (2018) have recently shown that GCC88, a protein specific of the TGN, regulates the transition between a ribbon-like shape closed to the nucleus structure and Golgi mini-stacks. Importantly, the balance in these structures is related to mTORC1 state [238]. A co-staining of CI60 with this marker (GCC88) would therefore indirectly indicate the state of mTORC1 in these cells, a very important regulator of VPS34 complex I.

4.2.3 Effect of CI60-associated complex I on Autophagy

One of my concerns was whether an exogeneous protein such as CI60 could be recognised by the autophagic machinery and degraded. There are several cargo receptors [109], but one of the most ubiquitously expressed is p62. Proteins that are recruited by p62 are usually ubiquitinated. They bind to p62 by its UBA domain and p62 binds to LC3 by its LIR domain. To dismiss the possibility that CI60 could be degraded via p62, I checked if there was a physical interaction between CI60 to either p62 or LC3 by IP. Results confirmed the lack of either of these direct interactions. Next, I investigated whether CI60 may be ubiquitin-tagged by IF. The outcome of this other approach correlated with the lack of binding of CI60 to p62 or LC3. Ubiquitin was in CI60 proximity only after puromycin treatment, which suggested CI60 proximity to the degradation machinery. In addition, degradation by the proteasome is unlikely, since the antibody

that I used to detect polyubiquitinated proteins also detects K-48 linked poly-ubiquitin chains, which are targeted to the 26S proteasome [271]. Altogether, this data ruled out the possibility that CI60 could be degraded by autophagy pathway.

Next, I investigated the possible effects of CI60 in autophagy using the specific autophagic markers LC3, p62 and WIPI2.

As expected, CI60 was found to co-localise to LC3 and p62 (marker of autophagosomes), and WIPI2 (marker of phagophores). This, together with ER co-localisation reported in 4.2.2, confirmed the specificity of CI60 for VPS34 complex I at the cellular level.

HeLa and U2OS cells were used to assess the autophagic flux in CI60 transfected cells because of their different rates of autophagy (basal autophagy is higher in HeLa than in U2OS cells [123]). The assessment on autophagic activity indicated that there was already a difference in complete medium between CI60 and the GFP controls cells in HeLa cells as assessed by the LC3 and p62 staining. In CM, LC3 and p62 punctae were reduced in CI60 transfected cells compared to control and interestingly, correlated with the LC3 punctae number measured in control cells upon starvation in HeLa cells. This data was ambiguous, since a reduction in LC3 punctae can indicate less autophagosomes being produced or more autophagosomes being degraded.

To be able to interpret the result obtained in HeLa cells, starved cells were treated with Bafilomycin A1, an inhibitor of lysosomal fusion. Results showed that autophagosomes were indeed formed in CI60 transfected cells, suggesting that more autophagosomes were produced and degraded, i.e. their autophagic flux was increased. In addition, the effect in CI60 transfected in CM was identical to the EBSS condition, indicating that this increase in autophagy is most likely already observed in CM. To confirm this hypothesis, LC3 punctae number should be measured in cells in CM treated with Bafilomycin A1.

Preliminary results in U2OS cells confirmed that autophagosome formation was not impaired in this cell type either.

Very recently Runwal et al. (2019) [272] reported that autophagy-deficient cells could have LC3 positive structures. These were less frequent in number but bigger in size. To rule out the case in these settings, size of

the particles was measured and it was confirmed that the size in my experiments had not increased to the same extent as it was reported (~4µm^2).

p62 staining was used to complement the data from LC3. In a similar trend to LC3 results, there was a pronounce decrease in p62 punctae in CI60 transfected cells in CM, which was parallel to the decrease observed upon starvation in control and CI60 transfected cells. p62 is a cargo binder present in autophagosomes and degraded at the lysosome. To discern whether this drop in p62 punctae was due to less autophagosomes being produced or more autophagosomes being degraded, Bafilomycin A1 was added to starved cells. Results showed not only was p62 present in starved condition but upon CI60 transfection there was more than a 2-fold increase in p62 punctae.

This suggest that the p62 degradation rate is higher than in control cells and is in line with the increase of p62 observed after Bafilomycin A1 treatment.

Altogether, this data indicate that CI60 expression does not affect autophagosomes formation, and that CI60 expressing cells have a faster rate of autophagic flux, suggesting that CI60 is most likely an inducer of autophagy. Further experiments will be required to further confirm this hypothesis.

To confirm this hypothesis, I also measured the level of autophagic PtdIns3P pools using WIPI2 as a marker. WIPI2 is a PtdIns3P binding protein recruited by VPS34 complex I. WIPI2 positive pools were monitored in complete medium and after 15mins or 1H of nutrient starvation. In HeLa cells, no difference in WIPI2 punctae number was observed between CI60 and control cells in CM. After 15 min of nutrient starvation, an increase in WIPI2 punctae number was observed in control and CI60 transfected cells. Intriguingly while WIPI2 intensity decreased after 1h of starvation in the control cells, this remain unchanged in CI60 transfected cells, suggesting that induction of autophagy might be preserved longer in these cells. Interestingly, U2OS cells show an increase in WIPI2 punctae in CI60 transfected cells compared to control already in CM. This increased after 15 min of starvation, and was maintained for 1hr under these conditions similar to what I observed in HeLa cells.

These data further supports the hypothesis that CI60 positively controls autophagy. Assessment of WIPI2 punctae in inducible cell lines with a homogenous expression of CI60 will help to confirm these findings.

In HeLa cells, further differences were noticeable after Bafilomycin A1 treatment. Control cells showed a 2-fold increase in the number of WIPI2 punctae in the presence of Bafilomycin A1 in CM compared to CI60 transfected cells which maintained the number of WIPI2 punctae. This phenotype has previously been reported [273] and explained by the fact that WIPI2 stays at the autophagosome. This result was striking because it points towards an inhibition of the autophagy, and if this was the case, reduction of LC3 and p62 punctae formation would be observed. An additional hypothesis is that at the lysosomal level, there could be some feedback loop that signals back to the initiation of autophagy machinery and regulates the formation of autophagosomes, as it has been recently reported in some settings [274].

To further confirm the hypothesis whereby CI60 positively modulates autophagy, a recently published marker, the phosphorylated version of ATG16L1, was used as an indicator of newly formed autophagosomes [128]. Preliminary data suggested an increase of phosphorylated ATG16L1 punctae number and intensity in CM and in EBSS in CI60 cells compared to the GFP controls. This will need to be repeated in order to quantify and confirm this result.

Altogether, this data suggest that CI60 is a specific VPS34 complex I binder that activates the autophagy activity of VPS34 complex I. This is further supported by the fact that my observations are very similar to the ones reported for a known autophagy inducer identified by Beth Levine's group called Tat–beclin 1, at least at the 10µM dose [200]. Interestingly, the authors reported a dose dependent of Tat–beclin 1 with lower doses (10µM) that resembled effects seen during starvation (more LC3 and WIPI2 and less p62) while higher dose (30µM) reduced p62 to more than half of that during starvation in HeLa cells.

Upon CI60 transfection in complete medium, lysosome number was not affected, but they seemed swollen in comparison with controls. This was observed in EBSS condition as well, where the number of lysosomes seemed reduced. Since this phenotype was mild, it was difficult to draw final conclusions, but it is striking to note that other inducers of autophagy

such as Tat–beclin 1 (20 μM) [200] increase the number of autolysosomes.

The presence of enlarge lysosomes is one of the hallmarks of VPS34 inhibition [248]. To properly assess lysosome biology, mTORC1 signalling should be assessed as well. Positioning of lysosomes is an indicative of mTORC1 activity [32]. Using LAMP1 staining, I observed that CI60 transfected cells seemed to have their lysosomes more perinuclear, indicative of mTORC1 inhibition. To address this question the mean distance of the lysosomes to the nucleus should be measured, as performed in Marat et al.(2017) [275]. In addition, it is known that mTORC1 activation upon amino acid stimulation is impaired in VPS34 deficient cells [178], therefore, it would be crucial to measure mTORC1 activity (by WB using phosphorylated forms of mTORC1 substrates or kinase assays). It is not clear which VPS34 complex is indeed responsible for mTORC1 activation upon amino acid stimulation.

In conclusion, data in this study indicates that CI60 behaves as an inducer of autophagy. However, the amplitude of this activation remains to be determined in future experiments.

4.2.4 CI60-mediated effects independent of VPS34 complex I

In addition to characterize CI60 function in the complex I specific context, I aimed to assess whether there were any off-target effects in other VPS34 complexes. Firstly, I checked whether other PtdIns3P pools besides the autophagic pool represented by WIPI2 were affected. VPS34 only accounts for 35% of the total PtdIns3P (at least in MEFs, this % may be cell dependent and depend on the nutritional status of the cell) [161]. However, preliminary results using a GFP-2xFYVE^{Hrs} probe in CI60-HA transiently transfected cells and in CI60-HA stable cell lines showed that CI60 expressing cells experienced a decrease in their global PtdIns3P levels, more apparent in cells with higher levels of CI60 levels (i.e. transiently transfected cells). In the CI60 stable cell line changes were less apparent but still present in complete medium where PtdIns3P punctae number decrease but these punctae were bigger as assessed by their size and INTDEN analysis. These unexpected results suggested that even small amounts of CI60 were able to influence global PtdIns3P activity and that CI60 may exert different effects not only in a cell-specific

(based on the difference observed in Hela and U2OS), but also dose-dependent, manner.

These differences may be explained by CI60 having some role outside the autophagic complex. It is possible that CI60 promotes the stabilisation of active complex I over the rest of the complexes, not allowing enough free core proteins (VPS34, VPS15 and Beclin 1) to form UVRAG-associated complex II, thus resulting in its depletion and consequent reduction in global PtdIns3P pools.

However, EEA1 staining experiments suggested that the endocytic pathway is not affected by CI60 expression as no changes in morphology or number in early endosomes was observed in CM or nutrient starvation (EBSS condition). This was surprising taken into account the previous results on global PtdIns3P. This difference may be partially explained by the heterogeneous expression of the CI60 and an inducible model stably expressing CI60 would be the right model for addressing this question. For instance, measuring EGFR degradation (as part of the endosomal sorting pathway) would be informative since it has been shown that VPS34 controls this process [178].

4.2.5 CI60 overexpression drives cell death

Live cell imaging experiments were done in HeLa cells to try to shed some light on the reason behind the low rate of transfection and the heterogeneity of CI60 expression. Surprisingly, I found out that as soon as CI60 started to be expressed in the cells, these would die within 4h, and that most of them displayed a characteristic blebbling, which pointed towards apoptosis as the ultimate mechanism. This could explain both the low rate of transfection in the transient experiments and the low expression of the nanobody observed in the stable cell line.

When HeLa cells were infected to stably express CI60, 80-90% of the cells infected with either version of the nanobody, or 50% of the cells expressing the GFP or 3xFlag tag version, were dead the following day. I also realised that many daughter cells that underwent mitosis would die after the cytokinetic bridge had been formed. Due to limitations in the resolution, it could not be assessed if the daughter cells achieved separation. At the early time points when expression was low, CI60 expression appeared to be mainly cytoplasmic which changed to a

punctate pattern at later time points with increased expression. I repeated the experiment in U2OS cells to determine whether this effect was cell type specific and found that although the pattern of expression and cell death was the same as observed in HeLa cells, the cell death was delayed and happened around 3H later.

Cell death occurred in complete medium suggesting that stress condition was not required for the CI60-induced cell death. Since this cell death was only present in CI60 expressing cells and not in other nanobody expressing cells and given that CI60 is a complex I binder, it is tempting to speculate that CI60 induced cell death occurs through regulation of autophagy.

Other argument towards this hypothesis was that U2OS have a lower autophagic rate compared to HeLa cells and this could explain the difference in cell death induction between these two cell lines.

Flow cytometry was used to compare cell death at different timepoints (12, 24 and 48H) in HeLa, U2OS, HCT116 (colorectal carcinoma cells), HCT116 Bax^{-}/Bak^{-} (apoptosis deficient) and U87MG cells (glioblastoma cells) and showed that CI60 effect is cell-type dependent. Importantly, these cells have different rates of autophagy. U87MG cells have been reported to die upon inhibition of autophagy [276, 277] and they have lower autophagic flux than the rest of the cell lines by comparison of LC3-I *vs*. LC3-II in these cells under basal conditions. Interestingly, I noticed that the rate of CI60-induced cell death was higher in cell lines that have high rate of autophagy. For instance, in basal conditions, HeLa cells, which have the highest rate of autophagy from the tested cell lines, showed a rapid induction of cell death upon CI60 expression compared to U87, a cell line that have a much lower rate of autophagy and did not show any cell death by CI60. Altogether, these data suggested that cell death correlated with the intrinsic level of basal autophagy and supported the hypothesis that autophagy was responsible for CI60-induced cell death. In addition, cell death was rescued in the apoptosis-deficient HCT116 cell line. Implication of the crosstalk between apoptosis and autophagy will be discussed in the following section.

Using live imaging, cell death was observed already after 4h of the onset of CI60 expression, which translated to ~15-20h post-transfection. Using flow cytometry the most noticeable difference in cell death was observed

after 48H post-transfection. The median of the GFP intensity was calculated for the 24h timepoint in all the samples to understand this particularity and results showed that the intensity of the GFP control was very high, to the point where it drives high toxicity. However, the intensity of the CI60-GFP nanobody was quite low and it triggered the same amount of cell death as the control. This could explain the discrepancy between the flow cytometry and live cell imaging data.

Lastly, inhibitors were used in HeLa cells to explore different mechanism of cell death. Flow cytometry data showed that cell death in CI60 was only partially recovered with the use of ZVAD, a pan-inhibitor of caspases. This correlates to the data obtained using live imaging and with the result observed using the apoptosis deficient HCT116 cell line, in which CI60 failed to induce cell death. These experiments should be repeated using an inducible cell line to assure homogeneity of results.

Based on the data presented on this study, it is fair to conclude that CI60 is a specific binder of VPS34 complex I and inducer of autophagy. Although autophagic cell death has been controversial over the years [252], Liu et al. (2013) [253] recently showed that inducers of autophagy such as autophagy-inducing peptides, starvation, or cerebral hypoxia–ischemia prompted a unique cellular death that they termed autosis and that depends on the cellular Na^+, K^+-ATPase.

Similar to the autophagy-inducer peptide Tat–beclin 1 described by Beth Levine's group [253], CI60-induced cell death seemed to be dose dependent. Low levels of CI60 expression are relatively well tolerated by the cells, whereas high levels trigger cell death. Data from flow cytometry experiments suggested that cell death was dependent on the rate of the basal autophagy of the individual cell lines. ER and mitochondria in cells treated with Tat–beclin 1 looked abnormal, similar as well to what was observed with CI60.

However, unlike CI60, Tat–beclin 1 induced autosis was not rescued by ZVAD treatment (even at high concentration), or in Bax^-/Bak^- MEFs, indicating that autosis is a cell death mechanism independent of apoptosis. Moreover, in Tat–beclin 1 treated cells no cleaved caspase 3 was observed, and cells that were dying were adhered to the surface instead of floating (like I observed with CI60) and there was increased presence of vacuoles.

Therefore, I partly ruled out autosis as the main cause of CI60-induced cell death. Electron microscopy of cells expressing CI60 could shed some light on the similarities with this process. Autosis can be rescued with the used of glycosides. Treatment of CI60 expressing cells with cardiac glycosides such as digoxin could thus help to distinguish the importance of autosis in CI60-induced cell death.

Inhibition of apoptosis reduced CI60-induced cell death. The most obvious link between apoptosis and VPS34 complex I is Bcl2. Bcl2 family are important regulators of the intrinsic pathway of apoptosis. Briefly, apoptosis is controlled by two main pathways. The extrinsic pathway triggers activation of death receptors at the plasma membrane that bind their ligands and sets off a cascade of caspase activations that starts with activation of caspase 8, which in turn activates caspase 3 and 7, which will promote cell death. The intrinsic pathway is activated by different stress signals such as ER stress or DNA damage. Pro-apoptotic factors released from the mitochondrial outer membrane triggers the pathway which results in other cascade of caspases this time initiated by caspase 9. Bcl2 family proteins regulate this later branch of apoptosis [278]. At the ER, Bcl2 binds Beclin 1 and prevents its binding to VPS34 complex I [45]. In their study, Pattingre et al. (2005) showed that Beclin 1 mutants that cannot bind to Bcl2 promote caspase-independent cell death. The binding of Beclin 1 to Bcl2 is disrupted by phosphorylation of Beclin 1 by JNK1 [279] and DAPK [244]. It would be interesting to check the state of JNK1 phosphorylation sites in Beclin 1, since DAPK site was tested and it was phosphorylated. When Beclin 1 binding is disrupted from Bcl2, other pro-apoptotic proteins are still bound to Bcl2, but if stress is maintained, they finally dissociate and apoptosis is activated. This is a very attractive way to explain the CI60 induced cell death, at least partially, as seen by the improvement in cell survival upon inhibition of apoptosis. It could be hypothesised that CI60 stabilises VPS34 complex I in an active state and therefore Beclin 1 is not able to bind Bcl2. To prove this, Beclin 1 and Bcl2 IPs should be performed in the presence and absence of CI60. CI60 inducible expression would facilitate the realization of these.

Importantly, two of the organelles that harbour Bcl2, ER and mitochondria, showed certain signs of being compromised. Since ER stress and mitophagy could also be implicated in the phenotype and the resolution of confocal microscopy was not enough to properly assess the state of both

organelles, higher resolution microscopy such as electron microscopy should be used in future experiments.

Although Bcl2 involvement partially explains the cell death phenotype, it does not explain some of the results. When IPs using UVRAG antibody were performed in the CI60 stable cell lines, less VPS34, VPS15 and Beclin 1 were bound to the stable CI60 cell lines than to the parental HeLa control. The coiled-coil domain in Beclin 1 is the region where ATG14L, UVRAG, Bif1 and Rubicon engage in the complex [229], a region that is strongly exposed after binding of CI60, according to our HDX-MS results (later explained). When affinity to Beclin 1 was measured, Li et al. [229] showed that UVRAG binds with higher affinity than ATG14L. Therefore, it is surprising that UVRAG pulled down less members of the complex in CI60 stable cell lines than in the parental line. Finally, when McKnight et al. [280] studied Beclin 1 KO, they reported that HeLa cells devoid of Beclin 1 had a huge decrease of complex II activity.

Altogether, it is tempting to suggest the possibility that CI60 might stabilise VPS34 complex I in an active conformation, and that this stabilisation would sequester the rest of the members of the complexes, preventing the formation of a VPS34 complex II containing UVRAG, which would provoke an imbalance between VPS34 complex I and II functions. This would be highly dependent on the amount of nanobody expressed, and could possibly explain the striking observed phenotypes such as drop in global PtdIns3P levels, the large lysosomes, which are usually seen after autophagy inhibition, and why many cells visualised in the videos seemed to die after trying to complete mitosis, or the reason why CI60 transfected cells stained for GM130 seemed to be in interphase. In addition, it complements the previous hypothesis of Bcl2 involvement and some of the induction of autophagy observations, as well as explaining why only cells expressing low levels of CI60 survive. A multifactorial cause of death would explain the early onset of the cell death onset. To note, Munson et al. [58] reported cell death in HeLa cells after 8h in cells depleted of UVRAG.

To further test my hypothesis, kinase activity assays using complex II obtained from a UVRAG IP could be performed in presence or absence of the nanobody to determine whether presence of the nanobody impacts complex II activity. Moreover, cellular processes involving complex II, such as EGFR trafficking could be examined. AMPK activation after

glucose starvation in U2OS cells could be measured (UVRAG KO does not show activation of AMPK in that setting [281]), or CI60 K_D could be measured, to see if it would actually outcompete UVRAG binding.

mTORC1 is upstream of VPS34 complex I, but downstream of other VPS34 complex, and if CI60 is “sequestering” VPS34 partners, it could therefore have some negative impact on mTORC1 pathway. mTORC1 phosphorylates UVRAG, and using phospho UVRAG antibodies [58] in cellular lysates from cells expressing CI60 would assess if this activation is prevented. HDX-MS using complex II instead of complex I would definitively confirm the specific binding affinity of CI60 to complex I.

Finally, the use of an inducible cell line to confirm the dose-dependent effect of CI60 in induction of autophagy would be crucial. This would define a window for a dose that would stimulate autophagy without necessarily provoking cell death.

4.2.6 Mapping of the contact sites using HDX-MS

The HDX-MS used in this study was one of the most powerful approach to confirm and map the interaction of CI60 with VPS34 complex I. To interpret HDX-MS, the complex I bound to CI60 was compared to the complex I with no nanobody (apo complex). In this comparison, different regions showed up: protected and exposed. Protected regions found in the complex-associated proteins can be the result from the direct contact of CI60 in those regions, or an indirect conformational change of the complex rendering this site less accessible. In contrast, exposed regions represent regions that became accessible upon CI60 binding. Results showed that CI60 binding protected regions within three proteins: VPS34, VPS15 and ATG14L whereas exposed regions are found in VPS15, ATG14L and Beclin 1.

The data suggested that CI60 may bind at the base of the complex and more specially at the hinge where conformational changes occurs to open and close the V-Shape structure of the complex in order to adapt to membrane curvature.

Region in ATG14L- The most protected region in the complex is the linker region between ATG14L’s coiled-coil domains, which may weaken the CC1 interaction between Beclin 1 and ATG14L. The CC1-CC1 linker may act as a hinge that would affect the flexibility of the complex thus affecting

the curvature depending binding. It is not clear at the moment whether CI60 interaction would modify this flexibility. The fact that no changes in kinase activity on GUVs were observed in presence or absence of CI60 suggest that the CI60 interaction does not close further the V shape of the complex, otherwise a reduced activity would have been detected on GUVs. High curvature vesicles (i.e. omegasomes or phagophores) would be able to bind, but binding to lower curvature membranes (i.e. expanding/matured autophagosomes) could be affected. However, the assays using GUVs showed that this was not the case.

In addition, there is also a region of exposure upstream of the linker, at the CC1 domain of ATG14L. Interestingly, this CC1-CC2 linker region is in close contact with the CC1 domain of Beclin 1, which has been also found more exposed after CI60 interaction using HDX. This suggests that the nanobody binds to the linker between CC1 and CC2 of ATG14L, which may weaken the CC1 interaction between Beclin 1 and ATG14L and potentially affect the flexibility at the hinge of the complex.

Unfortunately, the status of the CC1-CC2 linker in Beclin 1 could not be assessed because peptides in that region were not covered. Moreover, NRBF2 binds to the N-terminal end of the coiled-coil domains of ATG14L and Beclin 1 at the base/hinge of the complex [282]. IPs have shown that this partner is indeed found in the complexes with CI60, suggesting that NRBF2 recruitment to the complex is not affected by CI60. Altogether, we speculate that VPS34 complex I could be stabilised by CI60 in a conformation that could favour the binding of complex I to high curvature membranes.

Regions in Beclin 1- As mentioned above, the CC1 region of Beclin 1 was found more exposed and no other regions in Beclin 1 were found to be protected suggesting that CI60 is unlikely binding Beclin 1. Nevertheless, the regions closed to the CC1 domain can be subjected to indirect conformational changes as well. Interestingly, just upstream of Beclin 1's CC1 region lies the BH3 domain by which Bcl2 binds to Beclin 1. This domain is particularly important because Bcl2 – Beclin 1interaction prevents Beclin 1 to bind to VPS34 complex I and thus prevents autophagy activation [283]. To address this question, a Beclin 1 and Bcl2 co-IP in cells expressing CI60 should be performed and it should be assessed whether the presence of CI60 disrupts the Beclin 1-Bcl2 interaction.

In addition, binding of Dapper1 to the complex could also be altered. Dapper1 is a nucleocytoplasmic protein that was identified to negatively regulate Wnt signalling [284], but promotes VPS34 complex I binding and enhances its activity by binding ATG14L and Beclin 1 in the region exposed by CI60 [69].

Regions in VPS34 – The HDX-MS revealed that the CBR1 loop in the C2 domain of VPS34 is protected, and Rostislavleva et al.(2015) [42] showed that in yeast complex II, this loop contacts VPS38 (the yeast homolog of UVRAG). There are no high resolution human structures of complex I/II available so we cannot assure that UVRAG binds to this region as well, but if this binding is conserved in human, it is very much possible that the presence of CI60 on that region would prevent the recruitment of UVRAG. This competition model could explain the specificity of CI60 for complex I over complex II.

Regions in VPS15-. Protected regions were located in the helical domain of VPS15, where the CBR1 in VPS34 and the linker between CC1 and CC2 in ATG14L are gathered, and where no PTMs, mutations or binding of additional partners have been reported. However, exposed regions were found in the WD40 domain. This domain is particularly important for GTP-Rab5 interaction with complex II and binding of PAQR3, a positive regulator of VPS34 complex I [43]. A possible scenario to test could be that this weak exposure could facilitate the interplay between these effectors, potentially enhancing VPS34 activity in complex I.

Potential implications in PTMs in VPS34 complex I

Importantly, the protected and exposed regions observed upon CI60 interaction can allosterically affect the accessibility to post-translational modifications (PTMS) occurring in VPS34 complex I. Protected regions are possible regions where CI60 may bind, but also regions that are no longer available for PTMs, while the exposed regions could allow a higher frequency of PTMs.

Based on my cell based functional study showing a potential role of CI60 in inducing autophagy, I wondered whether this modulation could result from changes in the 3D structure of VPS34 complex I by CI60. Thanks to the HDX-MS we discovered that CI60 binding modified the exposure of certain regions of the complex I-associated proteins. I aimed to investigate whether such regions contains residues that have a particularly important

regulatory function for complex I activity (for instance as being subjected to known PTMs).

PTMS in ATG14L- One of such residues is the Ser29 in ATG14L. CI60 binding exposed the CC1 region of ATG14L (residues 66-98) very close to Ser29, which is phosphorylated by ULK1 and participates in VPS34 complex I activation [52]. I found that pATG14^{Ser29} was increased upon EBSS starvation in both control and CI60 transfected lines confirming that autophagy induction increase pATG14^{Ser29}. IP experiments showed that CI60 binding did not interfere with the phosphorylation of ATG14L suggesting that the potential change in conformation most likely did not abolish activation of VPS34 complex I by ULK1. It would be interesting to assess whether this binding is actually promoted.

PTMS in Beclin 1- There are no PTMs reported within the residues found exposed by HDX-MS. However, exposed regions are surrounded by inhibitory PTMs (the N-terminal of Beclin 1 harbours sites for PTMs that tend to be activatory while the rest of the proteins display sites for inhibitory PTMs [43])., One of these residues is Thr119 in Beclin 1. Dissociation from Bcl2 is a crucial step for Beclin 1 to bind VPS34 complex I, and it is achieved by DAPK phosphorylation of Beclin 1 at Thr119 [244]. To assess whether CI60 was interfering with this binding, IP using a Beclin 1 antibody was performed in CI60 and GFP transfected cells. The data show that phosphorylation of Beclin 1 at that site is not prevented by CI60, indicating that Beclin 1 can still be dissociated from Bcl2. To properly confirm this finding, a GFP trap assay such as the one performed for pATG14^{Ser29} should be done. Pull down of CI60 would clarify the amount of Beclin 1 that is bound to complex I in CI60 transfected cells and whether there is any change in its level after autophagy induction.

Regarding VPS34 and VPS15, no PTMs have been described within the protected/exposed residues. However, it would be interesting to assess if kinase consensus motifs are present within the new exposed motifs that could alter the activity of the complex.

Altogether, the HDX-MS data together with the pull downs assays strongly suggest that CI60 does not have any inhibitory effect on VPS34 complex I as most of the interactions and PTMs have been preserved upon CI60 binding. In line with the autophagic activity assays performed in cells, I speculate that CI60 is an autophagy activator. From the HDX-MS

analysis, it can be hypothesised that, by interacting in the hinge region of the complex I, CI60 would stabilise the complex in closed conformation with less flexibility to low curvature membrane binding, thus conferring a specificity property of CI60 to bind specifically complex I over complex II.

4.2.7 Potential uses of CI60

I identified CI60 nanobody as a specific binder of VPS34 complex I. The outcome of this study brought some relevant questions regarding the use of such nanobody. Since certain diseases rely on autophagy, either to progress or to regress, some of these disease models would considerably help to test the modulatory function of CI60.

Inducers of autophagy have been actively studied during the last years. Many beneficial effects have been observed in different disease models, ranging from cancer, neurodegenerative or immune diseases, lifespan extension or aging [14].Importantly, the effects shown by CI60 mimicked starvation-induced autophagy, suggesting that induction of CI60 could improve situations where physiological levels of autophagy have dropped such as tumour initiation, during infection, ageing, cardioprotection and, although controversial, autoimmune diseases [82].

Cancer

The relationship between autophagy and cancer is complex and often a subject of debate. While some studies suggest autophagy has tumour suppressor functions, others suggest that it may promote tumour growth [82]. This complex interplay very much depend on the type of cancer and the context. The general picture depicts autophagy as a tumour suppressor in the context of cancer initiation whereas it is considered as pro-tumorigenic for tumour maintenance as tumour cells seem to rely on autophagy to promote cell growth and proliferation [16]. Indeed, it has been shown that autophagy competent cells improve anti-tumour immune surveillance and promotes chemotherapy response after induction of autophagy [285]. However, this needs to be studied carefully, since the genetic background within the cancer type is important. For instance, presence or absence of p53 determines whether inhibition of autophagy prevents the formation of high-grade pancreatic intraepithelial neoplasia or accelerates tumour growth, respectively [286]. Induction of autophagy in the latter case could slow tumour growth and could be one of the settings where CI60 could be applied.

Neurodegenerative disease

KI mutations in Beclin 1 that diminish its Bcl2 binding (and induce autophagy) have shown to have many advantages, such as protection against Alzheimer's like disease and HER2-mediated breast cancer, and extended life and health span [287-289]. If CI60 is confirmed to be an autophagy inducer, any of these models could open new interesting ways to use CI60. In the context of neurodegenerative diseases as well, Winslow et al. [290] reported that overexpression of α-synuclein, which occurs in Parkinson disease, inhibits autophagy in the early stage of autophagosome formation. Besides, autophagy inhibition increases the production of aggregates (called Lewy bodies in Parkinson disease). Although the authors postulate that this inhibition is Rab1 and ATG9 dependant, it is appealing to speculate that treatment with CI60 could alleviate this inhibition and potentially decrease the formation of Lewy bodies. Other neurodegenerative diseases, such as Huntington's disease, could also benefit from an activation of autophagy [291].

Bacterial Infection

The autophagic machinery eliminates cytoplasmic bacterial infections in a selective form of autophagy called xenophagy. These bacteria have evolved mechanisms to escape from this primary innate immune system barrier. Activators of autophagy ameliorate the resistance to the infection of the host while dampening the growth of bacteria [82].

Other applications

Importantly, if CI60 turns out to be only a specific binder and not a modulator, the use of CI60 can be useful to confirm certain controversial functions of VPS34 complex I. CI60 could be used as a biosensor for VPS34 complex I. This can be done in several ways. If purified as recombinant protein conjugated to a fluorophore, it can be used as a probe on fixed cells and would be used to uncover complex I specific functions (chromobody), or if transfected in cells, it could trace complex I to study its dynamic upon certain conditions. An example of this is the observation of complex I role in cytokinesis. I repeatedly observed the nanobody in the cytokinetic bridge, as well as other autophagic markers such as LC3, p62 or ATG16L1. The role of VPS34 complex II in cytokinesis has been confirmed [55, 154] but the role of VPS34 complex I is yet to be explored. While some studies report that autophagy is

impaired during mitosis [156], few have focused on a possible role of VPS34 complex I in the degradation of cytokinetic machinery [155].

Future perspective

If CI60 is proven to be an inducer of autophagy, long term strategy would be to screen for an allosteric small molecule that would mimic CI60 interaction to VPS34 complex I at the same contact site. Such screening can be done using DNA- encoded libraries that contain a collections of small molecules covalently attached to DNA tags.

Of note, if the screening of nanobodies were to be done again, immunization with recombinant complex I or II locked in an active or inactive conformation would increase the possibilities of finding a modulator of the activity of VPS34 complex I or II.

5 Appendix

Table 5.1. Major phenotypes of mice with targeted class III PI3K genes

	Target tissue	Mouse model	Viability	Major phenotypes	Reference
VPS34	**global**	Meox-Cre (epiblast)	Lethal between E7.5 and E8.5	Early embryonic lethality with severely reduced cell proliferation. Heterozygous mice show no overt phenotypes.	[292]
		VPS34 kinase-dead knock-in	Lethal between E6.5 and E8.5	Heterozygous mice are viable, healthy and display a robustly enhanced insulin sensitivity and glucose tolerance.	[162]
	heart	mck-Cre	Post-natal lethality between 5 and 13 weeks	Cardiomegaly	[178]
		mck-Cre	Post-natal lethality between 11 and 15 weeks	Hypertrophic cardiomyopathy. Accumulation of $CryAB^+/desmin^+/p62^+/K63pUb^+$ aggregates.	[293]
	liver	Alb-Cre	Post-natal lethality at 1 year	Hepatomegaly and hepatic steatosis, increased liver protein content, lack of glycogen deposition.	[178]
	skeletal muscle	Ckmm-Cre (creatine kinase)	Post-natal lethality between 4 and 9 weeks	Muscular dystrophy and severe dilated cardiomyopathy.	[294]
		Acta1 -Cre	Post-natal lethality at 14 weeks	Mild myopathic abnormalities. Exacerbates the Mtm1 KO phenotype.	[295]
	kidney	Nphs2-Cre (podocyte)	Post-natal lethality between 3–9 weeks	Rapid podocyte degeneration and early-onset glomerulosclerosis, proteinuria.	[296]
		Pax8-Cre (proximal tubular cells)	Post-natal lethality at 4 weeks	proximal tubular cell vacuolation and intracellular sequestration of megalin.	[8]

	Target tissue	Mouse model	Viability	Major phenotypes	Reference
		Podocin-Cre (podocyte)	Post-natal lethality at 9 weeks	Severe kidney lesions, with severe glomerulosclerosis. Renal tubular dilation, severe proteinuria, and mild to moderate interstitial inflammation and fibrosis	[297]
		Wnt4-Cre and Pax8-Cre (proximal tubular cells)	Post-natal lethality at ~2 weeks	primary mislocalization of apical membrane solute carriers and endocytic receptors (resulted in early Fanconi-like syndrome), lysosomal alterations and ineffective autophagy	[10]
	white adipose tissue	Fabp4-Cre	Viable	Improved glucose tolerance and reduced adiposity in middle and old age mice. Adipose tissue browning.	[298]
	retina	Rhodopsin-Cre and iCRE-75 (retinal rod cells)	Viable	Rapid rod cell degeneration. Retinas have an increased number of apoptotic cells.	[181]
		MLR10-Cre	Viable	Congenital cataract and microphthalmia.	[299]
		Pcp2-Cre	Lethality before 10 months of age	Selective death of ON-BCs; aberrant accumulation of LC3, p62, and ubiquitin membranes, accumulation of Rab7 endosomes, and accumulation of lysosomes. Severe and progressive ataxia.	[300]
	megakaryocyte / platelet	PF4-Cre	Viable	Impaired thrombus formation, aggregation, granule secretion.	[301]
		PF4-Cre	Viable	Mild microthrombocytopenia and platelet granule abnormalities.	[9]
	Schwann cell	myelin protein zero (P0)-Cre	Viable	Severe hypomyelination in peripheral nerves. Unsteady gait, hind limb weakness, and tremor. Defective myelination in VPS34 mutant nerves.	[302]
	immune system	Lck-Cre (T cell)	Viable	T lymphocytes exhibit increased apoptosis and reduced IL-7Rα surface expression.	[180]

	Target tissue	Mouse model	Viability	Major phenotypes	Reference
		CD4-Cre (T cell)	Viable	Inflammatory wasting syndrome characterised by weight loss, intestinal inflammation, and anemia at 18 to 24 weeks.	[303]
		CD4-Cre (T cell)	Viable	T cell lymphopenia. Reduced number of T cells but normal T cell development. Impaired autophagy in T cells.	[179]
	nervous system	CaMKII-Cre (hippocampus, pyramidal neurons)	Viable	Loss of dendritic spines, neurodegeneration, reactive gliosis.	[304]
		Advillin-Cre (sensory neurons)	Post-natal lethality at 2 weeks	Neurodegeneration, increased lysosomes in small diameter neurons, vacuolization in large diameter sensory neurons.	[182]
	thyroid	Pax8-Cre	1 month	Irregular follicle shape; hypothyroidism; impaired apical polarity; defective Tg iodination and trafficking; infiltrated macrophages cells present in the colloidal space late endosome/lysosome enlargement and defective lysosomal function.	[11]

Table 5.2. Summary of the peptide and regions mapping found protected/exposed in complex I-associated proteins with CI60 nanobody using HDX-MS. Data obtained and analysed by Y.Ohashi.

	start	end	sequence	Protection/exposure with Nanobody	secondary structure/domain
ATG14L	66	76	VYFDGRDRERF	Small exposure	CC1
	77	83	IDKKERL	Big exposure	
	77	86	IDKKERLSRL	Big exposure	
	87	98	KSKQEEFQKEVL	Exposure	
	99	110	KAMEGKWITDQL	Large protection	Linker between CC1 and CC2
	101	110	MEGKWITDQL	Large protection	
	106	116	ITDQLRWKIMS	Large protection	
	106	117	ITDQLRWKIMSC	Large protection	
	111	117	RWKIMSC	Protection	
Beclin1	153	167	NVTENECQNYKTCLE	big exposure	CC1
VPS34	42	49	PMLKFSGL	protection	CBR1 in C2 domain
VPS15	679	685	ITVVARQ	protection	ha17/Helical domain
	682	691	VARQISTADV	Protection	linker-ha18/Helical domain
	682	692	VARQISTADVY	protection	
	692	705	YCKLMPYLDPYTQ	Protection	ha19/Helical domain
	693	705	CKLMPYLDPYITQ	Protection	
	694	705	KLMPYLDPYITQ	Protection	
	696	705	MPYLDPYITQ	Protection	
	710	716	IERLLVL	Protection	
	717	730	LSVLKEPVSRSIFD	Protection	ha19-ha20/Helical domain
	1015	1026	GTVKIWNSQKME	exposure	Blade1b3/WD40
	1037	1050	TYSRIGGRVKTLTF	weak exposure	Blade1b4-Blade2b2/WD40
	1038	1050	YSRIGGRVKTLTF	weak exposure	Blade1b4-Blade2b2/WD40

References

1. Bilanges, B., Y. Posor, and B. Vanhaesebroeck, *PI3K isoforms in cell signalling and vesicle trafficking.* Nat Rev Mol Cell Biol, 2019. **20**(9): p. 515-534.
2. Vanhaesebroeck, B., et al., *The emerging mechanisms of isoform-specific PI3K signalling.* Nat Rev Mol Cell Biol, 2010. **11**(5): p. 329-41.
3. Balla, T., *Phosphoinositides: tiny lipids with giant impact on cell regulation.* Physiol Rev, 2013. **93**(3): p. 1019-137.
4. Fruman, D.A., et al., *The PI3K Pathway in Human Disease.* Cell, 2017. **170**(4): p. 605-635.
5. Stark, A.K., et al., *PI3K inhibitors in inflammation, autoimmunity and cancer.* Curr Opin Pharmacol, 2015. **23**: p. 82-91.
6. Vanhaesebroeck, B., M.A. Whitehead, and R. Pineiro, *Molecules in medicine mini-review: isoforms of PI3K in biology and disease.* J Mol Med (Berl), 2016. **94**(1): p. 5-11.
7. Backer, J.M., *The intricate regulation and complex functions of the Class III phosphoinositide 3-kinase Vps34.* Biochem J, 2016. **473**(15): p. 2251-71.
8. Carpentier, S., et al., *Class III phosphoinositide 3-kinase/VPS34 and dynamin are critical for apical endocytic recycling.* Traffic, 2013. **14**(8): p. 933-48.
9. Valet, C., et al., *A dual role for the class III PI3K, Vps34, in platelet production and thrombus growth.* Blood, 2017. **130**(18): p. 2032-2042.
10. Grieco, G., et al., *Vps34/PI3KC3 deletion in kidney proximal tubules impairs apical trafficking and blocks autophagic flux, causing a Fanconi-like syndrome and renal insufficiency.* Sci Rep, 2018. **8**(1): p. 14133.
11. Grieco, G., et al., *Class III PI3K Vps34 Controls Thyroid Hormone Production by Regulating Thyroglobulin Iodination, Lysosomal Proteolysis, and Tissue Homeostasis.* Thyroid, 2020. **30**(1): p. 133-146.
12. Itakura, E., et al., *Beclin 1 forms two distinct phosphatidylinositol 3-kinase complexes with mammalian Atg14 and UVRAG.* Mol Biol Cell, 2008. **19**(12): p. 5360-72.
13. Kim, J., et al., *Differential regulation of distinct Vps34 complexes by AMPK in nutrient stress and autophagy.* Cell, 2013. **152**(1-2): p. 290-303.
14. Levine, B. and G. Kroemer, *Biological Functions of Autophagy Genes: A Disease Perspective.* Cell, 2019. **176**(1-2): p. 11-42.
15. Stead, E.R., et al., *Agephagy - Adapting Autophagy for Health During Aging.* Front Cell Dev Biol, 2019. **7**: p. 308.
16. Dikic, I. and Z. Elazar, *Mechanism and medical implications of mammalian autophagy.* Nat Rev Mol Cell Biol, 2018. **19**(6): p. 349-364.
17. Lahiri, V., W.D. Hawkins, and D.J. Klionsky, *Watch What You (Self-) Eat: Autophagic Mechanisms that Modulate Metabolism.* Cell Metab, 2019. **29**(4): p. 803-826.
18. Di Paolo, G. and P. De Camilli, *Phosphoinositides in cell regulation and membrane dynamics.* Nature, 2006. **443**(7112): p. 651-7.
19. Vanhaesebroeck, B., L. Stephens, and P. Hawkins, *PI3K signalling: the path to discovery and understanding.* Nat Rev Mol Cell Biol, 2012. **13**(3): p. 195-203.
20. Dall'Armi, C., K.A. Devereaux, and G. Di Paolo, *The role of lipids in the control of autophagy.* Curr Biol, 2013. **23**(1): p. R33-45.

21. Wallroth, A. and V. Haucke, *Phosphoinositide conversion in endocytosis and the endolysosomal system.* J Biol Chem, 2018. **293**(5): p. 1526-1535.
22. Marat, A.L. and V. Haucke, *Phosphatidylinositol 3-phosphates-at the interface between cell signalling and membrane traffic.* EMBO J, 2016. **35**(6): p. 561-79.
23. Rameh, L.E. and L.C. Cantley, *The role of phosphoinositide 3-kinase lipid products in cell function.* J Biol Chem, 1999. **274**(13): p. 8347-50.
24. Raghu, P., et al., *Phosphoinositides: Regulators of Nervous System Function in Health and Disease.* Front Mol Neurosci, 2019. **12**: p. 208.
25. Simonsen, A., et al., *The role of phosphoinositides in membrane transport.* Curr Opin Cell Biol, 2001. **13**(4): p. 485-92.
26. Baskaran, S., et al., *Two-site recognition of phosphatidylinositol 3-phosphate by PROPPINs in autophagy.* Mol Cell, 2012. **47**(3): p. 339-48.
27. Wang, H., W.T. Lo, and V. Haucke, *Phosphoinositide switches in endocytosis and in the endolysosomal system.* Curr Opin Cell Biol, 2019. **59**: p. 50-57.
28. Alliouachene, S., et al., *Inactivation of the Class II PI3K-C2beta Potentiates Insulin Signaling and Sensitivity.* Cell Rep, 2015. **13**(9): p. 1881-94.
29. Liu, G.Y. and D.M. Sabatini, *mTOR at the nexus of nutrition, growth, ageing and disease.* Nat Rev Mol Cell Biol, 2020. **21**(4): p. 183-203.
30. Saxton, R.A. and D.M. Sabatini, *mTOR Signaling in Growth, Metabolism, and Disease.* Cell, 2017. **168**(6): p. 960-976.
31. Zhang, C.S., et al., *The lysosomal v-ATPase-Ragulator complex is a common activator for AMPK and mTORC1, acting as a switch between catabolism and anabolism.* Cell Metab, 2014. **20**(3): p. 526-40.
32. Korolchuk, V.I., et al., *Lysosomal positioning coordinates cellular nutrient responses.* Nat Cell Biol, 2011. **13**(4): p. 453-60.
33. Gulluni, F., et al., *Class II PI3K Functions in Cell Biology and Disease.* Trends Cell Biol, 2019. **29**(4): p. 339-359.
34. Wang, H., et al., *Autoregulation of Class II Alpha PI3K Activity by Its Lipid-Binding PX-C2 Domain Module.* Mol Cell, 2018. **71**(2): p. 343-351 e4.
35. Bridges, D., et al., *Phosphatidylinositol 3,5-bisphosphate plays a role in the activation and subcellular localization of mechanistic target of rapamycin 1.* Mol Biol Cell, 2012. **23**(15): p. 2955-62.
36. Nemazanyy, I., et al., *Class III PI3K regulates organismal glucose homeostasis by providing negative feedback on hepatic insulin signalling.* Nat Commun, 2015. **6**: p. 8283.
37. Wen, X. and D.J. Klionsky, *An overview of macroautophagy in yeast.* J Mol Biol, 2016. **428**(9 Pt A): p. 1681-99.
38. Schu, P.V., et al., *Phosphatidylinositol 3-kinase encoded by yeast VPS34 gene essential for protein sorting.* Science, 1993. **260**(5104): p. 88-91.
39. Lindmo, K. and H. Stenmark, *Regulation of membrane traffic by phosphoinositide 3-kinases.* J Cell Sci, 2006. **119**(Pt 4): p. 605-14.
40. Workman, P. and R.L. van Montfort, *Unveiling the secrets of the ancestral PI3 kinase Vps34.* Cancer Cell, 2010. **17**(5): p. 421-3.
41. Volinia, S., et al., *A human phosphatidylinositol 3-kinase complex related to the yeast Vps34p-Vps15p protein sorting system.* EMBO J, 1995. **14**(14): p. 3339-48.

42. Rostislavleva, K., et al., *Structure and flexibility of the endosomal Vps34 complex reveals the basis of its function on membranes.* Science, 2015. **350**(6257): p. aac7365.
43. Ohashi, Y., S. Tremel, and R.L. Williams, *VPS34 complexes from a structural perspective.* J Lipid Res, 2019. **60**(2): p. 229-241.
44. Stoetzel, C., et al., *A mutation in VPS15 (PIK3R4) causes a ciliopathy and affects IFT20 release from the cis-Golgi.* Nat Commun, 2016. **7**: p. 13586.
45. Pattingre, S., et al., *Bcl-2 antiapoptotic proteins inhibit Beclin 1-dependent autophagy.* Cell, 2005. **122**(6): p. 927-39.
46. Ranaghan, M.J., et al., *The Autophagy-Related Beclin-1 Protein Requires the Coiled-Coil and BARA Domains To Form a Homodimer with Submicromolar Affinity.* Biochemistry, 2017. **56**(51): p. 6639-6651.
47. Tsukada, M. and Y. Ohsumi, *Isolation and characterization of autophagy-defective mutants of Saccharomyces cerevisiae.* FEBS Lett, 1993. **333**(1-2): p. 169-74.
48. Matsunaga, K., et al., *Two Beclin 1-binding proteins, Atg14L and Rubicon, reciprocally regulate autophagy at different stages.* Nat Cell Biol, 2009. **11**(4): p. 385-96.
49. Sun, Q., et al., *Identification of Barkor as a mammalian autophagy-specific factor for Beclin 1 and class III phosphatidylinositol 3-kinase.* Proc Natl Acad Sci U S A, 2008. **105**(49): p. 19211-6.
50. Fan, W., A. Nassiri, and Q. Zhong, *Autophagosome targeting and membrane curvature sensing by Barkor/Atg14(L).* Proc Natl Acad Sci U S A, 2011. **108**(19): p. 7769-74.
51. Tan, X., et al., *PtdIns(4,5)P2 signaling regulates ATG14 and autophagy.* Proc Natl Acad Sci U S A, 2016. **113**(39): p. 10896-901.
52. Park, J.M., et al., *The ULK1 complex mediates MTORC1 signaling to the autophagy initiation machinery via binding and phosphorylating ATG14.* Autophagy, 2016. **12**(3): p. 547-64.
53. Yuan, H.X., R.C. Russell, and K.L. Guan, *Regulation of PIK3C3/VPS34 complexes by MTOR in nutrient stress-induced autophagy.* Autophagy, 2013. **9**(12): p. 1983-95.
54. Perelman, B., et al., *Molecular cloning of a novel human gene encoding a 63-kDa protein and its sublocalization within the 11q13 locus.* Genomics, 1997. **41**(3): p. 397-405.
55. Thoresen, S.B., et al., *A phosphatidylinositol 3-kinase class III sub-complex containing VPS15, VPS34, Beclin 1, UVRAG and BIF-1 regulates cytokinesis and degradative endocytic traffic.* Exp Cell Res, 2010. **316**(20): p. 3368-78.
56. Kim, Y.M., et al., *mTORC1 phosphorylates UVRAG to negatively regulate autophagosome and endosome maturation.* Mol Cell, 2015. **57**(2): p. 207-18.
57. Takahashi, Y., et al., *Bif-1 interacts with Beclin 1 through UVRAG and regulates autophagy and tumorigenesis.* Nat Cell Biol, 2007. **9**(10): p. 1142-51.
58. Munson, M.J., et al., *mTOR activates the VPS34-UVRAG complex to regulate autolysosomal tubulation and cell survival.* EMBO J, 2015. **34**(17): p. 2272-90.
59. Herman, P.K. and S.D. Emr, *Characterization of VPS34, a gene required for vacuolar protein sorting and vacuole segregation in Saccharomyces cerevisiae.* Mol Cell Biol, 1990. **10**(12): p. 6742-54.
60. Herman, P.K., et al., *A novel protein kinase homolog essential for protein sorting to the yeast lysosome-like vacuole.* Cell, 1991. **64**(2): p. 425-37.

61. Herman, P.K., J.H. Stack, and S.D. Emr, *An essential role for a protein and lipid kinase complex in secretory protein sorting.* Trends Cell Biol, 1992. **2**(12): p. 363-8.
62. Furuya, N., et al., *The evolutionarily conserved domain of Beclin 1 is required for Vps34 binding, autophagy and tumor suppressor function.* Autophagy, 2005. **1**(1): p. 46-52.
63. Lu, J., et al., *NRBF2 regulates autophagy and prevents liver injury by modulating Atg14L-linked phosphatidylinositol-3 kinase III activity.* Nat Commun, 2014. **5**: p. 3920.
64. Cao, Y., et al., *NRBF2 regulates macroautophagy as a component of Vps34 Complex I.* Biochem J, 2014. **461**(2): p. 315-22.
65. Zhong, Y., et al., *Nrbf2 protein suppresses autophagy by modulating Atg14L protein-containing Beclin 1-Vps34 complex architecture and reducing intracellular phosphatidylinositol-3 phosphate levels.* J Biol Chem, 2014. **289**(38): p. 26021-37.
66. Xu, D.Q., et al., *PAQR3 controls autophagy by integrating AMPK signaling to enhance ATG14L-associated PI3K activity.* EMBO J, 2016. **35**(5): p. 496-514.
67. Fimia, G.M., et al., *Ambra1 regulates autophagy and development of the nervous system.* Nature, 2007. **447**(7148): p. 1121-5.
68. Antonioli, M., et al., *AMBRA1 interplay with cullin E3 ubiquitin ligases regulates autophagy dynamics.* Dev Cell, 2014. **31**(6): p. 734-46.
69. Ma, B., et al., *Dapper1 promotes autophagy by enhancing the Beclin1-Vps34-Atg14L complex formation.* Cell Res, 2014. **24**(8): p. 912-24.
70. Zhao, Y., et al., *RACK1 Promotes Autophagy by Enhancing the Atg14L-Beclin 1-Vps34-Vps15 Complex Formation upon Phosphorylation by AMPK.* Cell Rep, 2015. **13**(7): p. 1407-1417.
71. Zhong, Y., et al., *Distinct regulation of autophagic activity by Atg14L and Rubicon associated with Beclin 1-phosphatidylinositol-3-kinase complex.* Nat Cell Biol, 2009. **11**(4): p. 468-76.
72. Cheng, X., et al., *Pacer Mediates the Function of Class III PI3K and HOPS Complexes in Autophagosome Maturation by Engaging Stx17.* Mol Cell, 2017. **65**(6): p. 1029-1043 e5.
73. Miller, S., et al., *Shaping development of autophagy inhibitors with the structure of the lipid kinase Vps34.* Science, 2010. **327**(5973): p. 1638-42.
74. Stjepanovic, G., et al., *Vps34 Kinase Domain Dynamics Regulate the Autophagic PI 3-Kinase Complex.* Mol Cell, 2017. **67**(3): p. 528-534 e3.
75. Young, L.N., et al., *Dynamics and architecture of the NRBF2-containing phosphatidylinositol 3-kinase complex I of autophagy.* Proc Natl Acad Sci U S A, 2016. **113**(29): p. 8224-9.
76. Mercer, T.J., A. Gubas, and S.A. Tooze, *A molecular perspective of mammalian autophagosome biogenesis.* J Biol Chem, 2018. **293**(15): p. 5386-5395.
77. Matsunaga, K., T. Noda, and T. Yoshimori, *Binding Rubicon to cross the Rubicon.* Autophagy, 2009. **5**(6): p. 876-7.
78. McKnight, N.C. and Y. Zhenyu, *Beclin 1, an Essential Component and Master Regulator of PI3K-III in Health and Disease.* Curr Pathobiol Rep, 2013. **1**(4): p. 231-238.
79. Sun, T., et al., *Acetylation of Beclin 1 inhibits autophagosome maturation and promotes tumour growth.* Nat Commun, 2015. **6**: p. 7215.
80. Cianfanelli, V., et al., *Ambra1 at a glance.* J Cell Sci, 2015. **128**(11): p. 2003-8.

81. Strappazzon, F., et al., *Mitochondrial BCL-2 inhibits AMBRA1-induced autophagy.* EMBO J, 2011. **30**(7): p. 1195-208.
82. Galluzzi, L., et al., *Pharmacological modulation of autophagy: therapeutic potential and persisting obstacles.* Nat Rev Drug Discov, 2017. **16**(7): p. 487-511.
83. Levine, B. and G. Kroemer, *Autophagy in the pathogenesis of disease.* Cell, 2008. **132**(1): p. 27-42.
84. Kaushik, S. and A.M. Cuervo, *The coming of age of chaperone-mediated autophagy.* Nat Rev Mol Cell Biol, 2018. **19**(6): p. 365-381.
85. Ktistakis, N.T. and S.A. Tooze, *Digesting the Expanding Mechanisms of Autophagy.* Trends Cell Biol, 2016. **26**(8): p. 624-35.
86. Axe, E.L., et al., *Autophagosome formation from membrane compartments enriched in phosphatidylinositol 3-phosphate and dynamically connected to the endoplasmic reticulum.* J Cell Biol, 2008. **182**(4): p. 685-701.
87. Ikonomov, O.C., et al., *Class III PI 3-kinase is the main source of PtdIns3P substrate and membrane recruitment signal for PIKfyve constitutive function in podocyte endomembrane homeostasis.* Biochim Biophys Acta, 2015. **1853**(5): p. 1240-50.
88. Viaud, J., et al., *Phosphatidylinositol 5-phosphate: a nuclear stress lipid and a tuner of membranes and cytoskeleton dynamics.* Bioessays, 2014. **36**(3): p. 260-72.
89. Vicinanza, M., et al., *PI(5)P regulates autophagosome biogenesis.* Mol Cell, 2015. **57**(2): p. 219-34.
90. De Tito, S., et al., *The Golgi as an Assembly Line to the Autophagosome.* Trends Biochem Sci, 2020. **45**(6): p. 484-496.
91. Hosokawa, N., et al., *Nutrient-dependent mTORC1 association with the ULK1-Atg13-FIP200 complex required for autophagy.* Mol Biol Cell, 2009. **20**(7): p. 1981-91.
92. Walker, S.A. and N.T. Ktistakis, *Autophagosome Biogenesis Machinery.* J Mol Biol, 2020. **432**(8): p. 2449-2461.
93. Shaw, R.J., et al., *The LKB1 tumor suppressor negatively regulates mTOR signaling.* Cancer Cell, 2004. **6**(1): p. 91-9.
94. Gwinn, D.M., et al., *AMPK phosphorylation of raptor mediates a metabolic checkpoint.* Mol Cell, 2008. **30**(2): p. 214-26.
95. Egan, D., et al., *The autophagy initiating kinase ULK1 is regulated via opposing phosphorylation by AMPK and mTOR.* Autophagy, 2011. **7**(6): p. 643-4.
96. Kim, J., et al., *AMPK and mTOR regulate autophagy through direct phosphorylation of Ulk1.* Nat Cell Biol, 2011. **13**(2): p. 132-41.
97. Russell, R.C., et al., *ULK1 induces autophagy by phosphorylating Beclin-1 and activating VPS34 lipid kinase.* Nat Cell Biol, 2013. **15**(7): p. 741-50.
98. Park, J.M., et al., *ULK1 phosphorylates Ser30 of BECN1 in association with ATG14 to stimulate autophagy induction.* Autophagy, 2018. **14**(4): p. 584-597.
99. Wold, M.S., et al., *ULK1-mediated phosphorylation of ATG14 promotes autophagy and is impaired in Huntington's disease models.* Mol Neurodegener, 2016. **11**(1): p. 76.
100. Kim, B.W., et al., *The C-terminal region of ATG101 bridges ULK1 and PtdIns3K complex in autophagy initiation.* Autophagy, 2018. **14**(12): p. 2104-2116.
101. Matsunaga, K., et al., *Autophagy requires endoplasmic reticulum targeting of the PI3-kinase complex via Atg14L.* J Cell Biol, 2010. **190**(4): p. 511-21.

102. Egan, D.F., et al., *Small Molecule Inhibition of the Autophagy Kinase ULK1 and Identification of ULK1 Substrates.* Mol Cell, 2015. **59**(2): p. 285-97.
103. Dunlop, E.A., et al., *ULK1 inhibits mTORC1 signaling, promotes multisite Raptor phosphorylation and hinders substrate binding.* Autophagy, 2011. **7**(7): p. 737-47.
104. Orsi, A., et al., *Dynamic and transient interactions of Atg9 with autophagosomes, but not membrane integration, are required for autophagy.* Mol Biol Cell, 2012. **23**(10): p. 1860-73.
105. Dooley, H.C., et al., *WIPI2 links LC3 conjugation with PI3P, autophagosome formation, and pathogen clearance by recruiting Atg12-5-16L1.* Mol Cell, 2014. **55**(2): p. 238-52.
106. Zientara-Rytter, K. and S. Subramani, *Role of actin in shaping autophagosomes.* Autophagy, 2016. **12**(12): p. 2512-2515.
107. Mizushima, N., *The ATG conjugation systems in autophagy.* Curr Opin Cell Biol, 2019. **63**: p. 1-10.
108. Nakatogawa, H., *Two ubiquitin-like conjugation systems that mediate membrane formation during autophagy.* Essays Biochem, 2013. **55**: p. 39-50.
109. Johansen, T. and T. Lamark, *Selective Autophagy: ATG8 Family Proteins, LIR Motifs and Cargo Receptors.* J Mol Biol, 2020. **432**(1): p. 80-103.
110. Hurley, J.H. and L.N. Young, *Mechanisms of Autophagy Initiation.* Annu Rev Biochem, 2017. **86**: p. 225-244.
111. Birgisdottir, A.B., et al., *Members of the autophagy class III phosphatidylinositol 3-kinase complex I interact with GABARAP and GABARAPL1 via LIR motifs.* Autophagy, 2019. **15**(8): p. 1333-1355.
112. Wang, H., et al., *GABARAPs regulate PI4P-dependent autophagosome:lysosome fusion.* Proc Natl Acad Sci U S A, 2015. **112**(22): p. 7015-20.
113. Liang, C., et al., *Beclin1-binding UVRAG targets the class C Vps complex to coordinate autophagosome maturation and endocytic trafficking.* Nat Cell Biol, 2008. **10**(7): p. 776-87.
114. Jiang, P., et al., *The HOPS complex mediates autophagosome-lysosome fusion through interaction with syntaxin 17.* Mol Biol Cell, 2014. **25**(8): p. 1327-37.
115. Diao, J., et al., *ATG14 promotes membrane tethering and fusion of autophagosomes to endolysosomes.* Nature, 2015. **520**(7548): p. 563-6.
116. Takats, S., et al., *The Warburg Micro Syndrome associated Rab3GAP-Rab18 module promotes autolysosome maturation through the Vps34 Complex I.* FEBS J, 2020.
117. Cheng, X., et al., *Pacer Is a Mediator of mTORC1 and GSK3-TIP60 Signaling in Regulation of Autophagosome Maturation and Lipid Metabolism.* Mol Cell, 2019. **73**(4): p. 788-802 e7.
118. Yu, L., et al., *Termination of autophagy and reformation of lysosomes regulated by mTOR.* Nature, 2010. **465**(7300): p. 942-6.
119. Liang, C., et al., *Autophagic and tumour suppressor activity of a novel Beclin1-binding protein UVRAG.* Nat Cell Biol, 2006. **8**(7): p. 688-99.
120. Rong, Y., et al., *Clathrin and phosphatidylinositol-4,5-bisphosphate regulate autophagic lysosome reformation.* Nat Cell Biol, 2012. **14**(9): p. 924-34.
121. Sridhar, S., et al., *The lipid kinase PI4KIIIbeta preserves lysosomal identity.* EMBO J, 2013. **32**(3): p. 324-39.

122. Schulze, R.J., et al., *Lipid droplet breakdown requires dynamin 2 for vesiculation of autolysosomal tubules in hepatocytes.* J Cell Biol, 2013. **203**(2): p. 315-26.
123. Mizushima, N., T. Yoshimori, and B. Levine, *Methods in mammalian autophagy research.* Cell, 2010. **140**(3): p. 313-26.
124. Yoshii, S.R. and N. Mizushima, *Monitoring and Measuring Autophagy.* Int J Mol Sci, 2017. **18**(9).
125. Mizushima, N. and T. Yoshimori, *How to interpret LC3 immunoblotting.* Autophagy, 2007. **3**(6): p. 542-5.
126. Klionsky, D.J., et al., *Guidelines for the use and interpretation of assays for monitoring autophagy (3rd edition).* Autophagy, 2016. **12**(1): p. 1-222.
127. Polson, H.E., et al., *Mammalian Atg18 (WIPI2) localizes to omegasome-anchored phagophores and positively regulates LC3 lipidation.* Autophagy, 2010. **6**(4): p. 506-22.
128. Tian, W., et al., *An antibody for analysis of autophagy induction.* Nat Methods, 2020. **17**(2): p. 232-239.
129. Zhang, X.J., et al., *Why should autophagic flux be assessed?* Acta Pharmacol Sin, 2013. **34**(5): p. 595-9.
130. Eskelinen, E.L., *To be or not to be? Examples of incorrect identification of autophagic compartments in conventional transmission electron microscopy of mammalian cells.* Autophagy, 2008. **4**(2): p. 257-60.
131. Kimura, S., T. Noda, and T. Yoshimori, *Dissection of the autophagosome maturation process by a novel reporter protein, tandem fluorescent-tagged LC3.* Autophagy, 2007. **3**(5): p. 452-60.
132. Elkin, S.R., A.M. Lakoduk, and S.L. Schmid, *Endocytic pathways and endosomal trafficking: a primer.* Wien Med Wochenschr, 2016. **166**(7-8): p. 196-204.
133. Jones, A.T. and M.J. Clague, *Phosphatidylinositol 3-kinase activity is required for early endosome fusion.* Biochem J, 1995. **311 (Pt 1)**: p. 31-4.
134. Posor, Y., et al., *Spatiotemporal control of endocytosis by phosphatidylinositol-3,4-bisphosphate.* Nature, 2013. **499**(7457): p. 233-7.
135. Simonsen, A., et al., *EEA1 links PI(3)K function to Rab5 regulation of endosome fusion.* Nature, 1998. **394**(6692): p. 494-8.
136. Callaghan, J., et al., *Direct interaction of EEA1 with Rab5b.* Eur J Biochem, 1999. **265**(1): p. 361-6.
137. Nielsen, E., et al., *Rabenosyn-5, a novel Rab5 effector, is complexed with hVPS45 and recruited to endosomes through a FYVE finger domain.* J Cell Biol, 2000. **151**(3): p. 601-12.
138. Schnatwinkel, C., et al., *The Rab5 effector Rabankyrin-5 regulates and coordinates different endocytic mechanisms.* PLoS Biol, 2004. **2**(9): p. E261.
139. Fukuda, M., *TBC proteins: GAPs for mammalian small GTPase Rab?* Biosci Rep, 2011. **31**(3): p. 159-68.
140. Christoforidis, S., et al., *Phosphatidylinositol-3-OH kinases are Rab5 effectors.* Nat Cell Biol, 1999. **1**(4): p. 249-52.
141. Murray, J.T., et al., *Role of Rab5 in the recruitment of hVps34/p150 to the early endosome.* Traffic, 2002. **3**(6): p. 416-27.
142. Law, F., et al., *The VPS34 PI3K negatively regulates RAB-5 during endosome maturation.* J Cell Sci, 2017. **130**(12): p. 2007-2017.
143. Stein, M.P., et al., *Human VPS34 and p150 are Rab7 interacting partners.* Traffic, 2003. **4**(11): p. 754-71.

144. Jaber, N., et al., *Vps34 regulates Rab7 and late endocytic trafficking through recruitment of the GTPase-activating protein Armus.* J Cell Sci, 2016. **129**(23): p. 4424-4435.
145. Law, F. and C.E. Rocheleau, *Vps34 and the Armus/TBC-2 Rab GAPs: Putting the brakes on the endosomal Rab5 and Rab7 GTPases.* Cell Logist, 2017. **7**(4): p. e1403530.
146. Raiborg, C., et al., *FYVE and coiled-coil domains determine the specific localisation of Hrs to early endosomes.* J Cell Sci, 2001. **114**(Pt 12): p. 2255-63.
147. Raiborg, C., et al., *Hrs recruits clathrin to early endosomes.* EMBO J, 2001. **20**(17): p. 5008-21.
148. Raiborg, C., et al., *Hrs sorts ubiquitinated proteins into clathrin-coated microdomains of early endosomes.* Nat Cell Biol, 2002. **4**(5): p. 394-8.
149. Yan, Q., et al., *CART: an Hrs/actinin-4/BERP/myosin V protein complex required for efficient receptor recycling.* Mol Biol Cell, 2005. **16**(5): p. 2470-82.
150. Raiborg, C., K.O. Schink, and H. Stenmark, *Class III phosphatidylinositol 3-kinase and its catalytic product PtdIns3P in regulation of endocytic membrane traffic.* FEBS J, 2013. **280**(12): p. 2730-42.
151. Makaraci, P. and K. Kim, *trans-Golgi network-bound cargo traffic.* Eur J Cell Biol, 2018. **97**(3): p. 137-149.
152. Hu, C.K., M. Coughlin, and T.J. Mitchison, *Midbody assembly and its regulation during cytokinesis.* Mol Biol Cell, 2012. **23**(6): p. 1024-34.
153. Schiel, J.A. and R. Prekeris, *Membrane dynamics during cytokinesis.* Curr Opin Cell Biol, 2013. **25**(1): p. 92-8.
154. Sagona, A.P., et al., *PtdIns(3)P controls cytokinesis through KIF13A-mediated recruitment of FYVE-CENT to the midbody.* Nat Cell Biol, 2010. **12**(4): p. 362-71.
155. Zheng, K., et al., *Selective Autophagy Regulates Cell Cycle in Cancer Therapy.* Theranostics, 2019. **9**(1): p. 104-125.
156. Odle, R.I., et al., *An mTORC1-to-CDK1 Switch Maintains Autophagy Suppression during Mitosis.* Mol Cell, 2020. **77**(2): p. 228-240 e7.
157. Naufer, A., et al., *pH of endophagosomes controls association of their membranes with Vps34 and PtdIns(3)P levels.* J Cell Biol, 2018. **217**(1): p. 329-346.
158. Byfield, M.P., J.T. Murray, and J.M. Backer, *hVps34 is a nutrient-regulated lipid kinase required for activation of p70 S6 kinase.* J Biol Chem, 2005. **280**(38): p. 33076-82.
159. Hirsch, D.S., et al., *pp60c-Src phosphorylates and activates vacuolar protein sorting 34 to mediate cellular transformation.* Cancer Res, 2010. **70**(14): p. 5974-83.
160. Hirsch, D.S., et al., *Insulin activation of vacuolar protein sorting 34 mediates localized phosphatidylinositol 3-phosphate production at lamellipodia and activation of mTOR/S6K1.* Cell Signal, 2014. **26**(6): p. 1258-68.
161. Devereaux, K., et al., *Regulation of mammalian autophagy by class II and III PI 3-kinases through PI3P synthesis.* PLoS One, 2013. **8**(10): p. e76405.
162. Bilanges, B., et al., *Vps34 PI 3-kinase inactivation enhances insulin sensitivity through reprogramming of mitochondrial metabolism.* Nat Commun, 2017. **8**(1): p. 1804.
163. Settembre, C., et al., *TFEB links autophagy to lysosomal biogenesis.* Science, 2011. **332**(6036): p. 1429-33.

164. Ma, X., et al., *MTORC1-mediated NRBF2 phosphorylation functions as a switch for the class III PtdIns3K and autophagy.* Autophagy, 2017. **13**(3): p. 592-607.
165. Furuya, T., et al., *Negative regulation of Vps34 by Cdk mediated phosphorylation.* Mol Cell, 2010. **38**(4): p. 500-11.
166. Wei, Y., et al., *The stress-responsive kinases MAPKAPK2/MAPKAPK3 activate starvation-induced autophagy through Beclin 1 phosphorylation.* Elife, 2015. **4**.
167. Nobukuni, T., et al., *Amino acids mediate mTOR/raptor signaling through activation of class 3 phosphatidylinositol 3OH-kinase.* Proc Natl Acad Sci U S A, 2005. **102**(40): p. 14238-43.
168. Gulati, P., et al., *Amino acids activate mTOR complex 1 via Ca2+/CaM signaling to hVps34.* Cell Metab, 2008. **7**(5): p. 456-65.
169. Hong, Z., et al., *PtdIns3P controls mTORC1 signaling through lysosomal positioning.* J Cell Biol, 2017. **216**(12): p. 4217-4233.
170. Raiborg, C., et al., *Repeated ER-endosome contacts promote endosome translocation and neurite outgrowth.* Nature, 2015. **520**(7546): p. 234-8.
171. Bago, R., et al., *The hVps34-SGK3 pathway alleviates sustained PI3K/Akt inhibition by stimulating mTORC1 and tumour growth.* EMBO J, 2016. **35**(17): p. 1902-22.
172. Bago, R., et al., *Characterization of VPS34-IN1, a selective inhibitor of Vps34, reveals that the phosphatidylinositol 3-phosphate-binding SGK3 protein kinase is a downstream target of class III phosphoinositide 3-kinase.* Biochem J, 2014. **463**(3): p. 413-27.
173. Malik, N., et al., *Mechanism of activation of SGK3 by growth factors via the Class 1 and Class 3 PI3Ks.* Biochem J, 2018. **475**(1): p. 117-135.
174. Ravikumar, B., et al., *Rab5 modulates aggregation and toxicity of mutant huntingtin through macroautophagy in cell and fly models of Huntington disease.* J Cell Sci, 2008. **121**(Pt 10): p. 1649-60.
175. Dou, Z., et al., *The class IA phosphatidylinositol 3-kinase p110-beta subunit is a positive regulator of autophagy.* J Cell Biol, 2010. **191**(4): p. 827-43.
176. Dou, Z., et al., *Class IA PI3K p110beta subunit promotes autophagy through Rab5 small GTPase in response to growth factor limitation.* Mol Cell, 2013. **50**(1): p. 29-42.
177. Whitecross, D.E. and D.H. Anderson, *Identification of the Binding Sites on Rab5 and p110beta Phosphatidylinositol 3-kinase.* Sci Rep, 2017. **7**(1): p. 16194.
178. Jaber, N., et al., *Class III PI3K Vps34 plays an essential role in autophagy and in heart and liver function.* Proc Natl Acad Sci U S A, 2012. **109**(6): p. 2003-8.
179. Willinger, T. and R.A. Flavell, *Canonical autophagy dependent on the class III phosphoinositide-3 kinase Vps34 is required for naive T-cell homeostasis.* Proc Natl Acad Sci U S A, 2012. **109**(22): p. 8670-5.
180. McLeod, I.X., et al., *The class III kinase Vps34 promotes T lymphocyte survival through regulating IL-7Ralpha surface expression.* J Immunol, 2011. **187**(10): p. 5051-61.
181. He, F., et al., *Phosphatidylinositol-3-phosphate is light-regulated and essential for survival in retinal rods.* Sci Rep, 2016. **6**: p. 26978.
182. Zhou, X., et al., *Deletion of PIK3C3/Vps34 in sensory neurons causes rapid neurodegeneration by disrupting the endosomal but not the autophagic pathway.* Proc Natl Acad Sci U S A, 2010. **107**(20): p. 9424-9.

183. Petiot, A., et al., *Distinct classes of phosphatidylinositol 3'-kinases are involved in signaling pathways that control macroautophagy in HT-29 cells.* J Biol Chem, 2000. **275**(2): p. 992-8.
184. Blommaart, E.F., et al., *The phosphatidylinositol 3-kinase inhibitors wortmannin and LY294002 inhibit autophagy in isolated rat hepatocytes.* Eur J Biochem, 1997. **243**(1-2): p. 240-6.
185. Ito, S., et al., *3-Methyladenine suppresses cell migration and invasion of HT1080 fibrosarcoma cells through inhibiting phosphoinositide 3-kinases independently of autophagy inhibition.* Int J Oncol, 2007. **31**(2): p. 261-8.
186. Backer, J.M., *The regulation and function of Class III PI3Ks: novel roles for Vps34.* Biochem J, 2008. **410**(1): p. 1-17.
187. Powis, G., et al., *Wortmannin, a potent and selective inhibitor of phosphatidylinositol-3-kinase.* Cancer Res, 1994. **54**(9): p. 2419-23.
188. Vanhaesebroeck, B., et al., *Synthesis and function of 3-phosphorylated inositol lipids.* Annu Rev Biochem, 2001. **70**: p. 535-602.
189. Miller, S., et al., *Finding a fitting shoe for Cinderella: searching for an autophagy inhibitor.* Autophagy, 2010. **6**(6): p. 805-7.
190. Ronan, B., et al., *A highly potent and selective Vps34 inhibitor alters vesicle trafficking and autophagy.* Nat Chem Biol, 2014. **10**(12): p. 1013-9.
191. Dowdle, W.E., et al., *Selective VPS34 inhibitor blocks autophagy and uncovers a role for NCOA4 in ferritin degradation and iron homeostasis in vivo.* Nat Cell Biol, 2014. **16**(11): p. 1069-79.
192. Honda, A., et al., *Potent, Selective, and Orally Bioavailable Inhibitors of VPS34 Provide Chemical Tools to Modulate Autophagy in Vivo.* ACS Med Chem Lett, 2016. **7**(1): p. 72-6.
193. Pasquier, B., *Autophagy inhibitors.* Cell Mol Life Sci, 2016. **73**(5): p. 985-1001.
194. Mizushima, N., et al., *Autophagy fights disease through cellular self-digestion.* Nature, 2008. **451**(7182): p. 1069-75.
195. Kimmelman, A.C. and E. White, *Autophagy and Tumor Metabolism.* Cell Metab, 2017. **25**(5): p. 1037-1043.
196. Poillet-Perez, L. and E. White, *Role of tumor and host autophagy in cancer metabolism.* Genes Dev, 2019. **33**(11-12): p. 610-619.
197. Wang, Y., et al., *Autophagy inhibition specifically promotes epithelial-mesenchymal transition and invasion in RAS-mutated cancer cells.* Autophagy, 2019. **15**(5): p. 886-899.
198. Yang, Y. and E. White, *Autophagy suppresses TRP53/p53 and oxidative stress to enable mammalian survival.* Autophagy, 2020: p. 1-3.
199. Galluzzi, L., J.M. Bravo-San Pedro, and G. Kroemer, *Defective Autophagy Initiates Malignant Transformation.* Mol Cell, 2016. **62**(4): p. 473-4.
200. Shoji-Kawata, S., et al., *Identification of a candidate therapeutic autophagy-inducing peptide.* Nature, 2013. **494**(7436): p. 201-6.
201. Wu, S., et al., *Targeting the potent Beclin 1-UVRAG coiled-coil interaction with designed peptides enhances autophagy and endolysosomal trafficking.* Proc Natl Acad Sci U S A, 2018. **115**(25): p. E5669-E5678.
202. Chiang, W.C., et al., *High-Throughput Screens To Identify Autophagy Inducers That Function by Disrupting Beclin 1/Bcl-2 Binding.* ACS Chem Biol, 2018. **13**(8): p. 2247-2260.
203. Zachari, M., et al., *The identification and characterisation of autophagy inhibitors from the published kinase inhibitor sets.* Biochem J, 2020. **477**(4): p. 801-814.

204. Pavlinov, I., M. Salkovski, and L.N. Aldrich, *Beclin 1-ATG14L Protein-Protein Interaction Inhibitor Selectively Inhibits Autophagy through Disruption of VPS34 Complex I.* J Am Chem Soc, 2020. **142**(18): p. 8174-8182.
205. Feige, M.J., L.M. Hendershot, and J. Buchner, *How antibodies fold.* Trends Biochem Sci, 2010. **35**(4): p. 189-98.
206. Hamers-Casterman, C., et al., *Naturally occurring antibodies devoid of light chains.* Nature, 1993. **363**(6428): p. 446-8.
207. Flajnik, M.F., N. Deschacht, and S. Muyldermans, *A case of convergence: why did a simple alternative to canonical antibodies arise in sharks and camels?* PLoS Biol, 2011. **9**(8): p. e1001120.
208. Pardon, E., et al., *A general protocol for the generation of Nanobodies for structural biology.* Nat Protoc, 2014. **9**(3): p. 674-93.
209. Rasmussen, S.G., et al., *Structure of a nanobody-stabilized active state of the beta(2) adrenoceptor.* Nature, 2011. **469**(7329): p. 175-80.
210. Geertsma, E.R., et al., *Structure of a prokaryotic fumarate transporter reveals the architecture of the SLC26 family.* Nat Struct Mol Biol, 2015. **22**(10): p. 803-8.
211. Steyaert, J. and B.K. Kobilka, *Nanobody stabilization of G protein-coupled receptor conformational states.* Curr Opin Struct Biol, 2011. **21**(4): p. 567-72.
212. Jahnichen, S., et al., *CXCR4 nanobodies (VHH-based single variable domains) potently inhibit chemotaxis and HIV-1 replication and mobilize stem cells.* Proc Natl Acad Sci U S A, 2010. **107**(47): p. 20565-70.
213. Paalanen, M.M., et al., *The development of activating and inhibiting camelid VHH domains against human protein kinase C epsilon.* Eur J Pharm Sci, 2011. **42**(4): p. 332-9.
214. Aguilar, G., et al., *Using Nanobodies to Study Protein Function in Developing Organisms.* Antibodies (Basel), 2019. **8**(1).
215. Irannejad, R., et al., *Conformational biosensors reveal GPCR signalling from endosomes.* Nature, 2013. **495**(7442): p. 534-8.
216. Buser, D.P., et al., *A versatile nanobody-based toolkit to analyze retrograde transport from the cell surface.* Proc Natl Acad Sci U S A, 2018. **115**(27): p. E6227-E6236.
217. Kuo, C.L., G.A. Oyler, and C.B. Shoemaker, *Accelerated neuronal cell recovery from Botulinum neurotoxin intoxication by targeted ubiquitination.* PLoS One, 2011. **6**(5): p. e20352.
218. Rothbauer, U., et al., *A versatile nanotrap for biochemical and functional studies with fluorescent fusion proteins.* Mol Cell Proteomics, 2008. **7**(2): p. 282-9.
219. Herce, H.D., et al., *Cell-permeable nanobodies for targeted immunolabelling and antigen manipulation in living cells.* Nat Chem, 2017. **9**(8): p. 762-771.
220. Ramirez, D.H., et al., *Engineering a Proximity-Directed O-GlcNAc Transferase for Selective Protein O-GlcNAcylation in Cells.* ACS Chem Biol, 2020.
221. Huet, H.A., et al., *Multivalent nanobodies targeting death receptor 5 elicit superior tumor cell killing through efficient caspase induction.* MAbs, 2014. **6**(6): p. 1560-70.
222. Chaussade, C., et al., *Evidence for functional redundancy of class IA PI3K isoforms in insulin signalling.* Biochem J, 2007. **404**(3): p. 449-58.
223. Hammond, G.R., G. Schiavo, and R.F. Irvine, *Immunocytochemical techniques reveal multiple, distinct cellular*

pools of PtdIns4P and PtdIns(4,5)P(2). Biochem J, 2009. **422**(1): p. 23-35.
224. Rodriguez-Berriguete, G., et al., *Nucleoporin 54 contributes to homologous recombination repair and post-replicative DNA integrity.* Nucleic Acids Res, 2018. **46**(15): p. 7731-7746.
225. Burke, J.E., *Structural Basis for Regulation of Phosphoinositide Kinases and Their Involvement in Human Disease.* Mol Cell, 2018. **71**(5): p. 653-673.
226. Masson, G.R., et al., *Recommendations for performing, interpreting and reporting hydrogen deuterium exchange mass spectrometry (HDX-MS) experiments.* Nat Methods, 2019. **16**(7): p. 595-602.
227. Burke, J.E., *Dynamic structural biology at the protein membrane interface.* J Biol Chem, 2019. **294**(11): p. 3872-3880.
228. Mei, Y., et al., *Identification of BECN1 and ATG14 Coiled-Coil Interface Residues That Are Important for Starvation-Induced Autophagy.* Biochemistry, 2016. **55**(30): p. 4239-53.
229. Li, X., et al., *Imperfect interface of Beclin1 coiled-coil domain regulates homodimer and heterodimer formation with Atg14L and UVRAG.* Nat Commun, 2012. **3**: p. 662.
230. Hailey, D.W., et al., *Mitochondria supply membranes for autophagosome biogenesis during starvation.* Cell, 2010. **141**(4): p. 656-67.
231. Gelebart, P., M. Opas, and M. Michalak, *Calreticulin, a Ca2+-binding chaperone of the endoplasmic reticulum.* Int J Biochem Cell Biol, 2005. **37**(2): p. 260-6.
232. Williams, D.B., *Beyond lectins: the calnexin/calreticulin chaperone system of the endoplasmic reticulum.* J Cell Sci, 2006. **119**(Pt 4): p. 615-23.
233. Bravo-Sagua, R., et al., *Caveolin-1 impairs PKA-DRP1-mediated remodelling of ER-mitochondria communication during the early phase of ER stress.* Cell Death Differ, 2019. **26**(7): p. 1195-1212.
234. Yamamoto, H., et al., *Dual role of the receptor Tom20 in specificity and efficiency of protein import into mitochondria.* Proc Natl Acad Sci U S A, 2011. **108**(1): p. 91-6.
235. Westermann, B., *Mitochondrial fusion and fission in cell life and death.* Nat Rev Mol Cell Biol, 2010. **11**(12): p. 872-84.
236. Xiao, B., et al., *Flow Cytometry-Based Assessment of Mitophagy Using MitoTracker.* Front Cell Neurosci, 2016. **10**: p. 76.
237. Huang, S. and Y. Wang, *Golgi structure formation, function, and post-translational modifications in mammalian cells.* F1000Res, 2017. **6**: p. 2050.
238. Gosavi, P., et al., *The Golgi ribbon in mammalian cells negatively regulates autophagy by modulating mTOR activity.* J Cell Sci, 2018. **131**(3).
239. Liu, J., et al., *STK16 regulates actin dynamics to control Golgi organization and cell cycle.* Sci Rep, 2017. **7**: p. 44607.
240. Klionsky, D.J., et al., *Guidelines for the use and interpretation of assays for monitoring autophagy in higher eukaryotes.* Autophagy, 2008. **4**(2): p. 151-75.
241. Tanida, I., et al., *Lysosomal turnover, but not a cellular level, of endogenous LC3 is a marker for autophagy.* Autophagy, 2005. **1**(2): p. 84-91.
242. Nascimbeni, A.C., P. Codogno, and E. Morel, *Local detection of PtdIns3P at autophagosome biogenesis membrane platforms.* Autophagy, 2017: p. 1-11.

243. Fujita, N., et al., *The Atg16L complex specifies the site of LC3 lipidation for membrane biogenesis in autophagy.* Mol Biol Cell, 2008. **19**(5): p. 2092-100.
244. Zalckvar, E., et al., *DAP-kinase-mediated phosphorylation on the BH3 domain of beclin 1 promotes dissociation of beclin 1 from Bcl-XL and induction of autophagy.* EMBO Rep, 2009. **10**(3): p. 285-92.
245. Gurkar, A.U., et al., *Identification of ROCK1 kinase as a critical regulator of Beclin1-mediated autophagy during metabolic stress.* Nat Commun, 2013. **4**: p. 2189.
246. Fujiwara, N., et al., *Regulation of Beclin 1 Protein Phosphorylation and Autophagy by Protein Phosphatase 2A (PP2A) and Death-associated Protein Kinase 3 (DAPK3).* J Biol Chem, 2016. **291**(20): p. 10858-66.
247. Korolchuk, V.I. and D.C. Rubinsztein, *Regulation of autophagy by lysosomal positioning.* Autophagy, 2011. **7**(8): p. 927-8.
248. Johnson, E.E., et al., *Gene silencing reveals a specific function of hVps34 phosphatidylinositol 3-kinase in late versus early endosomes.* J Cell Sci, 2006. **119**(Pt 7): p. 1219-32.
249. Mills, I.G., A.T. Jones, and M.J. Clague, *Involvement of the endosomal autoantigen EEA1 in homotypic fusion of early endosomes.* Curr Biol, 1998. **8**(15): p. 881-4.
250. Lippai, M. and P. Low, *The role of the selective adaptor p62 and ubiquitin-like proteins in autophagy.* Biomed Res Int, 2014. **2014**: p. 832704.
251. Pankiv, S., et al., *p62/SQSTM1 binds directly to Atg8/LC3 to facilitate degradation of ubiquitinated protein aggregates by autophagy.* J Biol Chem, 2007. **282**(33): p. 24131-45.
252. Kroemer, G. and B. Levine, *Autophagic cell death: the story of a misnomer.* Nat Rev Mol Cell Biol, 2008. **9**(12): p. 1004-10.
253. Liu, Y., et al., *Autosis is a Na+,K+-ATPase-regulated form of cell death triggered by autophagy-inducing peptides, starvation, and hypoxia-ischemia.* Proc Natl Acad Sci U S A, 2013. **110**(51): p. 20364-71.
254. Wang, C. and R.J. Youle, *Predominant requirement of Bax for apoptosis in HCT116 cells is determined by Mcl-1's inhibitory effect on Bak.* Oncogene, 2012. **31**(26): p. 3177-89.
255. Vanhaesebroeck, B., et al., *Signalling by PI3K isoforms: insights from gene-targeted mice.* Trends Biochem Sci, 2005. **30**(4): p. 194-204.
256. Longhin, E., et al., *Isolation and Characterization of Nanobodies against a Zinc-Transporting P-Type ATPase.* Antibodies (Basel), 2018. **7**(4).
257. Plazinska, A., et al., *Molecular interactions between fenoterol stereoisomers and derivatives and the beta(2)-adrenergic receptor binding site studied by docking and molecular dynamics simulations.* J Mol Model, 2013. **19**(11): p. 4919-30.
258. Bruce, V.J., M. Lopez-Islas, and B.R. McNaughton, *Resurfaced cell-penetrating nanobodies: A potentially general scaffold for intracellularly targeted protein discovery.* Protein Sci, 2016. **25**(6): p. 1129-37.
259. Schumacher, D., et al., *Nanobodies: Chemical Functionalization Strategies and Intracellular Applications.* Angew Chem Int Ed Engl, 2018. **57**(9): p. 2314-2333.
260. Daniel, K., et al., *Conditional control of fluorescent protein degradation by an auxin-dependent nanobody.* Nat Commun, 2018. **9**(1): p. 3297.

261. Mitchell, L.S. and L.J. Colwell, *Analysis of nanobody paratopes reveals greater diversity than classical antibodies.* Protein Eng Des Sel, 2018. **31**(7-8): p. 267-275.
262. Geng, J., et al., *Post-Golgi Sec proteins are required for autophagy in Saccharomyces cerevisiae.* Mol Biol Cell, 2010. **21**(13): p. 2257-69.
263. Ge, L., et al., *The ER-Golgi intermediate compartment is a key membrane source for the LC3 lipidation step of autophagosome biogenesis.* Elife, 2013. **2**: p. e00947.
264. Davis, S., J. Wang, and S. Ferro-Novick, *Crosstalk between the Secretory and Autophagy Pathways Regulates Autophagosome Formation.* Dev Cell, 2017. **41**(1): p. 23-32.
265. Pavel, M. and D.C. Rubinsztein, *Mammalian autophagy and the plasma membrane.* FEBS J, 2017. **284**(5): p. 672-679.
266. Rambold, A.S., et al., *Tubular network formation protects mitochondria from autophagosomal degradation during nutrient starvation.* Proc Natl Acad Sci U S A, 2011. **108**(25): p. 10190-5.
267. Graef, M., *A dividing matter: Drp1/Dnm1-independent mitophagy.* J Cell Biol, 2016. **215**(5): p. 599-601.
268. Yamashita, S.I., et al., *Mitochondrial division occurs concurrently with autophagosome formation but independently of Drp1 during mitophagy.* J Cell Biol, 2016. **215**(5): p. 649-665.
269. Kihara, A., et al., *Beclin-phosphatidylinositol 3-kinase complex functions at the trans-Golgi network.* EMBO Rep, 2001. **2**(4): p. 330-5.
270. Nakajima, K., et al., *RAB30 regulates PI4KB (phosphatidylinositol 4-kinase beta)-dependent autophagy against group A Streptococcus.* Autophagy, 2019. **15**(3): p. 466-477.
271. Leestemaker, Y. and H. Ovaa, *Tools to investigate the ubiquitin proteasome system.* Drug Discov Today Technol, 2017. **26**: p. 25-31.
272. Runwal, G., et al., *LC3-positive structures are prominent in autophagy-deficient cells.* Sci Rep, 2019. **9**(1): p. 10147.
273. Bakula, D., et al., *WIPI3 and WIPI4 beta-propellers are scaffolds for LKB1-AMPK-TSC signalling circuits in the control of autophagy.* Nat Commun, 2017. **8**: p. 15637.
274. Scotto Rosato, A., et al., *TRPML1 links lysosomal calcium to autophagosome biogenesis through the activation of the CaMKKbeta/VPS34 pathway.* Nat Commun, 2019. **10**(1): p. 5630.
275. Marat, A.L., et al., *mTORC1 activity repression by late endosomal phosphatidylinositol 3,4-bisphosphate.* Science, 2017. **356**(6341): p. 968-972.
276. Han, L., et al., *Autophagy flux inhibition, G2/M cell cycle arrest and apoptosis induction by ubenimex in glioma cell lines.* Oncotarget, 2017. **8**(64): p. 107730-107743.
277. Zhang, X., et al., *Inhibition of autophagy enhances apoptosis induced by proteasome inhibitor bortezomib in human glioblastoma U87 and U251 cells.* Mol Cell Biochem, 2014. **385**(1-2): p. 265-75.
278. Rubinstein, A.D. and A. Kimchi, *Life in the balance - a mechanistic view of the crosstalk between autophagy and apoptosis.* J Cell Sci, 2012. **125**(Pt 22): p. 5259-68.
279. Wei, Y., et al., *JNK1-mediated phosphorylation of Bcl-2 regulates starvation-induced autophagy.* Mol Cell, 2008. **30**(6): p. 678-88.
280. McKnight, N.C., et al., *Beclin 1 is required for neuron viability and regulates endosome pathways via the UVRAG-VPS34 complex.* PLoS Genet, 2014. **10**(10): p. e1004626.

281. Liu, Y., et al., *TLR9 and beclin 1 crosstalk regulates muscle AMPK activation in exercise.* Nature, 2020. **578**(7796): p. 605-609.
282. Ohashi, Y., et al., *Characterization of Atg38 and NRBF2, a fifth subunit of the autophagic Vps34/PIK3C3 complex.* Autophagy, 2016. **12**(11): p. 2129-2144.
283. Sinha, S. and B. Levine, *The autophagy effector Beclin 1: a novel BH3-only protein.* Oncogene, 2008. **27 Suppl 1**: p. S137-48.
284. Gao, X., et al., *Dapper1 is a nucleocytoplasmic shuttling protein that negatively modulates Wnt signaling in the nucleus.* J Biol Chem, 2008. **283**(51): p. 35679-88.
285. Pietrocola, F., et al., *Caloric Restriction Mimetics Enhance Anticancer Immunosurveillance.* Cancer Cell, 2016. **30**(1): p. 147-160.
286. Rosenfeldt, M.T., et al., *p53 status determines the role of autophagy in pancreatic tumour development.* Nature, 2013. **504**(7479): p. 296-300.
287. Fernandez, A.F., et al., *Disruption of the beclin 1-BCL2 autophagy regulatory complex promotes longevity in mice.* Nature, 2018. **558**(7708): p. 136-140.
288. Rocchi, A., et al., *A Becn1 mutation mediates hyperactive autophagic sequestration of amyloid oligomers and improved cognition in Alzheimer's disease.* PLoS Genet, 2017. **13**(8): p. e1006962.
289. Vega-Rubin-de-Celis, S., et al., *Increased autophagy blocks HER2-mediated breast tumorigenesis.* Proc Natl Acad Sci U S A, 2018. **115**(16): p. 4176-4181.
290. Winslow, A.R., et al., *alpha-Synuclein impairs macroautophagy: implications for Parkinson's disease.* J Cell Biol, 2010. **190**(6): p. 1023-37.
291. Ravikumar, B., R. Duden, and D.C. Rubinsztein, *Aggregate-prone proteins with polyglutamine and polyalanine expansions are degraded by autophagy.* Hum Mol Genet, 2002. **11**(9): p. 1107-17.
292. Zhou, X., J. Takatoh, and F. Wang, *The mammalian class 3 PI3K (PIK3C3) is required for early embryogenesis and cell proliferation.* PLoS One, 2011. **6**(1): p. e16358.
293. Kimura, H., et al., *Vps34 regulates myofibril proteostasis to prevent hypertrophic cardiomyopathy.* JCI Insight, 2017. **2**(1): p. e89462.
294. Reifler, A., et al., *Conditional knockout of pik3c3 causes a murine muscular dystrophy.* Am J Pathol, 2014. **184**(6): p. 1819-30.
295. Sabha, N., et al., *PIK3C2B inhibition improves function and prolongs survival in myotubular myopathy animal models.* J Clin Invest, 2016. **126**(9): p. 3613-25.
296. Bechtel, W., et al., *Vps34 deficiency reveals the importance of endocytosis for podocyte homeostasis.* J Am Soc Nephrol, 2013. **24**(5): p. 727-43.
297. Chen, J., et al., *mVps34 deletion in podocytes causes glomerulosclerosis by disrupting intracellular vesicle trafficking.* J Am Soc Nephrol, 2013. **24**(2): p. 198-207.
298. Ghosh, A.K., et al., *Novel role of autophagy-associated Pik3c3 gene in gonadal white adipose tissue browning in aged C57/Bl6 male mice.* Aging (Albany NY), 2018. **10**(4): p. 764-774.
299. Morishita, H., et al., *Deletion of autophagy-related 5 (Atg5) and Pik3c3 genes in the lens causes cataract independent of programmed organelle degradation.* J Biol Chem, 2013. **288**(16): p. 11436-47.

300. He, F., et al., *Critical Role for Phosphatidylinositol-3 Kinase Vps34/PIK3C3 in ON-Bipolar Cells.* Invest Ophthalmol Vis Sci, 2019. **60**(8): p. 2861-2874.
301. Liu, Y., et al., *Class III PI3K Positively Regulates Platelet Activation and Thrombosis via PI(3)P-Directed Function of NADPH Oxidase.* Arterioscler Thromb Vasc Biol, 2017. **37**(11): p. 2075-2086.
302. Logan, A.M., et al., *Schwann cell-specific deletion of the endosomal PI 3-kinase Vps34 leads to delayed radial sorting of axons, arrested myelination, and abnormal ErbB2-ErbB3 tyrosine kinase signaling.* Glia, 2017. **65**(9): p. 1452-1470.
303. Parekh, V.V., et al., *Impaired autophagy, defective T cell homeostasis, and a wasting syndrome in mice with a T cell-specific deletion of Vps34.* J Immunol, 2013. **190**(10): p. 5086-101.
304. Wang, L., K. Budolfson, and F. Wang, *Pik3c3 deletion in pyramidal neurons results in loss of synapses, extensive gliosis and progressive neurodegeneration.* Neuroscience, 2011. **172**: p. 427-42.